Characterisation and Correction of Respiratory-Motion Artefacts in Cardiac PET-CT

Sarah J. McQuaid

UCL

A thesis submitted to University College London
for the degree of Doctor of Philosophy (Ph.D.)
in Nuclear Medicine.

September 2009

I, Sarah McQuaid, confirm that the work presented in this thesis is my own. Where information has been derived from other sources, I confirm that this has been indicated in the thesis.

Abstract

Respiratory motion during cardiac Positron Emission Tomography (PET) – Computed Tomography (CT) imaging results in blurring of the PET data and can induce mismatches between the PET and CT datasets, leading to attenuation-correction artefacts. The aim of this project was to develop a method of motion-correction to overcome both of these problems.

The approach implemented was to transform a single CT to match the frames of a gated PET study, to facilitate respiratory-matched attenuation-correction, without the need for a gated CT. This is beneficial for lowering the radiation dose to the patient and in reducing PET–CT mismatches, which can arise even in gated studies.

The heart and diaphragm were identified through phantom studies as the structures responsible for generating attenuation-correction artefacts in the heart and their motions therefore needed to be considered in transforming the CT. Estimating heart motion was straight-forward, due to its high contrast in PET, however the poor diaphragm contrast meant that additional information was required to track its position. Therefore a diaphragm shape model was constructed using segmented diaphragm surfaces, enabling complete diaphragm surfaces to be produced from incomplete and noisy initial estimates. These complete surfaces, in combination with the estimated heart motions were used to transform the CT.

The PET frames were then attenuation-corrected with the transformed CT, reconstructed, aligned and summed, to produce motion-free images. It was found that motion-blurring was reduced through alignment, although benefits were marginal in the presence of small respiratory motions. Quantitative accuracy was improved from use of the transformed CT for attenuation-correction (compared with no CT transformation), which was attributed to both the heart and the diaphragm transformations. In comparison to a gated CT, a substantial dose saving and a reduced dependence on gating techniques were achieved, indicating the potential value of the technique in routine clinical procedures.

Acknowledgements

I would like to thank everyone at the Institute of Nuclear Medicine, UCL for making my time in the department such an enjoyable one. I am particularly indebted to my primary supervisor Brian Hutton, for the many ideas and valuable discussions, which were so important to the progression of the project and for all the help and encouragement. I would also like to thank Vincent Cunningham, my secondary supervisor, for his useful input to the project.

Thank you to all of the other members of the INM physics research group, who have provided answers to many of my questions and provided support and friendship during my time in the group. A particular thank you to Kjell Erlandsson and Tryphon Lambrou for the invaluable feedback on my thesis and for giving advice on many aspects of my work. I am also very grateful to John Dickson and Ian Cullum, who have assisted with many of the practical aspects of the project.

There are a number of people who have provided clinical data with which I was able to develop and test my methods, to whom I am extremely grateful. Firstly, thank you to Valentino Bettinardi and Maria Carla Gilardi for providing the PET-CT datasets that were so crucial to the project and to Valentino for his perseverance in finding methods of reconstructing my datasets. Thank you to Tinsu Pan for allowing me to use the respiratory-gated CT datasets and to Mike King and Joyoni Dey for their assistance in supplying these images. Also thank you to Joyoni for making her data on heart motion available to me, which I was able to incorporate into my investigations.

Finally, thank you to my family and friends, particularly to my parents for their support over the years and to my sisters for their friendship. And a huge thank you to my husband, Dualta, for his love, support and encouragement, which has been a tremendous source of strength and inspiration for me throughout the PhD.

Contents

List of Figures

List of Tables

List of Abbreviations

3D	3-dimensional
4D	4-dimensional
AAM	Active Appearance Model
ACF	Attenuation Correction Factor
CAD	Coronary Artery Disease
CT	X-ray Computed Tomography
CTA	CT Angiography
ECG	Electrocardiogram
FBP	Filtered Back Projection
FWHM	Full Width at Half Maximum
HLA	Horizontal Long Axis
HU	Hounsfield Units
ICA	Independent Component Analysis
IDL	Interactive Data Language
LOR	Line-of-Response
LVEF	Left-Ventricular Ejection Fraction
MLEM	Maximum Likelihood Expectation Maximisation
MPI	Myocardial Perfusion Imaging
MRI	Magnetic Resonance Imaging
NCAT	NURBS-based Cardiac Torso Phantom

NMI	Normalised Mutual Information
NURBS	Non-Uniform Rational B-Splines
OSEM	Ordered Subsets Expectation Maximisation
PCA	Principal Component Analysis
PDM	Point Distribution Model
PET	Positron Emission Tomography
PMT	Photo-Multiplier Tube
SA	Short Axis
SNR	Signal-to-noise ratio
SSD	Sum of Squared Differences
SSM	Statistical Shape Model
TLC	Total Lung Capacity
VLA	Vertical Long Axis
XCAT	Extended Cardiac Torso Phantom

Chapter 1

Introduction

The occurrence of respiratory motion during myocardial perfusion imaging (MPI) with a combined Positron Emission Tomography (PET) – X-ray Computed Tomography (CT) system can lead to a degradation in image quality, due to the blurring effects introduced into the PET data as a result of motion-averaging as well as from motion-induced mismatches between the PET and CT datasets. This latter issue can result in artefacts being introduced into the PET data, through the attenuation-correction being performed using the mismatched CT. Overcoming the motion effects is clearly desirable, with the potential of improving the efficacy of such studies, due to the increased quantitative accuracy and improved resolution.

The effects of motion-averaging due to respiratory motion are well documented and methods of overcoming them have been previously investigated, although this work has predominantly focused on lung motion-correction. A well-established method is to perform gating, where the PET data are split into motion-limited frames and subsequently realigned, such that blurring is reduced but with no loss to the count-statistics.

The effects of PET–CT mismatch however have previously received less attention, despite attenuation being an important correction in obtaining quantitative images. The increasing use of PET (rather than Single Photon Emission Computed Tomography (SPECT)) for performing MPI, as well as the advent of combined PET-CT systems where the CT is used for attenuation-correction has led to an increasing interest in this area, not only as a result of the higher dependence of PET on attenuation, but also due to the emergence of specific issues relating to the different effects of motion on PET and CT acquisitions. The resulting PET–CT mismatches have been found to be problematic in clinical studies, where the acquisition of a single CT frame, either during free-breathing or with breath-hold, does not always produce a good match for the motion-averaged PET. The resulting attenuation-

correction artefacts often have the appearance of a perfusion defect and hence need to be resolved for false-positive results to be avoided.

The requirement for an accurate attenuation-correction is also present in the case that the PET study is respiratory-gated; in order for quantitatively accurate results to be obtained, it is necessary for every frame to be corrected with a respiratory-matched attenuation map, prior to reconstruction and motion-correction. One potential method of achieving this is to acquire a gated CT study, such that respiratory-matched CT frames exist for all gated PET frames. There are a number of ongoing issues with this approach however, relating to the dose associated with such studies and to the issues of variations in respiratory cycles, which can lead to PET–CT mismatches, even in the gated frames.

For these reasons, the primary objective of this project was to develop a method of motion-correction that would allow quantitatively accurate, motion-free PET images of the left-ventricular myocardium to be produced. For this to be achieved, it was important to overcome the issues of PET–CT mismatch and therefore the aim was to implement a method based on acquiring only a single CT, which would be transformed to match the respiratory positions of each PET frame. In this way, the patient dose would not be increased from that associated with current acquisition protocols and the problems of residual PET–CT mismatches in the gated frames would be reduced. The aim was to use data-driven methods to determine the motion of anatomy over the respiratory cycle, to facilitate the subsequent transformation of the single CT and thereby overcome the ongoing issues associated with gated CT acquisitions.

The application of the respiratory-matched attenuation-correction would then allow quantitative accuracy to be maintained during the subsequent motion-correction, producing a final result that is free from blurring effects and attenuation-correction artefacts caused by respiratory motion.

1.1 Overview of Thesis

The thesis is broadly divided into two parts; the characterisation of respiratory motion artefacts in cardiac PET-CT and the further development and implementation of methods with which to overcome these problems.

Some of the issues relating to the problem of motion-correction in cardiac PET studies, as well as existing methods of correction are outlined in the background chapter (Chapter 2), from which the main considerations in the development of a motion-correction approach were determined.

Chapter 3 addresses the issue of the source of attenuation-correction artefacts with the use of a software phantom (the NCAT phantom). By controlling the type of emission–

transmission mismatches present, it was possible to ascertain which types of motion were important in the generation of artefacts that specifically affect cardiac studies. This was used to determine which structures needed to be considered in the CT transformation and the heart and diaphragm were both highlighted as important structures from this study.

Having determined the importance of the diaphragm, further investigations were undertaken to study its shape and motion in more detail. This required the segmentation of the diaphragm in gated images, for which a segmentation algorithm was developed. The considerations in the development of the algorithm, the final methods used and its validation are described in Chapter 4. This was applied to ten gated CT datasets, giving 100 segmented diaphragm surfaces in total.

The region of the diaphragm exhibits poor contrast in gated cardiac PET images and hence ascertaining its shape and motion for subsequent transformation required additional information from that obtainable from the PET images alone. For this reason, the segmented diaphragm surfaces were used to construct a Statistical Shape Model, such that knowledge of typical diaphragm shapes and motions could be used to complement the PET-derived information. The construction and testing of this model is described in Chapter 5, where testing was performed to determine its ability to describe diaphragm shapes and motions as well as its performance in the presence of missing data and noise, which are both relevant when applying the methods to PET images. The model output comprised of complete sets of diaphragm surfaces over the respiratory cycle, facilitating the subsequent transformation.

The methods developed to transform the CT incorporated the results of the shape model and of a rigid-registration on the heart activity. These methods are described in Chapter 6. Having obtained the transformed CT, the respiratory-matched attenuation-correction was performed and the corrected PET frames were reconstructed and aligned according to the heart registration results, to form motion-corrected images. These stages and the final assessment of the images produced are described in Chapter 7. Finally, a summary of the findings of each chapter and potential areas for future investigation are outlined in the Conclusions (Chapter 8).

Chapter 2

Background

This chapter outlines the background to the main areas dealt with in the rest of the thesis. An introduction to the imaging modalities with which this research is concerned is given in Sections 2.1 and 2.2, and 2.3 introduces Myocardial Perfusion Imaging (MPI) and how it is performed using these modalities. The issues that are central to this project are related to attenuation and motion effects, which are introduced in Sections 2.4 and 2.5, and an overview of respiratory gating methods for both PET and CT is given in Section 2.6. Finally, there is a large body of work in relation to existing motion-correction methods, which is summarised in Section 2.7 and a discussion regarding how these works relate to this project is also included.

2.1 PET Imaging

This project is based on improving image quality in Positron Emission Tomography (PET), which is an imaging modality involving the administration of a radio-labelled pharmaceutical to a patient and mapping its distribution with the use of a dedicated camera. The technique has been in use since the 1970's, most commonly in oncology with the use of F-18 fluoro-deoxy-glucose (FDG) (Ter-Pogossian, 1995). More recently, it has been used in conjunction with other radionuclides, such as Rb-82 for the purposes of myocardial perfusion imaging (Selwyn et al., 1982) and hence its clinical applications have been widened.

The principle of PET is to image the distribution of a positron-emitting radionuclide indirectly with the detection of annihilation photons. Positrons are emitted from unstable, proton-rich nuclei, where the decay of a proton into a neutron with the emission of a positron brings the nuclei closer to a stable state. The presence of the positron cannot be measured directly due to its short range (typically a few mm in water) and hence most are absorbed within the body. The cause of this limited range is the interaction between the positron and

atomic electrons, which initially causes the positron to lose momentum and finally results in an annihilation with an atomic electron. This occurs when the positron momentum is small and results in the combined rest-mass energy of the positron and electron being converted into photons, such that energy and momentum are conserved. This most commonly occurs with the emission of two 511 keV gamma-rays at approximately 180^{o} to each other.

These annihilation photons have a much longer range than that exhibited by positrons, allowing for easier detection and hence can be used as a substitute for detecting the positron emitter. However, the finite distance travelled by the positron prior to annihilation limits the accuracy with which the positron-emitter can be imaged, with the degradation in accuracy dependent on the initial positron energy. The mean distances travelled by positrons emitted by ^{18}FDG and ^{82}Rb in water are 0.6 mm and 5.9 mm respectively, corresponding with maximum positron energies of 0.64 MeV and 3.4 MeV (Bailey et al., 2005). This indicates that the higher energy of the ^{82}Rb positron is capable of producing a degradation in image quality, particularly in low density regions such as the lungs where the mean positron ranges are greater (Sanchez-Crespo et al., 2004).

Detecting a photon requires the deposition of its energy in the detector, commonly a scintillation device, in which photons with a frequency in the visible range are produced from the deposited energy. These then reach a photomultiplier tube (PMT), where the incoming photons are converted to electrons by means of a photocathode and amplified to produce a measurable signal. The size of the signal produced is proportional to the energy deposited in the detector, allowing photons to be detected and their energy measured.

In order to record an annihilation event, both annihilation photons need to be detected. Most PET scanners are therefore arranged in a ring pattern, allowing photons emitted in opposite directions to be detected simultaneously. If two photons are detected within a given time of each other, they are recorded as a coincidence event and are assumed to have originated from the same annihilation. The detection of the first photon opens a timing window, during which time the detection of a second photon in another detector results in a coincidence being recorded. It is then possible to specify a line along which the annihilation occurred (assuming the photons were co-linear), known as a line-of-response (LOR), which is a straight line between the two detectors. Many such coincidence events are recorded and their corresponding LORs obtained. Reconstructing an image of the activity distribution therefore involves determining where along their LORs each event is likely to have originated. Figure 2.1a shows the location of an annihilation (indicated by the star) and the path of the two photons towards the detector ring, forming the LOR.

Not all annihilation events are detected by the scanner; only a small proportion of those emitted are at an angle subtended by the detectors and some emitted photons are absorbed within the body and other surrounding materials, giving rise to an attenuation of the emitted intensity. Photon scatter also occurs, which may either cause the photon to be deflected

away from the detector and hence be missed, or result in the photon reaching a different detector, causing an erroneous measurement of the LOR. These processes are illustrated in Figure 2.1b and c.

The scatter and attenuation processes result in a degradation of quantitative accuracy of the measured radiotracer distribution. PET is particularly susceptible to attenuation effects, due to the need to detect both photons in opposite detectors; therefore the attenuation experienced by a single photon pair is the combined path length for the two photons. The transmitted intensity, I, from an initial intensity I_0 is given as follows:

$$I = I_0 \cdot \exp\left(-\int \mu(x, E)\, dx\right) \tag{2.1}$$

where $\mu(x, E)$ (cm^{-1}) is the linear attenuation coefficient at position x, which is a function of energy (E). The total attenuation is therefore dependent on the attenuating properties of all materials in the path of the beam and also on the energy of the incident photons. For a photon pair therefore, Equation 2.1 involves materials encountered by both photons, since both need to be detected for a single event to be registered.

The detection of "random coincidences" is also problematic for PET imaging:- this occurs when two photons from separate annihilations arrive at two detectors within the timing window and hence appear to have originated from the same event. Such an occurrence causes the LOR to be mis-positioned and hence adds to the apparent background activity in the reconstructed image. This process is illustrated in Figure 2.1d.

Other factors that need to be addressed in PET imaging are the non-colinearity of the emitted photons, the effects of the finite spatial resolution of the detector and the effects of dead-time. The first of these relates to the fact that the photons are not emitted at exactly 180^o to each other, due to the small remaining positron momentum at the time of annihilation. Since the production of LORs assumes co-linearity, deviations from this introduces errors, which manifests as a degradation of the reconstructed spatial resolution. The spatial resolution achievable is also affected by the precision with which the detector can determine the point of intersection of the incoming photon. The combination of these effects results in a spatial resolution of typically 6 mm in the reconstructed image on modern scanners (Beyer et al., 2000; Bettinardi et al., 2004; Teräs et al., 2007), determined by the width of the peak produced by a point-source at half the maximum intensity (or full-width at half-maximum: FWHM). Dead-time is problematic at high count-rates (Germano and Hoffman, 1990) and is caused by the finite time needed by the detectors to respond to incoming photons. Therefore, if a second photon arrives while the system is still responding to a previous photon, it is unable to respond properly and can result in the loss of the second photon causing a reduction in sensitivity. If two scattered photons have a combined energy

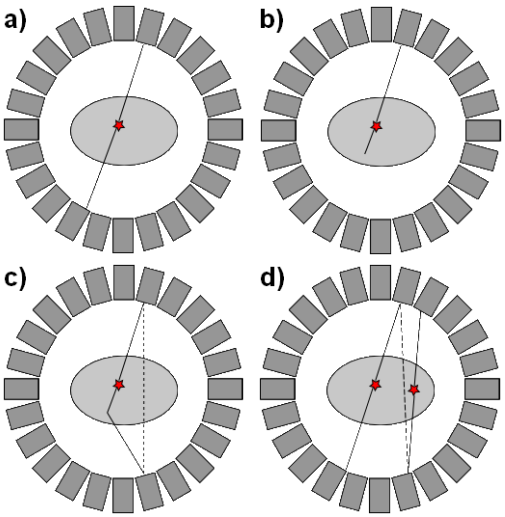

Figure 2.1: An illustration of PET detection processes: a) a true coincidence: a pair of photons detected in coincidence at opposite detectors, b) attenuation: absorption of the photon results in no event being recorded, c) scatter: the change of direction of the photon due to scatter produces an erroneous LOR, d) random coincidence: two photons from different annihilation events are detected in coincidence, again producing an erroneous LOR.

close to 511 keV, their arrival in close succession may appear to be from a single annihilation photon and therefore mis-placed LORs can result (Badawi and Marsden, 1999).

In order to achieve good image quality, it is important to minimise the impact of all of the above factors. In addition to hardware arrangements that can be optimised for achieving good image quality (e.g. having small crystal sizes, which minimises dead-time effects and the use of shielding to reduce scatter from activity outside of the field-of-view), software-based corrections also need to be employed. Such corrections can be applied either prior to, or during the reconstruction process. The implementation of these corrections will result in the final image being a better representation of the initial activity distribution and hence more quantitatively accurate. Of particular interest to this project is the correction for attenuation, and methods of implementing this correction are therefore described in more detail in Section 2.5.

Finally, to produce the 3-dimensional (3D) map of the activity distribution, it is necessary to perform a reconstruction such that the distribution of counts over the LORs is estimated. The reconstruction is performed on the projection data (sets of parallel LORs), to which the corrections for attenuation and scatter, etc. have already been applied. (The projections can also be viewed in sinogram space, which is a graph of the distance along the projection against the angle of the projection.) One algorithm that can be used to reconstruct images in PET is Filtered Back Projection (FBP), which involves back-projecting the recorded activity over the LORs. Although it is straight-forward to implement, it does not take

into account noise characteristics and is therefore most suited to low-noise situations, such as CT acquisitions. PET imaging however, suffers from much poorer count statistics and reconstruction techniques that allow better modelling of the emission and detection processes are therefore advantageous. The greater degree of complexity from the additional modelling requires iterative approaches, such as Maximum Likelihood Expectation Maximisation (MLEM) to be adopted. MLEM iteratively estimates the activity map by comparing the projections from the current estimate with the actual measured projections. The difference ratio of the two sets of projections are then calculated and used to modify the estimate before repeating the loop. Acceleration can be achieved with the use of Ordered Subsets Expectation Maximisation (OSEM) (Hudson and Larkin, 1994), which considers only a subset of the projections within each iterative loop and has been found to converge to a solution significantly faster than when all projections are considered together. The datasets used in this project were reconstructed using either FBP (CT datasets) or OSEM (PET datasets).

2.2 CT Imaging

X-ray Computed Tomography (CT) is also a method of imaging a 3D volume non-invasively, but unlike PET and other nuclear medicine procedures, it is based on the transmission of X-rays through the body, rather than the emission of an administered radionuclide. It therefore represents a method of obtaining anatomical information, as opposed to being a functional imaging modality.

X-rays are produced by accelerating electrons through a vacuum tube towards a target (typically made of tungsten), where their rapid deceleration results in the emission of "Bremsstrahlung" radiation, which is directed towards the patient. The rate of production of these X-rays is dependent on the current applied to the X-ray tube to accelerate the electrons (mA) as well as the size of the tube voltage (kV). The voltage also determines the maximum energy of the emitted X-rays, with a continuous range of energies up to this maximum (Alvarez and Macovski, 1976).

A detector is placed on the opposite side of the patient to the X-ray source, such that the X-rays transmitted through the patient can be recorded. Projections are obtained by measuring the spatial distribution of transmitted X-rays, which forms the basis of planar X-ray imaging. The transmitted intensity of a given X-ray beam is given in Equation 2.1, but unlike the monoenergetic annihilation photons, an integration over the energy spectrum is required to obtain the total attenuation experienced by the incident radiation. The energy of the X-ray beam is chosen such that the photoelectric-effect is the dominant cause of attenuation (typically with a tube voltage of 120 kV_p), to allow differentiation of materials with different atomic numbers. This is the main mechanism with which contrast is achieved

in this imaging modality and results in a high level of contrast between bone and soft tissue, for example but lower contrast between different types of soft tissue (such as heart and liver), which have similar μ values.

To obtain 3D volumes, the process of measuring the transmission through the body is repeated at different angles, to obtain information about the 3D distribution of attenuation coefficients rather than the summed attenuations as in planar X-ray images. This is achieved by rotating the X-ray tube and the detector round the patient on a circular gantry while X-rays are continually emitted. The measured transmissions are then reconstructed to produce a 3D volume, where the resulting image is a map of the attenuation experienced by the X-ray beam, which in turn is dependent on the atomic number of the materials within the patient.

Due to the high photon flux with this type of imaging, it is possible to image quickly, with a single pass of the scanner over the patient. This can be done in either circular or helical mode, depending on the bed motion. The former involves a "step-and-shoot" technique, where the X-ray tube and detector rotate around the patient while the bed is static, before the beam is switched off and the bed moves to its next position. Helical acquisitions however, allow a continuous acquisition, where the patient couch moves slowly and continuously through the scanning bore with a pre-defined "pitch" while the X-ray tube and detector rotate, causing the X-ray source to trace out a helical pattern. The pitch is defined as the number of slice-widths travelled by the couch within a single rotation of the X-ray gantry and is dependent on the couch speed, the gantry rotation time and the slice width. It must be adequately small to allow sufficient data sampling, while not oversampling and increasing the dose to the patient.

Since CT acquisitions involve ionising radiation, the dose to the patient from this type of study is an important consideration. The dose delivered is dependent on the tube current and voltage, as well as the duration for which the X-ray beam is switched on (Wu et al., 2004; Gould et al., 2008; Hausleiter et al., 2006; Morin et al., 2003). The settings chosen for these parameters are dependent on the clinical requirements of the study, which is discussed in more detail in Section 2.4.

2.3 The Function of the Heart and Methods of Perfusion Imaging

2.3.1 The Heart

The primary function of the heart is as a pump, so that blood is continually pumped around the body, allowing oxygen to be transported. It consists of four main chambers as indicated in Figure 2.2; the left and right atria, which receive and collect blood, and the left and

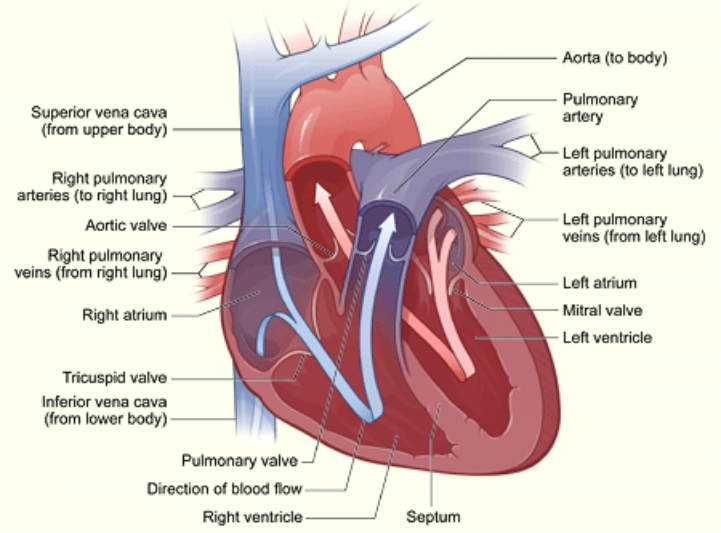

Figure 2.2: The anatomy of the heart.
Figure from www.nhlbi.nih.gov/health/dci/Diseases/hhw/hhw_anatomy.html.

right ventricles, which pump the blood to the body. The right ventricle pumps blood to the lungs for oxygenation, whereas the blood from the left ventricle supplies the rest of the body. The requirements of the muscle (the myocardium) of the left ventricle are therefore greater compared with the right ventricle; its myocardium is therefore thicker, allowing it to contract with a greater force. The cycle of the ventricles filling and emptying is repeated approximately every second, or less under exercise conditions.

In order to sustain this cycle of contraction (systole) and relaxation (diastole), a good blood supply to the myocardium itself must be present, particularly to that of the left ventricle. A diminished blood supply (resulting in ischaemia) indicates the presence of coronary artery disease (CAD), which narrows the arteries supplying the myocardium and restricts the blood supply. It has been found that even in highly constricted vessels, perfusion at rest is often unaffected. Under exercise conditions however, the oxygen requirements of the myocardium are increased and the narrowed vessels may then prevent the blood flow reaching the required level. Severe disruptions in the myocardial blood supply can lead to myocardial death (infarction), which is irreversible and can prevent the left-ventricular myocardium from functioning properly. Such events are associated with a poor prognosis and hence preventative treatments are administered where appropriate (Gould et al., 2000).

CAD is one of the leading causes of death worldwide, particularly in developed countries, for both men and women (Rosamond et al., 2007). Determining the optimal course of treatment for a patient with CAD relies on determining whether the myocardial tissue is viable and whether ischaemia is present. Functional imaging methods therefore have an important role

in assessing these factors and providing additional information regarding the functionality of the left ventricle, as described in the following section.

2.3.2 Myocardial Perfusion Imaging

Myocardial Perfusion Imaging (MPI) is a routinely performed clinical study in Nuclear Medicine and can involve the use of PET or SPECT (Single Photon Emission Computed Tomography). Both involve the intra-venous administration of a radio-pharmaceutical labelled with a radionuclide that perfuses into the myocardium. The distribution of the radionuclide within the left-ventricular myocardium is imaged using a gamma-camera or PET camera, enabling the clinician to assess the extent, location and severity of any perfusion abnormalities present. An advantage of using PET for this type of study is that the data are inherently quantitative (DeGrado et al., 2000), and therefore the potential exists for absolute measurements of myocardial perfusion to be performed (Bateman, 2004). This is more difficult with SPECT imaging, since the attenuation experienced by a single photon is depth-dependent (unlike the two photon case in PET) and it is therefore more challenging to determine the original distribution with quantitative accuracy. Another advantage of PET is the superior spatial resolution achievable, with $>$ 10 mm FWHM typical of SPECT studies (DePuey et al., 2000), compared with 6 mm FWHM for PET. This could result in improved detection of small perfusion defects with PET compared with SPECT, however this spatial resolution is not achievable for all radionuclides. As discussed in Section 2.1, the range of the positron prior to annihilation depends on its energy, which is substantially larger for ^{82}Rb than for ^{18}F, for example. The resulting effect of this positron range on the achievable spatial resolution is negligible for ^{18}F, but worsens the resolution of ^{82}Rb images such that it is not significantly higher than that achieved with SPECT (Lodge et al., 2005).

^{82}Rb is a commonly used radionuclide in the clinical setting for PET MPI and provides an indication of left-ventricular myocardial perfusion by acting as a potassium analogue – its retention requires the myocardium to be functional, allowing a map of perfusion to be obtained. For adequate perfusion to the myocardium (and hence uptake of tracer), the sodium-potassium pump of the myocardial cells must be functional and the blood supply must be present (Schwaiger, 1995). The failure of the sodium-potassium pump generally indicates cell death (infarct) and therefore results in an absence of tracer uptake in this region. Ischaemia however may not induce perfusion defects under normal resting conditions, but the abnormalities become apparent when the patient is under exercise (stress) conditions. For this reason and to differentiate between infarct and ischaemia, images are normally acquired under stress and rest conditions, where sttressing is normally achieved with the administration of a pharmaceutical, such as adenosine or dobutamine. A perfusion abnormality present in only the stress image indicates a reversible defect caused by CAD, and indicates that the tissue is still viable. Alternatively, a matched defect is a sign of

infarct and the presence of non-viable tissue. This distinction has an important impact on the optimal treatment for the patient and hence the stress-rest protocol is standard practice in Nuclear Medicine perfusion imaging.

Other tracers can also be used for cardiac PET imaging: ^{13}N-ammonia and ^{15}O-water both allow assessments of perfusion to be performed, however the fact that they are cyclotron-produced tracers with short half-lives (9.96 and 2.07 minutes for ^{13}N and ^{15}O respectively) limits their use to centres with an on-site cyclotron. ^{82}Rb also has a short half-life (76 s) but is produced from a generator; it is a daughter of the decay of ^{82}Sr, which has a half-life of 25.5 days, making it easier to distribute over a wider area. ^{18}F-FDG is also used in cardiac imaging, but acts as a measure of metabolism rather than of perfusion (Bax, 2005). This is used to assess myocardial viability, since the presence of metabolism is indicative of cell viability. The datasets used in this research were acquired with ^{18}F-FDG, however the techniques developed are intended to also be applicable to ^{82}Rb studies. The differences between the distributions of these radionuclides in clinical studies is discussed in more detail in Section 5.4.2.1 on page 152.

The assessment of the reconstructed images normally involves a visual inspection using the short- and long-axis slices through the left ventricle, as illustrated in Figure 2.3. In a normally perfused myocardium, the tracer distribution should be even throughout each of these slices, with no regions of reduced uptake, or defects. The uniformity is normally assessed qualitatively in the clinical setting, with the clinician reporting on the presence of any defects as well as their severity and extent. Assessing the results in a more quantitative manner can be done with the use of a polar map, where the entire left ventricle is displayed as a circular region, with the apex of the ventricle at the centre and the base at the edge. This can be divided into segments so that the uptake can be compared in different regions of the myocardium. One such method of dividing the polar map is illustrated in Figure 2.4, which is the arrangement recommended by the American Heart Association (Cerqueira et al., 2002). Other parameters that can be reported are the left-ventricular ejection fraction (LVEF), which is the proportion of blood expelled from the left ventricle during contraction and is a good prognostic indicator, as well as observations related to wall motion and thickness.

The apparent tracer distribution in an MPI study can be erroneously altered by factors such as attenuation and the effects of motion occurring during the acquisition. In some scenarios it may be sufficient simply to be aware of the effect these factors may have on the reconstructed images, to avoid incorrect diagnoses being made. It is generally preferable however to implement a correction, such that the images viewed are a better representation of the true tracer distribution and ambiguities between real and artefactual defects are resolved. Moreover, in the case that quantitative measurements are required, the importance of correction is enhanced. For example, in the presence of triple vessel disease, where a widespread reduction in uptake is present, absolute measures of perfusion would detect

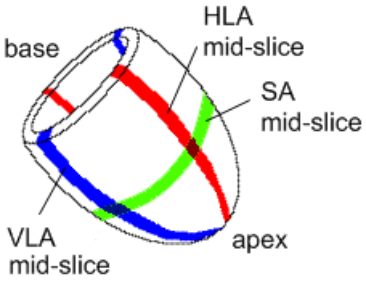

Figure 2.3: The approximate shape of the left ventricle and the orientation of its axes: HLA: horizontal long axis, VLA: vertical long axis, SA: short axis.

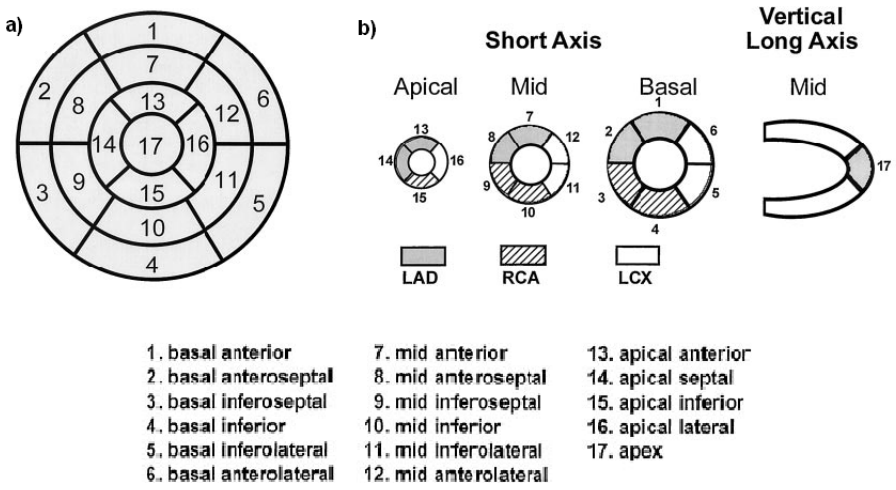

Figure 2.4: a) The circumferential polar plot and the arrangement of the 17 segments recommended for assessing left-ventricular myocardial uptake. b) The territories associated with each segment: LAD: left anterior descending, RCA: right coronary artery, LCX: left circumflex coronary artery. Figure from Cerqueira et al. (2002).

the reduction, whereas only assessing the relative uptake between the regions may not. Quantitative measurements also facilitate the direct comparison of different datasets, e.g. in the case that serial studies are performed and a measure of change is required. The effects of attenuation and motion on PET MPI (and other types of emission study) are outlined in the following sections in addition to a discussion on the methods of correction for these effects currently in the literature.

2.4 Attenuation Effects and Methods of Correction

As previously discussed, PET acquisitions suffer from attenuation, due to absorption of photons within the body and other structures within the scanner field-of-view. Photons originating from the centre of the body are attenuated to a greater degree than those at the surface and those in denser regions, such as the liver are affected more than those in low attenuating regions such as the lungs. These processes result in an apparent distortion of activity if not corrected for, particularly noticeable in the lungs and the edge of the body (which appear artificially active) and in the centre of the abdomen (where activity appears reduced). An illustration of this in a clinical study is shown in Figure 2.5. Images that have not been corrected for attenuation are not quantitative, and while it may be possible to perform some visual assessments on non-attenuation corrected images, it is essential to correct for attenuation if any quantitative measures of tracer distribution are to be obtained.

For PET, the total attenuation along a given line-of-response is independent of the depth of the event, so the attenuation-correction process needs knowledge of only this total attenuation. The attenuation is also independent of the radionuclide being imaged, since all annihilation photon-pairs have an energy of 511 keV. For a tracer distribution $f(x, y)$ and an attenuation map $\mu(x, y)$, the measured projections are given by:

$$EM(s,\theta) = \exp\left(-\int\limits_{L(s,\theta)} \mu(x,y)dt\right) \cdot \int\limits_{L(s,\theta)} f(x,y)\,dt \tag{2.2}$$

where s is the distance along the projection and θ is the angle of the projection. $L(s, \theta)$ therefore represents the LORs for a given slice. The attenuation correction factors (ACF) are therefore given by:

$$ACF(s,\theta) = \exp\left(+\int\limits_{L(s,\theta)} \mu(x,y)\,dt\right) \tag{2.3}$$

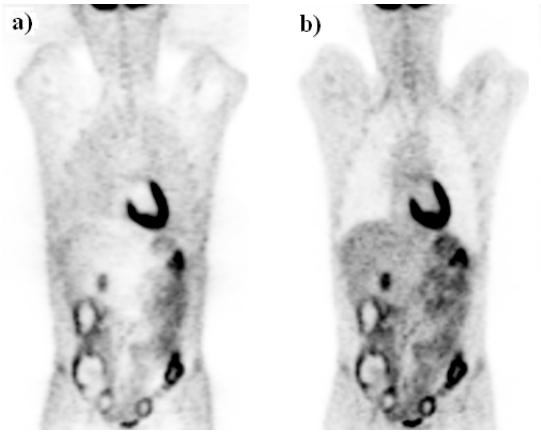

Figure 2.5: Whole-body FDG PET images a) before and b) after correction for attenuation. Differences can be seen most clearly in the lungs and in the centre of the dense sub-diaphragmatic tissues

which needs to be multiplied by $EM(s, \theta)$ in order to produce the corrected projections that are ready for reconstruction.

On stand-alone PET scanners (before the advent of combined PET-CT systems), an attenuation map was commonly obtained with the use of a transmission source, such as ^{137}Cs or ^{68}Ge (deKemp and Nahmias, 1994; Karp et al., 1995; Huesman et al., 1988). This source rotated around the gantry and the transmitted photons were detected using the PET detectors, providing a map of attenuation. Since ^{68}Ge is a positron-emitter, its photons have an energy of 511 keV and hence the energy-dependent linear attenuation coefficients ($\mu(x, E)$) they experience are identical to those experienced by the emitted photons. ^{137}Cs on the other hand is a single-photon emitter, with photons of energy 662 keV. To account for the difference in energies, the ^{137}Cs photon attenuation coefficients had to be scaled to match those of 511 keV photons, although this is a fairly straight-forward process, due to the fact that both emissions involved a mono-energetic source.

To achieve reasonable count statistics using this method, the source had to be uncovered for several minutes, which added significantly to the overall scan time. This did however result in an attenuation map that was produced on a similar time-scale to the PET acquisition, where measurements are acquired continuously over a number of minutes and are therefore averaged over the cardiac and respiratory cycles. If it is assumed that similar motions occurred during the transmission and emission scans, it can be seen although motion-blurring occurred, this blurring was matched between the two. The averaged transmission scan therefore represented an appropriate method of correcting motion-averaged emission images.

More recently, hybrid PET-CT scanners have been manufactured and have largely replaced the stand-alone PET systems (Beyer et al., 2000; Townsend and Beyer, 2002). The main

motivation behind the combination of these systems is the ability to obtain anatomical images to complement the function PET information without re-positioning the patient. Many types of PET studies benefit from the addition of CT images, to aid localisation and to compare the PET findings with the anatomical findings (Kluetz et al., 2000; Hany et al., 2002; Blodgett et al., 2006).

The CT can also be used for attenuation-correction of the PET data, due to it being based on transmission measurements. This has replaced the rotating source for attenuation-correction, due to its higher photon flux and resulting decreased acquisition time. A typical transmission scan with a rotating source took up to 20 minutes (Chatziioannou et al., 1994; Daube-Witherspoon et al., 1988), whereas the same volume could be scanned using CT in just a few seconds. This reduced scan time has advantages both in terms of increased patient throughput and in lowering the risk of patient motion during the acquisition. This difference in time-scale does result in a different manifestation of motion in CT images compared with the slowly rotating sources, which means that differences with the motion-averaged PET images may arise. A more detailed discussion on this issue is given in Section 2.5.3, but the motion-induced emission–transmission mismatches when attenuation-correcting with CT is an important area of ongoing investigation. It is also one of the primary focuses of the research presented here.

Most modern PET-CT scanners do not feature the rotating source and hence CT-based attenuation-correction is the only option. There are extra challenges relating to CT attenuation-correction however, in addition to the motion effects already described, which require attention to ensure they do not adversely affect the PET image quality. One such challenge is that of converting the Hounsfield Units (HU) of the CT images to attenuation coefficients at 511 keV. This requires different techniques compared with the 662 keV to 511 keV conversion used for ^{137}Cs transmission maps, firstly due to the fact that the X-ray beam is not mono-energetic and secondly due to the dominant type of interaction changing from being predominantly Compton scatter at 511 keV to being largely photoelectric absorption at CT energies. Due to the higher atomic number of bone compared with soft tissues, it is associated with a higher proportion of photoelectric absorption and its attenuation coefficient therefore exhibits a different scaling between 511 keV and CT energies compared with soft tissues. A global linear scaling would hence not be suitable and segmentation prior to scaling is needed such that different factors can be applied to bone and soft tissue (Kinahan et al., 1998; Bai et al., 2003). Problems with this method can arise in the presence of materials with high anatomic numbers (i.e. where contrast agents such as iodine or barium have been administered or in the presence of metallic implants) that do not conform to the scaling method used for biological materials. Imaging in the presence of these materials should be avoided where possible, since it can lead to artefacts in the attenuation-corrected PET images (Bockisch et al., 2004; Beyer et al., 2004).

The spectrum of energies in the X-ray beam also needs to be accounted for, since the linear attenuation coefficient (μ) is energy dependent and hence the scaling factors are also energy dependent. Obtaining the scaling factor for a spectrum of energies would require an integral of μ over all energies, however an effective beam energy can be used as a substitute (LaCroix et al., 1994; Kinahan et al., 1998). For typical CT acquisitions with tube voltages of $100-140$ kV_p, assuming a mono-energetic beam of $50-80$ keV allows a good approximation of μ to be made (LaCroix et al., 1994; McCullough, 1975). These methods of segmenting and scaling the CT using an effective beam energy generally produce good estimates of attenuation at the energy of PET photons, provided that the scaling issues with high atomic numbers do not degrade the attenuation map.

Another consideration of using CT in place of rotating sources is the increased dose associated with CT acquisitions. While the dose from rotating sources was negligible and did not therefore add noticeably to the dose from a cardiac PET study, the CT doses are often comparable to that from the PET component of the study and limiting the dose to an acceptable level is therefore an important consideration. The selection of the CT acquisition parameters (particularly tube voltage, current and acquisition time) are influential in determining the dose from a CT acquisition, and are chosen according to the clinical requirements of the study. In particular, the parameters are different depending on whether the scan is intended for diagnostic purposes (as in an independently acquired diagnostic CT), or whether it is required only to supplement the PET data. In general, higher quality images require larger doses, to ensure sufficient statistics to limit the presence of noise and to obtain adequate contrast. Therefore, if the purpose of the CT is predominantly for attenuation-correction purposes or to aid localisation in PET, the requirements for detailed anatomical information are lessened and the dose can be lowered (Souvatzoglou et al., 2007). Conversely, if the CT images are required for diagnostic purposes independently of the PET study, a reduction in image quality may be detrimental to the efficacy of the study. In both cases, the dose to the patient must be justified in terms of the potential benefit of performing the study. The dose from a CT acquisition intended for attenuation-correction of ^{82}Rb data used by Gould et al. (2008) was estimated to be 1.33 mSv, for a helical acquisition at 120 kV_p, with a tube current of 200 mA and a rotation time of 0.5 s on the GE "Discovery ST" PET-CT scanner. For comparison, the dose from a single injection of 1850 MBq of ^{82}Rb was estimated to be 2.22 mSv.

Many cardiac patients have other diagnostic CT scans (in addition to the CT component of the PET-CT study), to obtain further diagnostic information regarding the presence of calcium in the coronary artery (known as calcium scoring) (Achenbach et al., 2004) or to investigate the presence of any obstruction in the vessels supplying the heart (CT angiography, CTA) (Hoffmann et al., 2006), which involves the administration of a contrast medium (a radio-opaque material such as iodine) as part of the acquisition. To permit the investigation of small vessels for CTA, good spatial resolution and low noise levels are

required, which result in higher patient doses (Morin et al., 2003). Einstein et al. (2007b) found that the reported doses for calcium scoring studies varied between 1.0 and 6.2 mSv, whereas the doses for CTA studies ranged from 4.0 – 21.4 mSv between different centres, employing different acquisition protocols. It is clear therefore that the patients referred for MPI with PET-CT who have already undergone previous CT-based cardiac investigations may have received significant radiation doses. While the doses associated with the CTs acquired with PET-MPI are lower, it is still important to limit the dose where possible, while maintaining an acceptable level of diagnostic accuracy.

2.5 Respiratory Motion

The main mechanism of respiration is via the contraction and relaxation of the diaphragm, which is a large muscle that separates the thorax and abdomen. It contracts during inhalation, resulting in air entering the lungs and relaxes again during exhalation and air leaves the lungs. The anatomy of the diaphragm is shown in Figure 2.6, where it can be seen that its superior surface is immediately adjacent to the lungs and the heart and lies approximately in the transverse plane. This region is referred to as the diaphragm dome. It also extends inferiorly, where it is adjacent to the chest-wall, known as the apposition zone (Gauthier et al., 1994). This region experiences the largest contraction during respiration, resulting in a shortening of its length (in the superior–inferior direction) and a subsequent downwards motion of the diaphragm dome. The upper limit of the apposition zone is therefore the point at which the diaphragm diverges from the chest-wall. Towards the posterior portion of the diaphragm, it is intersected by the descending aorta and by the spine. When moving in a posterior direction through coronal slices therefore, the diaphragm appears to separate into two parts, and remains in this configuration until its posterior limit. In anterior slices however, the diaphragm appears to be a continuous sheet of muscle, spanning the width of the thoracic cavity.

The diaphragm is fixed to surrounding structures, including the ribs and lumbar vertebrae. These fixed points are predominantly at the base of the apposition zone (Cluzel et al., 2000) and hence the respiratory motion of this region is limited. The contraction of the apposition zone generates the largest motions in the diaphragm dome, with cranio-caudal translations of 10 – 20 mm typical of normal respiration, or more if deep breathing is employed (Wade, 1954; Wang et al., 1995; Danias et al., 1999; Segars et al., 1999; McLeish et al., 2002; Keall et al., 2006).

Many of the structures in the thorax and abdomen exhibit motions induced by that of the diaphragm. The organs affected to the greatest degree are those in close proximity to the diaphragm, such as the liver and stomach in the abdomen and those in the inferior part of the thorax, such as the heart. The motions of abdominal organs has been found to be

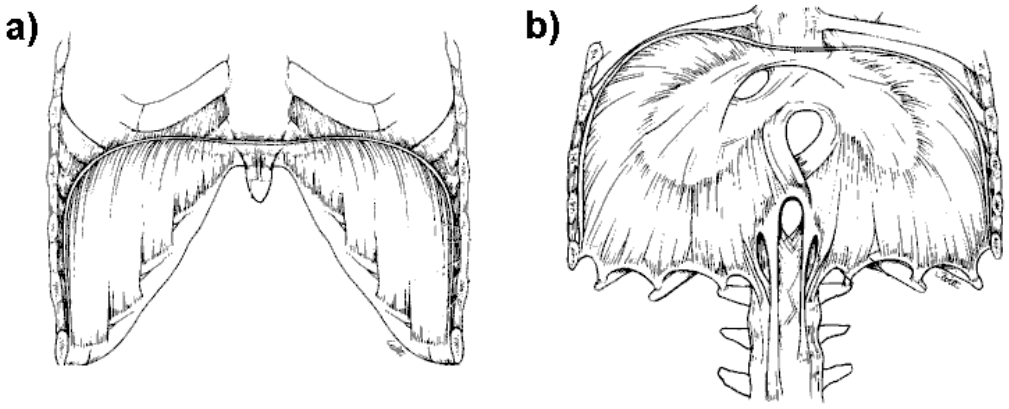

Figure 2.6: The diaphragm at the a) inner anterior and b) inner posterior chest walls. Figure from Cluzel et al. (2000).

dominated by cranio-caudal motions, with minimal displacement in the anterior–posterior and lateral directions (Korin et al., 1992; Davies et al., 1994; Clifford et al., 2002), indicating the influence of the diaphragmatic motion.

The other process causing an increase in lung volume is the motion of the chest-wall. The inter-costal muscles contract during inhalation, such that the rib-cage tilts upwards and outwards, allowing the lungs to expand (Wade, 1954; Segars et al., 1999). The contribution of the chest-wall motion to the overall increase in lung volume is variable, but typically less than that from diaphragm contraction (Cluzel et al., 2000). The total increase in lung volume from the combined effects of diaphragm contraction and chest-wall motion is approximately 500 ml with normal breathing (Biancia et al., 2005), and up to 4 times larger with deep breathing (Vedam et al., 2003b). The nature of the motion observed is dependent on many factors, such as posture (e.g. supine or upright), breathing type (whether breathing is predominantly using the chest or abdomen), depth of breathing (e.g. normal tidal breathing or deep breathing) and gender (Wade, 1954). These factors influence the extent of both the diaphragm and chest-wall motions and therefore affect the motions of internal organs.

The period of the respiratory cycle is typically around 5 s (Nehmeh et al., 2004b; Ruan et al., 2006; Abdelnour et al., 2007), but is also variable across the population and is dependent on exercise levels. The form of the cycle approximates a sine wave but with a quiescent phase (in which little motion occurs) often observed around end-exhale (Seppenwoolde et al., 2002). Variations in both the depth of respiration and the period of the respiratory cycle are frequently observed (Nehmeh et al., 2004b; McCall and Jeraj, 2007), even over the time-frames relevant for clinical imaging (e.g. 3 to 5 minutes for a ^{82}Rb MPI study). These variations result in complex respiratory motions of organs such as the heart and liver, which are continually changing in amplitude and possibly direction over time.

2.5.1 The Respiratory Motion of the Heart

Since the heart is situated immediately superior to the diaphragm (as illustrated in Figure 2.7), it is one of the organs most affected by respiratory motion (Ter-Pogossian et al., 1982; Wang et al., 1995; Danias et al., 1999; McLeish et al., 2002; Shechter et al., 2004; Dey et al., 2005). It therefore moves with the diaphragm, with an inferior translation during inhalation. This translation is consistently lower than that of the liver however: Danias et al. (1999) found a mean heart to liver ratio of 0.57 (range 0.17 to 0.93 over 12 patients) and McLeish et al. (2002) recorded a mean of 0.45 (0.28 to 0.73 over 8 volunteers and 8 patients). This results in a heart–liver geometry that varies over the respiratory cycle, with maximum overlap occurring at end-exhale.

The motion of the heart is also influenced by that of the chest-wall, with an anterior translation during inhalation (Shechter et al., 2004), although this motion is small in comparison to that caused by the diaphragm. This is partly due to the greater degree of motion experienced by the diaphragm compared with the chest-wall and partly due to the different interactions between the organs. A close link with diaphragm motion is expected, since the heart rests on the diaphragm surface, whereas the influence of the chest-wall on the heart is lower. The superior-inferior translation is therefore the dominant component of motion, with small translations in the anterior-posterior and left-right directions as well as rotations, which are more variable in amplitude and possibly also direction (Dey et al., 2005; Keegan et al., 2002; Shechter et al., 2004).

The motion of the heart with respiration has been found to be approximately rigid-body in nature (Korin et al., 1992; Livieratos et al., 2005), meaning that it experiences translations and rotations with little deformation. Some deformation has been observed however, with McLeish et al. (2002) measuring deformations of $3 - 4$ mm in the left ventricle wall when imaging using Magnetic Resonance Imaging (MRI) at breath-hold. These deformations may not be typical of normal breathing however, since breath-hold often results in deeper levels of inhalation than would be typical of normal respiration (Pan et al., 2005; Blackall et al., 2006). The deformations measured are therefore likely to be upper limits, confirming that the rigid-body motion accounts for the majority of the respiratory-related changes.

Hysteresis effects, where the motion during exhalation is different to that during inhalation, have been investigated extensively for lung tumour motion (Seppenwoolde et al., 2002; Blackall et al., 2006; Chi et al., 2006; Boldea et al., 2008; Ruan et al., 2008b) but less so for heart motion. Nehrke et al. (2001) however, looked at the correlation between the cranio-caudal motions of the heart and the right hemi-diaphragm of 10 volunteers using free-breathing MRI. In their study, 8 of the 10 volunteers were found to exhibit hysteresis to some degree, with only the remaining 2 volunteers having a linear relationship between the heart and diaphragm positions. The hysteresis was in the same direction in every case,

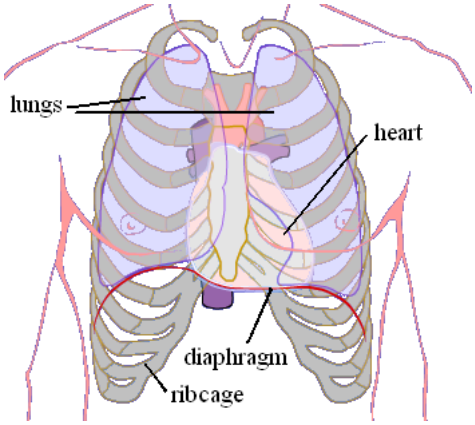

Figure 2.7: Illustration of the chest anatomy, showing the position of the heart within the thorax and in relation to the diaphragm.

representing a delay in the respiratory motion of the heart with respect to that of the diaphragm.

2.5.2 The Implementation of Respiratory Motion in the NURBS-based Cardiac Torso (NCAT) Phantom

The NCAT digital software phantom Segars et al. (1999); Segars (2001); Segars et al. (2001) was developed for the purposes of analysing the effects of respiratory and cardiac motions on activity distributions and the subsequent effect on reconstructed images. It involves the organs of the torso and abdomen and allows the user to generate activity and attenuation maps for a given phase within the respiratory and cardiac cycles. There are several parameters, which allow the user to specify the type and period of respiratory motion as well as the sizes and positions of some of the organs, such as the heart and liver. Each organ also has a user-defined activity level.

The phantom was constructed using typical organ shapes, sizes and positions from The Visible Human Project (Ackerman, 1998) and these define the default parameter values relating to the static organ shape in the NCAT phantom. The model of respiratory motion implemented in the phantom was based on that observed in an MRI study of a volunteer at two breath-hold positions, corresponding with 5% of the total lung capacity (TLC) and 40% TLC (Segars, 2001). Landmarks in the lung were used to track the displacements between the two respiratory states and to construct a motion model of thoracic and abdominal organs over a normal breathing cycle. This was incorporated into the phantom using Non-Uniform Rational B-Splines (NURBS) to construct realistically shaped organs that moved and distorted with respiration.

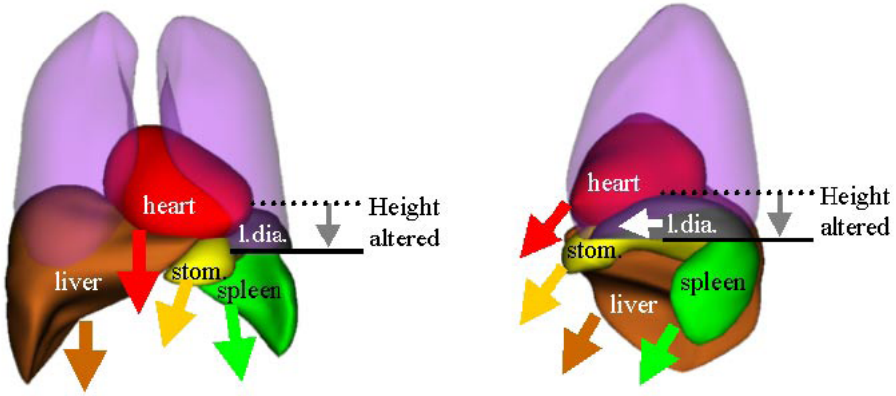

Figure 2.8: The motions of the heart, liver, diaphragm, stomach and spleen in the NCAT phantom during inhale. Figure from Segars (2001).

To generate a series of activity and attenuation maps, the user has the ability to select the extents of both the diaphragmatic and chest-wall motions and thereby assess the influence on the imaging process of different breathing manoeuvres. The motion of the NCAT heart is induced by both the diaphragm and the chest-wall and is in phase with both of these motions. Its amplitude of motion is matched to that of the diaphragm in the superior-inferior direction and to that of the chest-wall in the anterior-posterior direction. This is a departure from the real case, where the heart motion is typically less than that of the diaphragm and chest-wall, as discussed in Section 2.5.1. The NCAT phantom has recently been extended (to the extended cardiac torso phantom, XCAT) to include more realistic organ motions and to improve the resolution, such that it can be used for simulations involving high-resolution modalities, such as CT and MRI (Segars et al., 2003, 2008).

2.5.3 Effects of Respiratory Motion During Cardiac PET-CT Imaging

The occurrence of respiratory motion during a cardiac PET scan is unavoidable due to the duration of the scan (typically $3-5$ minutes). The effects of motion during a cardiac PET-CT scan are two-fold. Firstly, motion during a PET acquisition will result in a blurring of the image:- the field-of-view of a PET scan is constant over the acquisition, so therefore any motion occurring during this time will be included in the data and a motion-averaged image results. Due to the length of the acquisition, cardiac and respiratory motions occur during the scan, potentially causing noticeable image degradation (Ter-Pogossian et al., 1982).

The second effect of motion arises from the attenuation-correction process. If either or both of the PET or CT data are affected by motion, mismatches between the two will likely result. Using the mismatched CT scan for attenuation-correction of the PET data will then introduce errors into the PET data, via the generation of erroneous correction factors

and may lead to artefacts in the reconstructed image. Due to the different nature of CT imaging compared with PET, motions during the acquisitions affect the images in different ways. In helical CT scans, the couch moves continually during image acquisition and the scanner therefore performs a single pass over the patient. Therefore, unlike PET, motion is not averaged in CT images, but it can instead produce distortions of the apparent shape and position of moving structures. In circular acquisition mode, the positions of structures may vary from one couch position to the next and therefore produce distortions that are noticeable at the boundaries between couch positions. The extent of distortion is dependent on the velocities of the organs concerned in relation to the scanner. Motions in the superior-inferior directions therefore produce the most significant distortions and respiratory motions are hence particularly susceptible. In clinical studies, this has been frequently observed in the region of the lower lungs and diaphragm, where the translation of the diaphragm during acquisition can result in an erroneous appearance of the lung / liver boundary. In some cases this can even separate the liver into more than one region due to repeated scanning (Goerres et al., 2002a; Pan et al., 2004; Rietzel et al., 2005; Nehmeh et al., 2007), as illustrated in Figure 2.9. The heart is also subject to motion artefacts due to its respiratory motion as well as its contractions over the cardiac cycle, since different parts of the heart may be imaged at different states of contraction, depending on the speed of the acquisition.

Such artefacts can be problematic for clinical interpretation and using the CT for attenuation-correction can result in the CT errors propagating into the PET data. Emission–transmission mismatch was identified as a problem for cardiac PET-CT by McCord et al. (1992), who simulated shifts and rotations between the emission and transmission scans and found that shifts of 2 cm could produce significant errors in the reconstructed PET images, with regional activities changing by up to 30%. Such a distortion in the apparent myocardial uptake would clearly limit the efficacy of the study and potentially lead to false-positive results being reported.

The frequency of PET-CT mismatches in cardiac images due to respiratory motion has been found to be very high: Nye et al. (2007) and Lautamäki et al. (2008) have reported that approximately 70% of clinical cases were affected in this manner when a free-breathing protocol was employed throughout the acquisition. Furthermore, Martinez-Möller et al. (2007a) reported that PET-CT mismatches resulted in artefactual myocardial defects in approximately 20% of cases. Gould et al. (2007) found the percentage of cardiac PET-CT studies exhibiting attenuation-correction artefacts to be 40%, of which 23% were classified as being moderate to severe. It is clear that the issue of attenuation-mismatches is important in the clinical setting, not only due to its high prevalence but also the severity of the artefacts that can result.

A number of other studies have investigated effect of different breathing protocols during the CT acquisition (Chin et al., 2003; Goerres et al., 2003; Cook et al., 2005; Le Meunier

Figure 2.9: A CT scan exhibiting motion artefacts at the level of the diaphragm, affecting the appearance of the liver and other sub-diaphragmatic tissues. From Goerres et al. (2002a).

et al., 2006; Fitzpatrick and Wells, 2006). It has been found that the CT breathing protocol implemented will affect the severity of mismatch errors occurring. By performing studies on systems where both the CT scanner and the rotating source were present, it was possible to determine the proportion of defects that resolved when the rotating transmission source was used in place of the CT. In this way, it was possible to identify false-positive defects that were due to PET-CT mismatches. Acquiring the CT at maximum-inspiration was found to produce the most significant artefacts due to the respiratory state being very different to that during the PET acquisition. This breath-hold CT would be free from the effects of respiratory motion, hence it can be seen that even in the absence of CT motion-artefacts, mismatches with PET can still arise. Furthermore, these mismatches due to the differing respiratory phases can result in substantial levels of artefact. Since a typical breathing cycle involves more time closer to exhale than inhale, a breath-hold at end-exhale has been found to match the PET data more closely and hence produce results closer to that obtained with the rotating source based attenuation-correction, considered the gold-standard. However, in the case that the motion-averaged PET is being corrected, the end-exhale CT may still not provide a good match in all cases and some regions of the left-ventricle may still be subject to over- or under-correction.

The effect of emission-attenuation mismatches has also been observed in the apparent uptake of lung tumours in whole-body oncology studies. Correcting a respiratory-averaged PET for attenuation with a single CT frame has been found to produce different measurements of uptake compared with those obtained when a respiratory-matched attenuation-correction is performed (Erdi et al., 2004; Nehmeh et al., 2004a; Nagel et al., 2006; Ponisch et al., 2008). This type of acquisition involves splitting the PET data into frames according to respiratory position and acquiring multiple CT images at matching respiratory positions. Changes

in measured uptake can therefore be attributed to the presence of mismatches at some respiratory positions occurring in the single CT case, leading to erroneous measurements of uptake in these frames, which are resolved in the respiratory-matched attenuation-correction case.

Avoiding these problems therefore requires both the prevention of motion corruption in the acquired data as well as the accurate matching of the emission and transmission datasets. Eliminating the effects of motion from both the emission and transmission scans is particularly important if quantitatively accurate images are required. Work carried out in this area is described in the following sections.

2.6 Respiratory Gating

Gating is a technique in which the acquired data are divided into frames according to a physiological signal, recorded concurrently with the image acquisition. It is applicable for periodic motions, such that each gated frame contains only the data associated with a specific part of the cycle. Each frame of the gated acquisition will therefore contain little motion if gating has been successful and can be applied to both the respiratory cycle (with use of a respiratory trace) and the cardiac cycle (with use of an electrocardiogram (ECG) trace). One application of this method is to observe motion over the cycle in question: for example, the motion of the left-ventricular wall can be assessed over the cardiac cycle, or the respiratory motion of a tumour can be evaluated, for the purpose of improving radiotherapy plans. Alternatively, dividing the data into motion-limited frames can be used as a starting point for motion-correction, where the frames are subsequently aligned and re-summed. This allows motion-free images to be obtained, as a single frame of a gated study is, but with the inclusion of most or all of the acquired data, resulting in much lower noise characteristics in the final image.

A number of different techniques for recording respiratory traces using external measures have been developed, many for use with radiotherapy (Nehmeh and Erdi, 2008), where the presence of organ motion due to respiration could reduce the accuracy of treatment delivery. Many of these techniques are based on measuring the motion of the chest-wall or abdomen, and include the tracking of reflective markers (Keall et al., 2001; Kubo et al., 2000; Nehmeh et al., 2002a; Vedam et al., 2003b), the use of a strain gauge or pneumatic bellows placed around the chest or abdomen (Klein et al., 1998b; Kubo and Hill, 1996; Ohara et al., 1989) and a linear variable differential transducer to track chest-wall position (Ritchie et al., 1994). Other techniques are based on measuring changes in volume, including the use of a spirometer (Hanley et al., 1999), a temperature-sensitive thermocouple placed in the nostril of the patient (Kubo and Hill, 1996) and a thermistor (Boucher et al., 2004; Kubo and Hill,

1996). It has been suggested that the spirometer gives the most accurate reflection of lung motion, but is often not tolerated well by patients (Nehmeh and Erdi, 2008).

All of these measurements are surrogate markers for the motion of internal organs and therefore assume that the measured parameter can be related to internal motion. This assumption breaks down in scenarios where the motion of the organ is complex. In this case, predicting the motion from a single parameter (such as lung volume or abdominal circumference) may not fully account for the motion trajectories of the structure of interest. One such example of this is in the presence of hysteresis, where the position of a structure cannot be determined by the respiratory amplitude alone, but also requires knowledge of whether the respiratory cycle is in its inhale or exhale phase. Hysteresis has been observed in the respiratory motions of the heart (Nehrke et al., 2001) (as described in Section 2.5.1) and of tumours (Seppenwoolde et al., 2002; Blackall et al., 2006; Chi et al., 2006; Boldea et al., 2008; Ruan et al., 2008b). Chi et al. (2006) looked at the relationship between external markers on the chest and abdomen and the motion of a lung tumour, using 4D CT. The CT was acquired continually for the duration of the respiratory cycle (and was not therefore dependent on gating measurements) and images were reconstructed with a temporal separation of 0.3 s. They found that the relationship between the tumour motion and the markers varied between successive respiratory cycles for a given patient, which was explained by the presence of varying phase shifts between the motions, or varying degrees of hysteresis. This indicates that a prediction of tumour motion solely from abdominal or chest-wall markers would likely result in errors, reducing the effectiveness of gating.

Some of the problems associated with external markers and their assumed correlations to internal motion can be overcome with the use of data-driven gating techniques, where information in the acquired data is used to derive a respiratory trace and thereby circumvent the need for external measurement. This method has been used with PET data (Klein et al., 2001b; Visvikis et al., 2003; Bundschuh et al., 2008; Schleyer et al., 2009), where very short time-frames (< 1 s) are used such that negligible motion will have occurred over the duration of a given frame. Provided that a suitable method of ascertaining the respiratory state from these short frames is obtained, a respiratory trace can be derived, from which the data are retrospectively binned into the appropriate respiratory frame. As with external marker methods of gating, the data from corresponding respiratory positions are summed and therefore some of the count statistics are recovered. Extremely high levels of noise are present in the initial frames using this technique, due to the need to achieve an adequate temporal resolution for deriving the respiratory curve. Noise in emission images is Poisson in nature and is given by $\sqrt{n}$, where n is the number of counts detected. The signal-to-noise ratio (SNR) is then given by $\sqrt{n}$. The SNR of short, count-limited frames is therefore particularly poor and it is important that the signal extraction methods used are robust to these effects, to prevent erroneous measurements resulting.

Having obtained a respiratory trace, there is a question regarding how best to divide the data into frames. Methods based on the phase (Shirato et al., 2000; Ford et al., 2003; Vedam et al., 2003a; Keall et al., 2004; Mageras et al., 2004; Pan et al., 2004) and amplitude (Low et al., 2003; Lu et al., 2005b) are both used , where the former splits the data according to the time elapsed from the start of the cycle, and the latter requires a retrospective measurement of the overall amplitude of motion and then splits the data over this range. These processes are illustrated in Figure 2.10, showing the methods of splitting the data between the frames.

One of the factors influencing the optimal method for gating is the variability of the breathing cycle. The presence of irregular breathing, which is a common occurrence, presents an additional challenge to respiratory gating (Berbeco et al., 2005b; Plathow et al., 2005). Figure 2.11 shows the respiratory traces recorded over 5 minutes for 3 patients, measured using dynamic MRI scans (Cai et al., 2007). These traces show the large degree of variability observed in some patients, with variations in the amplitude of motion, the period of the respiratory cycle and the baseline position. It is not surprising therefore that the respiratory-induced motions of organs are also variable, adding to the difficulties associated with respiratory gating. Phase-based gating has been found to be more susceptible to these variations than amplitude-based gating, since the equivalent phases of the cycle are summed, regardless of the depth of breathing (Vedam et al., 2001; Rietzel et al., 2005). Amplitude-based gating on the other hand, is more robust to changes in breathing depth but does not account for the effects of hysteresis and assumes that the position of a structure is constant for a given lung volume. This can be overcome however by binning the data according to both the amplitude and the gradient (positive or negative) of the trace (Lu et al., 2006b). In practice, phase-based techniques for respiratory gating are used more frequently, due to the simpler techniques required for its implementation. ECG gating, which is used routinely in clinical practice is performed with a phase-based method, and hence the hardware and software are often set up to perform this type of gating.

Phase gating is performed with the use of a trigger signal, which sends a pulse to the scanner when the respiratory trace reaches a pre-defined point within the cycle, e.g. the peak of the trace. The time-width of each bin is determined by interpolating between successive triggers, allowing the data to be assigned to the appropriate bin during the acquisition, and hence no processing is required after the acquisition. The respiratory signal is recorded concurrently to the acquisition, but only the trigger signals are needed to initiate the gating process. This is different to amplitude-based gating, where the full respiratory signal is required to ascertain the appropriate bin at a given time. Currently, PET-CT scanners cannot perform this type of gating on-line and the data sorting needs to be undertaken post-acquisition, using list-mode data. List-mode acquisitions are where the information associated with every detected event, such as the time at which it was recorded, is stored in a file. Also recorded in the file is the occurrence of trigger signals, which can be used to synchronise the respiratory trace with the emission acquisition (Bruyant et al., 2007). This allows the two to

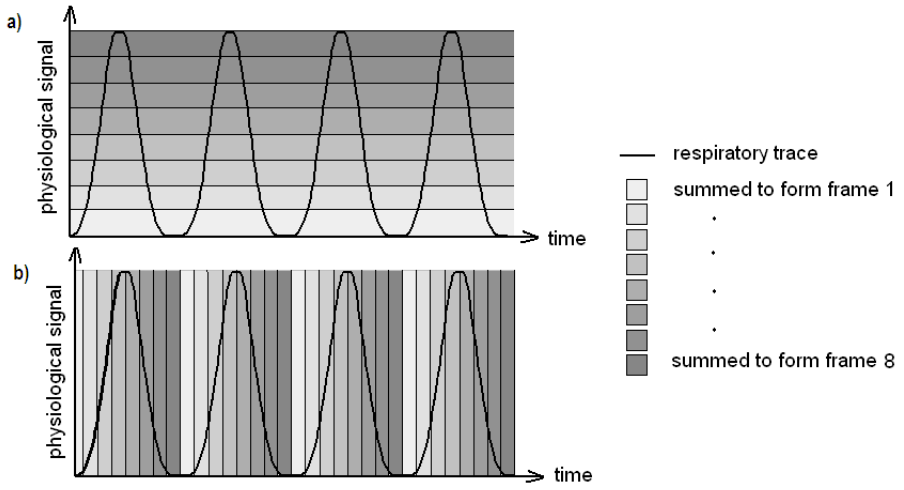

Figure 2.10: An illustration of a) amplitude and b) phase based gating of a regular respiratory signal.

be compared post-acquisition and the emission data can then be sorted into bins according to the respiratory trace reading. These list-mode manipulations are currently confined to the research setting and hence amplitude-based gating, despite its advantages, is not currently widely used in the clinical setting.

2.6.1 Respiratory Gating in PET and CT

The methods with which gating is performed is dependent upon the modality it is being applied to and hence different issues need to be considered for gating PET and CT acquisitions. The primary difference is that gating a PET study involves dividing the total counts between several frames, giving rise to noise-related issues, whereas gating in CT generally involves longer overall acquisitions and hence larger associated doses. These issues need to be addressed in determining the optimal acquisition protocol of a gated study.

Applying the gating scheme illustrated in Figure 2.10 (either the phase or amplitude version) to PET data, will result in each gated frame containing $^1/_8$ of the counts compared with the ungated acquisition and hence substantially more noise. Fewer frames would of course lessen the problem of noise, but result in a lower temporal resolution and hence more motion within each frame. Therefore between 6 and 10 frames is typical of gated PET studies. If the noise levels in the gated frames were tolerable, a simple way to avoid the effects of motion in PET images would be to only use a single frame of the gated study, which should be approximately motion free. It has been found though, for lesion detection, that the increase in noise from gating can outweigh the advantages of reducing the motion effects (Visvikis

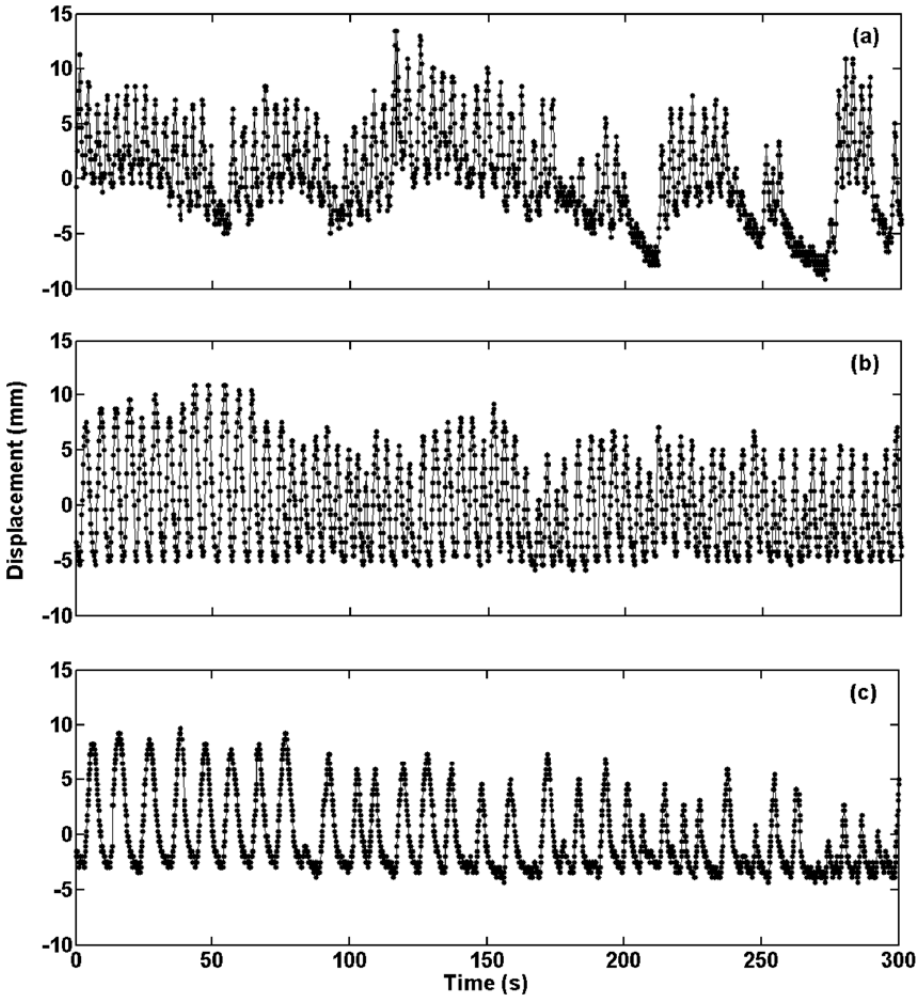

Figure 2.11: The respiratory traces of 3 patients, acquired over a 5 minute time period using MRI. Large variations can be seen, particularly in the first trace, in terms of the amplitude and period of the respiratory cycle and of the baseline position. From Cai et al. (2007).

et al., 2004). This can only be improved upon only by substantially increasing the scanning time or the administered activity, neither of which is desirable in the clinical setting. For this reason, most applications involve the use of gating in PET as an initial step in motion-correction. By performing respiratory gating, measurements of respiratory motion can be obtained and used as an input to a motion-correction algorithm, which then attempts to recombine the frames and hence recover the initial, lower levels of noise.

Gating in CT does not necessarily result in a poorer image quality, since each frame can be acquired with the same acquisition parameters as for a single image, rather than dividing the information between the frames. However, maintaining image quality results in an increase in dose by a factor equal to the number of respiratory frames acquired (Kamel et al., 2002; Pan et al., 2004), which may not always be justified ethically, particularly for a diagnostic study. For the scan parameters used by Gould et al. (2008), a gated acquisition was found to give a dose of 2.36 mSv, compared with 0.67 mSv for a single helical acquisition. The gated acquisition was obtained by acquiring for 10 s at each bed position, to ensure inclusion of the complete respiratory cycle. For doses of other types of CT acquisition and for ^{82}Rb PET, see the final two paragraphs of section 2.4. In radiotherapy, the use of gated CTs is increasing, to get a better estimate of tumour motion with respiration and to subsequently improve the treatment plan (Shirato et al., 2000; Keall et al., 2001; Wagman et al., 2003). In MPI with PET-CT on the other hand, the additional motion information obtained from gating is used primarily for improving the attenuation-correction of the gated PET and is not always required for diagnostic purposes in its own right. Limiting the dose to an acceptable level in this scenario is therefore an important consideration. One such way of achieving this is by lowering the X-ray tube current and recent advances have led to substantial reductions in dose in this way (Bacharach, 2007; Kamel et al., 2002), and the low-dose images which result have been found to be sufficient for the purposes of attenuation-correction (Pan et al., 2004). Dose levels can still be problematic however, even with the low-dose protocols and consequently, single CT acquisitions are used in place of gated CT where possible.

The issue of irregular breathing cycles was mentioned in the previous section and this is also a factor which affects PET and CT images in different ways. In both cases, respiratory cycle variations will contribute to a degradation of the gating, which leads to a degree of motion-corruption occurring in the gated images. In PET images, this manifests as a limitation to the blurring reduction that can be achieved, since the approximation that each of the gated frames are motion-free begins to break down. In phase-based gating for example, a varying depth of breathing will cause equivalent phases in the cycle to correspond with different anatomical positions and blurring will remain when the data from the varying positions are added together to form a gated frame. This is in addition to the blurring present from the residual motion occurring within a frame, due to its finite length. The residual motion can be improved with the use of a larger number of frames and hence improved temporal

resolution, at the expense of the increased noise by dividing the data into a larger number of frames.

Gated CT acquisitions are not subject to blurring effects, due to the higher temporal resolution of the acquisition. Motion artefacts can still occur however, despite the gating process, the appearance of which are dependent on the method of acquiring the data. Methods of obtaining CT images over the respiratory cycle can be split into cine (Low et al., 2003; Pan et al., 2004) and helical (Ford et al., 2003; Vedam et al., 2003a) acquisitions. Cine acquisitions are performed in circular mode, but involve repeated rotations of the gantry at a single couch position, before the X-ray beam is turned off, the couch is moved and the process is repeated. The X-ray beam is normally on for the duration of the respiratory cycle, allowing the reconstruction of images from different parts of the cycle. Forming 3D volumes over a number of couch positions then requires retrospective sorting such that a suitable image for each couch position and respiratory position is selected. Helical gating is performed in the same way as normal helical scanning, except that a much smaller pitch is required to ensure that every part of the volume is imaged over the full respiratory cycle. As with cine mode acquisitions, sorting is required to form a set of 3D volumes over the respiratory cycle.

Both of these acquisition modes are susceptible to motion artefacts: cine acquisitions can exhibit discontinuities at boundaries between successive couch positions and helical acquisitions are subject to spiral-like patterns (Rietzel et al., 2005). These artefacts are due to irregularities in breathing patterns, meaning that the respiratory cycle observed in one position may not be the same as that observed elsewhere. When sorting the reconstructed images to form volumes therefore, the images corresponding with the same portion of the respiratory cycle may contain repetitions in the anatomy imaged, or contain gaps, where a section of anatomy has not been imaged at that particular respiratory position.

The issues of the residual motion and the limitations of gating in the presence of varying respiratory cycles should be remembered when acquiring or viewing gated images. It should be noted that structures affected by motion may not have the expected appearance in either PET or CT, due to the residual blurring or distortions in shape. Motion measurements may also be affected by these issues and lastly, the use of motion-corrupted CT images for attenuation-correction may introduce additional errors into the PET data. These are some of the main factors driving research into data-driven methods of gating and motion-correction that are less susceptible to these effects.

2.7 Existing Motion-Correction Techniques in Emission Computed Tomography

A large body of work exists on motion correction methods in different imaging modalities and relating to different types of motion, including periodic motions such as the respiratory and cardiac cycles and other discrete motions, such as a shift or rotation. This project is concerned with the correction of respiratory motion for cardiac PET studies, however the methods developed for other types of motions (particularly those of a periodic nature) and those for SPECT studies are still highly relevant, since the general aims and the types of technique that are implemented exhibit many similarities.

In the case of cardiac perfusion studies, the primary aim of motion-correction is to reduce the blurring induced by respiratory motion, with the aim of improving the sensitivity of the technique: a motion-free image of the left-ventricular myocardial uptake could potentially show low-level defects that could not be identified in a motion-averaged image and a better measure of defect location, severity and extent would be expected in a motion-corrected image. Some groups have already undertaken work in this field, which is summarised in Table 2.1. The heart also exhibits motion due to its own contractions, however this motion is not normally corrected, since observation of the contractile motion often forms part of the diagnostic assessment: the data are split into frames according to the phase of the cardiac cycle, allowing the left-ventricular wall motion to be assessed and a measure of the LVEF to be performed. However, some groups have investigated correcting for cardiac contraction and these findings (listed in Table 2.2) will also be included in the discussion.

In addition to cardiac related literature, there are also many publications on the correction of respiratory motion with regards to FDG-PET studies, acquired for oncologic purposes. This is primarily directed at lung cancer patients, with the aim being to recover the activity within a tumour as seen in PET (which would otherwise be blurred by motion) to improve the estimates of both size and uptake. Although this lung-related work is not specific to the heart, the focus of these works is on the correction of respiratory induced motions and therefore many of the issues are common to heart-related correction techniques. Some of the literature in this area and the type of correction employed is listed in Table 2.3.

There are two main problems to address in motion-correction: firstly in determining the motion that has occurred during the acquisition and secondly in determining how best to remove the motion, such that the resulting motion-free image is quantitatively correct. Applying a matched attenuation map prior to the motion-correction can also present challenges. These aspects to the overall motion-correction process and how the published work in Tables 2.1 to 2.3 have addressed each stage are described in the following sections.

Reference	Study Type	Gating Method	Correction Method
Klein et al. 2001b	PET	Centre-of-mass tracking in 10 ms list-mode segments	Affine registration between list-mode frames
Bruyant et al., 2002	SPECT	NCAT frames regularly spaced in phase (respiratory phase already known)	Centre-of-mass tracking of thresholded projections
Livieratos et al., 2005	PET	Amplitude gated using an inductive respiration monitor with an elasticised belt around the chest	Rigid registration of reconstructed frames - correction performed in sinogram space
Kovalski et al. 2007	SPECT	Amplitude gated using an elastic strap with a resistor sensor	Translations determined from alignment of an ellipse fitted to the reconstructed short-axis slices. Correction applied to projections.
Dawood et al. 2008b	PET	Amplitude gated using video camera tracking of a marker placed on the abdomen	Optical flow registration between reconstructed frames

Table 2.1: Recent literature on correcting cardiac emission studies for respiratory motion. Gating is performed using the emission data, unless otherwise stated.

Reference	Study Type	Correction method
Klein et al. 1997	PET	Optical flow registration on reconstructed frames
Gilland et al. 2002	ECT (PET or SPECT)	Motion model incorporated into reconstruction with the use of spatial and bio-mechanical penalty terms. Simultaneous reconstruction and motion-estimation.
Cao et al. 2003	ECT (PET or SPECT)	Motion model incorporated into reconstruction with the use of spatial and bio-mechanical penalty terms. Simultaneous reconstruction and motion-estimation.
Gravier and Yang 2005, Gravier et al. 2006	SPECT	Motion model incorporated into reconstruction with the use of a temporal prior.
Gilland et al. 2008	ECT (PET or SPECT)	Optical flow registration on reconstructed frames
Suzuki et al. 2008	SPECT	Non-linear thin-plate spline warping between reconstructed frames

Table 2.2: Recent literature on correcting cardiac emission studies for cardiac motion. The gating method for the studies performed using clinical data was ECG triggered phase-based gating (where the NCAT phantom is used, the cardiac phase is already known).

2.7.1 Determining Motion from a Patient Study

Ascertaining the motion that has occurred during an emission acquisition can often be the most challenging aspect to motion-correction. The first stage of this is to obtain data that are not corrupted by motion, i.e. to split the data into motion-free frames and subsequently to determine the motion occurring between each of the frames. Obtaining motion-free frames can be done by gating the PET data, where the data from equivalent parts of the respiratory cycle are summed, as described in Section 2.6. This applies to most of the publications listed in Tables 2.1 to 2.3. As already discussed, these gated images suffer from high noise levels as a result of the reduced number of counts in each frame. This has an impact on the ability to determine the motion from such images, particularly in regions of low contrast or poor uptake.

An alternative method to determining the motion directly from gated emission studies, is to acquire a gated CT study, in conjunction with the gated PET. The anatomically detailed CT images can be used to obtain a measure of motion that is not adversely affected by noise when gated like gated emission images. This can be particularly useful if the particular area of interest, where the motion is required, exhibits poor contrast or low uptake in the PET images. In this case, a reliable measurement of the motion directly from gated PET images would be difficult and potentially unreliable and hence the acquisition of a gated CT

Reference	Study Type	Gating Method	Correction method
Lu and Mackie 2002	ECT - also applicable to CT	Time-varying scaling of sinogram	Re-scaling in sinogram space
Woo et al. 2004	PET	Phase-based gating using a laser optical sensor	Affine transformation determined from CT-inhale to CT-exhale registration, applied to reconstructed PET frames.
Dawood et al. 2006	PET	Phase-based gating using a pneumatic sensor attached to abdomen	Optical flow registration on reconstructed PET frames
Kinahan et al. 2006	PET	NCAT frames regularly spaced in phase (respiratory phase already known)	Non-rigid registration on respiratory-gated CT (matched frames to PET). Registration parameters applied to reconstructed PET frames.
Li et al. 2006b	PET	Amplitude-based gating using infrared reflection from a marker on the chest (the Realtime Position Management (RPM) system, Varian)	Motion model constructed using B-spline non-rigid registration of gated CT frames. Correction incorporated into reconstruction.
Thorndyke et al. 2006	PET	Amplitude-based gating using infrared reflection from a marker on the chest (the Realtime Position Management (RPM) system, Varian)	B-spline deformable image registration
Qiao et al. 2006b	PET	Phantom study: known motion	Motion model constructed using B-spline non-rigid registration of gated CT frames. Correction incorporated into reconstruction.
Lamare et al. 2007a	PET	NCAT frames regularly spaced in phase (respiratory phase already known)	Non-rigid (elastic) registration on NCAT CT frames. Correction incorporated into reconstruction.
Lamare et al. 2007b	PET	NCAT frames regularly spaced in phase (respiratory phase already known)	Affine registration on reconstructed frames applied to list-mode data
Bundschuh et al. 2008	PET	Centre-of-mass tracking in short time frames (250 – 750 ms)	Translations determined from centre-of-mass of rebinned frames. Applied to tumour volume-of-interest only.

Table 2.3: Recent literature on correcting whole-body emission studies for respiratory motion. Gating is performed using the emission data, unless otherwise stated.

could be useful for providing additional anatomical detail. A few groups have implemented this method, where a gated CT is acquired, from which the motion is determined and subsequently used to correct the gated PET frames (Kinahan et al., 2006; Qiao et al., 2006b) (or in the case of Lamare et al. (2007a), attenuation maps over the respiratory cycle from the NCAT phantom were used). Such an approach allows non-rigid transformations to be performed, without the concerns regarding reliability, which often accompany such transformations in noisy PET frames. The different approaches to registration and the situations in which they are most suited are described in more detail in Section 2.7.1.1.

There are issues with this type of acquisition however, which limit their widespread use. The first of these is the increased dose associated with a gated CT study, compared with a single CT, as described in Section 2.6.1. Despite the introduction of low-dose protocols, where the tube current is significantly lower than when acquiring diagnostic quality CTs, dose still remains to be an issue. This is particularly true of diagnostic studies (as opposed to studies for radiotherapy treatment planning), where doses from ionising radiation need to be minimised, while still obtaining the necessary diagnostic information. Even in the scenario of a gated CT having an acceptable dose associated with it, it would still be decreased further by the acquisition of only a single CT where the same acquisition parameters are used. Hence for limiting dose, it is always advantageous to avoid gating.

The second issue is that of the requirement for respiratory correspondence between the PET and CT frames, to avoid mismatches remaining and contributing to attenuation-correction errors. This may occur if a difference in the respiratory pattern between the PET and CT acquisitions exists. Although the two acquisitions are normally performed in close succession, changes in the depth or period of breathing over this time-frame are not uncommon, as illustrated in the respiratory traces of 3 patients acquired over 5 minutes, shown in Figure 2.11 (Cai et al., 2007). These types of changes will produce emission–transmission mismatches as a result of the mismatched respiratory positions at supposedly matching phases or amplitudes. Phase-based gating is particularly susceptible to these effects, due to its sensitivity to breathing irregularities.

Mismatches are further worsened by motion artefacts, particularly in CT. The problems of mismatches in cardiac and oncology PET scans were addressed in Section 2.5.3. The presence of residual motion in either the PET or the CT acquisition will lead to mismatches and therefore affect the attenuation-correction accuracy. Of the two modalities, a motion-corrupted CT is likely to produce larger effects than a motion-corrupted PET, due to the potential of shape distortions possible in CT. The averaging effect in PET prevents these distortions occurring and is instead affected by residual blurring.

The issues of gated CT doses and the presence of residual mismatches between PET and CT have led to the investigation of alternative techniques of determining the respiratory motion occurring during patient studies. This is the focus of this project, where methods

of performing quantitatively correct motion-corrections are sought in the absence of a gated CT acquisition. This both provides advantages in terms of the reduced dose as well as overcoming some of the problems of mismatch associated with gated CT studies. Implementing such a technique is challenging however, due to the lack of the highly detailed anatomical information from which the motion can be derived.

Once the emission data have been split into segments that are approximately motion-free, a method must then be implemented to determine the motion that has occurred between each of the segments, such that the motion can be subsequently removed. Registration is a common method by which this is performed, which is described below.

2.7.1.1 Registration

The aim of a registration algorithm is to determine the transformation needed to map a given image dataset onto a second image dataset. The datasets being aligned are referred to as the target image, which remains fixed and the floating image, which is to be transformed such that it aligns with the target image. There are three parts to the registration process: the transformation, the calculation of the cost-function and the optimisation, where normally these three stages are performed in an iterative loop.

Normally an initial guess is made at the transformation parameters required to align the two images, this is applied to the floating image and the two images are then compared, using the cost-function as a measure of the alignment. Next, new transformation parameters are chosen by the optimisation algorithm and the process is repeated. The optimisation algorithm assesses the cost-functions for the two parameter sets tested to determine the selection of the next set. In this manner, parameter space is searched and the values of the transformation parameters are updated according to which have given the best alignment (according to the cost-function). This process continues until some stopping criterion is reached, e.g. when the cost-function change between successive steps is below a given threshold. The three stages and the considerations involved in the implementation of each one are described in the following paragraphs.

Transformation

The simplest transformation is that of a rigid body, where the structure retains its shape and can therefore only be subject to translations and rotations. This gives rise to 6 parameters for a 3D object: 3 translations and 3 rotations. This type of transformation can be used for structures such as the head, since it does not exhibit deformations. If two serial scans of the brain were performed on the same patient, for example, a rigid transformation would be sufficient to align the two datasets, provided no major anatomical change had occurred between the two. It can also be used for a localised region of an image: (Bundschuh et al.,

2008) used centre-of-mass tracking (involving translations only) of a tumour by considering only a volume-of-interest placed around the tumour and therefore excluded the surrounding structures which would have exhibited different motions. Many of the techniques for motion-correction of the respiratory motion of the heart have assumed rigid-body motion of the heart (Bruyant et al., 2002; Livieratos et al., 2005; Kovalski et al., 2007), since its deformations are small compared with its translations and rotations.

If alignment between different patients is required however, additional scaling parameters would be needed to account for different sizes, giving a total of 9 parameters (again, for a 3D object). Shear can also be included, which together with the translations, rotations and scaling, describes what is known as an affine transformation. This has been used to describe the motion of the heart with respiration (Klein et al., 2001b) and that of the lungs (Woo et al., 2004; Lamare et al., 2007b): Lamare et al. (2007b) commented however that although an affine transformation reduced the effects of motion in the heart and lungs, improvements were not seen in the abdomen as a result of the differing motions between the thorax and abdomen.

Registering objects that do deform is more challenging and requires a larger number of parameters. For example, the contraction of the heart over the cardiac cycle could not be described with rigid-body parameters and consequently all examples listed in Table 2.2 have corrected for cardiac contractions using non-rigid transformations. Complex, non-rigid motions also occur with respiration and many authors have investigated the use of non-rigid transformations for whole-body PET studies (Dawood et al., 2006; Kinahan et al., 2006; Thorndyke et al., 2006; Qiao et al., 2006b; Lamare et al., 2007a). Although such transformations allow a much greater degree of flexibility, constraints are still required to ensure that the changes they induce in an object are realistic for the type of object in question. In medical imaging, such constraints would limit the degree of deformation allowed, ensuring that organs do not move through other organs, for example. This often involves the use of control points, where the transformation of one control point is related to those in close proximity, enforcing smoothness in the resulting deformations. There are a large number of non-rigid transformation types, which differ in the constraints they employ, allowing the characteristics of the object being transformed to be taken into account. The number of parameters in non-rigid transformations is dependent on the number of control points used, but could be in the region of 10^4 or more (Rueckert et al., 1999). Therefore, it is important to ensure that the results obtained from such transformations are reliable, since problems could arise if there is insufficient information in the image to fit the large number of parameters reliably.

Cost-Functions

The purpose of the cost-function is to produce a quantitative measure of how well two image datasets are aligned. Examples of cost-functions include sum-of-squared differences (SSD), where the differences between pairs of voxels are squared and summed as follows:

$$\mathrm{SSD} = \sum \left(x_i - \mathrm{T}(y_i)\right)^2 \tag{2.4}$$

where x represents the target dataset and y represents the floating dataset, which has undergone a transformation to obtain $\mathrm{T}(y)$. The summation is performed over all overlapping voxels in x and $\mathrm{T}(y)$. An alternative cost-function is the correlation coefficient, given by:

$$\mathrm{CC} = \frac{\sum \left(x_i - \overline{x}\right)\left(\mathrm{T}(y_i) - \mathrm{T}(\overline{y})\right)}{\sqrt{\sum \left(x_i - \overline{x}\right)^2 \sum \left(\mathrm{T}(y_i) - \mathrm{T}(\overline{y})\right)^2}} \tag{2.5}$$

where $\overline{x}$ and $\overline{y}$ are the mean voxels values of the two datasets. These two measures are suitable for intra-modality registrations, where a fixed relationship between the intensities in the two datasets is expected. This is the case for most of the examples in Tables 2.1 to 2.3, which involve intra-PET or intra-SPECT registrations in the case of emission-driven gating or intra-CT registrations where the motion is obtained from a gated CT.

Mutual information (Viola and Wells, 1995) is often used for cross-modality registrations (e.g. PET to CT), due to its ability to take into account the complex relationship between voxel intensities in the two image types. Despite the different intensity patterns, it is expected that there is an interdependence between the images (for example a homogeneous region in one is likely to be homogeneous in another) and hence when they are aligned, the ability of one image to explain the other is maximised. Normalised mutual information (NMI) (Studholme et al., 1999) is commonly used version of mutual information, which shows a greater invariance with respect to overlap and therefore improved behaviour in many scenarios. NMI is given by the following:

$$\mathrm{NMI} = \frac{\mathrm{H(A)} + \mathrm{H(B)}}{\mathrm{H(A,B)}} \tag{2.6}$$

where H(A) and H(B)are the entropies of images A and B and H(A, B) is the joint entropy. Entropy is a measure of information, Reza (1994) which is given as follows:

$$\mathrm{H(A)} = -\sum_a p_{\mathrm{A}}(a) \log(p_{\mathrm{A}}(a)) \tag{2.7}$$

where $p_{\mathrm{A}}(a)$ is the marginal probability distribution of the random variable, A. The joint entropy is given as follows:

$$\mathrm{H(A,B)} = -\sum_{a}\sum_{b} p_{\mathrm{AB}}(a,b)\log(p_{\mathrm{AB}}(a,b)) \tag{2.8}$$

where $p_{\mathrm{AB}}(a,b)$ is the joint probability of variables A and B. In the case that alignment has been achieved, the joint entropy is minimised and hence NMI is maximised. Obtaining optimal alignment, particularly between images of different modalities, can therefore be achieved by maximising NMI.

Optimisation Algorithms

The task of the optimisation algorithm is to organise the search for the optimal transformation parameters. This can be considered as a search for a minimum (or maximum, depending on the cost-function) in n-dimensional space, where n is the number of parameters. To minimise the computational cost of performing the registration, the optimisation algorithm needs to search parameter space in an efficient manner, so as to limit the number of iterations needed. An example of a widely used optimisation scheme is the simplex algorithm, which uses the shape of a simplex (a polytope in n-dimensional space, with $n+1$ vertices) to direct the search. The vertices of the simplex define the paths through parameter space that the algorithm is allowed to take, and are constructed such that the optimal solution is contained within its boundaries. As the algorithm proceeds towards the solution, the simplex can expand or contract around a vertex, to update the search space (Nelder and Mead, 1965).

One problem that can be encountered by the optimisation algorithm is that of local minima, which may have substantially higher cost-function values than the true global minimum. To overcome this, it is common to perform an initial broader and sparser search, before performing a more localised and thorough search, where the parameters found from the first search are used as an initialisation to the second. This reduces the chances of the global minimum being missed, while still allowing for an efficient search.

Registration for Measuring and Correcting Motion

Registering two images can be performed to obtain a measure of the motion that has occurred between the two. This is often implemented for obtaining measurements of respiratory motion, with the use of gated images. Normally a reference frame is selected (e.g. the end-exhale image) and a registration is performed between each of the other frames and this reference. The parameters resulting from the registrations can then be used as a measure of motion, which may be in the form of a global or localised transformation, depending on the transformation type employed.

Having performed a registration and obtained the transformation parameters, provided the images have been corrected for attenuation, a motion-correction can then be performed by applying the transformation parameters to the floating images. In this way, each frame of a gated study is brought into alignment with the reference frame, allowing them to be summed. The final summed image should be free from motion, if the registration has been successful.

2.7.2 Pre-Alignment Attenuation Correction

To perform a motion-correction with quantitative accuracy, it is necessary to perform the attenuation-correction prior to motion-correction. This is because the different geometries of attenuating structures in the frames to be aligned can result in different apparent activity distributions in each of the non-attenuation corrected images. For example, considering the respiratory motion of the heart, it is known that a varying overlap between the heart and liver occurs over the respiratory cycle (Danias et al., 1999; McLeish et al., 2002), resulting in a time-varying attenuation of projections though the heart. Reconstructing images at different points in the respiratory cycle without attenuation-correction could subsequently result in different myocardial uptake distributions in the reconstructed images. It would be incorrect therefore to align these images and to subsequently apply a single attenuation-correction. Instead, each frame of a gated study must be corrected with its corresponding attenuation map, such that the differences over the respiratory cycle caused by attenuation are corrected. The alignment can then be performed subsequent to this.

Applying the corrections in this order presents additional challenges to the overall motion-correction process in PET-CT: it is consequently a requirement that an attenuation map is obtained for every frame of a gated study and the anatomy has to be matched in each frame to avoid the generation of mismatch artefacts. The difficulties of achieving this have already been discussed (see Section 2.7.1). In previous motion-correction algorithms, the need to correct for attenuation first has been largely neglected. In some cases, the attenuation-correction has been omitted altogether (Bruyant et al., 2002; Dawood et al., 2006; Kovalski et al., 2007; Suzuki et al., 2008), in others a respiratory-averaged attenuation map has been used for correcting all respiratory frames (Klein et al., 1997; Thorndyke et al., 2006) and a single CT (e.g. a free-breathing CT) has also been used (Bundschuh et al., 2008), again with the single correction applied to all frames. Cases where a respiratory-matched attenuation-correction has been performed are those where a gated CT was also acquired (Kinahan et al., 2006; Qiao et al., 2006b) or where the respiratory-matched attenuation-maps were generated from the NCAT phantom (Lamare et al., 2007a).

A recent publication by Dawood et al. (2008b) presents some preliminary results regarding the derivation of respiratory-matched attenuation maps by obtaining non-rigid transformation parameters (using an optical flow registration) from gated PET frames and using these to

warp a single CT over the respiratory cycle. While these results have yet to be fully validated, this method of deriving attenuation maps from a single CT and a gated PET study has the potential to overcome some of the issues of gated CT studies and allows a quantitatively accurate motion-correction to be performed. Of the publications listed in Tables 2.1 to 2.3, this represents the method most similar to that investigated for this project.

2.7.3 Correcting for Motion

Once the motion occurring over the course of an emission study has been determined, the effects of this motion needs to be taken into account in order to eliminate its degrading effects on the reconstructed image. There are a number of different methods by which this can be achieved, some of which are described in the following paragraphs.

2.7.3.1 Post-Reconstruction Registration

This approach does not attempt to exclude motion from the original data, but instead involves the registration of images following reconstruction. It has been applied to images acquired on hybrid systems in order to better fuse images that would otherwise exhibit mismatches due to motion.Mattes et al. (2003) and Camara et al. (2002) have implemented such algorithms in PET-CT and found that non-rigid registration of the PET to the CT dataset reduced the mismatches present between the two. However, it does not necessarily produce quantitatively correct results, since the motion-induced errors are present during reconstruction. It can therefore improve the alignment of fused PET-CT datasets without requiring extra hardware or special acquisition modes, but its inability to fully overcome the effects of motion make this approach unsuitable for the application of motion-correction in cardiac PET and hence has not been considered further in this project.

2.7.3.2 Motion-Correction in Sinogram Space

This method involves the repositioning of events in sinogram space prior to reconstruction in order to compensate for motion. Since the correction is performed prior to reconstruction, this method is able to remove the motion from the reconstructed images, unlike post-reconstruction correction. Assuming the motion is known, transformations on list-mode data are applied event-by-event, on the basis of a geometric model of intersection of the LORs with the scanner. A disadvantage of this method however, is that it can only correct for rigid or affine motions and hence is not suitable where more complex motions need to be considered. Its main applications have therefore been in brain imaging (Menke et al., 1996; Qi and Huesman, 2002; Bloomfield et al., 2003; Thielemans et al., 2003; Rahmim et al., 2004), where rigid-body transformations describe motions of the head well.

Respiratory motion has also been considered: Lamare et al. (2007b) applied sinogram corrections to the lungs for oncology applications and Livieratos et al. (2005) utilised this correction method for respiratory motion of the heart for cardiac PET. This involved reconstructing individual frames of a gated PET study and performing a rigid-body registration between each frame and a reference frame to obtain the motion parameters due to respiration. These rigid-body parameters were subsequently used to modify the pre-reconstructed data in sinogram space. Once the sinogram data had been aligned with the reference frame, it was then reconstructed as a single, motion-free frame. This produced an improvement in the appearance of cardiac phantom images compared with the uncorrected version, with reduced blurring and a more accurate representation of the activity distribution. In this case, the rigid-body model was appropriate because the heart was considered in isolation. Due to the difficulty in extending this method to the non-rigid case, if motions of surrounding structures are also to be included, the rigid-body approximation is no longer appropriate and alternative correction methods therefore have to be sought.

2.7.3.3 Motion-correction Applied to Gated Data in Image Space

A motion-correction can also be performed post-reconstruction, which can provide an accurate means of correction provided the data in each frame is not motion-corrupted. This can be considered to be true if the data has been gated and therefore the motion within each frame is negligible. It is also necessary for the data to have been corrected for attenuation prior to the motion-correction for the final image to be error free. If these processes have been performed in the correct order then unlike the post-reconstruction method, this technique is capable of producing quantitatively correct results.

This is a widely used technique for motion-correction since it is applicable to all types of motion and is capable of producing accurate results. Many of the techniques outlined in Tables 2.1 to 2.3 therefore perform the correction in this manner.

2.7.3.4 Motion Model Incorporated into the Reconstruction Algorithm

Some authors have incorporated a motion model into the reconstruction algorithm and hence are able to simultaneously estimate the motion and reconstruct the image. Cao et al. (2003) and Gilland et al. (2002) have implemented methods to correct for cardiac contractions, which incorporate penalty terms related to the motion model in the reconstruction. Gravier and Yang (2005) have also performed motion-corrections for the cardiac cycle by including a temporal prior function. All of these report improvements in the image quality of cardiac images, however it has been noted that these methods are sensitive to the parameter selection associated with the prior or penalty term and should be given careful consideration (Qiao et al., 2006b). Other authors have considered the motion model as part of the system

model of photon detection probabilities: Qiao et al. (2006b) and Li et al. (2006b) have both constructed a motion model by performing a non-rigid registration on gated CT frames and incorporating this into the reconstruction. This allows data from all respiratory frames to be incorporated into the correction, which is advantageous from a statistical viewpoint, compared with corrections applied separately to individual respiratory frames. The major disadvantage with this approach is the requirement of a gated CT with which to construct the motion model, as discussed in relation to determining motion.

2.7.3.5 Summary of Motion-Correction Techniques

It can be seen that motion-correction is a major topic of research in PET and that a large body of work exists on proposed methods of tackling the issue. There is a wide variety of techniques that have been implemented, many of them specific to the particular task they have been designed to perform. The issues that have to be considered in the design of a motion-correction algorithm include how the data can be split into frames that are not corrupted by motion, how corrections for attenuation are implemented and how the motion-correction should be applied to the data. Specifically considering the correction of cardiac studies for the effects of respiratory motion, suitable methods of obtaining approximately motion-free frames include gating methods that are related to the motion of the diaphragm (such as an abdominal reflective marker or elasticised belt around the abdomen), since the heart motion is heavily influenced by that of the diaphragm. The issue of attenuation-correction is also important, since artefacts could be introduced into the appearance of the myocardium if not applied correctly. In a gated study, obtaining respiratory-matched attenuation maps is a major challenge, but important to the quantitative accuracy of the final result. The choice of alignment method depends on whether the heart is considered in isolation (in which case a rigid-body model is a good approximation) or whether other organs in the thorax or abdomen are also included in the correction process (in which case a non-rigid model would be more appropriate). Finally, the method with which the motion-correction is implemented is another important consideration, dependent on the type of motion being corrected and the method with which the motion has been obtained.

Chapter 3

Characterisation of Attenuation Artefacts in Cardiac PET-CT and SPECT-CT

3.1 Introduction

Respiratory motion during myocardial perfusion imaging is problematic, due to the blurring effects introduced into the emission study and due to mismatches being introduced between the emission and attenuation maps. The blurring effects arise as a result of the emission study being acquired over a few minutes, resulting in it being averaged over many respiratory cycles. Since the heart is subject to respiratory motion, this motion-induced blurring is an important consideration for cardiac studies. The second effect is that of mismatches between the emission and attenuation maps, which can occur as a result of the different manifestations of motion in the two acquisitions and can lead to attenuation-correction artefacts. An effective motion-correction algorithm should therefore address both of these issues, such that a quantitatively correct, motion-free result can be obtained.

Previously, MPI was performed either with a respiratory-averaged attenuation map from a rotating point source (deKemp and Nahmias, 1994; Karp et al., 1995; Huesman et al., 1988) or with the attenuation-correction omitted altogether. Where attenuation-correction was performed, the problem of mismatch did not arise, since the transmission scan was averaged over many respiratory cycles and was therefore matched to the emission data. However, the advent of hybrid systems (PET-CT and SPECT-CT) and the interest in motion-correction have resulted in emission–transmission mismatches becoming an important issue. Since the CT is effectively a snap-shot of the position of anatomy at each couch position, it therefore

only represents a single respiratory position. As a result, it frequently does not provide a good match for the respiratory-averaged emission data, which can lead to the production of attenuation-correction artefacts (Chin et al., 2003; Loghin et al., 2004; Fitzpatrick and Wells, 2006; Le Meunier et al., 2006; Gould et al., 2007; Martinez-Möller et al., 2007a; Nye et al., 2007; Lautamäki et al., 2008). In the case that motion-correction is performed, it is necessary to split the emission data into motion-limited frames, which gives rise to additional considerations in the attenuation-correction process, due to the need to perform an attenuation-correction on each frame. In this case, neither the averaged attenuation map from the rotating point sources nor the single CT frame would provide a good match to all frames of the emission data.

The effect of an emission–transmission mismatch is therefore an important consideration in the development of a motion-correction method, such that the best method of preventing the associated artefacts can be ascertained. In MPI studies, although data might exist over a larger volume, the only region that needs to be quantitatively accurate in the final reconstructed image is that containing the heart, since this is the region with diagnostic value in this particular study. Therefore mismatches elsewhere in the body are only important if they influence the appearance of the left-ventricular myocardium. This could occur if the motions of other organs affect the attenuation-correction factors through the heart, as given by Equation 2.3. This is possible where projections exist that traverse the heart as well as other moving organs. Due to the presence of complex motions and deformations occurring over the respiratory cycle, the heart, lungs and diaphragm do not exhibit a constant geometrical relationship with each other. Therefore the organs surrounding the heart will not necessarily contribute a constant attenuation in the projections that include the heart, meaning that their motions need to be accounted for.

For these reasons, it is important to know which structures are capable of producing attenuation-related artefacts in the heart, since this may apply to structures surrounding the heart, and not just the heart itself. The purpose of this study was therefore to analyse such mismatches and to ascertain their effect on the reconstructed myocardial activity, such that the organ motions affecting the attenuation-correction of the heart could be identified. This was a vital step prior to developing a motion-correction algorithm, to ensure that the algorithm dealt properly with the motions of these other organs and not just that of the heart. Conversely, if motion types were not found to adversely affect attenuation-correction accuracy, they could be disregarded by the motion-correction algorithm.

A number of studies have concentrated on the prevalence of attenuation artefacts (Loghin et al., 2004; Gould et al., 2007; Martinez-Möller et al., 2007a; Nye et al., 2007; Lautamäki et al., 2008), however the precise identification of their cause, in terms of the specific organs involved, has not previously been addressed. Most of these studies were performed using clinical data, preventing the possibility of examining specific motion types independently. In

this study, the motions involved during respiration were split into a number of components and isolated such that the effect of each one could be examined individually. This was done using the NCAT software phantom of the torso, allowing the generation of motion types that could not be observed in isolation in a patient study.

Although this project is primarily concerned with the motion-correction of PET studies, the effects of attenuation-mismatches in SPECT was also of interest, since it is a widely used modality for MPI studies and SPECT-CT acquisitions are becoming more common. Examining the causes of attenuation-correction artefacts in both modalities allowed an evaluation of whether their different attenuation properties influenced the manifestation of mismatches in either the extent or location of artefacts. Furthermore, this comparison between PET and SPECT attenuation-correction artefacts had not previously been reported.

3.2 Method

3.2.1 Generating NCAT Maps

The NCAT software phantom (Segars et al., 2001) was used for this investigation, due to the ability to manipulate the motions of organs and therefore investigate the specific causes of attenuation-correction artefacts. It allows the user to generate activity and attenuation maps at specified phases of the cardiac and respiratory cycles and thereby investigate the effect of motion on a reconstructed image. This investigation was concerned only with the effects of respiratory motion, so all datasets were generated at end diastole and the only cardiac motion was therefore caused by respiratory motion. Activity maps were defined with a value of 75 in the myocardium, 30 in the liver and a background value of 2 in all other organs. These values were chosen to represent a high level of activity in the heart and a comparatively low, diffuse activity in the liver, as seen in MPI studies. The liver uptake is dependent on the tracer used, with ^{99m}Tc tetrofosmin typically exhibiting a higher liver uptake than ^{82}Rb, for example. However, to enable a direct comparison between PET and SPECT, a constant value of liver uptake was chosen for both PET and SPECT simulations. Noiseless maps were used so that only the effects of mismatch were being examined and hence the units of the values given above are arbitrary and it is only the relative magnitude of these activities that is of importance. Parameters specifying the size of the patient and their internal organs were set to those determined by the visible male dataset (Ackerman, 1998). A coronal slice through an NCAT activity map, showing the activities as specified above and the corresponding attenuation map are shown in Figure 3.1.

To ascertain the effect of each type of mismatch, activity and attenuation maps were generated at end-exhale and end-inhale, with different breathing mechanisms and hence different mismatches simulated between the two respiratory points. The main parameters in

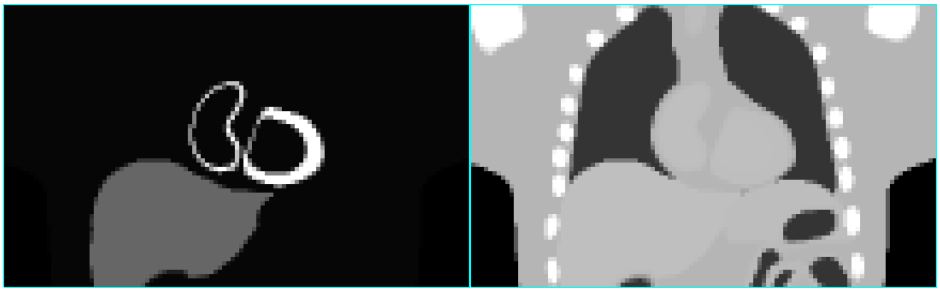

Figure 3.1: A coronal slice through a sample NCAT activity map (left) and the corresponding attenuation map (right). The activities shown are 75 in the myocardium, 30 in the liver and 2 elsewhere, within the body.

the phantom that influence the respiratory motion are the specifications of diaphragm and chest-wall amplitudes in the superior–inferior and anterior–posterior directions, respectively. The default motions for normal breathing in the NCAT phantom are 2.0 cm exhale to inhale translation for the diaphragm and 1.2 cm for the chest-wall (Segars, 2001). These give approximately equal contributions to the overall change in lung volume. With conventional use of the NCAT phantom, it is not possible to isolate each type of mismatch because heart and liver motions occur in conjunction with lung expansion, so would not normally be observed independently. The maps were therefore generated by using non-standard breathing parameters in the phantom to simulate the desired effect. In this way, each factor was isolated to allow its individual contribution to the overall effect to be deduced. The attenuation maps were generated at both 140 keV and 511 keV to represent attenuation at SPECT and PET energies, respectively, which is equivalent to the clinical situation using CT if it is assumed that the CT attenuation factors can be successfully convert to emission energies. All datasets were generated with a voxel size of $4{\times}4{\times}4$ mm^3.

The mismatches of interest in this study were those that could potentially influence the attenuation-correction factors of the heart. This included the motion of the heart itself, the changing geometry and attenuation of the surrounding lung tissue and a changing overlap between the heart and the liver. Although these changes occur together in normal breathing, in this study each effect was isolated and investigated individually.

One simplification of the NCAT phantom is that the lung attenuation-coefficient (μ_{lung}) is modelled as being constant over the respiratory cycle. This is not actually the case, since the lung tissue expands as air enters, which adds negligibly to the overall mass of attenuating tissue. Its expansion therefore causes a reduction in the measured attenuation-coefficient, which is averaged over both lung tissue and air. Since the effects of the changing μ_{lung} over the respiratory cycle were of interest in this investigation, a modification to the NCAT phantom was made for the relevant datasets. It was assumed that the total mass of the

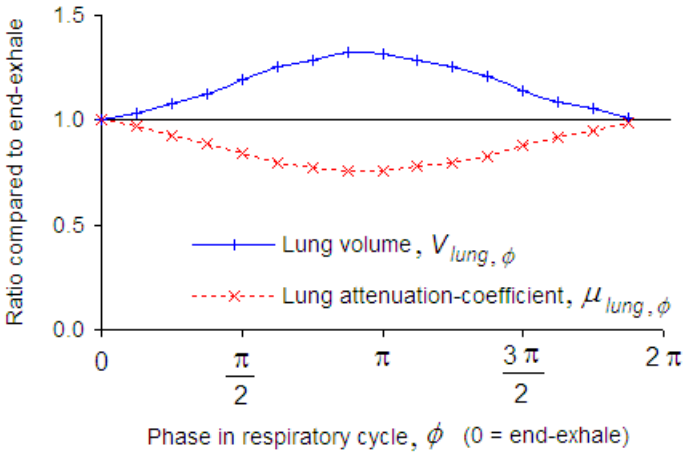

Figure 3.2: The NCAT lung volume over the respiratory cycle as a fraction of the end-exhale volume and the corresponding attenuation coefficient (also as a fraction of its end-exhale value) to compensate for the changes in volume.

lungs is constant with respiration and that expansion is even over the lung volume. To incorporate this model of lung expansion into the phantom, μ_{lung} is altered as follows:

$$\mu_{\text{lung},\phi} = \mu_{\text{lung},0} \times \frac{V_{\text{lung},0}}{V_{\text{lung},\phi}} \tag{3.1}$$

where $\mu_{\text{lung},0}$ and $\mu_{\text{lung},\phi}$ are the linear attenuation coefficients of the lung at phase 0 (end-exhale) and at phase ϕ of the respiratory cycle (where $0 \leq \phi < 2\pi$). $V_{\text{lung},0}$ and $V_{\text{lung},\phi}$ are the lung volumes at the two respiratory states. The resulting change in μ_{lung} with ϕ for the lung volumes of the NCAT phantom with a diaphragm motion of 2.0 cm is shown in Figure 3.2.

This modification was included in the datasets where the effect of a changing lung attenuation-coefficient was of interest. The datasets generated, the methods used to produce them and the resulting mismatches involved are described in the following paragraphs and illustrated in Figure 3.3. The motion types that were simulated are outlined in Table 3.1.

Cardiac position mismatch This dataset was generated with a heart translation over the respiratory cycle as would occur in normal breathing. To avoid the effects of a changing overlap between the heart and the liver (which could contribute to artefacts), the diaphragm also moved with the same amplitude as the heart. This dataset therefore contained mismatches because of cardiac translation but not those caused by varying overlap between heart and liver. Furthermore, the attenuation-coefficient of the lung (μ_{lung}) remained at a constant value between end-exhale and end-inhale (which is the default for the NCAT

phantom) to prevent possible artefacts from a changing μ_{lung} contributing to this dataset. The changes between exhale and inhale for this dataset are illustrated in Figure 3.3a.

Liver position mismatch (leading to heart–liver overlap mismatch) Although the heart and liver motions are equal in amplitude and are in phase in the NCAT phantom, in patients the heart motion is generally less than that of the liver (Danias et al., 1999; McLeish et al., 2002), as discussed previously, in Section 2.5.1. A difference in amplitude between the motions of the two organs will produce a time-varying overlap between them, which could result in attenuation-correction artefacts. This effect was simulated using the NCAT phantom by altering the height of the liver in the attenuation map, by an amount that represents the extent of its motion in normal breathing (2.0 cm). This was achieved by changing the NCAT parameter for the diaphragm right dome height between exhale and inhale and thereby creating a changing overlap without the additional effects of heart motion. This is illustrated in Figure 3.3b. As with the cardiac translation dataset, μ_{lung} was kept constant between the two frames generated, to ensure that the only mismatch observed was that from the changing liver overlap.

Lung mismatches due to diaphragmatic contraction (dataset referred to as "lung–diaphragm") The expansion of the lung caused by diaphragmatic contraction normally occurs with cardiac translation, however here the effects of lung expansion were isolated. A lung mismatch was created independently by altering μ_{lung} as previously described. By simulating lung expansion in this way, the geometry within each slice is unaffected, but the altered lung attenuation coefficient indicates expansion in the superior–inferior direction, as is the case with diaphragm contraction. The lung attenuation coefficient was changed by an amount to represent the volume increase from normal diaphragm motion (2.0 cm) using Equation 3.1. This is illustrated in Figure 3.3c, where the change in grey level of the lungs represents the change in attenuation-coefficient.

Lung mismatches due to chest-wall motion (dataset referred to as "lung–chest") This dataset was produced with a chest-wall motion of 1.2 cm as in normal breathing. Lung expansion caused by chest-wall motion occurs in the radial direction, causing a change in geometry within each transaxial slice. A change in μ_{lung} was included, again using Equation 3.1, corresponding with the increased lung volume resulting from the chest-wall motion. This is illustrated in Figure 3.3d, again with the change in grey level representing the change in μ_{lung}.

Baseline Finally, a dataset was created against which the others could be compared, i.e. one in which no attenuation mismatches were present. Consequently, an artefact-free reconstructed image was generated from this dataset.

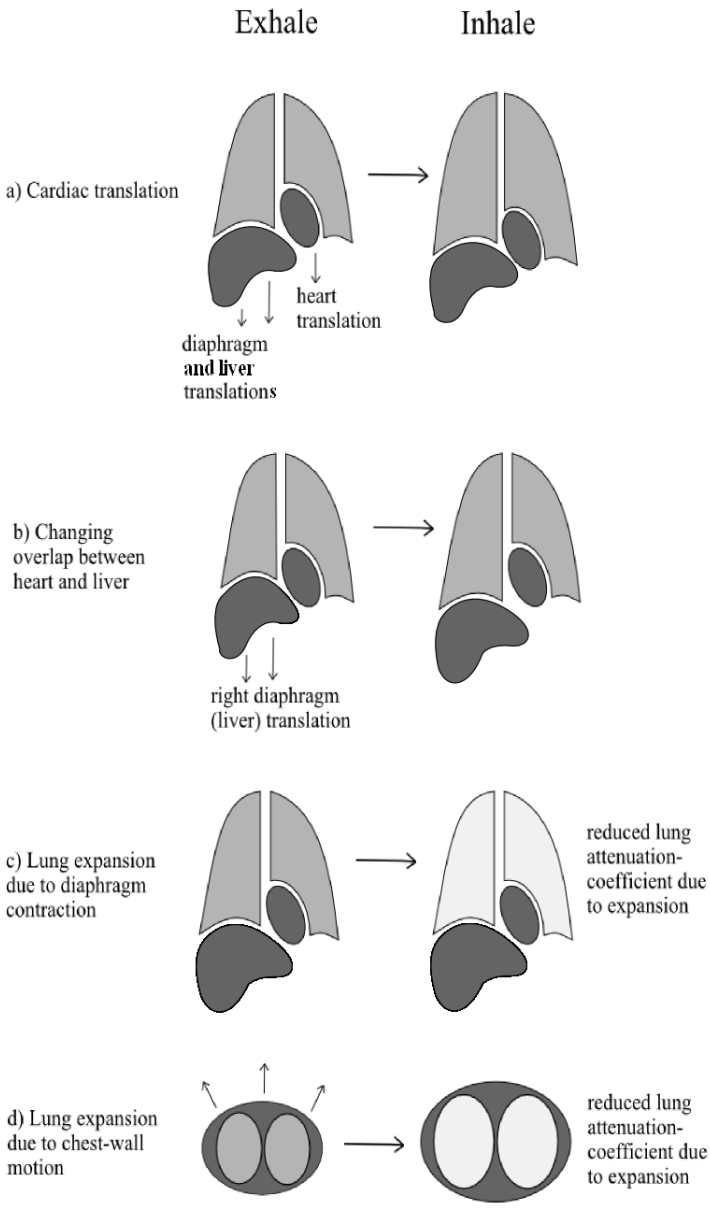

Figure 3.3: Diagrams illustrating the motions used to produce attenuation mismatches in the following datasets: a) cardiac position mismatch, b) mismatch in overlap between liver and heart, c) lung mismatch because of diaphragm contraction (simulated by changing the lung attenuation coefficient) and d) lung mismatch because of chest-wall motion (also involving an alteration of the lung attenuation coefficient).

Dataset	Diaphragm motion between end-exhale and end-inhale	Chest-wall motion between end-exhale and end-inhale	% decrease in μ_{lung} between end-exhale and end-inhale
Cardiac translation	2.0 cm	1.2 cm	0 %
Liver translation	2.0 cm simulated (diaphragm motion set to 0.0 cm, liver height changed by 2.0 cm)	0.0 cm	0 %
Lung–diaphragm	2.0 cm simulated (diaphragm motion set to 0.0 cm, μ_{lung} altered to reflect a diaphragm motion of 2.0 cm)	0.0 cm	17 %
Lung–chest	0.0 cm	1.2 cm	13 %
Baseline	0.0 cm	0.0 cm	0 %

Table 3.1: Values of the NCAT diaphragm and chest-wall motion parameters and the alterations to μ_{lung} used to generate each of the datasets. Where μ_{lung} was altered, the % decrease was equal to the increase in lung volume between end-exhale and end-inhale.

3.2.2 Generating Images from the NCAT Maps

As the overall aim of the study was to determine the potential effect of an attenuation mismatch, the images did not include noise, resolution or scatter effects. In this way, the mismatch effects were isolated by ensuring that compounding factors did not affect the result. It was also necessary to separate the effects of an attenuation mismatch with those arising from the blurring effects of motion and for this reason, single time points within the respiratory cycle were used in place of motion-averaged maps. For each dataset, activity maps were generated at end-exhale and attenuation maps were generated at end-exhale and end-inhale. Mismatches were then investigated by attenuating the end-exhale activity map according to the matched respiratory position and subsequently performing an attenuation-correction at end-inhale. The relative importance of individual mismatch types would remain to be true if effects such as motion were included; however their measurement would then become difficult because of the multiple factors involved.

The methods of producing reconstructed emission images from the activity and attenuation NCAT maps, for PET and SPECT, are outlined in the following sections:

3.2.2.1 PET

The main stages involved in generating reconstructed images were to forward-project the activity map to form sinograms, apply attenuation to the sinograms with the matched

attenuation map to produce an estimate of the measured data, correct again for attenuation but with a mismatched attenuation map and finally to reconstruct the attenuation-corrected emission sinogram to form an image. Each of these stages is described in more detail below:

Forward-projecting the NCAT maps to produce sinograms

Due to the simplified situation with no noise, resolution or scatter effects modelled, complex simulation techniques were not required and a forward projection incorporating the Radon transform was sufficient in this case. The Radon transform produces a sinogram from a distribution $f(x, y, z)$ as follows:

$$R(s, \theta, z) = \int_{-\infty}^{\infty} f(s\cos\theta - t\sin\theta, s\sin\theta + t\cos\theta, z)\, dt \tag{3.2}$$

where s is the distance from the origin and θ is the angle of the projection, as in Equations 2.2 and 2.3. This was used to create projections at an angular spacing of 3^{o} for all three maps for each dataset (the activity map at end-exhale and the attenuation maps at end-exhale and end-inhale).

Attenuating the activity sinograms with the matched attenuation maps

Since PET attenuation is independent of source depth, the end-exhale activity sinogram ($\mathrm{EM}(s, \theta, z)$) could simply be multiplied by the exponential of the end-exhale attenuation sinogram ($\mathrm{Att}(s, \theta, z)$) to produce the attenuated emission map, ($\mathrm{EM\_Att}(s, \theta, z)$). This required the activity and attenuation maps to have the same voxel sizes and field-of-views and also required the attenuation coefficients to be scaled correctly, according to the voxel size. The attenuated emission map was therefore produced as follows:

$$\mathrm{EM\_Att}(s, \theta, z) = \mathrm{EM}(s, \theta, z) \cdot \exp\left(-\mathrm{Att}(s, \theta, z)\right) \tag{3.3}$$

where $\mathrm{EM\_Att}(s, \theta, z)$ represents the projections that would have been measured by the camera in a real acquisition.

Attenuation-correcting the activity sinograms with a mismatched attenuation map

Correcting the emission sinogram for attenuation is carried out in the same way, but replacing the sinogram of the matched attenuation map for the sinogram of the mismatched attenuation map ($\mathrm{Att}_{\mathrm{mis}}(s, \theta, z)$). Additionally, the sign is reversed (from negative to positive) to correct for attenuation rather than apply it, as follows:

$$\text{EM\_corr}(s,\theta,z) = \text{EM\_Att}(s,\theta,z) \cdot \exp\left(\text{Att}_{\text{mis}}(s,\theta,z)\right) \tag{3.4}$$

$\text{Att}_{\text{mis}}(s,\theta,z)$ in this case represents the sinograms of the end-inhale attenuation map.

Reconstructing the activity sinograms to produce an image volume

$\text{EM\_corr}(s,\theta,z)$ was then reconstructed to produce an image using a 2D OSEM algorithm (Hudson and Larkin, 1994) with four iterations and 15 subsets. This reconstruction algorithm was chosen since it is widely used in the clinical setting, however in the absence of scattered photons or noise, non-iterative algorithms, such as filtered back-projection would also be expected to perform well. The use of a 2D reconstruction meant that each axial slice was reconstructed separately and a volume was then produced from the set of reconstructed slices.

3.2.2.2 SPECT

The procedure for processing the NCAT maps for producing SPECT images was similar to the PET images, but differences in the methods accounted for the different detection geometries between the modalities and the different attenuation effects. The projector was therefore specific to SPECT to simulate the emission of single photons. Unlike PET, the attenuation of SPECT projections are depth-dependent, since it involves the detection of a single photon rather than a co-linear pair. Accounting for attenuation is therefore more complex and was incorporated into the reconstruction, rather than as a pre-correction as described for PET above. In generating the SPECT images, the forward-projection and reconstruction stages were both performed with the incorporation of the attenuation application / correction. Therefore the first two stages of the PET image generation were combined for SPECT, as were the second two stages. In order to enable a direct comparison between PET and SPECT artefacts, the SPECT images were simulated over 360°, although cardiac images would normally be acquired over only 180°. The impact of the difference in acquisition angle is discussed in Section 3.4.

3.2.3 Assessing the Reconstructed Images

Reconstructed images were aligned to produce HLA, VLA and SA slices using the "Myovation" software (GE Healthcare, Haifa, Israel). Polar maps of the left-ventricular myocardial uptake were then produced from the SA slices, again using Myovation. The polar plots in conjunction with the 17-segment model as shown in Figure 2.4 (Cerqueira et al., 2002) were used to enable a quantitative comparison between each dataset and the

baseline. As the only difference between the datasets was the attenuation-correction process, any change from the baseline was attributed to the simulated mismatches. This was assessed both in terms of the qualitative change in appearance and the variation in scores over the 17 segments, as a measure of non-uniformity. The non-uniformity was calculated as follows:

$$\text{Non-uniformity}_{\text{image}} = 100 \times \frac{S_{\text{image}}}{S_{\text{baseline}}} \tag{3.5}$$

where S_{image} and S_{baseline} are the standard deviations of scores in the 17 segments in the mismatch and the baseline images, respectively. This analysis was repeated three times to ascertain the magnitude of errors expected from inconsistencies in the dataset reorientation and significance values were calculated using a one-tailed t-test to ascertain which results were significantly different to the baseline. [1]

3.3 Results

The polar plots from each dataset are shown in Figure 3.4 for PET and Figure 3.5 for SPECT, and the VLA slices through the centre of the LV are shown for PET and SPECT in Figures 3.6 and 3.7. A number of qualitative observations can be made from these images: the baseline or artefact-free images, which contained no attenuation mismatches, appear fairly uniform apart from reduced counts in the septal wall, which is attributable to partial volume effects because of this wall being narrower than other walls of the left ventricle. This effect arises when more than one material contributes to a given voxel; in the case of the myocardium, an apparent reduction in activity will arise from the inclusion of background activities within the voxel. The appearance of the myocardium in the initial NCAT activity map is shown in Figure 3.1, where the narrower width of the septal wall can be seen.

Of the images created with mismatches, it can be seen that in general the apparent defects appear to affect the modalities in a similar manner, in that they appear in the same locations and cover approximately the same extent of the myocardium. However, the artefacts appear more pronounced in the PET images. The most striking non-uniformity can be seen in the anterior wall of the left ventricle in the dataset involving a cardiac position mismatch and is also apparent in both modalities. Prominent artefacts are also visible in the septal wall when liver mismatches are present, again, particularly in the PET images. A lesser defect can be seen in the PET image involving lung mismatch due to diaphragm contraction but cannot be seen in the SPECT equivalent.

These observations are supported by segment variation comparisons, which are summarised in Figure 3.8. These results confirm that introducing certain types of mismatch between

[1] It should be noted that the standard deviations quoted here do not infer a normal distribution and are used as simply a measure of spread about the mean. The segmental scores used in the calculation of the standard deviations would not be expected to be normally distributed.

the activity and attenuation maps can increase the variation over the myocardium. In agreement with the qualitative observations, the largest increase in variation was recorded with cardiac position mismatch and the change was larger for PET images (an increase of $84 \pm 11\,\%$) compared with SPECT ($61 \pm 8\,\%$ increase). These variations were significantly above the baseline with $p < 0.001$ for both. A similar result is true for the liver position mismatch but with a slightly smaller overall effect, giving an increase of $59 \pm 10\,\%$ for PET and $34 \pm 8\,\%$ for SPECT. These increases were also significant ($p < 0.01$). It was found that the less prominent defect seen in the diaphragm motion PET image also produced a significant increase in the variation ($p < 0.01$) by $25 \pm 7\,\%$, whereas the equivalent variation for the SPECT image was not above the baseline ($-2 \pm 7\,\%$, $p = 0.33$). Also no significant increase in variation was observed for datasets involving lung mismatches because of chest-wall motion (PET: $4 \pm 6\,\%$, SPECT: $-4 \pm 6\,\%$, $p > 0.05$).

The significance of the differences between PET and SPECT was also assessed for each dataset. In every case where a significant change from the baseline was observed (i.e. all mismatch types with the exception of mismatched lung because of chest-wall motion), the difference between PET and SPECT was also significant, with the PET non-uniformities being greater in every case ($p < 0.01$).

3.4 Discussion

It can be seen from this investigation that the issue of attenuation mismatches needs to be addressed in both PET and SPECT to avoid the artefacts that may result. In the extreme case, the artefacts can be very severe and cause the study to be non-diagnostic, although it should be noted that the situations simulated in this study are extreme cases and less severe mismatches would be expected clinically. The purpose of the study was to determine the potential effect of attenuation-correction artefacts in the absence of confounding factors, such as the blurring effects of motion or the presence of noise, which could obscure the effects of the attenuation mismatches. The artefacts present in a clinical study result from a combination of attenuation mismatches with other factors, which may confound the effects from the mismatches alone.

The effects of attenuation mismatches are more prominent in PET studies compared with SPECT, because of the dual-photon emission, compared with the single photon in SPECT. The resulting effect of the gamma rays having to travel a greater distance within the patient for a coincidence detection outweighs the effect of the reduced attenuation coefficient (at the higher photon energy) and hence PET attenuation factors are typically greater than those in SPECT. For example, a projection passing through the centre of a spherical object of 20 cm diameter, exhibiting a uniform attenuation equal to that of soft tissue ($0.09\,\mathrm{cm}^{-1}$ at 511 keV and $0.15\,\mathrm{cm}^{-1}$ at 140 keV) will experience approximately double the attenuation in PET

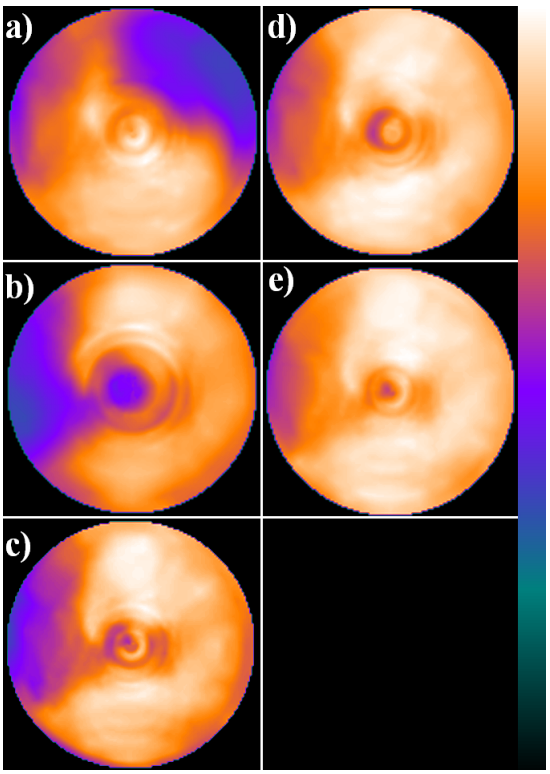

Figure 3.4: Polar plots of the five PET datasets produced from the reconstruction of NCAT maps with attenuation mismatches. a) Cardiac position mismatch, b) Liver position mismatch, c) Lung mismatch because of diaphragm contraction, d) Lung mismatch because of chest-wall motion and e) Baseline (artefact-free dataset). The orientation of the plots are as per the standard orientation for the 17-segment model, as shown in Figure 2.4.

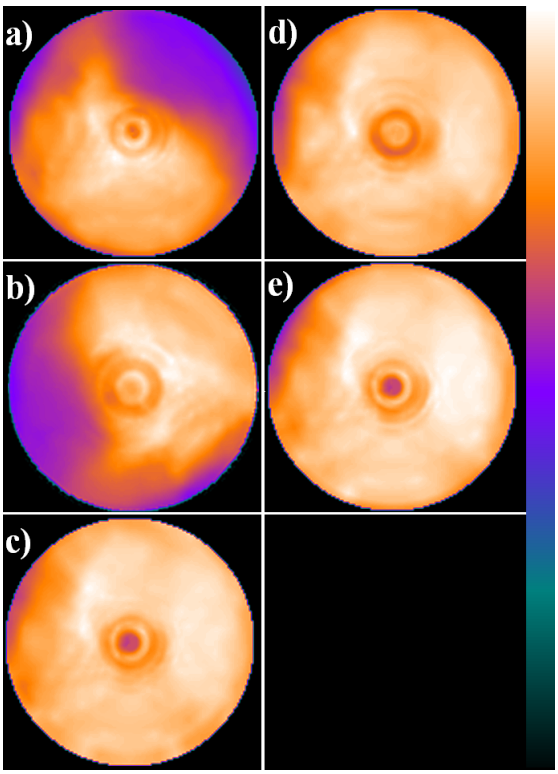

Figure 3.5: Polar plots of the five SPECT datasets produced from the reconstruction of NCAT maps with attenuation mismatches. a) Cardiac position mismatch, b) Liver position mismatch, c) Lung mismatch because of diaphragm contraction, d) Lung mismatch because of chest-wall motion and e) Baseline (artefact-free dataset). The orientation of the plots are as per the standard orientation for the 17-segment model, as shown in Figure 2.4.

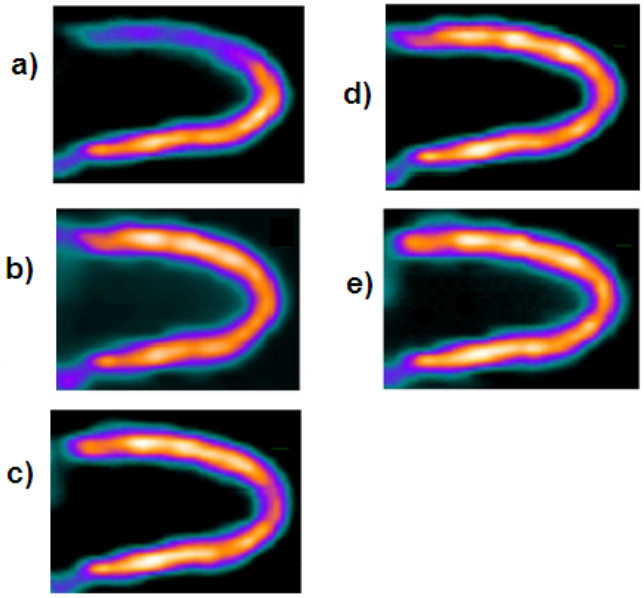

Figure 3.6: The VLA mid-slice for each of the PET datasets. a) Cardiac position mismatch, b) Liver position mismatch, c) Lung mismatch because of diaphragm contraction, d) Lung mismatch because of chest-wall motion and e) Baseline (artefact-free dataset). See Figure 2.3 for an illustration of the position of the VLA mid-slice.

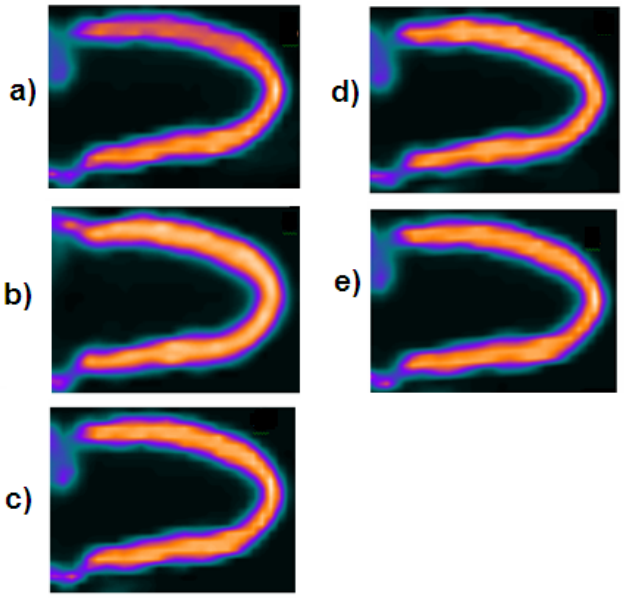

Figure 3.7: As for Figure 3.6, but for SPECT datasets.

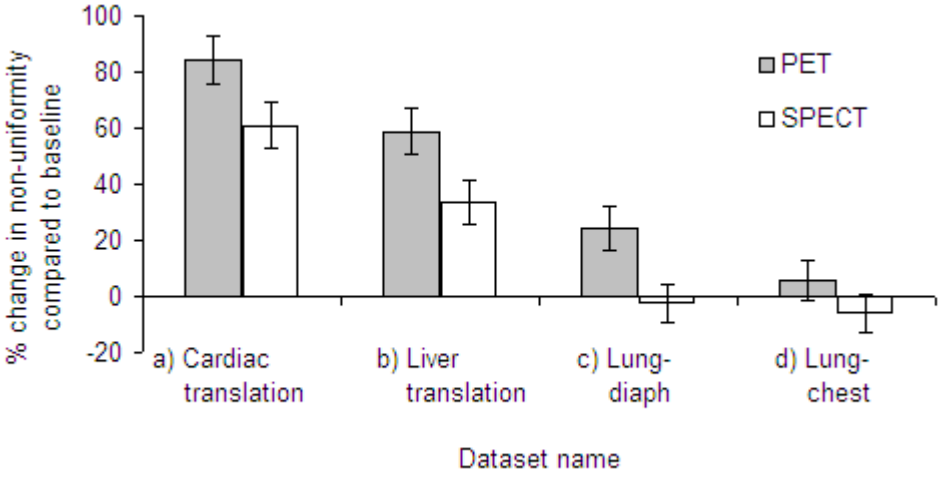

Figure 3.8: Change in the non-uniformity from the baseline for the following datasets: a) Cardiac position mismatch, b) Liver position mismatch, c) Lung mismatch because of diaphragm contraction and d) Lung mismatch because of chest-wall motion.

compared with SPECT (16 % of emitted photons unattenuated with PET and 33 % with SPECT). These factors are of course highly dependent on the geometry of the attenuating materials. The decreased severity of SPECT artefacts compared with PET was noticeable in the images involving cardiac position mismatch, liver position mismatch and lung mismatch due to diaphragm contraction, both qualitatively and quantitatively. In the images with lung mismatch due to diaphragm contraction, an increase in the non-uniformity was measured in PET whereas no increase above the baseline was observed in SPECT. The lower dependence of SPECT images on the attenuation map may have prevented a low-contrast artefact from being measurable in this case.

The largest error induced was that from cardiac position mismatch. Since the organ of interest in this case was also the organ exhibiting motion, the local effects of mismatch artefacts were maximised and a large contrast between the superior and inferior walls of the left ventricle resulted. The effects of mismatches in the liver position were also found to be prominent and followed a similar trend to the cardiac mismatch artefacts, in that the PET images were affected to a larger degree than the SPECT images. Mismatching lung geometry because of diaphragm motion was found to cause an increase in variation in the PET image, whereas mismatches caused by chest-wall motion did not.

The propagation of mismatch errors in PET have previously been investigated (McCord et al., 1992; Meikle et al., 1993; Goerres et al., 2003), and in general the effects of a mismatch have been found to be fairly localised. Goerres et al. (2003) for example, performed attenuation-correction on a whole-body PET image with both end-exhale and end-inhale

CT images and found that the differences between the two reconstructed PET images was correlated with the differences between the CT images. This indicated that attenuation mismatches propagate directly into the PET data, causing a localised effect.

The findings reported here support this, although it was also found that mismatches in organs surrounding the heart can distort the apparent uptake in the left ventricle. This suggests that the effects are not limited to the organ in which the mismatch occurs, but that mismatches can also produce artefacts in nearby organs. This can be explained by the presence of projections that traverse both the organ of interest and the mismatched structure. For PET, the attenuation correction factors (ACFs) of some of the projections through the heart may therefore be altered by mismatches in the liver position. Since the measured emission map is multiplied by the ACFs prior to reconstruction (see Equations 2.2 and 2.3), ACF errors can lead to errors in the reconstructed image. This observation is consistent with the findings of Gould et al. (2007), who found that artefacts arose in clinical MPI studies where the heart borders were matched between PET and CT, but where the diaphragm position was mismatched, i.e. where the heart–diaphragm relation had changed. They concluded that the three causes of false-positive defect observed in PET-CT scans were a) PET-CT heart misregistration, b) diaphragm–heart mismatching and c) residual motion artefacts in CT. This provides further evidence that it is not only local effects that can produce artefacts in the heart, but that surrounding organs that share projections with the heart can also have an effect.

The liver mismatch results have particular importance in relation to current clinical practises for PET studies. One method in use of overcoming the problems of mismatch involves a simple translation of the reconstructed activity distribution with respect to the attenuation map if a mismatch is evident on visual inspection. The translation ensures that all myocardial activity overlies the heart region on the attenuation map rather than overlying the lower attenuating lung tissue. After performing the translation, the attenuation-correction and reconstruction are repeated to obtain the revised activity image. This method is likely to be successful in correcting the artefacts arising from heart translation and subsequent mismatch; however, it does not take into account the possible effect of liver mismatch, which may therefore remain after translation to correct for heart position mismatch. This investigation has shown that these errors could be significant and that a more accurate attenuation-correction could be obtained by accounting for the liver position. The correction method described above is currently applied to motion-averaged images, but the liver mismatch would be an equally important factor in performing respiratory-matched attenuation-correction prior to motion-correction.

In this study, SPECT acquisitions were also found to be affected by liver position mismatches, but to a lower degree, for the reasons already discussed. It is not surprising that a mismatch in liver position is capable of creating a significant artefact because of the

large difference in attenuation coefficients between the lung and the liver and because of the size of the liver. This results in a large difference in the total attenuation experienced and consequently, the errors produced can be significant. The acquisition simulated here involved projections over 360^o to be consistent with the PET simulation for subsequent comparison, however different results may be obtained if a 180^o acquisition were simulated, which is the normal extent of rotation for cardiac SPECT acquisitions. By excluding emissions that traverse a large portion of the body, the effects of mismatch from structures distant to the heart are likely to be lessened, since many of the emissions affected by mismatch will not be detected. The artefacts caused by heart mismatch would remain in this case, but the severity of the liver mismatch artefact may be reduced in this scenario. A simulation of this type of acquisition would be required to ascertain the extent of this change.

Lung mismatches of different types were also investigated as a potential non-cardiac source of error. A small error was observed in PET when a mismatching lung geometry due to diaphragm motion was simulated, but mismatching lung geometry due to chest-wall motion had no effect. The explanation for this difference lies with the radiological path-length experienced by gamma rays in these two scenarios. In this experiment a 2D reconstruction algorithm was used, which means that each transaxial slice can be considered independently. When the lungs expand with diaphragm contraction, the geometry within a transaxial slice in the heart does not change (if cardiac motion is eliminated), but the attenuation coefficient of the surrounding lung tissue decreases. As a result, the overall radiological path length through the patient changes and hence mismatches of this type can lead to errors in the reconstructed image. The same effect does not occur with chest-wall motion because the total radiological path length is not affected by this type of lung expansion. Although the lung attenuation-coefficient decreases during expansion, this is counteracted by the increased radius of the chest and the resulting increased distance of lung tissue a photon needs to traverse. The net effect is that the total attenuation path length and the ACF are largely maintained, and as a result, artefacts do not arise from this source.

It should be remembered that the uniform lung expansion assumed here is an approximation and may not be a realistic model of how the lungs expand. Heterogeneities in the change in lung density over the respiratory cycle have been observed (Verschakelen et al., 1993; Simon, 2005), and complex relationships between lung density and factors such as patient orientation (upright or prone / supine) and the presence of lung disease have also been found. This is therefore a patient-specific factor, which may alter the findings for changes in lung density shown here. The uniform expansion approximation does however allow for a simple improvement to the NCAT phantom, which would otherwise involve an increasing lung mass with inhalation.

3.5 Conclusions

Both PET and SPECT images can suffer from the effects of attenuation-correction artefacts if mismatches are present, and PET images are generally affected to a larger extent than SPECT. This is because of the dual-photon detection of PET resulting in larger attenuation factors and therefore an increased sensitivity to errors present in the attenuation map. Although the subsequent work in this thesis is related to PET imaging, the similar manifestation of attenuation mismatch artefacts in the modalities means that a similar consideration of the effects of mismatch would be needed in SPECT studies. Although a reduced severity of artefact was seen in SPECT, the heart and liver positions were still the key factors in artefact production and hence, as with PET, both would need to be considered in performing a correction for respiratory motion.

It was found that artefacts from attenuation-correction mismatches have a number of contributing factors of varying importance. The most prominent factor leading to artefacts was the global position of the heart, resulting in clinically significant artefacts that contributed to a large increase in variation across the myocardium. The other important factor was found to be the liver position that, if not matched correctly, was also capable of producing significant artefacts. Lesser artefacts were observed when a mismatch in lung geometry because of diaphragm contraction was simulated, however this was only observed in the PET dataset. Finally no effect was observed for mismatches in lung geometry because of chest-wall motion, which can be attributed to the constant total attenuation resulting from this type of motion.

These artefact quantification results are important, firstly in recognising the potential errors that could occur in PET and SPECT datasets and secondly in determining the factors that need to be addressed in developing a motion-correction algorithm. As discussed in Section 2.7.2 on page 61, correction for attenuation prior to correcting for motion is important in maintaining quantitative accuracy and when a study is split into frames according to respiratory state, each frame must be corrected with the matched attenuation map. These results have shown that when performing this respiratory-matched attenuation-correction, the focus should lie primarily on obtaining the correct positions for the heart and diaphragm over the respiratory cycle, where lung geometry is less critical. It is therefore not necessary to perform motion correction over the whole thorax volume for cardiac studies, which could reduce the complexity of the algorithm needed to perform this. On the other hand, it is important not to neglect the liver position if artefacts are to be avoided.

Chapter 4

Diaphragm Segmentation and Tracking

This chapter describes the development of a semi-automatic segmentation algorithm for application to the diaphragm in gated CT images and the subsequent use of the segmented surfaces in assessing its motion over the respiratory cycle, in relation to that of the heart. The motivation behind this work is outlined in Section 4.1 and background information relating to segmentation methods is given in Section 4.2. The segmentation algorithm development and validation are described in Section 4.3 and the subsequent comparison of diaphragm and heart motions is outlined in Section 4.4.

4.1 Motivation

Earlier investigations showed that diaphragm motion is one of the key factors in determining the attenuation-correction accuracy of cardiac PET imaging (see Chapter 3). Consequently, further investigation of its motion was required to determine suitable correction methods. Although the appearance of the diaphragm itself in the motion-corrected PET image is not of interest, its importance in the attenuation-correction process means that its position has to be known over the respiratory cycle. A direct measure of the diaphragm position could be obtained with the use of a gated CT, however due to the dose-related issues and the problems of residual PET-CT mismatches discussed in Section 2.7.1, alternative methods of obtaining a measure of diaphragm position could be advantageous.

The absence of a gated CT presents new problems, since the respiratory motion of organs cannot be obtained from a single, static CT. Motion information would be available from a gated PET study, however its high levels of noise and lack of anatomical detail limit the

information that could be obtained in this way. Tracking the heart position in such images is less problematic, due to the high level of uptake in the myocardium, reducing the issue of noise, but the diaphragm exhibits poor contrast, particularly in non-attenuation-corrected images. These issues are discussed in more detail in the following chapter, in Sections 5.1 and 5.4.2. Information from additional sources other than just the gated PET images would therefore likely be beneficial in determining the diaphragm position as a function of respiratory position.

For these reasons, measures of diaphragm position, shape and motion were required to determine what additional information could be extracted for subsequent use in diaphragm tracking in gated PET. For example, if common heart–diaphragm relationships were observed over a patient population, this information could be used to ascertain the diaphragm position from knowledge of the heart position, which is more easily obtained. Knowledge of the typical form of the diaphragm surface could also be useful in determining its position in noisy images. To investigate these possibilities, a method of segmenting the diaphragm was required, such that its shape could be visualised and measurements of its motion could be obtained.

Gated CT datasets were available for assessing diaphragm shape and motion, which enable an anatomically detailed description of the diaphragm to be obtained. A segmentation algorithm was therefore required specifically for identifying the diaphragm in images of this modality. Since a segmentation needed to be performed in every frame of the gated CT study (comprising 10 frames) and the process was to be repeated over a number of patient datasets, an automatic or semi-automatic algorithm was needed to reduce the time burden of manually segmenting the diaphragm multiple times. Automating the process also reduces the chances of subjective assessments of diaphragm position, which may not be reproducible. Segmenting the diaphragm is a complex task, due to its close proximity to other organs with similar intensities in CT. Therefore an algorithm specific to this task was required to perform the segmentation.

4.2 Background

Segmentation describes the action of separating a particular structure from its surroundings, or partitioning the image into segments. These are normally non-overlapping regions that exhibit a common characteristic, e.g. intensity or texture (Pal and Pal, 1993). Segmentation allows the shape of the structure of interest to be analysed and measurements of volume of closed structures are also possible. Obtaining such measurements have many medical applications, for example determining tissue volume (Larie and Abukmeil, 1998), diagnosis (such as segmentation of the left ventricle of the heart for determining its ejection fraction)

(Taylor, 1995), the study of anatomical structure (Worth et al., 1997) and to assist in treatment planning for radiotherapy (Khoo et al., 1997).

Segmentation can be performed manually, where an expert identifies the structure to be segmented and manually outlines it, usually by clicking on an interactive display of the image. This can be very time-consuming and prone to errors, particularly due to the subjective placement of boundaries. When a user manually segments a structure repeatedly, there will most likely be variations in the placement of the outline between each attempt (the intra-user variability). Furthermore, if different users segment the same structure, there will be a difference between the results obtained by each user (the inter-user variability). There is therefore a need for automation in segmentation to improve the reliability and reproducibility of the procedure as well as to reduce the time-burden.

There has been a significant interest in this area, with many types of segmentation algorithm being developed for different tasks. In general, successful segmentation algorithms incorporate knowledge of the appearance of the image and of the object being segmented, in order to guide the segmentation process. As such, there is no general solution for segmentation; the algorithm is normally tailored for the specific task it is designed for. Additionally, expert knowledge of the user can also be incorporated: this prevents the segmentation being fully automated, but allows observer-based knowledge to further guide the result. Therefore, when a new task is considered, it is likely that modifications to existing methods are required to make them appropriate for the new task, or that a new approach needs to be considered.

The trade-off between automation and the level of guidance from the user is an important consideration. The requirements of the algorithm are lessened as the level of input from the user is increased, since expert judgement can be incorporated that would be very challenging to include in a fully automated algorithm. On the other hand, the time advantages are lessened as more input is needed and could give rise to the re-introduction of subjective results that suffer in their reliability. Many segmentation algorithms therefore aim to minimise the level of user input needed while maintaining the accuracy of the result obtained. Having obtained the segmented region from an image, validation is then an important stage to assess the result (Zhang, 1996). The most common method of performing this is by comparison with a manual segmentation, which is considered the measure of ground-truth. There are limitations with this approach, since the manual segmentation may be subject to errors and is laborious to perform. Alternatives could involve the use of a phantom, in which case ground-truth is known. In order to get a good measurement of the segmentation performance however, the phantom must be a good representation of the situation it is designed to test and replicating clinical images is challenging.

4.2.1 Existing Segmentation Techniques

When considering potential methods for a segmentation task, it is useful to review methods that are already in use, so that their suitability for the task being considered can be assessed. Some of the currently used techniques for image segmentation are outlined in the following sections. Due to the large number of different segmentation algorithms in existence, this is not intended to be a comprehensive review of all of the available methods; instead an overview of the main techniques on which most currently used segmentation algorithms are based is given. It should be noted that these techniques do not have to be used in isolation; it is common for a combination of methods to be incorporated into a single segmentation algorithm. The evaluation of these techniques in relation to the task of segmenting the diaphragm is described in Section 4.3.2.

4.2.1.1 Pixel Classification Methods

There are a number of methods used to classify pixels, with the aim of assigning the pixels in an image to a particular class based on a common feature, for example, image intensity. An example of this in medical imaging is the classification of brain MRI volumes into gray matter, white matter and cerebro-spinal fluid (CSF). Methods used to achieve this include thresholding, classifiers and clustering methods. Thresholding is a simple technique that assigns a class based on whether a pixel is above or below a particular threshold, resulting in a binary partitioning of image intensities. This has been used for digital mammography to separate tumours from healthy tissue (Polakowski et al., 1997) but is normally used as an initial step in the segmentation process, since it is sensitive to noise in the image and may not therefore produce an adequate segmentation unaided.

Classifiers and clustering methods are pattern recognition techniques, which work in feature space (Yakimovsky, 1976). A typical feature space used in this type of segmentation is a histogram of image intensities; the segmentation algorithm then partitions the histogram, thereby separating the pixels into classes. The main distinction between classifier and clustering methods are that classifier methods normally require manual input to assign labels to a sample of pixels, from which the remaining pixels are automatically classified. Clustering methods on the other hand are typically "unsupervised" and instead iteratively alternates between performing the segmentation and defining the classes. These methods allow for a more intelligent incorporation of image features compared with thresholding, however they still have limitations, due to the fact that they do not incorporate spatial modelling. This means that like thresholding, they can be sensitive to noise and image inhomogeneities (Pham et al., 2000).

4.2.1.2 Region Growing

Region growing techniques require the manual placement of a "seed", which is then expanded into a region according to the properties of the surrounding pixels (Haralick and Shapiro, 1985). All pixels in the resulting segmented region are therefore connected, since they have been included from the expansion from a single seed. The criterion determining how the region grows is normally based on image intensities, such that all pixels included have an intensity within a specified range of those included in the seed. Starting from the seed, an iterative process is undertaken, where all pixels surrounding the current region are evaluated, to determine whether they should be included in the region. The process terminates when no new surrounding pixels are added to the region.

Problems with this technique arise in the presence of noise and it also suffers from "leakage". Noise can result in a supposedly homogeneous region containing pixel values outside the specified range that are therefore excluded from the region. This gives rise to holes in the resulting region. Conversely, leakage can occur when more than one structure contributes to the signal in a given voxel and the region grows into an adjacent structure(Pham et al., 2000). This occurs when two structures of similar intensities are separated by a small distance and is therefore an issue when adjacent structures of similar intensities need to be separated. For these reasons, region growing techniques are also often used as an initial step in segmentation, with subsequent improvements needed to overcome the problems of holes and leakage.

4.2.1.3 Edge-Detection

Edge-detection is not itself a segmentation algorithm, but can be used in conjunction with other techniques to separate a particular structure. It assesses the gradients in image intensity to determine the positions of changes in intensity. One such method of performing this is with the Sobel edge enhancement operator (Duda and Hart, 1973), which convolves the image with the following masks:

$$\text{X mask} = \begin{bmatrix} -1 & 0 & 1 \\ -2 & 0 & 2 \\ -1 & 0 & 1 \end{bmatrix} \tag{4.1}$$

$$\text{Y mask} = \begin{bmatrix} 1 & 2 & 1 \\ 0 & 0 & 0 \\ -1 & -2 & -1 \end{bmatrix} \tag{4.2}$$

It is a useful starting point in many medical images, since adjacent structures often exhibit different intensities or are separated by a small region of a different intensity, which can be

detected with the use of an edge-detection algorithm. The initial result of edge-detection may consist of several unconnected lines or curves, that do not fully separate different structures as a closed boundary would do. Subsequent processing methods are therefore needed with edge-detection in order to produce the segmented regions as required.

4.2.1.4 Deformable Models

A widely used method of segmentation is one that involves deformable models (Bae et al., 1993; Kass et al., 1988; McInerney and Terzopoulos, 1996). The main principle is to impose constraints on the allowed form of a contour, such that the final result is physically realistic and closely conforms to the relevant features in the image. This is generally implemented with the inclusion of both internal and external forces on a closed boundary, where the internal forces impose smoothness and the external forces couple the contour with the features of the image. It is normally initialised with the placement of a pre-defined contour type, e.g. a circle or ellipse, which subsequently undergoes a deformation so as to fit to the relevant image features.

A commonly used deformable model is that known as "snakes", which is an active contour model based on the use of splines (Kass et al., 1988). In this case the internal "energy" of the contour is described in terms of two physical parameters of the contour: its tension and its rigidity (McInerney and Terzopoulos, 1996) and the external energy is related to features such as extrema in image intensity or edges. Local minima in the external potential are positioned on these image features, allowing the contour to lock onto them. Obtaining the final solution therefore involves minimising the energy of the contour in terms of both the internal and external effects.

This technique is more robust to the effects of noise than other methods described, due to the smoothness constraints employed. It also has its disadvantages however: the final result may be sensitive to the initial placement of the contour and suitable constraints must be applied in deforming the contour. Finally, it has also been found to be less successful in fitting boundary concavities, due to the design of the internal and external forces. However, improvements have been observed in this respect with the use of different external energy formulations (Pham et al., 2000).

4.2.1.5 Atlas-Guided Approaches

This technique involves compiling information about the structure-of-interest and using this to assist in the segmentation of the structure in a previously unseen image (Collins et al., 1995). This method is commonly used for brain studies, where the atlas is already segmented and labelled according to regions of gray matter, white matter and CSF. To segment these regions in a dataset, the atlas and the labelled regions are warped so as to align with the

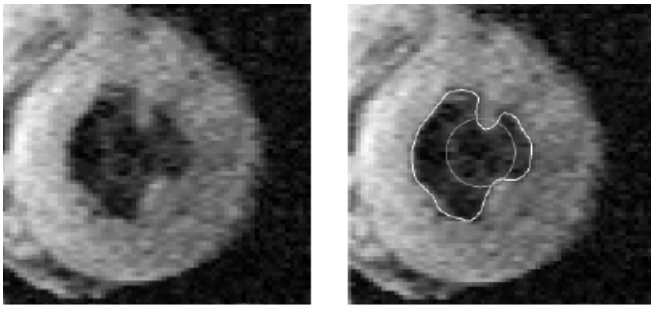

Figure 4.1: The segmentation of the left ventricle from an MRI study using an active contour model. a) The original image. b) The initial placement of the circle within the left ventricle and the final result after deformation of the circle. From Pham et al. (2000).

new dataset. This has the advantage that the regions are already defined and therefore by registering the atlas with the new dataset, the segmentation has been performed. It is only suitable for structures that exhibit similar shapes across the population however, since regions may be mis-assigned in the presence of large anatomical variations and is therefore limited to certain, well-defined structures.

4.3 Development of an Algorithm for Diaphragm Segmentation in Gated CT

The following describes the development of a segmentation algorithm, designed specifically for diaphragm segmentation in CT. The data for which the segmentation was required is described in Section 4.3.1. Taking into account the type of data available, the general form of the diaphragm and its appearance in CT, existing algorithms and established segmentation techniques can be assessed for their suitability for this task. These considerations are outlined in Section 4.3.2. Having established the most appropriate technique on which the algorithm should be based, a general form of the segmentation algorithm was established, which is described in Section 4.3.3 and methods were then developed to incorporate the technique into a semi-automatic algorithm. These methods are described in Sections 4.3.4 to 4.3.8, with the image pre-processing outlined in 4.3.4 to 4.3.6, the body of an initial segmentation attempt described in 4.3.7 and that of the final segmentation method implemented described in 4.3.8.

4.3.1 CT Data

A segmentation algorithm was required for use with respiratory-gated CT datasets, which covered the thorax and upper abdomen. Twenty-four such datasets were available for segmentation, which were acquired at the M.D. Anderson Cancer Center, Texas, USA for oncology purposes (Pan et al., 2004). Each patient dataset consisted of 10 volumes acquired at evenly-spaced phases throughout the respiratory cycle through the use of a cine-mode acquisition. The pixel size of each dataset was 0.98 mm^2 and the slice thickness was 2.5 mm. All volumes consisted of 512×512 pixels per transaxial slice and between 64 and 112 slices.

In order to obtain information regarding normal diaphragm shapes and motions, patient datasets that were found to exhibit abnormal respiratory patterns were discounted and not segmented. Additionally, those that exhibited residual motion artefacts, as described in Section 2.5.3 were also discarded. Lastly, every remaining dataset was checked to ensure that the full diaphragm dome was included in the field-of-view at every respiratory phase; since the datasets were acquired for the purposes of assessing the motion of lung tumours, the diaphragm was not always covered fully. This process led to the removal of 6 datasets due to respiratory abnormalities, 2 from motion artefacts and another 6 from incomplete imaging of the diaphragm (predominantly at the end-inhale images). The remaining 10 datasets were therefore deemed suitable for diaphragm motion assessment and were subsequently segmented.

4.3.2 Assessment of Existing Segmentation Techniques

Many methods already exist for segmentation, which have been developed for a number of different purposes. Some of the techniques which are commonly used in segmentation are outlined in Section 4.2.1. As discussed, there is no general solution to the problem of segmentation and algorithms typically incorporate knowledge of the properties of the structure being segmented and its appearance in an image to guide the segmentation process. Specifically considering the diaphragm, manual outlining has previously been performed for investigating its shape (Gauthier et al., 1994; Beichel et al., 2005), but due to the complexity of the diaphragm appearance in CT, few algorithms have been developed for automating this process: Fujita et al. (2005) investigated a method for outlining the diaphragm in fluoroscopy images, however due to the 2D nature of such images, this involved only a single outline based on the intensity changes in the images. Partial diaphragm surfaces have been obtained by segmenting the lungs (Reutter et al., 1997), but this does not include sections of the diaphragm that are not apposed with the lungs. Zhou et al. (2008) have recently published findings relating to a fully automatic diaphragm segmentation with the use of thin-plate splines, however this was published more recently than the work outlined here

and hence was not available for consideration at the outset of this investigation. The results obtained from this method are discussed in Section 4.3.10.

Due to the lack of existing algorithms for segmenting the diaphragm in CT, it was necessary to generate a new algorithm to perform this task. However, even new algorithms are generally based on existing segmentation techniques, which are then extended or modified such that they are applicable to the specific task. Some of these general techniques (as outlined in Section 4.2.1) were evaluated in relation to the task of segmenting the diaphragm to assess whether they could be incorporated into the solution. Some of the general features of the diaphragm and its appearance in the images available for segmenting which were considered when determining the best segmentation method are as follows:

- The diaphragm is a muscle that defines the boundary between the thorax and the abdomen, which has two main regions: the "apposition zone", which lies adjacent to the chest-wall in an approximately superior–inferior direction and the "diaphragm dome", which is approximately in the transverse plane, adjacent to the lungs and heart, as described in Section 2.5.

- Although it has a finite thickness, it is the upper surface of the diaphragm, apposed with the thorax that is of interest here, since it defines the boundary between the high-attenuating tissues of the abdomen and the low-attenuating lung tissue in the thorax. For segmentation purposes therefore, it can be considered a surface rather than a volume.

- The diaphragm dome is situated immediately superior to the liver and the two are indistinguishable in non-contrast enhanced CT images due to the similarity of the tissues' electron densities. However, the position of its upper surface can be determined where the diaphragm is adjacent to lung tissue due to the high contrast between diaphragm and lung tissue in CT images. The diaphragm can also be hard to distinguish in relation to sub-diaphragmatic tissues below the left hemi-diaphragm and again, its position is inferred from the lung–abdomen boundary.

- The apposition zone of the diaphragm in CT contracts during inhalation, causing the diaphragm dome to move in an inferior direction. It has a similar appearance to the tissues of the chest-wall as well as abdominal tissues, such as the liver. It is therefore very difficult to distinguish, and contrast-enhancement or an alternative imaging modality, such as MRI would be needed to segment this portion of the diaphragm reliably.

- The heart is situated superior to the diaphragm, in close proximity to the upper surface of the diaphragm dome. As with the liver, the heart exhibits very similar CT intensities to the diaphragm and abdominal tissues, making separation difficult in some regions.

Although there is often a small separation between these organs, partial volume effects mean that frequently there is little contrast between them in CT and the boundary between the two is therefore obscured.

Considering these properties, it was decided to only segment the diaphragm dome and not the apposition zone. This is because the apposition zone of the diaphragm is surrounded by tissues of similar densities, which makes its identification in CT very difficult, and also lessens its importance in relation to the attenuation-correction of cardiac PET studies. The diaphragm dome however, defines the boundary between high and low attenuating tissues and also exhibits the largest translation over the respiratory cycle. One possibility would be to only segment the portion of the diaphragm dome that is adjacent to lung tissue, and not that adjacent to the heart, since the attenuation changes in the heart region are small. However for obtaining relationships between diaphragm and heart motions, it would likely be advantageous to obtain measurements of its position and shape over the entire diaphragm dome and hence the segmentation was developed specifically for this region. Further references to the diaphragm therefore relate to the dome portion only.

Taking into account the diaphragm properties, it was possible to assess which of the techniques outlined in Section 4.2.1 would be applicable for incorporation into a segmentation method. Firstly, pixel clustering methods would not be suitable in this application, due to the inability to separate the diaphragm from surrounding structures (particularly the liver). A measure that would classify voxels corresponding with the diaphragm would also therefore include liver voxels, and possibly those of other abdominal structures or the heart. Furthermore, both the pixel clustering methods and region growing approaches are applicable to structures that are defined by a volume, rather than a surface, as is the case here and are hence unsuitable for diaphragm segmentation.

Edge-detection on the other hand would allow the high contrast diaphragm–lung boundary to be identified and could therefore be used as a basis for a segmentation algorithm, where the upper surface of the diaphragm is outlined. In isolation, edge-detection does not necessarily produce a segmented region, since unconnected lines can be produced (e.g. in the presence of noise) that do not correspond with a particular structure or surface. Performing segmentation using edge-detection would therefore necessitate the incorporation of other processes to obtain the required result. The reduced contrast present in the region of the heart would also provide challenges to this type of algorithm.

Deformable models, based on the formulation of internal and external energies of a contour, are generally applied to the segmentation of an enclosed volume (Pham et al., 2000). The general approach of guiding a contour towards pre-defined image features with the use of suitable constraints could however be applicable to diaphragm segmentation, provided the algorithm is reliable at segmenting an open surface.

Finally, atlas-guided approaches are used in situations where the form of the object is well known and anatomical variations are limited (Collins et al., 1995). Aside from the need to construct the atlas for the diaphragm, the level of anatomical variability of the diaphragm is unknown prior to segmentation and hence this technique is not suitable for use here.

Taking into account these observations, edge-detection was chosen as a starting point for an algorithm designed to obtain the diaphragm surface. An initial segmentation algorithm was constructed based on the assumption that the diaphragm–lung boundary is generally the first major change in voxel intensity encountered when moving in a superior direction through the image. This will subsequently be referred to as the "first boundary" method, which considered each column of voxels (in the transaxial direction) separately, to determine whether a simple technique such as this, with minimal prior knowledge of the diaphragm shape would be sufficient for obtaining a diaphragm surface. Difficulties with this method however led to the development of an alternative method, referred to as the "boundary tracking" method, which considered the relationship between neighbouring columns of voxels, rather than treating them independently. This allowed the incorporation of additional knowledge of the general form of the diaphragm to guide the segmentation process.

4.3.3 The General Form of the Segmentation Algorithms

Both algorithms were based on edge-detection and hence the same pre-segmentation processing was applied to both. This involved the automatic determination of the limits of the diaphragm dome (Section 4.3.4), the generation of an edge-enhanced image (Section 4.3.5) and the creation of a binary map of the positions of boundaries identified from the edge-enhanced image (described in Section 4.3.6). The methods by which the diaphragm surface was subsequently obtained from the binary map method were specific to the algorithm being investigated. These are described for the "first boundary" method in Section 4.3.7 and for the "boundary tracking" method in Section 4.3.8.

Both methods were constructed so as to work on a slice-by-slice basis, using coronal slices. Although it would be easier to ensure consistency between slices with the use of a 3D algorithm, the 2D method allowed for a simpler implementation and allowed the solution to one slice to guide the segmentation in an adjacent slice. Inter-slice consistency was achieved through the use of constraints and by smoothing the final result in the through-slice direction and was not therefore found to be a problem. Coronal slices were selected for this process since the diaphragm edge can be viewed clearly in this orientation, although the use of sagittal slices would also be possible.

The aim of the segmentation algorithm was to obtain an outline of the diaphragm in all coronal slices containing diaphragm tissue and to record the results as a series of heights, thereby building up a 3D surface. This approach meant that each surface could be stored as

a 2D array, containing zeros in the pixels outside the extent of the diaphragm and a value indicating the diaphragm height (in relation to the bottom of the image) within its extent.[1] This approach is suitable for the diaphragm dome, since it does not contain folds or vertical sections (i.e. sections that are parallel to the chest-wall, as with the apposition zone) and therefore can be described by a single value at every pixel position.

4.3.4 Automatic Diaphragm Limit Determination

The aim of the segmentation was to determine a value relating to the height of the diaphragm for every x, y position in which the diaphragm was present. Therefore, prior to segmentation, it was necessary to determine the area within which this process was to be performed, to exclude the regions beyond the extent of the diaphragm. An automatic method of determining these limits was required, since the diaphragm typically covered approximately 150 coronal slices for each phase in the CT datasets, making a manual approach impractical.

A method was developed for identifying the limits of the diaphragm in every coronal slice in which the diaphragm dome was present. It was based on identifying the lower left and right limits of lung tissue in each coronal slice, since these positions correspond with the limits of the diaphragm dome and the region to be segmented. Furthermore, the lungs can be easily identified with use of a region-growing technique, providing a near fully-automatic method of diaphragm limit determination. The region-growing technique, as implemented in IDL (Interactive Data Language) involved placing a seed in the centre of each lung (the manual component to the process), which was expanded in 3D until a boundary of a given threshold was encountered (as described in Section 4.2.1.2). The superior portion of the image volume was masked out for this procedure to avoid the seed from one lung filling both lungs by traversing the bronchi; this therefore ensured that the lung volumes obtained from region-growing remained separate.

From the lung binary maps, the diaphragm limits were determined by selecting the pixel within the lung region that had the smallest distance to the bottom corners of the image, for the left and right limits of the diaphragm dome. The result of carrying out this procedure is illustrated in Figure 4.2, which shows an example CT coronal slice, the binary maps resulting from the region-growing and the two fused, with the diaphragm dome limits determined for this slice displayed as blue circles.

A similar process was required in sagittal slices, to determine the limits in y, except that only the range of coronal slices was required for performing the above procedure and hence was

[1] In subsequent sections, the term diaphragm "height" will refer to the distance to the diaphragm from the inferior limit of the imaged volume. This is also its position in the z (superior–inferior) direction. The x and y positions will be used to refer to the left–right and anterior–posterior directions respectively. Additionally, the terms vertical and horizontal will be used to refer to the directions within a coronal slice: the horizontal direction is therefore the x-direction and the vertical direction is the z-direction.

Figure 4.2: An illustration of the automatic diaphragm limit determination method for a given coronal slice. a) The original coronal CT slice, b) the result of using a region-growing technique from seeds placed in the centre of each lung (right lung in red, left lung in green), c) a fusion of a) and b), with the blue circles indicating the pixels that define the diaphragm limits for this slice.

only required on one slice. Three positions needed to be obtained in order to ascertain the diaphragm extent: y_{ant}, corresponding with the anterior limit of the diaphragm dome, y_{post}, specifying the posterior limit and y_{split}, indicating the position at which the descending aorta intersects the diaphragm, causing it to split into two distinct sections. The locations of these limits on a 2D representation of the diaphragm surface are indicated in Figure 4.3. y_{ant} and y_{post} could easily be determined using the same lung region method as used for determining the limits in x, however the absence of lung tissue at the mid-line (where the split occurs) prevented the determination of y_{split} in this same way. This was therefore identified manually by locating the y-position of the intersection of the aorta with the diaphragm.

For the slices posterior of the diaphragm split (y_{split} to y_{post}), two sets of limits were required to describe the diaphragm extent, for which a similar method to that described above was used. The inner limits were determined by using the distance between the voxels of the left-lung volume and the reference point from the opposite side of the image and vice-versa.

In a few slices, the automatic determination of the diaphragm limit gave an erroneous result, due to the shape of the lung meaning that the lung pixel closest to the lower corner of the image was not that which defined the diaphragm limit, as illustrated in Figure 4.4. To overcome this problem, a weighting was applied to a component of the distance measurement to encourage the selection of different lung pixels. Since the majority of errors resulted in the selection of pixels that were higher than the true diaphragm boundary, the vertical distances were weighted such that lower lung pixels were preferentially selected. A factor of 3 applied to the vertical distances was found to correct the problem, giving a modified distance measure as follows:

$$\mathrm{D} = \sqrt{(x_{\text{lung}} - x_{\text{ref}})^2 + (3 \times (z_{\text{lung}} - z_{\text{ref}}))^2} \tag{4.3}$$

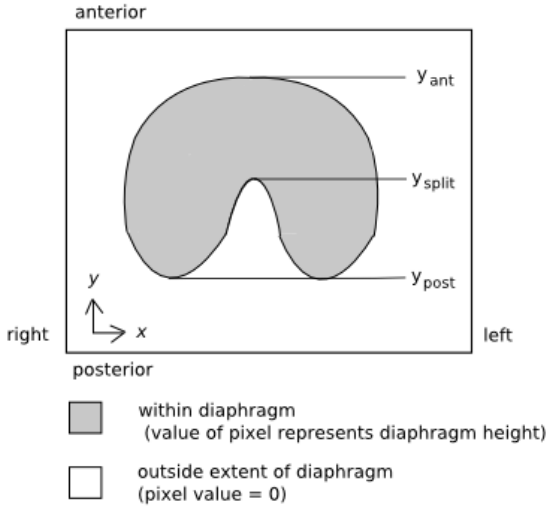

Figure 4.3: The representation of the diaphragm dome surface as a 2D array (512 × 512 pixels), where the values of pixels within its extent represent the height of the diaphragm with respect to the inferior edge of the image volume. The limits of the diaphragm extent in the anterior–posterior direction are described by y_{ant} and y_{post}. y_{split} specifies the point at which the descending aorta intersects the diaphragm and it hence splits into two regions.

where D is the pseudo-distance between the reference and lung pixels and x and z represent the distances between the pixels in the left–right and superior–inferior directions (horizontal and vertical directions in the coronal image).

Following this correction, reliable diaphragm limits were obtained to describe its extent in x and y, which defined the image section to be used during segmentation. The regions outside of these limits were then masked, so that they did not contribute to the image segmentation process. Finally, before edge-detection was performed, each coronal image was cropped in the z-direction, such that only the 40 most inferior slices were included. This ensured inclusion of the diaphragm surface, while removing as many other organs as possible, to simplify the subsequent segmentation.

4.3.5 Edge-Detection

Prior to edge-detection, the cropped images were smoothed in order to limit the effect of noise. Smoothing with a boxcar function of width 3 pixels was found to be sufficient for this task. Edge-detection was performed on the cropped and smoothed coronal slices produced by the above methods, using the Sobel operator (Duda and Hart, 1973), given in Equations 4.1 and 4.2 . This generated an image in which the value of a given pixel is related to the degree of change between the pixel and its surroundings, as illustrated in Figure 4.5.

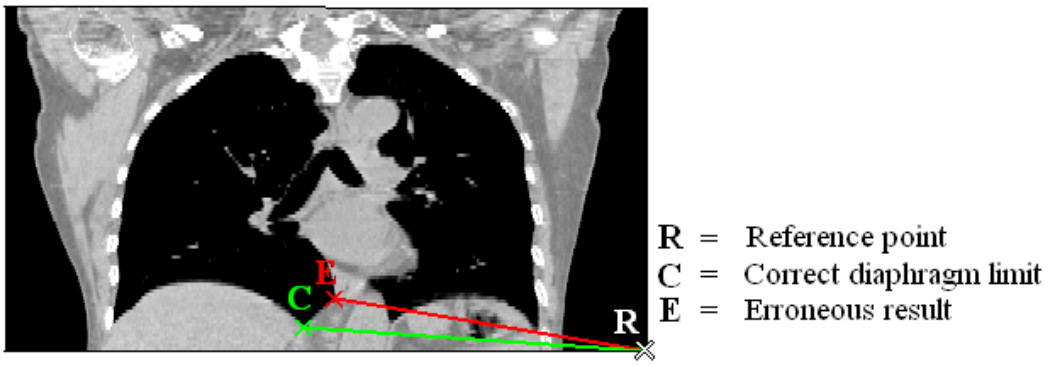

Figure 4.4: Erroneous diaphragm limit determination when distance weightings are not included. An illustration of an error in the determination of the diaphragm limit when vertical and horizontal weightings are not included. The error occurs because the distance R $\rightarrow$ C is greater than the distance R $\rightarrow$ E. This can be avoided by assigning larger penalties to the vertical distance such that lung pixels towards the lower edge of the image are preferentially selected.

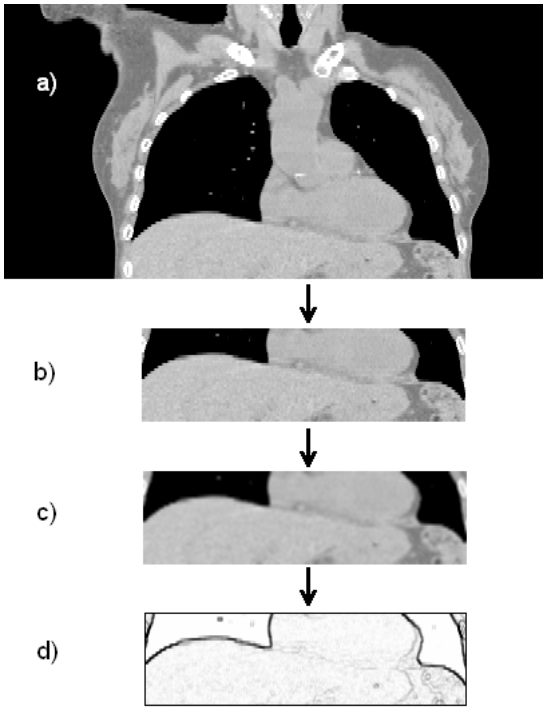

Figure 4.5: The generation of an edge-enhanced image from a coronal slice: a) the original coronal slice b) the cropped coronal slice following the automatic diaphragm limit determination and cropping in z, c) with smoothing applied and d) the result of applying the Sobel operator to the cropped, smoothed coronal slice.

4.3.6 Binary Map Generation

From the edge-enhanced image, a binary map of the positions of boundaries in the original image was generated, such that a pixel value of 1 represented the presence of a boundary and all other pixels had a value of 0. Using such an approach means that the intensity information in the edge-enhanced image was not used in the segmentation algorithm, since all boundary features included in the binary map were given an equal value. This method was used to allow for the low-contrast boundary present in the region of the heart, which would not benefit from the intensity values being taken into account.

The binary map was created by taking vertical profiles through the intensity map and identifying peaks in the intensity. Non-zero pixels in the binary map were used to represent the positions of these peaks. By considering only vertical profiles, only the intensity peaks that corresponded with horizontal features in coronal slices were included. Since the diaphragm dome lies approximately in the transaxial plane, this provided a method of preventing some of the non-diaphragm related features in the edge-enhanced image contributing to the binary map, while retaining the relevant features.

The upper surface of the diaphragm dome is identified by a reduction in CT intensity, which is a consistent feature across its whole surface, albeit a small reduction in some regions. Therefore the gradient direction was also used as a means of reducing the presence of unwanted boundaries. Only peaks in the edge-enhanced image that related to negative changes when moving in a superior direction through the image were included to reduce the input from the upper edges of abdominal air pockets and the lower edge of the heart, for example.

Further filtering of the identified peaks was performed prior to generation of the binary map, in order to reduce the presence of low-intensity peaks caused by noise. Suitable levels of filtering had to be determined, to ensure that peaks associated with the diaphragm edge in the low-contrast region of the heart were not also removed during this process. A threshold was applied to remove unwanted features, to mask low intensity regions. This is illustrated in Figure 4.6. The value selected for the threshold was based on removing as much noise as possible, while minimising the removal of low-level peaks associated with the heart–diaphragm boundary. A threshold of 100 was found to be appropriate for this task.

The remaining peaks were then included in the binary map, with the pixel in the location of the peak assigned a value of 1. The nonzero pixels in the binary map will be henceforth be referred to as edge-pixels, since they represent the presence of a boundary or edge in the CT intensities.

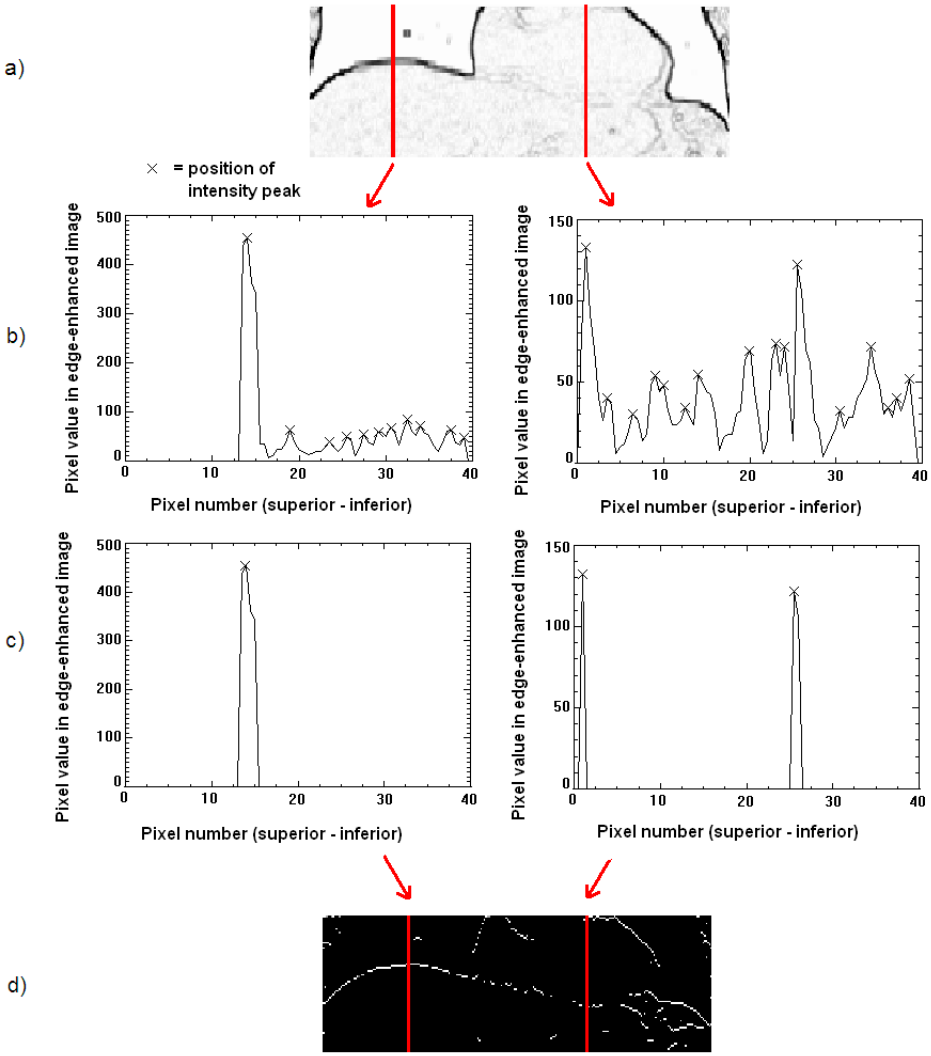

Figure 4.6: Producing a binary map of image boundaries from the edge-enhanced image. a) The edge-enhanced image, with red lines indicating the positions of two sample profiles (left profile: diaphragm adjacent to lung, right profiles: diaphragm adjacent to heart), b) plots of the selected profiles, with × marking the locations of all peaks, c) the remaining peaks following the application of the threshold-based mask and d) the resulting binary map of boundary positions for the edge-enhanced coronal slice shown in a).

4.3.7 Segmentation Algorithm: "First Boundary" Method

The region-of-interest of the CT images was such that in coronal slices, the abdomen–thorax boundary was often the first boundary encountered when moving in a superior direction from the lower edge of the image. A simple method of segmenting the diaphragm could therefore involve identifying this first boundary in the binary map in all columns over the extent of the diaphragm surface. If successful, this would represent a fast method of segmentation that is easy to implement.

Figure 4.7b shows the result of selecting the first nonzero pixel (edge-pixel) in each column of the binary map, starting from the bottom edge of the image. It can be seen that in some regions, particularly above the liver (left hand side of image), the diaphragm surface has been correctly identified, but in other regions the approach has been less successful and a lot of noise remains. In particular, the diaphragm surface has been missed on the right hand side of the image and lower features have instead been selected. The problems encountered are partly attributable to the choice of method where each column of pixels is treated separately and hence the selected position in one column does not influence that in its neighbouring columns. It is clear therefore that to use this approach to obtain a complete diaphragm surface, additional methods are required to reduce the presence of noise and to prevent the selection of erroneous features. Furthermore, some columns of the binary map do not contain any nonzero pixels and hence methods of filling these gaps would also be needed.

To overcome some of the problems associated with noise, any isolated edge-pixel that had been selected was removed from the solution. These pixels were identified by inspecting the immediate surroundings of each edge-pixel. Those that did not have any neighbouring edge-pixels were assumed to be outliers caused by noise and hence were removed from the solution. In these columns, the new "first pixels" were obtained from the modified binary map and the process repeated. The result of this is shown in Figure 4.7c, which contains no isolated pixels. The problem with the selection of non-diaphragmatic boundaries, however, remains.

The selection of erroneous features not associated with the diaphragm had two main causes. Firstly, the presence of air pockets or tissue density changes within the abdomen produced boundaries that contributed to the binary map. Such boundaries are encountered before the diaphragm when moving vertically from the bottom of the image and hence are selected using this method. This can be seen with the problem on the right hand side of the image in Figure 4.7, where the diaphragm has not correctly been identified due to the presence of abdominal features contributing to the binary map (as seen by comparison with the original image, shown in Figure 4.5). Secondly, the poor contrast in the region of the heart means that not all columns contained edge-pixels related to the diaphragm, as their contrast

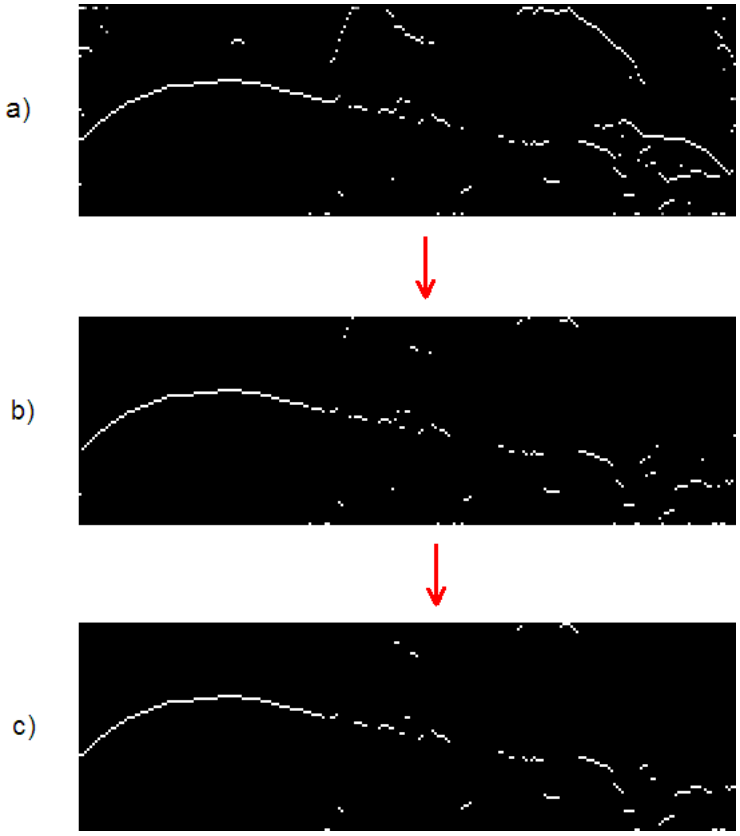

Figure 4.7: The "first boundary" method of diaphragm segmentation. a) The initial binary map of boundary positions. b) The result of selecting the first nonzero pixel in each column in moving in a vertical direction from the lower image edge. c) The result of removing isolated pixels and repeating the search for a nonzero pixel in these columns. Figure 4.5 shows the original image for this slice.

was not sufficient for inclusion in the binary map. When this occurred in several adjacent columns, an erroneous feature higher in the image to the diaphragm was sometimes selected.

It can be seen that the assumption that the diaphragm boundary is the first encountered breaks down in the presence of abdominal features that contribute to the binary map. This was found to be the case in many slices, preventing the algorithm from obtaining the correct solution. Overcoming such problems is challenging and indicates that the incorporation of additional knowledge into the segmentation process could potentially be beneficial. For these reasons, this algorithm was not developed any further and a different approach that was expected to be more robust in the presence of features such as air pockets was investigated instead.

4.3.8 Segmentation Algorithm: "Boundary Tracking" Method

Having determined that it is not sufficient to treat each column of pixels independently and that better results would likely be obtained from considering the relationship between nearby pixels, a new segmentation method was developed to address these issues. This method also started from the binary map previously described, but instead of simply selecting the first nonzero pixel in each column, this algorithm attempted to detect the presence of line segments and track these across the binary map. By looking for continuous lines of edge-pixels in the binary map, the algorithm took into account the relationships in the diaphragm position in adjacent pixel columns, so that a more plausible estimate of the diaphragm position could be obtained.

The following sections describe the method developed for obtaining an initial solution (Section 4.3.8.1), the scoring methods (Section 4.3.8.2) and the technique for improving the initial solution, to obtain the final solution (Section 4.3.8.3). The whole process is summarised in a flowchart in Figure 4.8.

4.3.8.1 Obtaining an Initial Solution

The "boundary tracking" algorithm worked by searching for continuous line segments in the binary map and using these to generate an estimate of the diaphragm position. Line segments were identified by the presence of multiple columns containing edge-pixels in close proximity to each other.

The process was initialised by assessing the edge-pixels within the first 5 columns on the left hand side of the image. This position was chosen, since it is in the region of the diaphragm–lung boundary above the liver, which is easily and reliably identifiable due to its high contrast. Line segments within these 5 columns were sought by assessing the relationships between nearby edge-pixels, to determine whether they formed a continuous line. The edge-pixels within these first 5 columns that were selected were those that exhibited the smallest variation in their positions.

From this point, a continuation of the line was sought by assessing the edge-pixels in the 6th column. If the 6th column contained an edge-pixel that was in an adjacent or nearby position to the edge-pixel selected in the 5th column, then it was also selected and the process continued for subsequent columns across the image. If no suitable edge-pixel was found, then the search range was widened and the following column was assessed. In the case that more than one suitable edge-pixel was identified, the direction of the line was determined from the existing selected edge-pixels and the edge-pixel that continued this gradient most closely was selected. Therefore if the previously selected edge-pixels exhibited a negative gradient, then the edge-pixel in the next column would be chosen in order to

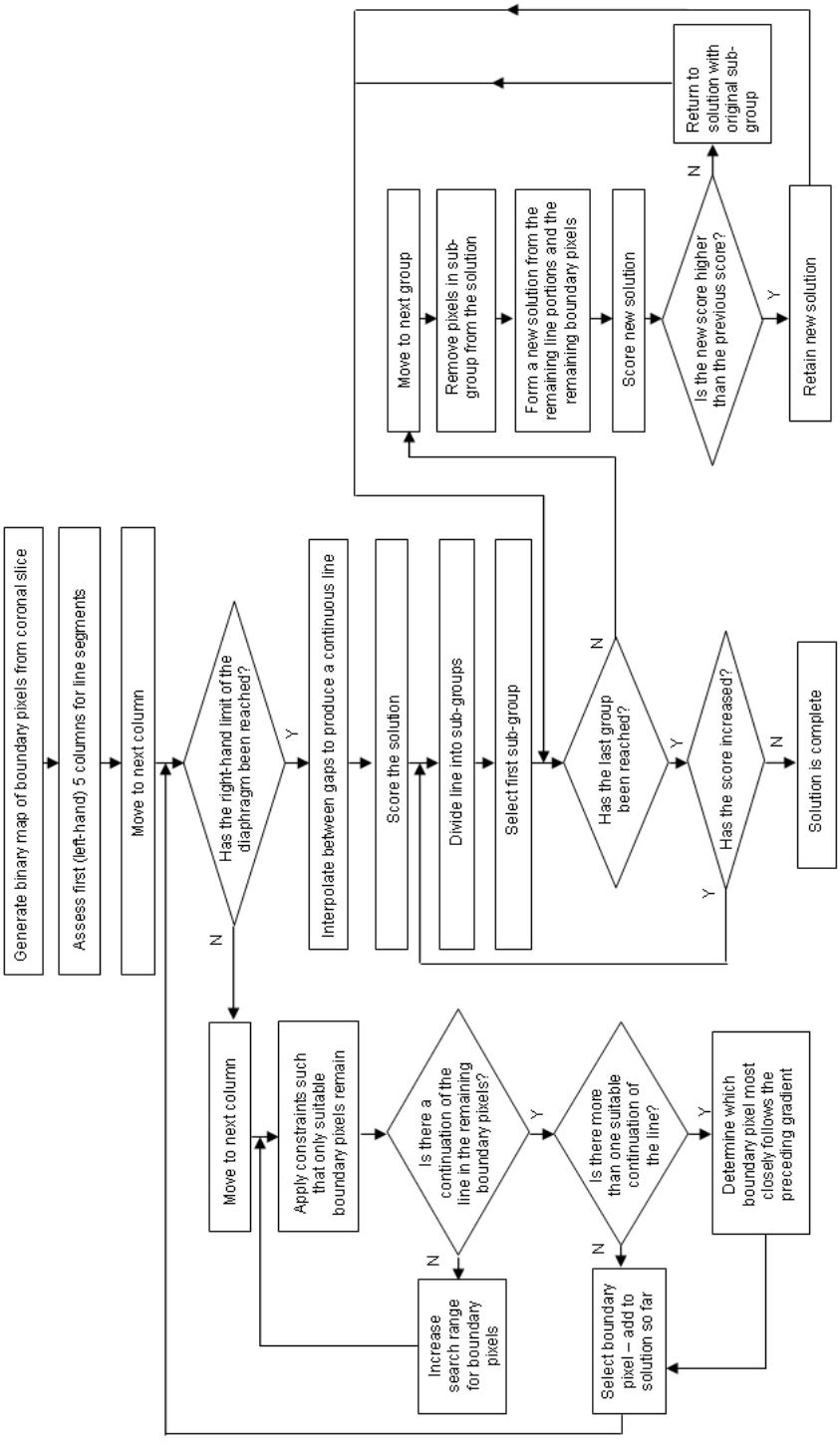

Figure 4.8: Flowchart showing the processes involved in the "boundary tracking" segmentation method.

continue the trend. In this manner, line-segments were tracked across the image from left to right. By tracking line segments in this direction, the relatively straight-forward diaphragm identification in the region of the liver was used as a good starting point from which to search for the diaphragm boundary in the more challenging region of the heart.

In order for the algorithm to produce reliable results, steps were needed to eliminate non-diaphragm related boundaries and to encourage selection of the diaphragm. Additionally, the segmented surface needed to be smooth and continuous, with a single diaphragm position identifiable in every column. These were achieved with the use of constraints on the allowed gradients, which took into account the known form of the diaphragm to guide the tracking.

Since it is known that the diaphragm dome lies approximately in the transaxial plane, steep gradients in the diaphragm surface were not expected. To prevent the occurrence of large gradients within the segmented outline (i.e. within a given coronal slice), a constraint was applied, which specified the maximum gradient allowed. This also assisted in producing a continuous and smooth outline, by removing all edge-pixels that did not fall within the range that satisfied the gradient constraint.

The maximum allowed in-plane gradient was set to ± 1, corresponding with an allowed slope of between $\pm 45^{o}$. This was also used in regions where no suitable edge pixels were identified, for example, in the heart region. In this case, the maximum gradient constraint was used to fan out the acceptance range, until the next edge-pixel was encountered, as illustrated in Figure 4.9.

Although this algorithm worked on a slice-by-slice basis, smoothness across slices was also required, therefore a through-plane gradient constraint was employed. The pixel size in the CT datasets used for this segmentation was 0.98 mm and hence only small changes in diaphragm position were expected between adjacent slices. Therefore, where a nearby slice had already been segmented, a range of allowed pixels centred on the previously segmented line was used, with all edge pixels outside of this range discarded. This range was applied prior to starting the tracking process, with the limits of the range applied in each column (limit_i) given by Equation 4.4, where h_i is the height of the diaphragm in column i of the previously segmented slice and Δs is the slice difference between the current and previously segmented slices in the coronal direction.

$$\text{limit}_i = h_i \pm 3 \times \Delta s \tag{4.4}$$

The effect of applying this constraint is shown in Figure 4.10, where boundaries distant to the outline in the nearby slice are eliminated, leaving only the diaphragm and other immediately adjacent boundaries and hence increases the algorithm's chance of selecting the correct boundary. Although a smaller gradient would be expected than that permitted,

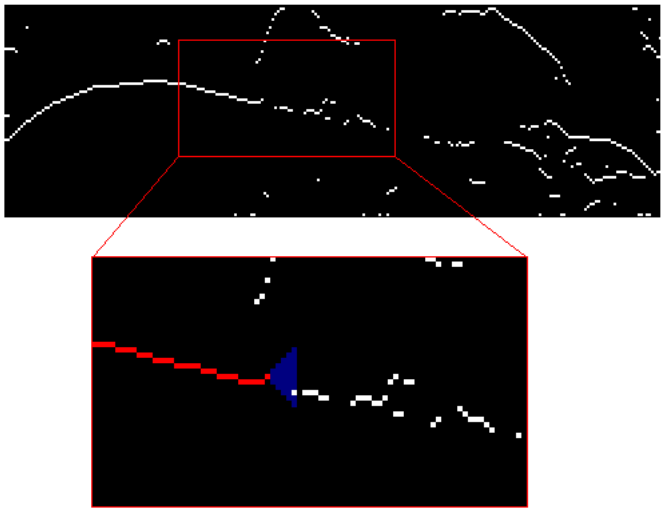

Figure 4.9: Method of implementing the left–right gradient constraint. The lower figure shows a zoomed portion of the binary map above, where the red pixels indicate those that have already been selected within the tracking process and the blue region shows the allowed region according to the gradient constraint. This area fans out until another edge-pixel within the specified range is encountered, as shown.

Figure 4.10: The effect of applying a distance constraint to eliminate distant pixels. The allowed range is shown in blue and edge-pixels outside of this region are discounted.

a generous range was chosen to ensure that no diaphragm boundaries were inadvertently eliminated.

With the use of these constraints, the diaphragm surface was tracked across each coronal slice, with the allowed edge-pixels being continually updated as the line was formed. This process had the effect that isolated pixels were not selected unless no suitable line segments existed in that column, therefore encouraging the tracking of structures rather than being influenced by noise. The constraints also ensured that discontinuities were not present, by limiting the range within which line segments could be sought.

Following the completion of the outline in the slice, a linear interpolation was performed to obtain values for columns in which no suitable edge pixels were identified. The interpolation ensured that estimates of the diaphragm height were available for every column across

the specified range of the diaphragm. This solution was then assessed and assigned a score, according to how well it met certain pre-defined criteria before ascertaining whether adjustments were needed. These processes are described in the following sections.

4.3.8.2 Scoring the Solution

The scoring was constructed so as to assess the solution in a given coronal slice in terms of its required attributes; namely its smoothness, its proximity to the diaphragm outline in an adjacent coronal slice and the number of edge-pixels in the binary map that were tracked in obtaining the solution. These attributes were encouraged during the line-tracking process, but a number of solutions may still be possible, from which the optimal solution which best describes the diaphragm outline needs to be chosen.

For a given diaphragm outline, a measure (a_k) associated with each attribute (k) was obtained, to which a score was assigned (s_k). Its total score (S_{total}), taking into account k attributes, was therefore given by:

$$S_{\text{total}} = \sum_k s_k(a_k) \tag{4.5}$$

All attributes were given an equal weighting, such that the maximum score obtainable from each one was 50 and the maximum possible score was therefore 150, considering the scores from the three attributes.

The first attribute, smoothness, was calculated by summing the differences in pixel heights (h_i) between adjacent pixels over the line (consisting of n columns) to get a measure of the total variation in diaphragm height (a_{var}), as follows:

$$a_{\text{var}} = \frac{\sum_{i=1}^{n} \mid h_{i+1} - h_i \mid}{n} \tag{4.6}$$

Using this measure, a smoothly varying line consisting of low-gradient lines (as expected for the diaphragm) would have a small variation, whereas one containing discontinuities or steeper gradients would have a large variation. The scoring for this term was therefore constructed such that low variation solutions scored highly and the score was reduced as the variation increased. At low variations however, a constant relation between score and variation was used, so as not to give preference to a completely flat line over a smoothly varying one. The switch to a linearly decreasing score was implemented at a variation that would be at the upper end of the typical variation over the outline; larger variations than this would therefore be considered undesirable. The upper limit of a_{var} for which a score was given was based on the maximum allowed gradient in this direction which limits the

maximum value of a_{var} possible. This scoring scheme is given in Equation 4.7 and illustrated in Figure 4.11.

$$s_{\text{var}} = \begin{cases} 50 & 0 \leq a_{\text{var}} \leq 0.5 \\ -100\, a_{\text{var}} + 100 & 0.5 < a_{\text{var}} \leq 1 \\ 0 & a_{\text{var}} > 1 \end{cases} \tag{4.7}$$

The second attribute to be scored was also related to smoothness and was based on the proximity of the current solution to that in an adjacent slice. This term therefore encouraged smoothness between slices, in order to achieve a smooth overall surface. It was calculated by summing the differences between pixel heights between the solution in the current (h_i) and the solution previously obtained in an adjacent slice (p_i) and dividing by the number of columns used in both solutions (n), as follows:

$$a_{\text{prox}} = \frac{\sum_{i=1}^{n} \mid h_i - p_i \mid}{n} \tag{4.8}$$

The scoring for this attribute (s_{prox}) was a linearly decreasing function for values of a_{prox} lower than or equal to 3 and 0 for values of a_{prox} greater than 3, as shown by Equation 4.9 and illustrated in Figure 4.11. This was constructed such that small changes between the solutions in nearby slices were scored highly, with the score decreasing to zero as the differences increased to values deemed to represent atypical diaphragm shapes. As with a_{var}, the upper limit of a_{prox} for which a score was given was based on the maximum that would be allowed due to the cross-slice gradient constraint.

$$s_{\text{prox}} = \begin{cases} -\frac{50}{3} \times a_{\text{prox}} + 50 & 0 \leq a_{\text{prox}} \leq 3 \\ 0 & a_{\text{prox}} > 3 \end{cases} \tag{4.9}$$

Finally, a term was included to encourage the tracking of edge-pixels. A good solution should track the edge-pixels closely and only use interpolation to fill in gaps in a few columns in the absence of suitable edge-pixels. The score related to this attribute was therefore highest for solutions where a high proportion of the columns contained tracked edge-pixels. The 'tracking' attribute (a_{track}) was calculated using Equation 4.10, where n_{track} is the number of columns that contained edge-pixels and n is the total number of columns in the solution:

$$a_{\text{track}} = \frac{n_{\text{track}}}{n} \tag{4.10}$$

The score relating to this attribute was a linear function, as given in Equation 4.11 and illustrated in Figure 4.11.

$$s_{\text{track}} = 50 \times a_{\text{track}} \tag{4.11}$$

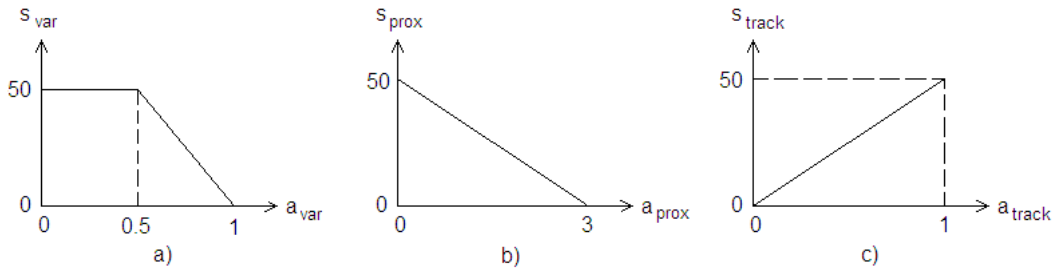

Figure 4.11: The functions used to assign scores to an estimated diaphragm outline in a given slice according to a) the smoothness, or variation in pixel heights over the outline, b) the proximity of the outline to that in an adjacent slice already been segmented and c) the fraction of pixels in the solution that corresponded with edge-pixels in the binary map of the detected boundaries. The overall score for a solution was the summation of the three contributions.

Once the score had been obtained for the outline in a given slice, a process was initiated to determine whether alternative solutions matched the diaphragm outline in that slice more closely, i.e. whether these alternative solutions scored more highly using the above scoring system. The method by which this was carried out is described in the following section.

4.3.8.3 Optimising the Solution

In obtaining a diaphragm outline in a given coronal slice, there was often a choice of boundaries from which the diaphragm outline could be produced, despite the use of constraints. In some cases, the first estimate was not the optimal solution and improvements could be made by selecting one of the other possible boundaries in one or more areas. To ascertain whether or not this was the case, a piece-wise search of alternative solutions was carried out.

The search entailed removing small groups of pixels from the current solution (i.e. putting those pixels to 0 in the binary map), thereby forcing the algorithm to consider alternative paths across that section of image. This was repeated for successive groups of pixels across the image, with the score being assessed in each instance. The solution with the highest score was then retained. If a new solution was chosen, then the process was repeated to determine whether further changes yielded additional improvements in the score. This continued until no further improvements in the score were obtained. At that point, the current solution was deemed to be optimal and was therefore stored as the true diaphragm position in that slice.

The effect of implementing this process is illustrated in Figure 4.12, which shows the changes made to the estimated solution as a result of performing the piece-wise search. In this example, it can be seen that although the initial estimate met the criteria imposed during the construction of the outline, in the region where the anterior boundary of the liver

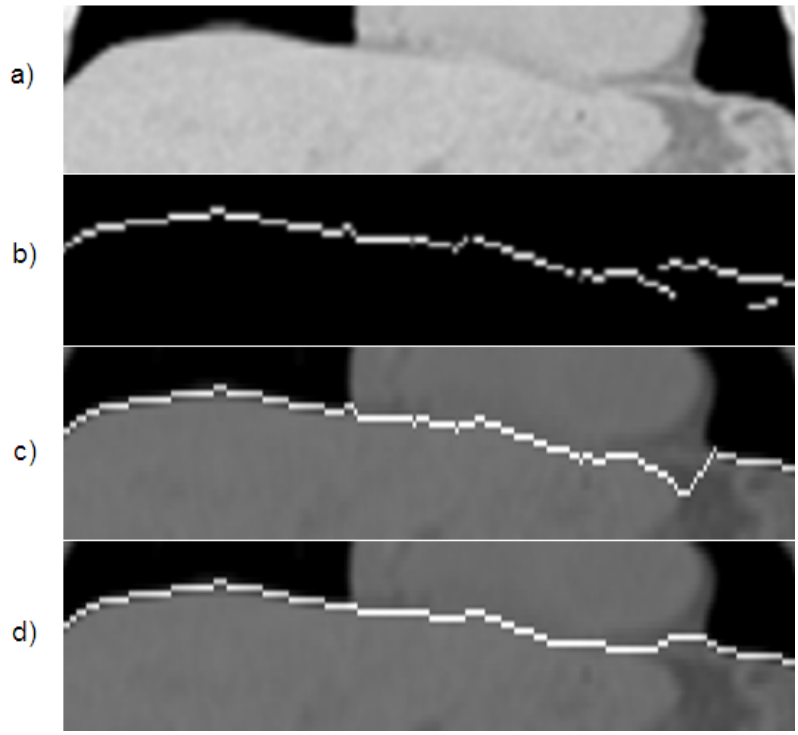

Figure 4.12: a) A coronal CT slice over extent of the diaphragm, b) the binary map of edge-pixels for this slice, c) the initial estimate of the diaphragm outline overlaid on the CT image, containing an error where the liver boundary deviates from the diaphragm and d) the final estimate following the piece-wise solution search, in which the error is rectified.

deviates from the diaphragm, the solution started to track the liver boundary instead of the diaphragm. The reason for this was a small area of poor contrast at the diaphragm boundary, resulting in a few columns in which no diaphragm edge-pixels existed. The algorithm therefore selected edge-pixels in the line created by the liver boundary before it ended due to the range constraint and an interpolation to the line of diaphragm edge-pixels was required.

This deviation meant that that the initial estimate was not a good representation of the diaphragm over the entire line, which was reflected by a reduced score. The scores related to variation (s_{var}) and to the proximity to its neighbouring slice (s_{prox}) were adversely affected by the incorrect region. In changing the solution such that it followed the diaphragm boundary instead of the liver, the score was increased due to improvements in its smoothness and its proximity to neighbouring slices, which outweighed the effect of a small reduction in the number of edge-pixels being tracked. Therefore this improved solution that was more consistent with the expected features of the diaphragm was retained and stored as one line of the diaphragm surface.

In the majority of slices, the automatic outlining described above was successful. However, errors were still present in some slices, which were identified by their low scores, even after optimisation. A score of less than 75 (out of a maximum of 150) was deemed to warrant further investigation. Additionally, viewing the entire diaphragm surface in its 2D array allowed any abrupt changes in diaphragm height, both within a slice and across slices to be identified. The potentially erroneous results were then investigated further using the display of the fused CT and diaphragm outline to ascertain the location of the error. When errors were identified, i.e. where the automated solution was found to be incorrect, further adjustments were performed to correct these errors. Three types of adjustment were implemented as follows:

1. An intensity threshold adjustment, to allow a manual alteration of the threshold of peaks included in the edge-pixel binary map
2. An option to prevent the removal of edge-pixels that are distant from adjacent solutions
3. The removal of a specified range of edge-pixels unrelated to the diaphragm that have been incorrectly selected by the algorithm

The first of these adjustments allowed the inclusion of lower intensity peaks than would otherwise have been included, which was useful for increasing the number of edge-pixels in the low contrast region around the heart. Conversely, binary maps could be made less noisy by increasing the threshold, provided that this did not adversely affect the heart region. Overriding the constraint that removed edge-pixels not in close proximity to an adjacent solution was needed in a few slices where a steep gradient present in the diaphragm surface caused part of the diaphragm to be outside the range applied. Although using this option typically resulted in the inclusion of many non-diaphragm related boundaries in the edge-pixel map, it was occasionally required to ensure none of the diaphragm was excluded.

Option 3 was required in a few slices where an incorrect boundary was selected due to it being in close proximity to the true diaphragm boundary and scored more highly than the diaphragm boundary itself. This was rare, due to the construction of the constraints and the scoring system, however where the occasional incorrect boundary was selected this method could be used to successfully overcome it. This did not constitute a fully manual intervention, since the option for the user to define a section of diaphragm was not available; instead the previously selected incorrect edge-pixels were removed from the binary map and the process of tracking was repeated with the remaining edge-pixels. Fully manual adjustments were avoided, even in the cases where the automatic algorithm was initially unsuccessful, in order to avoid subjective results that may not be reproducible.

To speed up the process of segmentation, and due to the pixel size being only 0.98 mm, the outlining procedure was performed only on alternate slices and averaging was used to obtain

the outlines in the in-between slices. Averaging was not performed across respiratory phases, since these differences were expected to be larger than those between coronal slices and it was also not known if a linear interpolation would be a sufficiently good approximation. Therefore every frame of the 10-phase CT studies was segmented separately.

Following the completion of the diaphragm segmentation in all respiratory phases, smoothing was applied to the entire dataset. Boxcar smoothing was applied in the anterior–posterior and left–right directions (x and y in the 2D diaphragm array, respectively) and in the temporal direction on a pixel-by-pixel basis. Due to the segmentation having been performed in the coronal slices, a lower level of smoothing was applied in the left–right direction compared with the anterior–posterior direction, since each left–right outline should already be smooth in nature. The widths of the boxcar smoothing were therefore 3 in the left–right direction, 5 in the anterior–posterior direction and 3 over the respiratory frames. This was the final stage in producing the 10 segmented diaphragm surfaces, which were stored in 10 floating-point arrays of 512×512 pixels.

4.3.8.4 Validation

In order to assess the results obtained from the segmentation process, a method of validation was required. A method that is commonly used to validate automatic segmentation algorithms is to compare its result with that obtained manually. Although this can be time-consuming, due to the need to perform a manual segmentation, it provides a straightforward method of obtaining a measure of its accuracy. It should be noted however, that the manual segmentation may not be a ground truth measure of the object being segmented, due to the subjective nature of manual segmentation and the possibility of human error in the landmark placements.

Obtaining fully segmented diaphragm surfaces of a selection of patients using only manual methods would be extremely time-consuming and defeat the purpose of developing an automatic technique. Therefore, in order to permit the validation, a selection of points were identified manually in 5 patients in 5 of the 10 respiratory phases and these individual points were compared with the diaphragm height in the corresponding location in the automatically derived surfaces.

Approximately 70 points per diaphragm surface were located manually in positions that were evenly spread over the entire surface. The even spacing ensured that subjective placement of points did not occur, which could have influenced the results obtained, e.g. if easily identifiable locations were preferentially selected, this would result in a biased measurement. The results of this validation are described in Section 4.3.9.

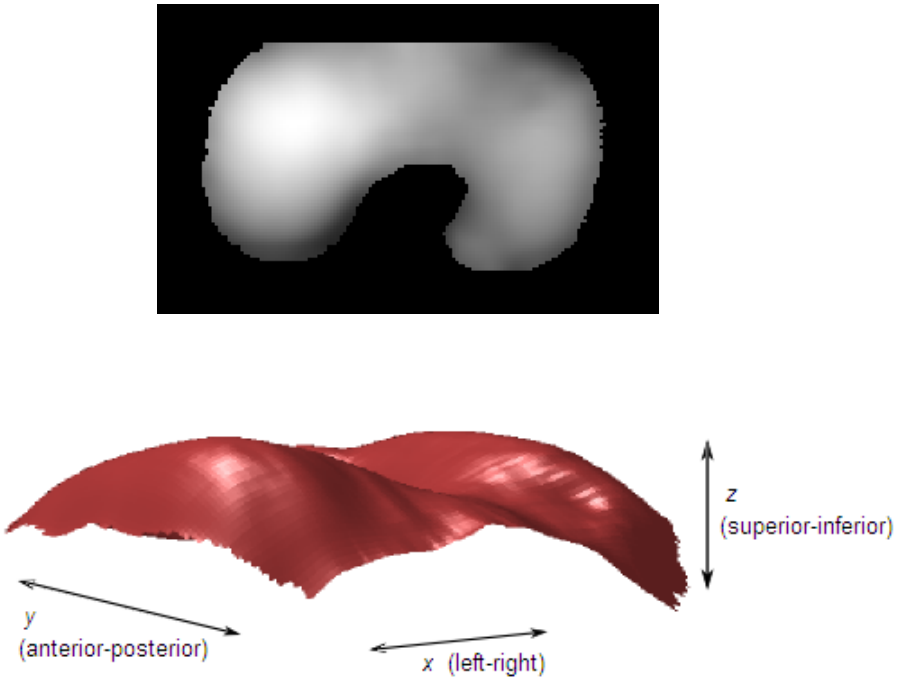

Figure 4.13: A segmented diaphragm surface at a single respiratory position, displayed in the 2D array (top) and as a 3D surface (bottom). See Appendix B.1 for an animation of the 3D surface across all respiratory frames.

4.3.9 Results

The "first boundary" method was found to be insufficient for producing a robust segmentation of the diaphragm, despite successful identification of its position in some regions. The presence of other structures within the abdomen meant that the assumption of the diaphragm being the nearest boundary to the bottom of the image often broke down. Problems with correctly identifying the diaphragm occurred in 7 of the first 10 slices tested with this method and hence substantial modifications would have been required to produce a feasible method of segmentation. For this reason, a different approach was taken and hence no further results were obtained using the "first boundary" method.

The "boundary tracking" method was found to produce much more reliable results and was therefore used to segment the diaphragm in the 100 CT volumes available (10 datasets consisting of 10 frames). An example of the final segmented surface is shown in Figure 4.13 and an animation showing the motion of this surface over the respiratory cycle is given in Appendix B.1.

Inspection of the completed diaphragm surfaces and their motion with respiration indicates that a successful segmentation has been achieved in all cases: each surface is smooth in nature and exhibits a form that would be expected of the diaphragm dome. The respiratory motion for each patient also looks realistic, with the superior–inferior motion being the dominant component, as expected, and some degree of shape change also observed. Additionally, inspection of the diaphragm outline overlaid on the original CT image in either coronal (as in Figure 4.12) or sagittal slices, gives further indication of the success of the segmentation. This shows that the general approach, involving edge-detection and boundary tracking, is appropriate for segmenting the diaphragm in CT.

The extent of manual intervention required was dependent on the level of noise apparent in the CT images and on the diaphragm–heart separation. Figure 4.14 shows sample coronal slices of two patients to illustrate the range of clarities present in the appearance of the diaphragm. Frequent adjustments of the threshold for the inclusion of boundaries in the binary map were needed to identify the diaphragm below the heart, sometimes in combination with the manual removal of edge-pixels from the binary map to overcome the increased inclusion of noise with the lower threshold. The time taken to segment the complete diaphragm surface consequently varied between approximately $30 - 50$ minutes per volume.

A quantitative measure of the accuracy of the algorithm was obtained by manually selecting points on the diaphragm surfaces and comparing these locations with those obtained from the algorithm, as described in Section 4.3.8.4. The results of this process are outlined in Table 4.1. These results show that the accuracy achieved was within 3 mm in all cases, and all but one achieved an accuracy of within 2 mm, averaged over approximately 350 points (70 per surface for 5 surfaces per patient). Figure 4.14 shows a sample coronal slice of patients 2 and 3, which are the datasets exhibiting the smallest and largest errors, respectively. It appears that the levels of noise present in the CT data had an influence on the accuracy achieved, in addition to an increase in the time required to perform the segmentation. It should be noted however that the accuracy of the manually selected points are also likely to have suffered poorer accuracy due to the noise levels, which may adversely affect the figures given in Table 4.1. The true accuracy of the segmentation may therefore be better than the validation results suggest, but is not possible to verify in the absence of a ground truth measure.

4.3.10 Discussion

The approach of constructing a segmentation algorithm based on edge-detection was found to be successful in diaphragm segmentation in CT images, which is a challenging task, due to the difficulties in distinguishing it from surrounding organs. The accuracy achieved however was good in all cases, even when the CT datasets exhibited high levels of noise. Zhou et al. (2008) recently described the use of thin-plate splines for automatic diaphragm segmentation

Patient #	Mean difference between manual and automatic estimates (mm)
1	1.3 ± 1.6
2	1.2 ± 1.5
3	2.7 ± 3.5
4	1.8 ± 2.3
5	1.4 ± 1.6

Table 4.1: Validation results for the "boundary tracking" segmentation algorithm.

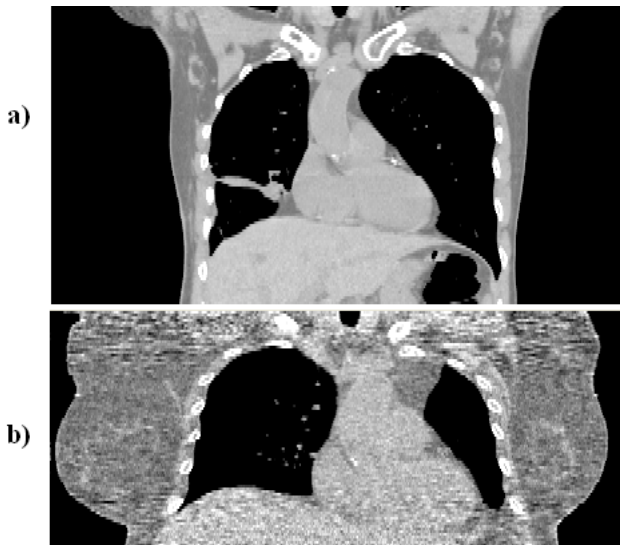

Figure 4.14: Sample coronal slices from the patient datasets exhibiting a) the smallest and b) the largest segmentation errors in comparison to the manually obtained results. These correspond with datasets 2 and 3 in Table 4.1.

in CT and used the mean distance between manual and automatic surfaces to categorise the segmentations into good and poor, using a threshold of 3 mm. According to this criterion, 21.6 % of their segmented surfaces using the thin-plate spline method were categorised as being poor. Using the same criterion for the datasets assessed here, none of the 5 segmented surfaces assessed would be classified as being poor, although the results for dataset 3 were not significantly below the threshold value. It should also be noted that only a small number of datasets were included in the analysis. These results however give further support to the conclusion that the methods developed were successful in performing the required task.

Although a fully automatic algorithm would be ideal, obtaining accurate results with the algorithm developed here was found to require supervision, with a subsequent increase in the time taken to perform. In some regions however, minimal supervision was required, for example in the posterior region, beyond the heart. An example of such a slice is given in Figure 4.4, where it can be seen that both the left and right hemi-diaphragms are clearly visible and are therefore easily segmented. This was found to be the case even in datasets suffering from large levels of noise and the slices requiring input were therefore restricted to those within the heart region. The segmentation times achieved here however, are still significantly faster than would be the case for a fully manual segmentation; Zhou et al. (2008) estimated that $1 - 2$ cases per day could be completed by manually segmenting the diaphragm in CT, compared with $30 - 50$ minutes achieved here. Their fully-automatic thin-plate spline method produced segmented surfaces in approximately 15 minutes, with no manual intervention required. The optimal choice of algorithm may depend on whether speed or a high level of accuracy is the main priority. In the research setting, longer processing times are often more acceptable but would be impractical for implementation into a routine clinical procedure. The priority here was to obtain an accurate description of diaphragm shape to facilitate subsequent analysis, which was found to be achieved with the algorithm developed. However, modifications would likely be needed prior to use in the clinical setting to improve processing times.

There are a number of possible developments to the existing algorithm that could be made to increase the level of automation. One improvement could be to consider not only coronal slices, but also sagittal slices, to ensure continuity across the whole surface. Values obtained from sagittal slices could then be used to constrain the outline obtained from coronal slices. Although this would not overcome the need for manual interventions, the additional through-plane information may result in overall speed improvements. Another possible adaption could be to identify the region of the heart and to automatically adjust the parameters (e.g. the threshold for inclusion of boundaries in the binary map) to account for the different appearance of the diaphragm in this area. This would overcome the need for the user to manually adjust the parameters based on a previous unsuccessful attempt. The use of splines, as used by Zhou et al. (2008) could also be beneficial, since they are smoothly varying functions that can be used in 3D and can therefore be used to generate realistic

diaphragm shapes without requiring post-segmentation smoothing. Methods for ensuring a good level of accuracy in all cases would however be needed with this approach.

4.3.11 Conclusions

The segmentation algorithm based on tracking features extracted from an edge-enhanced image was found to be successful in segmenting the diaphragm in gated CT images. The challenging nature of the task was illustrated by the results of an initial, unsuccessful algorithm, based on selecting the nearest boundary to the inferior edge of each coronal slice in each column of pixels. This indicated the importance of including knowledge regarding the expected relationships between neighbouring pixels in the segmented surface, which was incorporated in the boundary tracking method subsequently developed.

The accuracy of the boundary tracking segmentation was found to be within 3 mm in all cases assessed, indicating the success of the technique. Although improvements in the level of automation could be realised with further developments to the algorithm, the segmentation times achieved here were acceptable for the purpose. Since the priority in this case lay with accuracy, overall, it can be concluded that the boundary tracking method represents an appropriate method of segmentation, even in noisy CT images, provided that sufficient supervision is given.

4.4 Correlation Analysis between the Respiratory Motions of the Heart and Diaphragm

4.4.1 Introduction

One of the purposes of segmenting the diaphragm was to provide a means of comparing its motion with that of the heart over the respiratory cycle. The purpose of this comparison was to ascertain whether there is interplay between the motions, in which case knowledge of one could be used to help predict the other. Clearly, the respiratory motion of the heart needs to be determined in the motion-correction process, but as shown in the attenuation-mismatches phantom work in Chapter 3, the motion of the diaphragm also needs to be corrected, to avoid attenuation-related artefacts. Since the motions of both organs need to be determined, the existence of relationships between them could potentially be utilised in the construction of a predictive model. This would be beneficial in the case where limited motion information can be obtained and knowledge of interactions between the organs would then be used to complement this information.

The data available for determining the respiratory motions are respiratory-gated PET images, which, as already discussed in Section 4.1, suffer from high noise levels and poor

contrast in the region of the diaphragm. In such images therefore, depicting the diaphragm is very challenging and not possible in all regions. As a result, only a partial estimate that is heavily influenced by noise can be obtained directly. Incorporating knowledge of the heart–diaphragm interactions may therefore allow extra information to be obtained on the diaphragm position and assist in obtaining a more complete description of the motions of these organs.

To investigate this, regions on the already segmented diaphragm surfaces were selected and tracked over the respiratory cycle, to provide a simple characterisation of its motion. The measurements obtained were then compared with parameters describing the respiratory motion of the heart, obtained from a segmentation previously performed on the same sets of gated CT data. Correlations in the two sets of motion measurements were then evaluated, to ascertain whether relationships between the two existed and if so, which particular aspects of motion were connected.

4.4.2 Method

At the time of performing this investigation, 6 sets of diaphragm surfaces (60 surfaces in total for 6 patients) had been segmented using the boundary tracking method described in Section 4.3 and hence were available for this analysis. The heart had previously been segmented in these same datasets (Dey et al., 2005), allowing a direct comparison of the heart and diaphragm motions in these datasets.

In order to obtain measurements of diaphragm motion, 3 regions were selected for tracking that would give a representative measure of its overall motion; these regions were the two peaks of the left and right hemi-diaphragms and the trough in between the two. These positions are indicated on the diaphragm surface shown in Figure 4.15. The two peaks were identified automatically in the first frame (the end-inhale frame) by locating the highest positions in the left and right halves of the segmented surface. The trough was then located as being at the bottom of the dip between the two peaks; this was identified manually, since the global minimum could not be used, since it would select a region on the edge of the diaphragm surface. In order to minimise the effect of noise, the average heights of 100 pixels in circles centred on the points of interest were tracked.

Shape change was observed in some of the segmented surfaces, which could have an influence on the motion of the heart. Figure 4.16 shows examples of diaphragm outlines in coronal slices at end-exhale and end-inhale for two patients. In the first example, the diaphragm has exhibited a fairly uniform translation between the end-exhale and end-inhale points with little shape change. The second example however shows a nonuniform motion within this slice, with the right hemi-diaphragm (at the left hand side of the graph) moving to a much greater extent than the left hemi-diaphragm. The heart is located approximately in

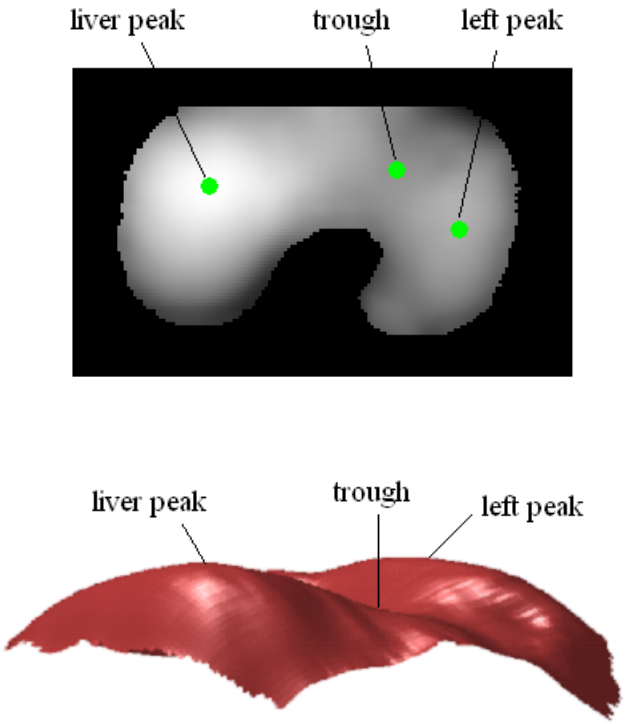

Figure 4.15: The locations of the regions tracked with respiration on the 2D array and on the 3D surface. The regions correspond with the peaks of the left and right hemi-diaphragms (labelled as the left peak and liver peak) and the trough between the peaks. The green circles on the array indicate the size of the regions over which the pixel motions are averaged.

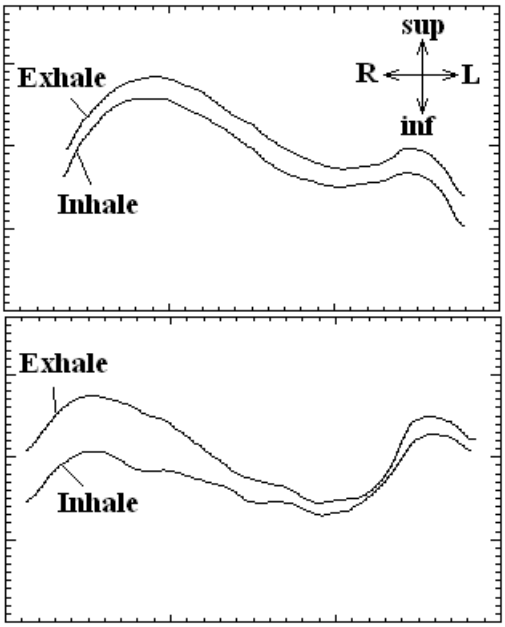

Figure 4.16: The end-inhale and end-exhale outlines in a sample coronal slice for two patients. In the top example the motion is uniform in nature, whereas shape change with respiration is seen between end-exhale and end-inhale in the bottom example.

the trough between the two peaks and a tilting effect as seen in the second example could therefore influence the motion of the heart.

In order to investigate this, a simple indication of the respiratory-induced shape change was obtained by calculating the ratios in the height changes of the 3 regions of interest. Therefore 6 motion measurements of the diaphragm were obtained in total: 3 describing the superior–inferior translations of the 3 selected regions and 3 assessing whether the relationships between the 3 regions varied over the respiratory cycle.

These 6 measurements and their variation over the respiratory cycle were compared with the respiratory motions of the heart for the same set of patients, using the same datasets. The heart had previously been segmented and the motion assessed with respiration by Dey et al. (2005). The heart segmentation was carried out by manually placing a truncated ellipse over the heart on the mid-coronal slice. The position, size and orientation of the truncated ellipse was then optimised using the intensity gradients in the image, so that the shape contour was matched as closely as possible to the borders of the heart. This re-orientated truncated ellipse was then used as an initialisation for the neighbouring slices, in which a similar procedure was performed, and this was repeated until all coronal slices containing heart tissue had been processed in this way. This initial segmentation was then modified using a region-growing technique within the volume defined, starting from a seed placed in the centre of the heart. This allowed deviations from the truncated ellipse shape to be

made, so that the volume accurately matched the heart outline and any remaining lung tissue within the volume was removed.

Once this procedure had been completed, the segmented 3D volumes at the different respiratory phases were affinely registered in order to determine the relationships between the heart position, and hence assess its respiratory motion. Although scaling factors and measurements of shear were produced during the affine registration, these were close to 1 (scale) and 0 (shear) in all cases, indicating that the contribution of these components to the description of motion was minimal. Therefore only the 3 translations and 3 rotations were used for comparison with the diaphragm motion. These 6 curves were temporally smoothed (using a 1-2-1 kernel) to reduce the effect of noise, prior to the correlation analysis being carried out.

The correlation analysis was performed on pairs of parameters, with one heart and one diaphragm parameter in each assessment. This therefore constituted 36 different parameter pairs, with the 6 diaphragm motion measurements and the 6 heart motion parameters. In each case, the correlation coefficient (r) was calculated as follows:

$$r_{pq} = \frac{\sum (p_i - \bar{p})\,(q_i - \bar{q})}{(n-1)\,s_p s_q} \tag{4.12}$$

where p_i and q_i are the data being assessed, s_p and s_q are their sample standard deviations and n is the number of data pairs. Two types of correlations were evaluated for each parameter pair; between the two motion-curves over the respiratory cycle in individual patients, and between the amplitudes of the parameters across the patients.

The analysis of pairs of motion-curves (i.e. the values of the parameters in the 10 time points over the respiratory cycle) in individual patients was performed to give an indication of the presence of phase relationships between the parameters. For a correlation to be present, the parameters need to be in phase (or completely out of phase), so if a pair of parameters was correlated in this manner for all patients, it indicated a constant phase relationship across patients. A correlation in an individual patient does not yield useful information alone, but where all patients exhibit correlations of this type, it is possible to detect a general rule relating the phase of pairs of parameters. The parameters were deemed to be in phase across the sample population where ≥ 5 of the 6 patients exhibited a correlation. This was determined by obtaining the critical value of r^2 from a look-up table for 8 degrees-of-freedom at the 95 % significance level, for a one-tailed test, and comparing this with the value of r^2_{pq} obtained from the data. The one-tailed test was chosen, since negative correlations (where the parameters are completely out of phase) were not expected, and hence only positive correlations were of interest.

Amplitude relationships were also assessed between parameter pairs, which involved calculating the maximum change in each parameter over the respiratory cycle by identifying

their maximum and minimum values. The maximum changes for all 6 patients were then compared for each pair of parameters to determine the presence of a correlation. Again, the critical value of r^2 was obtained to assess the significance of the correlations, but using 4 degrees-of-freedom.

4.4.3 Results

An example set of motion parameters for the heart and the diaphragm for one patient are shown in Figure 4.17. It can be seen that for this patient, similarities in the nature of the diaphragm and heart motion curves exist, particularly with the y- and z-translations of the heart. The extent of diaphragm motion is seen to be greater than that of the heart and differences in the 3 diaphragm curves indicates that some tilting or shape change occurred to the diaphragm. All the rotation measurements in this case were small, with the maximum rotation recorded being less than 2^o. Relationships between these rotation measurements and diaphragm translations are not immediately apparent.

The right hemi-diaphragm z-translation and the heart z-translation over the respiratory cycle are shown in Figure 4.18, as an example of a parameter pair that exhibited correlated motion curves. The values obtained in each respiratory frame are plotted for both parameters and for all patients. It can be seen that a clear relationship exists between the two parameters in every case, indicating that these parameters are in phase for all the patients within the study. Assessment of the correlation-coefficients confirmed that significant correlations were present for every patient ($p < 0.05$).

Figure 4.19 shows the amplitudes of the same two parameters across the 6 patients. Although some variability in the amplitude relationships was observed, a significant correlation was also found here, indicating that in addition to the heart and liver motions in the z-direction being in phase, they also exhibit a fixed relationship in the amplitudes, albeit with some patient variability. The equation of the least-squares line was found to have a gradient of 0.53, indicating that on average, the motion of the liver was approximately double that of the heart in the superior–inferior direction. This is in good agreement with the findings of Danias et al. (1999), who obtained a mean heart to liver ratio of 0.57 and McLeish et al. (2002), who obtained a mean value of 0.45. The range of ratios over the 6 patients obtained here was 0.27 to 0.70, again in good agreement with other ranges obtained, with Danias et al. (1999) observing a range of 0.17 to 0.93 and McLeish et al. (2002) measuring ratios of between 0.28 and 0.73. These published values were obtained by measuring the superior–inferior translations of the heart and liver in MRI datasets acquired over the respiratory cycle.

These results along with the phase and amplitude correlations for the other parameter pairs are listed in Table 4.2, where "P" indicates that the parameters changed in phase with each

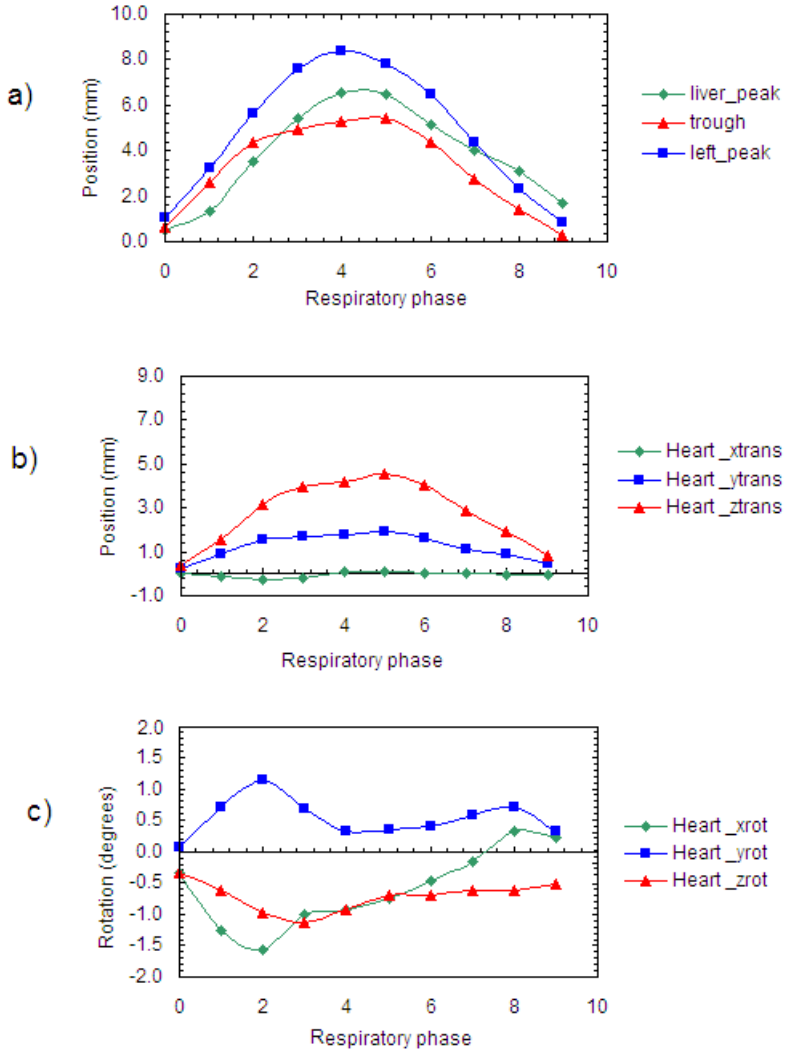

Figure 4.17: The heart and diaphragm motion tracking results for a single patient. a) The diaphragm translations in the superior–inferior (z) direction, b) the heart translations in x, y and z, and c) the heart rotations about x, y and z, where the centre-of-rotation is the centre of the segmented heart volume. Phase 0 corresponds with end-inhale. Positive changes in the translation measurements correspond with motion in the superior, anterior and left directions for x, y and z, respectively.

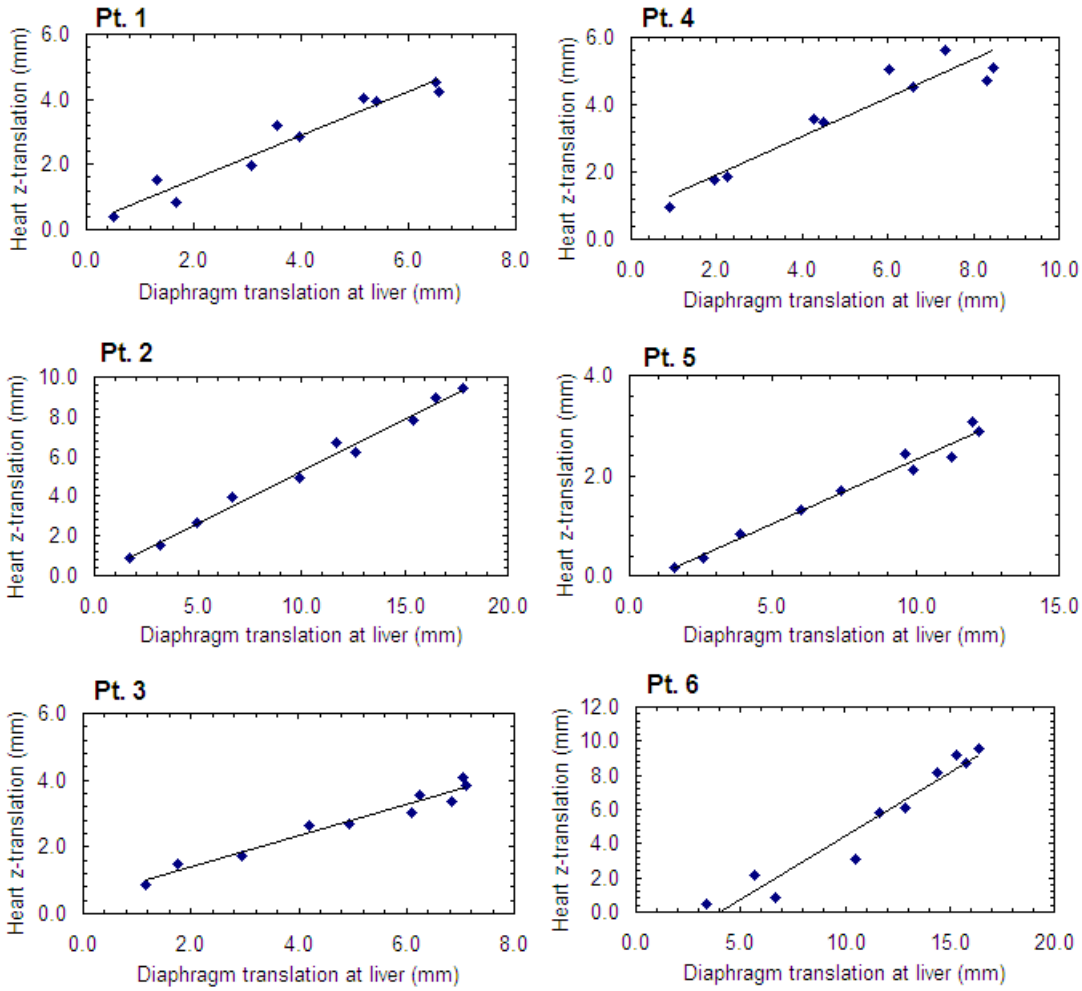

Figure 4.18: The z-translation of the heart as a function of the z-translation of the right hemi-diaphragm (at the peak of the liver) over the respiratory cycle. The black lines indicate the least-squared fit for every patient.

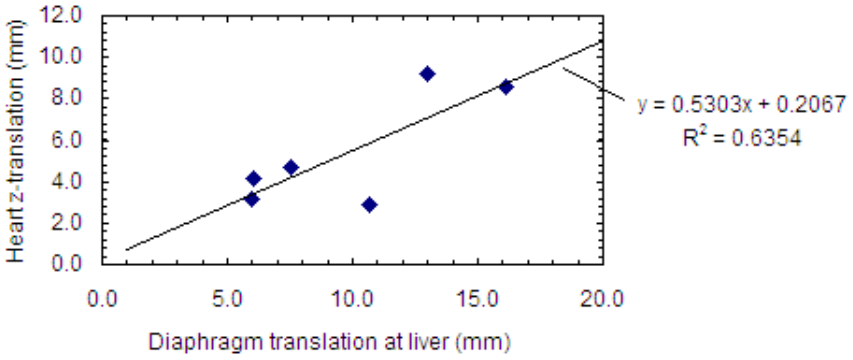

Figure 4.19: The amplitude of the z-translation of the heart as a function of the amplitude of the z-translation of the right hemi-diaphragm (at the peak of the liver). The black line indicates the least-squared fit.

other, "A" indicates that a relationship in the amplitude of the parameters existed over the patients and "–" represents the absence of a correlation.

4.4.4 Discussion

It can be seen in Table 4.2 that the relationships that were expected to be present have been identified. For example, the link between the diaphragm motion and the z-translation of the heart is well established (Wang et al., 1995; Danias et al., 1999; Nehrke et al., 2001; McLeish et al., 2002; Shechter et al., 2004), and the relationships obtained here were in good agreement with previously published results (Danias et al., 1999; McLeish et al., 2002). Although not a new finding, this showed that the known relationships in heart and diaphragm motions were being detected and hence supported the validity of the approach. Hysteresis, caused by a phase difference in the z-motions of the diaphragm and heart, has previously been observed by Nehrke et al. (2001) (as discussed in Section 2.5.1), however, the phase correlations obtained here indicate that these motions occurred in phase in these patients.

A number of less expected correlations were also seen. Considering the amplitude-based relationships, the ratio of motions in different regions of the diaphragm was found to be related to heart rotations. In particular, the right hemi-diaphragm to trough ratio and the right to left diaphragm ratio were both correlated with the z-rotation of the heart. It could be conjectured therefore that the extent to which the liver tilts (and hence the extent to which the ratio in diaphragm position in the two regions changes) influences the amount of heart rotation. Conversely, it could be argued that the tilting of the liver could be inferred from knowledge of the z-rotation of the heart; in a study where a partial identification of the

	Heart x-translation	Heart y-translation	Heart z-translation	Heart x-rotation	Heart y-rotation	Heart z-rotation
Right hemi-diaphragm (liver) peak	– A	P –	P A	– A	– A	– –
Diaphragm trough	– –	P –	P A	– A	– –	– –
Left hemi-diaphragm peak	– –	P –	P –	– –	– –	– –
Ratio: right hemi-diaphragm to trough	– –	– –	– –	– –	– –	– A
Ratio: right to left hemi-diaphragm	P –	– –	P –	P –	– –	– A
Ratio: trough to left hemi-diaphragm	– A	– –	– –	– –	– –	– –

Table 4.2: Correlation results for each parameter pair. The columns show the heart parameters, the top 3 rows are the diaphragm z-translations and the bottom 3 rows the ratios between the diaphragm translations. "P" represents the presence of a correlation in phase, observed in ≥ 5 of the 6 patients and "A" represents the presence of a correlation in amplitude, across the 6 patients. "–" indicates the absence of a correlation.

diaphragm is possible, an estimate of the diaphragm tilting obtained from measurement of the heart z-rotation could be used to aid the localisation of the remainder of the diaphragm surface. This would be challenging to implement however due to the small rotations present and the difficulty of determining the z-rotation with sufficient accuracy to make an estimate of tilting. Furthermore, patient variations around the trendline cause a reduction in the predictive value of such trends, since variations are not accounted for with this method.

The motion curves of diaphragm motion ratios were also found to be correlated with heart motions: the ratio of the left to right hemi-diaphragm motions was found to be correlated with the x- and z-translations and the x-rotation, indicating that these occurred in phase. Although a complete description of motion cannot be obtained from this knowledge alone, it does indicate that the two parameters can be expected to move in the same direction at the same time, which may be useful in tracking the diaphragm with respiration. The presence of other phase relationships (i.e. where a phase difference between the parameters is present) would not have been detected here, since this would not have produced correlated measurements. This could however be investigated by searching for correlations when a phase shift between the parameters is introduced. If present, this would give extra information regarding the diaphragm–heart relationships that has not so far been extracted.

An important observation from Table 4.2 is the large number of parameters pairs which are neither correlated in phase nor amplitude, signifying the large degree of variation between patients. This would limit the ability of a predictive model based on correlation information to describe the diaphragm shape from knowledge of the heart motions alone. One limitation of this investigation is the small number of patient datasets involved and the subsequent limited statistical power of the analysis. An increased number of patients would therefore improve this and potentially highlight the presence of weaker, but significant correlations that were not detected here. However, the usefulness of weak correlations in a predictive model is likely to be limited, due to the large degree of uncertainty in the predicted parameters that would result. Such relationships would probably not therefore significantly aid the detection of the diaphragm position and hence the most useful relationships have already been identified in this investigation.

Overall, it can be seen that the variations between patients are considerable, resulting in a complex relationship between the motions of the heart and diaphragm. While the results obtained here give a useful insight into the interactions of the heart and diaphragm, their use in a predictive model is questionable, due to the large patient variations observed.

4.4.5 Conclusions

It is well known that the motion exhibited by the diaphragm and heart varies between patients and that a complex interaction exists between the two organs. The information

obtained in this study supports this, with large variations in diaphragm shape change and heart motions observed, although relationships in aspects of the motions were also detected. In the case where limited information is available due to high levels of noise in the image (as in the case of gated PET studies), these links may be helpful in furthering the amount of information obtainable, although the limitations due to patient variation should be taken into account. Due to these limitations, a predictive model based on knowledge of correlations alone is unlikely to be sufficient for diaphragm tracking and alternative types of models may be more suitable for this task.

Chapter 5

The Construction and Testing of a Statistical Shape Model of the Diaphragm

This chapter describes the construction of a shape model of the diaphragm and how it can be applied to the problem of respiratory-matched attenuation-correction, which will form part of a motion-correction algorithm. Section 5.1 outlines the reasons for the construction of the model and Section 5.2 gives some background information relating to shape models. The construction and testing of the shape model is described in Section 5.3 and its application to gated PET studies is described in Section 5.4. Finally, a short summary of the findings obtained in both the construction and application of the model is given in Section 5.5.

5.1 Motivation

The importance of the diaphragm in the attenuation-correction of cardiac PET images has already been established, through the investigation of emission–transmission mismatches, described in Chapter 3 and has also been confirmed in the clinical setting (Gould et al., 2007). Therefore it is not only the heart position that needs to be considered, but matching the diaphragm position is also important in obtaining artefact-free cardiac images.

The aim here is to perform motion-correction on a respiratory-gated PET study. To maintain quantitative accuracy, attenuation-correction on every PET frame must be performed, prior to motion-correction (as discussed in Section 2.7.2) to avoid summing images that have been affected differently by attenuation. This means that the heart and diaphragm matching

requirements apply to every frame of the gated study, and hence a respiratory-matched attenuation-correction is needed.

One of the requirements of the motion-correction algorithm is that it is applicable to studies that do not involve a gated CT acquisition. This has advantages in terms of the reduced dose associated with a single CT acquisition and also avoids some of the ongoing issues related to CT acquisitions, namely the difficulties in obtaining artefact-free images at matched respiratory positions to the PET frames. These issues are discussed in more detail in Section 2.7.1. However, in the absence of a gated CT acquisition, alternative methods of obtaining attenuation maps over the respiratory cycle are needed, to allow the respiratory-matched attenuation-correction to be performed.

The solution to this problem proposed here is to transform the single CT to other respiratory frames, concentrating particularly on the heart and diaphragm transformations and using the set of transformed CT volumes for the respiratory-matched attenuation-correction. With this approach, the motions of structures due to respiration need to be obtained, particularly those of the heart and diaphragm, such that they can be transformed in the CT accordingly. It is clear that motion information needs to be extracted from the gated PET frames, firstly because they represent the only motion information available in the absence of a gated CT, and secondly, it is the position of the structures in the PET images that needs to be matched. Therefore if a direct measure of the location and shape of the relevant structures can be obtained from PET, this provides a means of ensuring matching in the transformed series.

Ascertaining whether or not this is possible requires inspection of the PET images, to determine what features can be extracted. The data used in this project were acquired using ^{18}F-FDG, although the aim was to develop methods that would also be applicable to ^{82}Rb studies. The implications of using ^{18}F-FDG instead of ^{82}Rb are discussed in Section 5.4.2.1, however, since ^{18}F-FDG was used here, the following discussion will relate to the appearance of the structures of interest in these images.

An example of a coronal slice through a single frame of an ^{18}F-FDG whole body study is shown in Figure 5.1. This study was acquired for oncology purposes where steps are normally taken to limit cardiac uptake, to avoid a high level of activity obscuring nearby features that may be of interest. However, the datasets selected for this work were chosen on the basis that cardiac uptake was present and it can be seen in Figure 5.1 that the heart is clearly identifiable.

It can be seen that although the heart position is clear (due to it exhibiting a higher level of uptake than other structures), the diaphragm is less clear, particularly at the peak of the right hemi-diaphragm. In the slice shown in Figure 5.1, the poorest contrast is in the region of the liver. The liver generally has a fairly low, diffuse uptake, which exhibits a large degree of attenuation due to its density and size. The lungs on the other hand exhibit very low levels of uptake, but also less attenuation. Therefore in non-attenuation-corrected

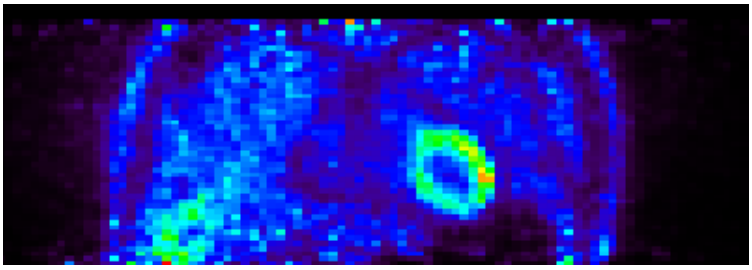

Figure 5.1: A coronal slice through a single frame of a respiratory gated PET study, acquired with ^{18}F-FDG that has not been corrected for attenuation.

images, their differences in uptake levels is counteracted to a large degree by the differences in attenuation and a poor contrast boundary results. Contrast is further reduced due to activity from other regions being wrongly attributed to the lungs in the non-attenuation-corrected image, resulting in their uptake appearing artificially high. In some studies, this effect leads to a virtually indistinguishable diaphragm–lung boundary prior to attenuation-correction. (Of course, since the purpose of the diaphragm identification is to facilitate subsequent attenuation-correction, it is not possible to use attenuation-corrected studies for this task.) In other regions, where there is very little uptake in the abdomen, the attenuation differences result in a greater abdomen–thorax contrast, where the lungs appear noticeably "hotter" than the abdomen. This can be seen below the left lung in Figure 5.1.

It can be seen therefore that although the heart position and motion may be measurable directly from gated PET images, the poor statistical quality, combined with the effects of attenuation, lead to difficult identification of the diaphragm in some regions. For this reason, additional methods for aiding this process would be beneficial in being able to accurately describe the diaphragm position over the respiratory cycle. As seen in the previous investigation of heart and diaphragm correlations (Section 4.4), although there are interactions between the heart and diaphragm motions, these are widely variable across patients. Knowledge of heart–diaphragm motion correlations would therefore not be sufficient for fully describing the diaphragm position in all respiratory frames and a method that is not adversely affected by such patient variations is therefore required.

A Statistical Shape Model (SSM) (also known as an Active Shape Model) could therefore represent an appropriate method of determining the diaphragm position and shape over the respiratory cycle, since it incorporates a set of patient datasets and takes into account the variation observed across the set. By constructing such a model therefore, additional information could be obtained regarding the typical shape and motion of the diaphragm, which could be used to improve its delineation in gated PET images. This would be particularly valuable in the regions exhibiting the poorest contrast, where an estimate of diaphragm position may not be possible otherwise. Subsequently, the obtained diaphragm

positions could be used to transform an attenuation map to facilitate a respiratory-matched attenuation-correction.

For these reasons, a SSM was constructed and was tested both in terms of its ability to describe diaphragm shape and motion and its ability to locate the diaphragm position in gated PET images. The general principles behind SSMs are described in Section 5.2 and the construction and testing of the diaphragm model are described in the subsequent sections.

5.2 Statistical Shape Models

Statistical Shape Models have been used in a number of areas of medical imaging. Their basic function is to obtain information about the shape of a given object to aid tasks such as segmentation, classification or registration (Cootes et al., 1995; Chen et al., 1999). This is done using a set of example objects (the training data), over which a set of corresponding landmarks are identified. The variation in the positions of these landmarks over the datasets is then used to characterise the types of shape variations observed across the training data. Principal Component Analysis (PCA) is the most common method with which to do this: its purpose is to extract modes of variation and thereby help simplify complex situations by greatly reducing the number of parameters with which a shape is defined, while still taking into account the majority of the variation.

The most common use of SSMs is in segmentation. The role of the model is to constrain the shape to the particular class of structure under investigation, while still allowing for the type of variations in shape that have been observed in the training data. In this manner, additional information is provided to the search for an intensity boundary, such that the segmented shape should be realistic for the particular class of structure. This can be used to automate the segmentation of a given object from an image as well as improving the accuracy of the segmentation through the additional information provided by the SSM. Although new methods are sometimes tested on 2D images in the first instance, the main application is for segmenting 3D structures from volumetric images, with the vast majority of publications relating to segmentation in CT or MRI. Examples of structures that have been segmented in this way include the left and right ventricles of the heart in MR (Frangi et al., 2002; Ordas et al., 2004; Lekadir et al., 2007) and CT (van Assen et al., 2008) images, various brain structures in MR (Kelemen et al., 1999; Shen et al., 2001; Davatzikos et al., 2003) and CT (Dalal et al., 2007), the vertebra and femur in CT (Kaus et al., 2003) and the outline of the diaphragm dome in CT (Beichel et al., 2001).

In constructing a SSM, landmarks in corresponding positions have to be obtained for every object within the training set and an important consideration is therefore the method of this landmark placement. The landmarks must be placed such that they adequately describe the object on which they are placed and are in corresponding locations in each of the datasets. If

correspondence is not achieved, these errors will be included as part of the variations due to shape differences and hence degrade the model. For simple 2D objects, landmark placement is commonly performed manually, based on a visual assessment. However, this can be a subjective and very time-consuming process, especially when many training sets are involved and when a complex object is involved, since enough landmarks must be placed in order to describe the object fully. This is further complicated where the object of interest does not exhibit easily identifiable and distinct features. In this scenario, accurate and reproducible landmark placement can be very challenging. In the 3D case, this problem is exacerbated and manually identifying a sufficient number of landmarks with suitable accuracy becomes impractical (Styner et al., 2003).

For these reasons, a number of groups have investigated methods to automate the landmark placing process and this is an area of ongoing research (Kotcheff and Taylor, 1998; Kelemen et al., 1999; Hill et al., 2000; Davies et al., 2002; Frangi et al., 2002; Kaus et al., 2003; Dalal et al., 2007; Brett and Taylor, 2008; Tobon-Gomez et al., 2008). The aims of such methods are to increase the speed of processing as well as to improve the reproducibility, by removing the subjective element present with manual placement. The basis of a large number of automatic landmark placing algorithms is to perform a non-rigid registration between pairs of training shapes, or between a training shape and a template. Once the objects are aligned, it is assumed that all points on their surfaces are corresponding and hence landmarks can then be placed. The use of automated methods is an important consideration in the case that a large number landmarks on complex 3D objects need to be placed.

Following landmark placement, a statistical method for extracting relationships between the landmark positions is required. PCA is the most commonly used technique for shape decomposition in the construction of shape models and involves analysing the data for the presence of linear relationships within the landmark positions across the datasets. This is achieved by constructing a covariance matrix from the landmark positions and obtaining the eigenvectors and eigenvalues of the covariance matrix. These stages are described in more detail in Section 5.3.2.1. Each eigenvector–eigenvalue pair are associated with a particular mode of variation of the input data, which describes the variation in shape present across the training set. These modes of variation can often be described in simple terms in respect to their effect on the appearance of the shape in question. For example, if the shape was that of a face, a given mode of variation might represent the size of the mouth and another could be related to the spacing of the eyes. This is not always the case however, and more complex variations can be contained within a single eigenvector.

The eigenvectors and eigenvalues can also be described in terms of the axes of an ellipsoid. Each object within the training set can be represented as a single point in n-dimensional space, where n is the number of measurements per object. The approximation is made that the points from all objects in the training data form an ellipsoid (Cootes et al., 1995),

which is true of data which are normally distributed (Koikkalainen and Lotjonen, 2004). The centre of the ellipsoid represents the mean shape, the eigenvectors represent the axes and the eigenvalues represent the length of these axes. It can be seen therefore that those axes with the largest eigenvalues represent the principal axes, which describe the largest proportion of the variation over the training sets. Sorting the modes of variation in order of decreasing eigenvalue therefore allows the principal components to be selected, while discarding the less important modes that account for little of the training data variation.

It is also possible in some situations to incorporate information regarding the gray-levels of the image to guide the model fitting. This is known as an Active Appearance Model (AAM), which allows the typical appearance of the structure of interest to be included in the model and thereby provide additional information to the subsequent segmentation. In order to adopt this type of approach, it is necessary for the data to which the model is to be fitted to be of the same modality as the training data. This is because the appearance "learning" is performed on the training data and the appearance is likely to differ substantially in a dataset of a different modality.

Although PCA is an established technique in the construction of SSMs, Independent Component Analysis (ICA) (Comon, 1994) is growing in popularity and has been shown to be advantageous in situations where the data cannot be approximated as being normally distributed (Koikkalainen and Lotjonen, 2004). It was originally developed for separating mixed audio signals into independent sources, where the signals can be assumed to be independent, but has more recently been used in medical applications, such as segmentation (Üzümcü et al., 2003). The priority of ICA is obtaining eigenvectors that are independent of one another, as opposed to PCA, where describing the maximum variance across the training data is its main objective (Hyvärinen et al., 2001). This results in the PCA modes having a global character, whereas the ICA modes are local. One of the main challenges of using ICA is that the eigenvectors are not ordered according to the size of the associated eigenvalues, as they are with PCA. It is therefore a much more complex problem to determine which eigenvectors should be retained and research continues into how they can be ordered (Üzümcü et al., 2003).

With both of these techniques, problems can arise due to a limited number of datasets in the training set. It is assumed that the set of shapes observed in the training set are typical of the population as a whole, but with small training set sizes this assumption may not be valid. Where the variations observed are not a good representation of the typical variations present over the population, it can lead to a limitation in the ability of the model to describe previously unseen shapes. This is particularly noticeable where the new shape contains features not previously encountered by the model in its training data.

Determining the required number of training set samples in a SSM is not straightforward, since it depends on both the complexity of the object being modelled and the accuracy of

fitting required (Rueckert et al., 2003; Ordas et al., 2004; Koikkalainen et al., 2008). In the case of low resolution images being used (such as PET), the number of training set samples needed to reach the required accuracy will be reduced. Conversely, high dimensionality data greatly increases the demands on the training set size due to the increased types of variation that such datasets could exhibit. Some authors (Davatzikos et al., 2003; Ordas et al., 2004) have conjectured that hundreds of sample sets would be ideal in complex cases. Such large numbers of training samples are often not available and in the case that landmark identification is performed manually, the time required to construct the model would become unfeasible. It is common therefore that smaller training set sizes are used, with the understanding that some features of a previously unseen dataset may not be described well, due to the limited variability experienced by the model. It is still possible however to assess the feasibility of utilising a shape model for a particular application with a limited training set, provided that its limitations are taken into consideration.

The use of statistical techniques for decomposing shape is still an active area of research, with efforts concentrating on the improvement of automatic landmark placement techniques (Styner et al., 2003), overcoming the issues associated with small training sets (Koikkalainen et al., 2008) and extending the areas of application of such models.

5.3 Diaphragm Shape Model Construction and Testing

5.3.1 Introduction

From the description of SSMs and their applications, it can be seen they are ideal for characterising the shape of anatomical structures, where a common general shape is observed, but variations exist from person to person. Such a technique therefore represents a potentially valuable method of obtaining additional knowledge of typical diaphragm shapes and motions, which could be used subsequently in its identification in gated PET images.

For these reasons, a SSM was constructed and tested to assess its suitability for this task. Different types of model construction were considered, in terms of the structures encompassed. Since it is both the heart and the diaphragm that need to be tracked over the respiratory cycle, one option considered was to construct a model that included both structures, as two objects within a single model. This would allow the relationships between the diaphragm and heart motions to be modelled, in addition to the variations in shape and motion of both structures. However, as already discussed, the greater the complexity of the model, the larger the requirements on the training set and models based on small training set sizes would likely be adversely affected by the increased complexity of including more than one structure. Since the training set available for this study is small and also because the heart can be easily identified in gated PET images without additional assistance, the model

was constructed for modelling only the diaphragm surface. This approach means that the relationships between the heart and diaphragm are not utilised and also means that separate methods of transforming the organs in the CT dataset are needed, but greatly reduces the requirements of the SSM, which is important in the absence of a substantial training set size. This is particularly relevant for this task, where the complexity of the model is already high, due to the need to model not only the shape, but also the motion over the respiratory cycle.

Statistical methods have previously been applied to the diaphragm: Beichel et al. (2005) constructed a model for segmenting the diaphragm outline, by placing landmarks in corresponding locations around the perimeter of the diaphragm dome. However, this is clearly different to obtaining a full description of the diaphragm, as is required here. The model constructed by Beichel et al. (2005) was an AAM, since it also incorporated the gray-levels of the image to guide the model fitting. This type of technique is not applicable here however, since in this case the model is to be fitted to a different type of data from that with which it was trained.

Therefore, the aim here was to construct a shape model of the diaphragm using the segmented surfaces from gated CT that could be applied to gated PET images. Very few examples of SSMs are found in the published literature, where the SSM is constructed using data of one modality for subsequent application to data of a different modality. A recent paper by Tobon-Gomez et al. (2008) however, describes the application of a CT-based SSM of the left ventricle of the heart, which was applied to SPECT images to aid measurement of the LVEF. The high contrast edges of the left ventricular myocardium compared with its surrounding materials however, make this a less challenging problem than that of diaphragm identification. The application of this model to PET is described later in this chapter; this section describes the construction of the diaphragm SSM and its initial testing using CT data, to assess its ability to describe diaphragm shapes and motions.

5.3.2 Methods

5.3.2.1 Model Construction

The SSM of the diaphragm was constructed by using the segmented surfaces already obtained from gated CT data, as described in Chapter 4. 100 volumes were segmented using the methods described, involving 10 datasets per patient, for 10 patients. Since the aim was to obtain information regarding the motion of the diaphragm in addition to its shape, it was necessary to treat each set of 10 respiratory-gated CT frames as a single dataset.

The first stage of model construction was to align the structures in the training set, such that they were in the same frame of reference, in terms of position and orientation and so that

they were normalised for size. This had to be done in a way that did not distort the shape of the structures being examined and hence only rigid transformations (plus scaling) were permitted. This was performed on the sets of diaphragm surfaces by aligning the sets of 2D arrays according to a rigid-registration. The 2D arrays contain pixel values that represent diaphragm height within its extent and 0 in the remaining pixels. Each patient dataset was therefore represented by ten 2D arrays and the registration was performed between the sets of 10. The registration involved 9 transformation parameters: 3 translations, 3 rotations and 3 scaling factors and was performed using a simplex optimisation algorithm (Nelder and Mead, 1965), implemented in IDL, with SSD as a cost-function.

Once the datasets were aligned, the next stage was to locate landmarks in each of the patient datasets, on which PCA was to be performed. In this case, the assumption was made that each set of aligned diaphragm surfaces were corresponding in their left–right (x) and anterior–posterior (y) directions and had been acquired at corresponding respiratory phases (ϕ). This greatly simplified the landmark placing methods needed, since it allowed a regular grid of landmarks to be placed on each surface, which did not require manual input.

This assumption was made based on the following observations: 1) the majority of diaphragm motion is in the superior–inferior direction, with little motion in other directions with respiration, meaning that landmarks could be tracked over the respiratory cycle by considering z only, 2) once aligned, the diaphragm outlines of each set were fairly closely matched, indicating approximate correspondence in x and y between diaphragm sets and 3) each dataset had been acquired at the same fixed respiratory phases, so correspondence in ϕ could also be assumed. Finally, the smoothly varying nature of the diaphragm with small gradients present across the surface meant that if correspondence errors were to occur, they would likely only have a small effect on the measurement of z. Therefore for this application it was deemed sufficient to consider each landmark as a measurement of height (z) as a function of x, y and ϕ. Another way of viewing this is that for a given landmark, there was no variation in the values of x, y and ϕ across patients and hence these measures could be omitted from the statistical analysis.

The landmark values were then obtained by placing a regular grid of points on the intersecting area of all datasets and all respiratory phases. For the purposes of investigating the optimal landmark spacing, this was repeated with grid-spacings of between 7 and 11 pixels (with a pixel size of 0.98 mm). This resulted in between 211 and 718 landmarks per diaphragm surface, or 2110 and 7180 landmarks in total per patient, over the 10 respiratory surfaces. The heights of pixels within a radius of half the grid-spacing from the grid point were averaged to produce a single measure of diaphragm height, which was assigned to the landmark. These averaged values were then entered into an array, $z_{i,j}$, where z is the diaphragm height corresponding with landmark i in dataset j. This is therefore an $n \times N$ array, where n is the number of landmarks and N is the number of datasets (10 in this case).

The mean position of every landmark, i, across the datasets was then calculated from the array of landmarks as follows:

$$\overline{z}_i = \frac{1}{N} \times \sum_{j=0}^{N-1} z_{i,j} \tag{5.1}$$

so that the mean shape, $\overline{\mathbf{z}}$ (of n elements) could be obtained:

$$\overline{\mathbf{z}} = [\overline{z}_0,\ \overline{z}_1,\ \ldots,\ \overline{z}_i,\ \ldots,\ \overline{z}_{n-1}] \tag{5.2}$$

The difference of every measurement from the mean was then obtained by subtraction of the mean:

$$\Delta\mathbf{z}_j = \mathbf{z}_j - \overline{\mathbf{z}} \tag{5.3}$$

where $\Delta\mathbf{z}_j$ also consists of n elements, which allows the distribution of the landmark positions around the mean to be observed for each dataset. It is the set of $\Delta\mathbf{z}_j$ for the corresponding landmarks that forms the Point Distribution Model (PDM), which is the basis on which the SSM is constructed. The SSM is essentially a statistical analysis of the relationships between the points in the PDM.

The input to PCA is the covariance matrix, $\mathbf{S}$ (an $n \times n$ matrix), which was constructed from the mean-subtracted data as follows:

$$\mathbf{S} = \frac{1}{N} \times \sum_{j=0}^{N-1} \Delta\mathbf{z}_j\, \Delta\mathbf{z}_j^{\mathrm{T}} \tag{5.4}$$

PCA was then performed with use of the "`pcomp`" function in IDL in order to obtain the vectors ($\mathbf{p}$) and scalars (λ) which observe the following relationship:

$$\mathbf{S}\mathbf{p}_k = \lambda_k \mathbf{p}_k \tag{5.5}$$

It is this process that allowed the overall training data variation to be separated into individual "modes of variation", where $\mathbf{p}_k$ is the eigenvector and λ_k is the corresponding eigenvalue associated with mode k, as introduced in Section 5.2. These modes were ordered such that $\lambda_k > \lambda_{k+1}$; since the magnitude of λ_k indicates the proportion of training data variation accounted for by mode k, this allowed the modes to be ordered according to their importance.

Prior to testing, the output of the model was assessed visually by forming new sets of diaphragm surfaces, using Equation 5.6 as follows:

$$\mathbf{z}_{\text{new}} = \overline{\mathbf{z}} + \sum_k b_k \mathbf{p}_k \tag{5.6}$$

where b_k is the weighting of eigenvector $\mathbf{p}_k$ associated with mode k. In general, Equation 5.6 is used to sum the contributions from the weighted eigenvectors over all modes of interest before adding them to the mean shape of all training data ($\overline{\mathbf{z}}$). Here however, to view the individual contribution of each mode to the change in shape, only a single mode was included in each calculation and b_k of all other modes was set to 0.

The variance of b_k over the training data is given by λ_k and therefore the range of allowed b_k was chosen to be: $-2\sqrt{\lambda_k} \leq b_k \leq 2\sqrt{\lambda_k}$, in order to restrict b_k to within 2 standard deviations of the mean. New sets of surfaces were created over the allowed range of b_k for the first 9 modes of variation, in steps of $0.25 \times \sqrt{\lambda_k}$ to allow a visualisation of the effect of each mode on the surfaces and the range of shapes possible from a single mode. Subsequent modes were not investigated since the number of nonzero eigenvalues is $N - 1$ (equal to 9 here) in situations where $N < n$, as is the case here.

In particular it was the modes that accounted for the largest training data variation that were of interest. The proportion of training data variation (V_k) associated with each mode was calculated as follows:

$$V_k = 100 \times \frac{\lambda_k}{\sum_k \lambda_k} \tag{5.7}$$

The number of modes required to describe 95 % of the total training data variation was then determined using Equation 5.8:

$$\sum_{k=1}^{m} V_k \geq 95 \tag{5.8}$$

where m is the minimum number of modes that need to be retained for this condition to be met. Therefore modes 1 to m were of interest, while all others were disregarded, due to their small value of λ_k and their resultant small impact on the diaphragm shape.

5.3.2.2 Model Testing

In order to test the performance of the constructed model, it was fitted to sets of diaphragm surfaces obtained from CT. Although fitting to CT is not its eventual intended application, it allowed the model's ability to describe diaphragm shapes to be evaluated, since the true diaphragm positions are known. This was performed using datasets within the model construction and using previously unseen datasets, with the first being a check that the model was able to describe datasets within its construction fully and the second being a

more general test of its ability to describe new surfaces. Additionally, for fitting to datasets within the model construction, model fitting was repeated using different landmark spacings, to determine the effect on the fitting accuracy achievable.

In all scenarios, model fitting was performed by minimising the differences between the positions of landmarks on the fitted surfaces produced by the model ($\mathbf{z}_{\text{new}}$) and those of the surfaces to which the model was attempting to match ($\mathbf{z}_{\text{patient}}$). This was achieved by generating fitted surfaces with the use of Equation 5.6 and obtaining values of b_k such that the SSD between the two sets of landmarks was minimised. This was achieved with the use of a simplex optimisation algorithm, which searched for the optimal values of b_k. The same restrictions on b_k were used as in Section 5.3.2.1, where the allowed range of eigenvector weighting was restricted to $\pm 2\sqrt{\lambda_k}$. This allowed variations typical of the training data to be included and prevented the new shape from containing unrealistic features. The new shape could therefore be different to any within the training set, but the restrictions on b_k ensured that it contained features that are typical of the training data.

Landmark Spacing Evaluation

Evaluating the effect of a varying grid-spacing of landmark placements involved applying this model fitting process to a patient included in the model construction for each grid spacing. This was then followed by an evaluation of the fitting accuracy achieved, where a SSD was calculated that involved all pixels in the fitted and patient surfaces, rather than just the landmark values. Having determined the optimal grid-spacing in this way, subsequent model fittings were only performed with the chosen grid-spacing. Evaluations of these model fittings were also only carried out in terms of the SSD between landmarks rather than over the entire sets of surfaces.

Model Fitting

Testing the ability of the model to describe a dataset within its construction was performed with all datasets, providing 10 measures of model fitting accuracy, corresponding with the 10 patients in the model. As it includes all available datasets, this model will subsequently be referred to as the "all-patient" model. For each patient dataset, model fitting was repeated for $1 \leq m \leq 9$, where m is the number of modes of variation retained, resulting in 90 instances of model fitting in total. This allowed the effect of each mode on the fitting accuracy achieved to be assessed by observing the change in the residual SSD (SSD_{res}) as modes are added.

To perform model fitting to datasets not included within the model construction, a "leave-one-out" approach was adopted. This involved selecting a dataset to be excluded from the model and constructing the SSM from the remaining 9 datasets. As a result, 10 separate

models were constructed, each of which omitted one dataset. These models will therefore be referred to as the leave-one-out models. This approach prevented the model being biased by the presence of the data within its construction and hence provided a better test of its ability to describe previously unseen diaphragm shapes. It also meant that multiple tests of model performance could be carried out, in the absence of extra datasets that are not included in the model. This model fitting was also performed for $1 \leq m \leq 9$, producing another 90 instances of model fitting.

Finally, the values of $\mathrm{SSD}_{\mathrm{res}}$ obtained were converted to measures of the mean error per landmark ($\overline{\triangle z}$), to enable an easier interpretation of the residual errors. $\overline{\triangle z}$ (mm) was calculated as follows:

$$\overline{\triangle z} = s \times \sqrt{\frac{\mathrm{SSD}_{\mathrm{res}}}{n}} \tag{5.9}$$

where s is the slice thickness (2.5 mm in this case) and n is the number of landmarks contributing to $\mathrm{SSD}_{\mathrm{res}}$, which is approximately 5000 in this case ($\sim$ 500 landmarks per surface over 10 respiratory frames).

5.3.3 Results

5.3.3.1 Model Output

Prior to fitting to patient data, the model output, namely the eigenvectors and eigenvalues and their effect on the shape of the diaphragm surfaces was evaluated. The percentage variation associated with each of the first 9 modes of the all-patient model and the cumulative variation are listed in Table 5.1. It can be seen from these results, that to describe 95 % of the total training data variation required 5 modes to be retained. Although this is dependent on the number of datasets within the training set and hence would change with expansion of the training set, for this model, this indicates that sufficient results should be obtained with the fitting of 5 parameters. All subsequent modes account for < 2 % of the total training data variation each and hence their impact on the overall model fitting is small.

The effect of each of these modes on the overall diaphragm shape was assessed by varying the weighting of one mode at a time (with all others set to 0), using Equation 5.6. This is illustrated in Figures 5.2 and 5.3. Figure 5.2 shows the surfaces produced by varying the weighting of the first 5 modes of variation between $\pm 2\sqrt{\lambda_k}$. Although the model fitting is performed on all respiratory phases, for clarity, only the end-inhale frame is shown. Figure 5.3 shows the difference between the end-inhale and end-exhale frames for different weightings of mode 1. For animations showing the variation of the surfaces as the weighting is varied between these two limits, see Appendix B, parts B.2.1 and B.2.2.

Mode (k)	Percentage of total training data variation associated with mode k (V_k)	Cumulative variation ($\sum_{k=1}^{m} V_k$)
1	52.8	52.8
2	26.6	79.4
3	7.8	87.2
4	4.7	91.9
5	3.2	95.1
6	1.9	97.0
7	1.1	98.1
8	1.2	99.3
9	0.7	100.0

Table 5.1: The percentage of the total training data variation associated with each mode of the "all-patient" model, constructed from 10 patient datasets.

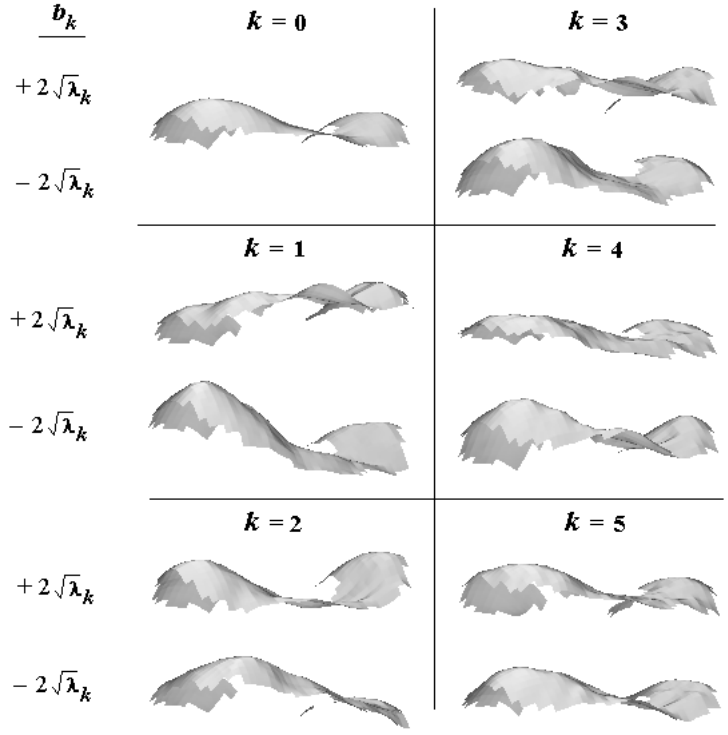

Figure 5.2: The end-inhale diaphragm shapes produced by setting the weighting of each mode of variation to $\pm 2\sqrt{\lambda_k}$, where λ_k is the eigenvalue associated with mode k. This illustrates the typical range of shapes encountered in the training data over the first 5 modes of variation. The first shape ($k = 0$) is the mean shape of the training data. See Appendix B.2.1 for an animation of the variation of these surfaces between $\pm 2\sqrt{\lambda_k}$.

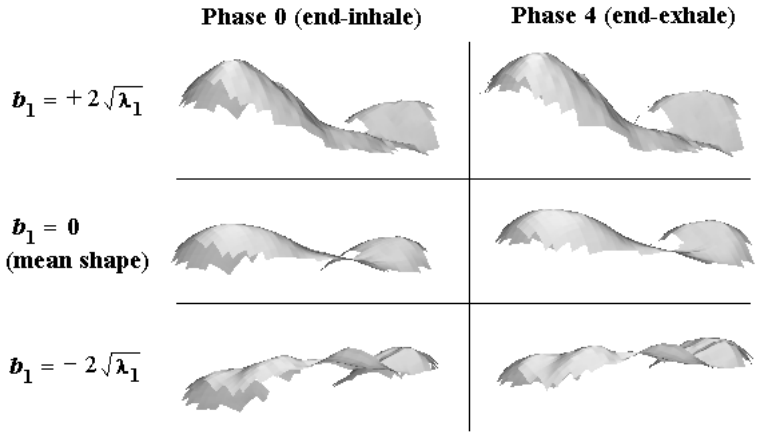

Figure 5.3: The end-inhale and end-exhale diaphragm shapes produced with b_1 set to $+2\sqrt{\lambda_1}$ (top), 0 (middle) and $-2\sqrt{\lambda_1}$ (bottom). Weightings of all other modes are set to zero (i.e. $b_{k>1} = 0$). See Appendix B.2.2 for an animation of the variation of these surfaces over the respiratory cycle.

From inspection of the diaphragm shapes produced by the model in Figures 5.2 and 5.3, it appears that the output of the model and the results of varying the mode weightings causes realistic looking deformations to the diaphragm shape. Although each mode is not clearly associated with the variation of one particular feature, general observations can be made regarding the types of variations that occur with changing mode weightings. For example, the relative heights of the left and right hemi-diaphragms and the depth of the trough in between are both influenced by the mode weightings. From a comparison of Figure 5.2 and Figure 5.3, it can be seen that the variation in shape of the diaphragm at a single respiratory state between patients is much larger than the change in shape experienced over the respiratory cycle. It was found however that in general, the posterior portion of the diaphragm moved to a greater extent than the anterior portion, resulting in some shape change. This is most noticeable by viewing the animated surfaces over the respiratory cycle, given in Appendix B.2.2.

Also evident from Figure 5.2 is the effect of the decreasing eigenvalue size with increasing mode number. This results in a smaller variation between the limits of $\pm 2\sqrt{\lambda_k}$ and only subtle variations can be observed in the 5th mode, which accounts for only 3.2 % of the total training data variation. Higher mode numbers therefore have little impact on the overall model fitting accuracy achieved.

The fact that the majority of the training data variation can be described with a small number of modes means that this type of approach is suitable for application to PET images, where the high levels of noise and poor contrast may prevent the accurate fitting of a larger number of parameters. This is, however, dependent on the number of patients in the model

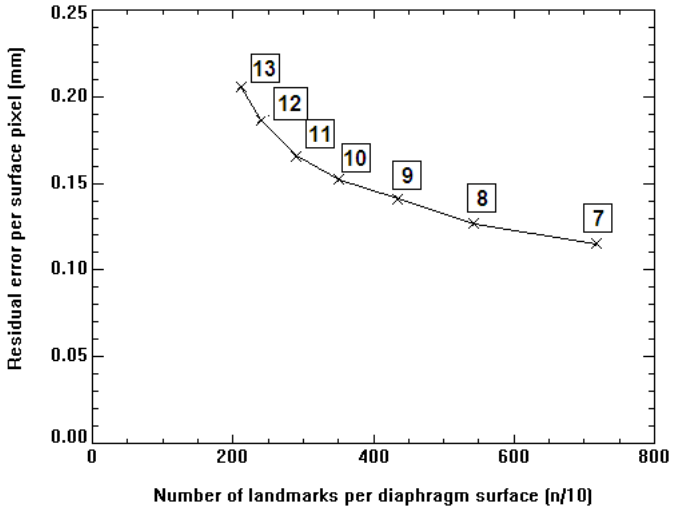

Figure 5.4: The residual error per surface pixel (mm) as a function of the number of landmarks placed per surface. The grid-spacings used are shown in boxes next to each point.

and would be likely to change if a larger training set was employed. In this case, the eigenvalues would have to be re-assessed to determine the number of modes required to reach the 95 % level.

5.3.3.2 Model Testing

Landmark Spacing Evaluation

The results of fitting the all-patient model to a patient dataset (patient 1), using different grid-spacings for landmark placement are shown in Figure 5.4. Although in all cases the residual errors per surface pixel are small, an improvement in fitting accuracy with increasing number of landmarks per surface can be seen. This is as expected, since a more detailed description of the diaphragm surfaces is included where a higher number of landmarks has been placed and hence the model is able to reproduce the surface more accurately. This improvement has to be weighed against the increase in computational time required to construct such a model. In particular, the calculation of the eigenvectors and eigenvalues from the covariance matrix, as in Equation 5.5 becomes more computationally expensive as the number of landmarks increases.

Considering these factors, a grid-spacing of 8 pixels was found to be optimal, since it allowed the model construction to be performed in approximately 1 hour, compared with 25 hours with a grid-spacing of 7 pixels, for a small increase in accuracy. It should be noted

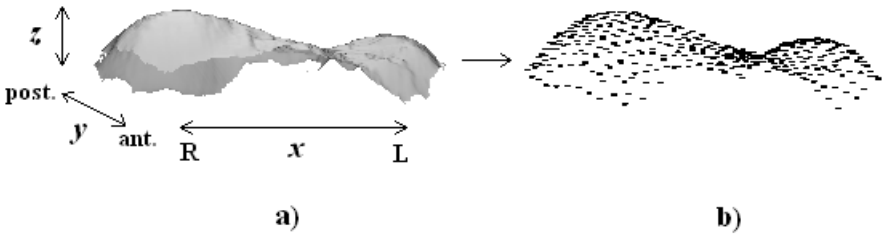

Figure 5.5: a) The segmented diaphragm surface of the end-inhale frame for a patient dataset used in the construction of the SSM and b) the locations of the grid-points with a grid-spacing of 8 pixels. The heights of pixels within a radius of 4 mm were averaged to generate the values for input into PCA.

however that different programmes can be used to perform PCA, which will differ in these computational times. Different platforms or computer specifications would also influence the processing times. A grid-spacing of 8 pixels (7.8 mm) allowed placing of approximately 500 landmarks per diaphragm surface, or 5000 per patient, considering the 10 respiratory frames. The original surface and its landmark positions are shown for a single diaphragm surface in Figure 5.5.

Model Fitting

Having ascertained that a separation of 8 mm was appropriate for landmark placement, all subsequent model testing was performed using this grid-spacing. Although retaining 5 modes of variation has been found to be appropriate for this model, fitting was performed for a varying number of modes, to assess the impact of each one on the model fitting accuracy. The results obtained from fitting the all-patient model to datasets used within its construction are shown in Figure 5.6 and from fitting the leave-one-out models to previously unseen datasets are in Figure 5.7. Additionally, the SSD values obtained were converted to the mean error per landmark, using Equation 5.9, with results shown in Figure 5.8. The values are shown for both model types for the starting difference prior to model fitting, which is the difference between the mean model surfaces and the patient surfaces ($m = 0$), the residual error when 95 % of the training data variation has been accounted for ($m = 5$) and the residual error when 100 % of the training data variation has been included ($m = 9$).

When fitting to datasets that were included in the model construction, i.e. when using the all-patient model, it was found that all datasets could be described completely when a sufficient number of modes were used. This is as expected, since the presence of the exact set of landmarks within the model means that exact matching should be possible. This does not therefore represent a test of the ability of the model to describe diaphragm shape and

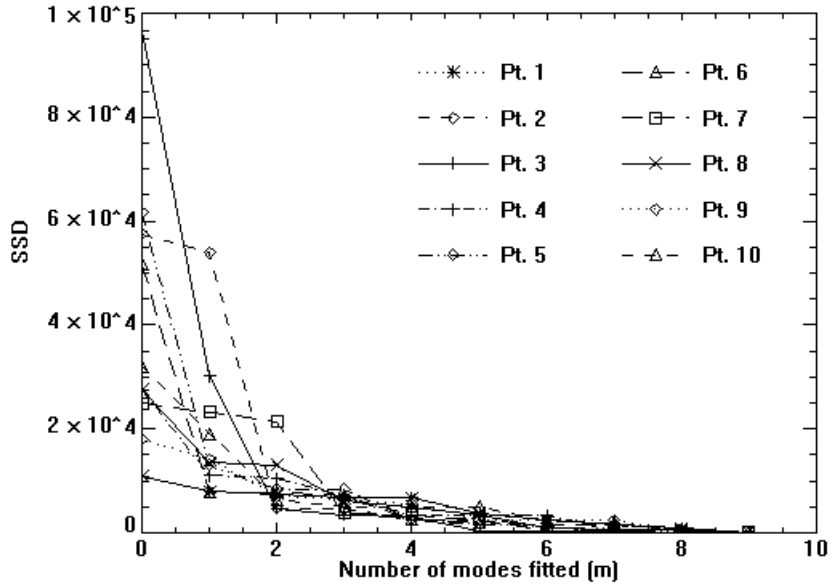

Figure 5.6: Results obtained with fitting the all-patient model to each of the datasets (Patient 1 to Patient 10) used within its construction. The SSD between the landmark positions of the fitted and patient datasets are plotted as a function of the number of modes of variation retained for each model fitting instance.

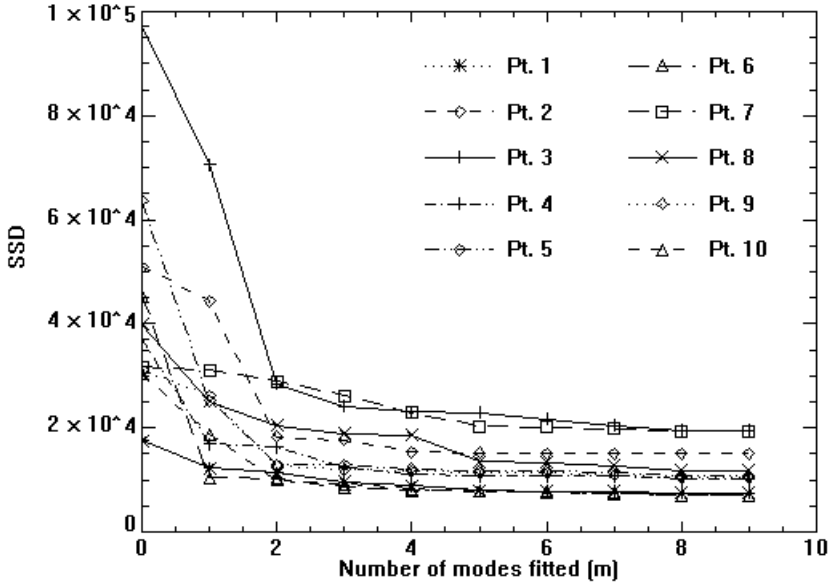

Figure 5.7: Results obtained with fitting the leave-one-out models to previously unseen datasets (Patient 1 to Patient 10). The SSD between the landmark positions of the fitted and patient datasets are plotted as a function of the number of modes of variation retained for each model fitting instance.

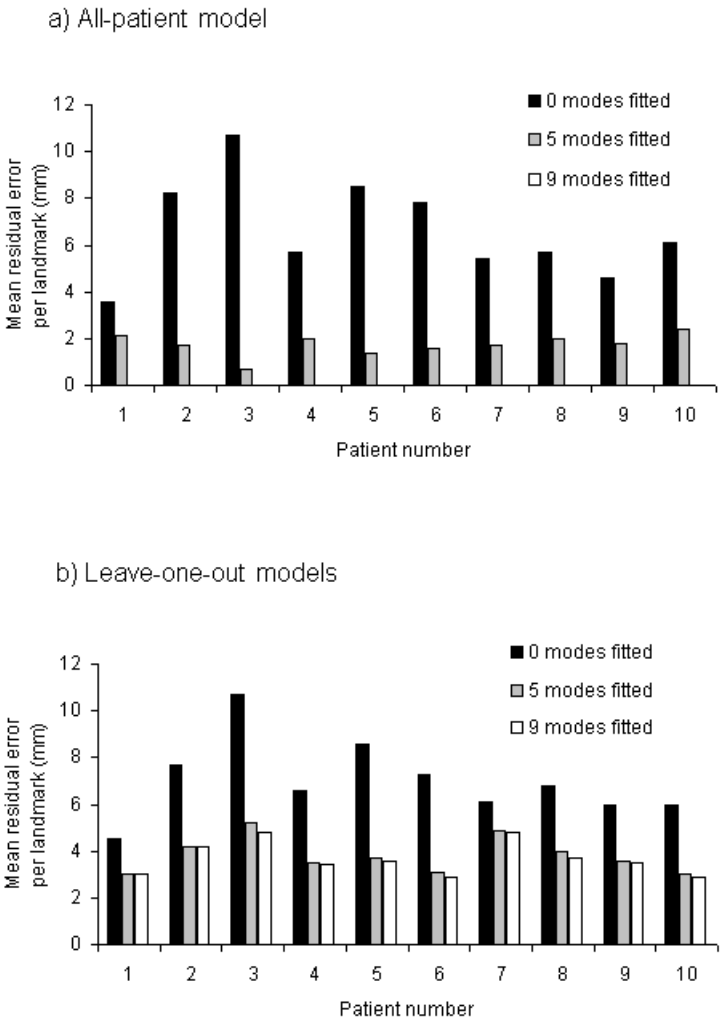

Figure 5.8: The residual error per landmark ($\overline{\triangle z}$, mm) following model fitting to each patient dataset, using a) the all-patient model and b) the leave-one-out models, with 0, 5 and 9 modes of variation retained. The fitted model shape involving 0 modes of variation is the same as the mean model shape, $\overline{\mathbf{z}}$. Note that the residual error in the all-patient model case with the fitting of 9 modes is 0.0 mm in every case.

motion, but instead provides a check that the model is working as expected and allows a measurement of the level of accuracy that can be achieved with a limited number of modes.

Where 5 modes of variation are fitted, this produced an average residual error of 1.7 ± 0.5 mm, compared with an average initial difference of 7.7 ± 2.1 mm. For this model therefore, when 5 modes are fitted, 1.7 ± 0.5 mm represents the best accuracy that could be expected. This residual error represents a very good level of accuracy, considering that the slice thickness of the CT data was 2.5 mm. Furthermore, the eventual application of the model is with PET, which had a slice thickness of 3.27 mm in this case. A residual error of 1.7 mm therefore corresponds with only 0.5 slices in PET, which would not be expected to be problematic.

In practice, other factors may be present that degrade the model fitting, such as the presence of correspondence errors or previously unencountered diaphragm features that cannot be explained well by the model. The combined effect of these two factors can be seen by inspection of the SSD curves for the leave-one-out models. With these curves, a similar trend to the all-patient model results can be seen, particularly within the first few modes, where the SSD drops rapidly. Rather than continuing this drop however, a plateau was reached, beyond which, little further improvement was seen. Even when all 9 modes were fitted, which resulted in a complete match in the all-patient model case, a residual error remained, which was found to be on average 3.7 ± 0.7 mm over the 10 patients. The effect of the plateau can be seen by considering that the residual error when fitting 5 modes was 3.8 ± 0.8 mm. This indicates a limitation in the model's ability to fully describe previously unseen datasets. Ideally, sub-voxel accuracy would be achieved, which for application to PET would require the landmark errors to be < 3.27 mm. While this was achieved with the leave-one-out models in some cases, the average error across all patients was greater than a single slice width in PET and the largest error found was 5.2 mm (for patient 3), indicating that the accuracy levels reached are not ideal in all cases. These measures relate to the model in its current form, rather than being fundamental to the overall approach and hence improvements may be realised with further development of the model.

5.3.4 Discussion

Fitting to previously unseen datasets was found to result in higher levels of residual error compared with fitting to datasets within the model construction, which could be a result of the presence of correspondence errors as well as the limited size of the training set. Ascertaining the contributions to the residual error from these sources however is not straight-forward. As previously discussed, the effects of correspondence mismatches were expected to be small for the diaphragm, although their effect on the model fitting accuracy is difficult to assess. One dataset which might be affected by landmark correspondence issues is that of patient 3, which exhibited a significantly larger initial SSD compared with other patients (see Figures 5.6 and 5.7). While some variation in the initial SSD would be

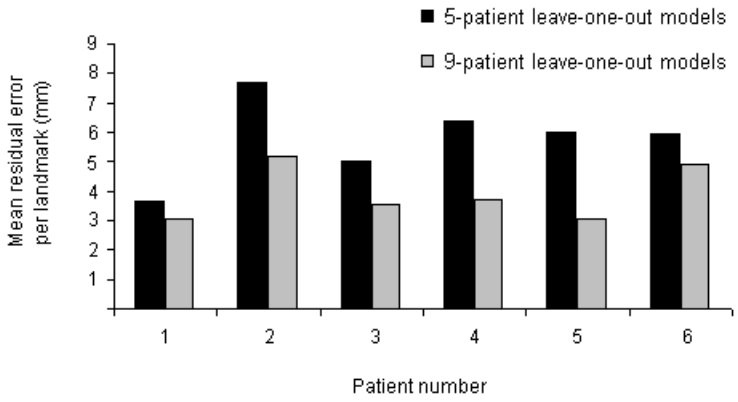

Figure 5.9: The residual error per landmark following model fitting using leave-one-out models constructed from 5 and 9 patient datasets, with 5 modes of variation retained.

expected across patients due to their varying similarities to the mean training data shape, the presence of correspondence errors could potentially add to the landmark differences, resulting in a larger than expected initial SSD. Since this is noticeably larger for patient 3 than for other patients, this could signify correspondence problems, although it should be noted that an unusual diaphragm shape with respect to the others within the training set could also produce this effect.

The other factor to consider is that of the small training set size, which is a known weakness of this model in its current form and was expected to produce a limitation in its fitting ability. This is partly due to the requirements of the model to describe not only the diaphragm shape at one respiratory position, but to fit 10 surfaces over the respiratory cycle, which increases the complexity of the situation. As with the potential effects of correspondence errors, the impact of a small training set is difficult to quantify. However, a preliminary assessment involving leave-one-out testing with a 5-patient model (fitted to a 6th patient) provided an indication of the impact of the addition of 4 patients to create the 9-patient leave-one-out models. This is illustrated in Figure 5.9, where the residual errors following the fitting of 5 modes of variation with the two models can be compared. For every patient, an improvement was seen, with an average reduction in SSD of $31 \pm 13\,\%$. Although this simple comparison does not allow a general relationship between training set size and fitting accuracy to be determined, it suggests that additional improvements in fitting accuracy would be realised with further expansion of the training set and that these improvements could be substantial. The size of the training set in this case was limited by the number of available datasets that met the criteria outlined in Section 4.3.1, but could be extended in the case that additional CT datasets were made available.

In order to address the issue of a limited training set size, alternative methods of model construction were considered. One such method was to consider each respiratory phase as a separate dataset, so that the model would contain 100 datasets rather than 10. This would require the model to be fitted 10 times, once for each respiratory frame, unlike the existing model, which fits to all 10 frames at once. The main disadvantage of such an approach is that the information regarding relationships between respiratory frames is discarded, necessitating the independent fitting of each frame. Although some shape change occurs with respiration, inspection of Figure 5.3 and the animation in Appendix B.2.2 shows that a high level of correlation in diaphragm shape is present between respiratory frames. Utilising this information is likely to be advantageous to the fitting process, which could outweigh the advantages of the increased number of samples in the training set. Furthermore, the training set in this case would not contain 100 independent samples of diaphragm shape, due to the respiratory correlations between phases and therefore the level of variation included would not be as wide as 100 diaphragm surfaces from 100 different patients. This would also most likely reduce the advantages of increasing the training set size. Lastly, there are additional considerations when fitting to PET images, which is the intended application for this model; if a single CT were available that could be incorporated into the fitting process, this could be used to benefit all respiratory frames in the format of the existing model, but not in one where each frame was treated separately.

Another approach which could overcome this last issue would be to treat each x, y landmark separately, but include all respiratory frames. This would require ~ 500 separate model fittings to be performed, to correspond with the number of landmarks per diaphragm surface, but each instance of model fitting would involve one point obtained from the single CT, which could be used to assist the model fitting to the PET data. This would however, be at the expense of knowledge regarding the relationships between landmarks over the diaphragm surface. More detail regarding the specific considerations of fitting to PET data is given in Section 5.4, but the limitations associated with this type of approach, for both the separate respiratory frames and the separate x, y landmarks methods, mean that the existing model is likely to be superior in its fitting abilities. These alternative approaches were not therefore investigated further. Additionally, the limitations associated with the existing model could be overcome with the extension of the training set, whereas the limitations of the other approaches are fundamental to their method of construction. All subsequent investigations were therefore carried out using the existing model, using the leave-one-out approach to get a measure of its current performance in the required task and using the all-patient model to assess the upper limit of performance possible with this type of model.

Overall, this approach to obtaining a description of the diaphragm over the respiratory cycle looks promising, particularly as in most cases an accuracy close to the desired level was achieved. It should be noted however that due to the small training set, the full potential of this technique has not been explored and therefore this study should be regarded as a

feasibility study, in which the suitability of a shape model for describing the diaphragm shape is assessed.

5.3.5 Conclusions

A SSM of the diaphragm, based on PCA was successfully constructed using surfaces that had been previously segmented from gated CT datasets. The model was constructed so that by optimising a single set of parameters, the diaphragm shape in 10 positions over the respiratory cycle were obtained simultaneously, which was found to require the fitting of only 5 parameters. The results outlined here were obtained using models constructed with a small number of patients in the training set and hence limitations in their ability to describe the diaphragm shape and motion were expected, due to the limited "experience" of the SSM. Therefore, the measures of the model performance obtained here served as a preliminary investigation into the suitability of such a technique, and improvements in performance would be expected with the expansion of the training set. Despite these known limitations, a suitable level of fitting accuracy (where the mean landmark error was within a single slice width in PET) was achieved in some patients, and the proportion of patients in which this is achieved would be expected to increase with an extension to the training set. Overall, this approach for diaphragm tracking looks promising, since it allows both the shape and respiratory motion of the diaphragm to be described, by utilising knowledge of relationships between landmark positions. Furthermore, this type of model provides flexibility, since it takes into account the variations observed in the training set; with sufficient training it should therefore be applicable to a wide range of diaphragm shapes and motions.

5.4 The Application of the Diaphragm Shape Model to Gated PET Data

5.4.1 Introduction

Having assessed the performance of a diaphragm SSM on segmented diaphragm surfaces in CT, the next issue to address was how this performance was affected when applying the model to gated PET images, which is its intended application. As seen in Figure 5.1, the contrast in the region of the diaphragm can be extremely poor and gated PET images can suffer from high noise levels as a result of the gating process. These factors mean that only a partial estimate of diaphragm position is obtainable directly from the images and inaccuracies could result because of the image noise. Improving this estimate and filling any gaps present is the motivation behind the construction of the shape model, but could

also provide difficulties in the fitting of the model, if insufficient information is present with which to "drive" the fitting process.

To assess this, the model was tested on two sets of respiratory gated PET-CT datasets, where both the PET and the CT components were respiratory-gated. Although in practice a gated CT would not be acquired, this provided a means of validation, based on the assumption that the true diaphragm position could be obtained from the CT frames. Measures of model performance were then compared under different scenarios to determine whether an adequate level of information is available in the PET images for fitting a diaphragm shape model reliably and what level of accuracy could be achieved in the resulting diaphragm description.

The layout of this part of the chapter is as follows: Sections 5.4.2 and 5.4.3 describe the methods employed for selecting appropriate data with which to test the model and the methods of including these additional data in the model construction. Since the outcomes of these investigations were required prior to proceeding with the model testing, the results are also outlined within these sections. The model testing itself, including the method of obtaining the input data are described in Section 5.4.4, with the results and discussion relating to this given in Sections 5.4.5 and 5.4.6, respectively. Finally, the conclusions, which also relate to the model fitting findings, are given in Section 5.4.7.

5.4.2 Selection of PET-CT Data

5.4.2.1 Tracer Comparison

Cardiac PET-CT datasets with gating of both components were required for this study, to enable a comparison of the fitted surfaces obtained from the model with the diaphragm position in the CT images, for validation purposes. Such datasets are not routinely acquired, particularly for cardiac studies, where the increased dose associated with a gated CT cannot easily be justified. Therefore, the majority of gated PET-CT acquisitions are obtained for oncology purposes, with ^{18}F-FDG as a tracer. Due to the importance of having a means of validation, the applicability of the model fitting technique to gated ^{18}F-FDG PET-CT studies was assessed, due to their wider availability compared with the ^{82}Rb equivalent. If the uptake patterns in the two types of study in the regions of interest were found to be sufficiently similar, then techniques that are applicable to one could also be used for the other. Therefore, a technique intended for ^{82}Rb studies involving a single CT could potentially be tested and validated using ^{18}F-FDG studies with a gated CT.

For this reason, a comparison of the appearance of ^{18}F-FDG and ^{82}Rb studies was performed, with particular attention paid to the diaphragm and the level of contrast in this region. Respiratory gated ^{82}Rb studies were not available for a direct comparison of the diaphragm

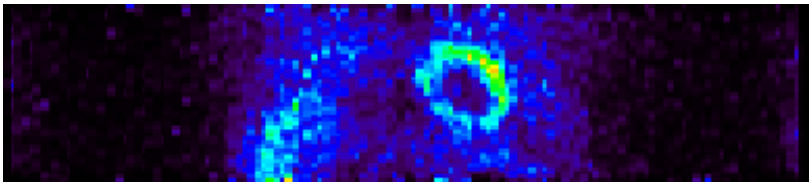

Figure 5.10: A coronal slice through a single frame of a respiratory gated PET study, acquired with ^{82}Rb that has not been corrected for attenuation.

appearance in motion-limited frames, however an ECG gated frame of a ^{82}Rb study was assessed, so that images with similar count statistics were compared. An example coronal slice through a frame of a study acquired with ^{82}Rb is shown in Figure 5.10.

Comparing the ^{82}Rb image (Figure 5.10) with a slice in a comparable position in a ^{18}F-FDG study (Figure 5.1), it can be seen that overall, the features of the images are very similar. The dominant feature in both is the myocardium of the left ventricle, with an apparent uptake in the lungs and abdominal tissues. The appearance of the diaphragm is the most important consideration for this study, since it determines whether techniques for identifying its shape and position can be developed using ^{18}F-FDG images and still be applicable to ^{82}Rb studies. Similar features are present in both images in the region of the diaphragm: there is particularly poor contrast at the peak of the right hemi-diaphragm (above the liver), which improves to some extent towards the trough between the two hemi-diaphragm peaks. A poorer contrast is seen below the left hemi-diaphragm in the ^{82}Rb image compared with the same region in the ^{18}F-FDG study, which indicates that the abdominal tissues in this region exhibited a higher tracer uptake, resulting in a lower level of contrast. However, some contrast is still present in this area. A higher level of noise is also apparent in the ^{82}Rb image; this is dependent on the injected activity, the acquisition time and the number of frames into which the data is divided and hence is not a fundamental difference between the two tracers.

These features indicate that the need for additional information to obtain complete diaphragm surfaces are relevant for ^{82}Rb and in fact the requirements for a model to assist in this task are possibly even greater. Due to the overall similarities of the uptake patterns however, the ^{18}F-FDG images were considered to be a suitable substitute for ^{82}Rb, since the same overall methods would be applicable to both. For this reason, and taking into account their wider availability, methods for applying a SSM to PET images were developed using respiratory-gated ^{18}F-FDG PET-CT datasets, and hence the rest of this chapter relates to the findings obtained using such studies.

5.4.2.2 Assessment of Respiratory Gated ^{18}F-FDG PET-CT Datasets for Inclusion in the Study

Twelve sets of respiratory-gated ^{18}F-FDG PET-CT studies were available for this study, which were acquired at Hospital San Rafaele, Milan, Italy. Like the gated CT data from which the SSM was constructed, these data were also gated with a phase-based method, such that the respiratory frames were equally spaced in terms of respiratory phase. This applied to both the PET and the CT components, such that frames were obtained at matching respiratory positions, on the assumption that changes in respiratory pattern did not occur between the two studies. The CT data were reconstructed with 512×512 pixels per transaxial slice, of size of 0.98×0.98 mm and with a slice thickness of 2.5 mm, which matched the previously used CT data. The PET frames consisted of 128×128 pixels per slice, where the pixel size was 5.47×5.47 mm and the slice thickness was 3.27 mm. The PET images were reconstructed using OSEM with 2 iterations and 28 subsets. The acquisition time for these studies was 12 minutes in total (giving approximately 2 minutes per respiratory frame); this extended acquisition time was due to the original application of these datasets being the assessment of tumour motion, preventing the summing of frames to improve count-statistics. Therefore typical cardiac studies could exhibit higher noise levels than the datasets used here.

Due to these studies being acquired for oncology purposes, rather than cardiac studies, uptake in the heart was frequently not present, making these datasets unsuitable for this investigation. For this reason, 8 of the 12 studies were eliminated and the remaining 4 were assessed in a similar manner to that performed for the CT datasets prior to segmentation (see Section 4.3.1). This was undertaken to ensure that the datasets involved in the investigation had normal respiratory patterns, had adequate coverage of the heart and diaphragm and were generally free of motion artefacts. On the basis of significant motion artefacts, two of the four datasets were excluded from the investigation and the remaining two were retained. An example of the motion artefacts exhibited by one of the excluded CT datasets is shown in Figure 5.11, which clearly demonstrates the types of problem that can occur with CT gating and the reasons for its exclusion from this study. In some regions, the diaphragm has been imaged more than once as a result of its motion during the acquisition and hence the gated CT in this case would not be suitable for use as a gold standard measurement of diaphragm position.

Additionally, the matching between the PET and CT frames was also assessed. Good PET-CT matching was required so that the CT provided a suitable means of validating the results, since PET – CT mismatches would result in an unfavourable assessment of the model fitting accuracy. The cardiac activity was used to check alignment, since it is easily visualised and is sensitive to the respiratory position. The two remaining studies exhibited a normal diaphragm appearance in all CT frames and exhibited a good level of matching between each frame of the PET and CT. Although ideally the process would be tested on a larger number

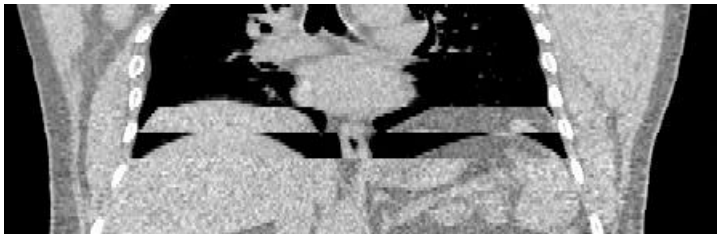

Figure 5.11: A coronal slice through a frame of a respiratory gated CT dataset exhibiting severe motion artefacts.

of patients, eliminating unsuitable studies was important to ensure that a fair measurement of model performance was obtained. The two remaining datasets therefore allowed two instances of model fitting success to be obtained and provided a means of demonstrating the overall approach.

Using the methods described in Chapter 4, the diaphragm surfaces were segmented in all frames of the CT studies for both patient datasets, which served as the ground-truth measure of diaphragm position. On the assumption that the PET and CT frames represented matching respiratory positions and hence matching anatomical positions, these segmented surfaces were used as a ground-truth measure of diaphragm position in not only the CT frames but also in the PET frames.

5.4.3 Downsampling Methods

Due to differences in acquisition protocols, a different number of respiratory frames were available for the PET-CT datasets compared with the CT datasets previously used to construct the SSM. Although the lower number of frames results in a larger degree of blurring in each frame of the PET data, the appearance of the CT frames should be unaffected, due to the different acquisition method. Additionally, the increased blurring in the PET frames is accompanied by an increase in the count statistics, which may provide some advantages.

Methods were required to account for the different number of respiratory frames acquired, so that the 10-phase diaphragm SSM would be applicable to the 6-frame data available for this aspect of model testing. Two methods were proposed for matching the number of frames in the existing training data and the additional CT datasets: the first method involved downsampling the segmented CT surfaces, prior to model construction and the second used the existing 10-frame model and performed the downsampling on the fitted surfaces.

Since the first method involved performing the interpolation before model construction, the model itself then comprised of 6 frames, rather than the original 10 described above. This model will therefore be referred to as the 6-frame model. A simple linear interpolation was used between the diaphragm heights in successive frames, such that a set of 6 frames were

	Patient B1: SSD	Patient B2: SSD
6-frame model (5 modes fitted)	8589	6111
10-frame model (5 modes fitted)	15721	15235

Table 5.2: The residual SSD when the 10-frame and 6-frame models were fitted to patients B1 and B2. In both cases, the model was constructed from 10 datasets and fitted to the CT component of the 6-frame PET-CT datasets.

produced at phases of 0, $\frac{\pi}{3}$, $\frac{2\pi}{3}$, π, $\frac{4\pi}{3}$ and $\frac{5\pi}{3}$, where 0 corresponds with end-inhale. The new model was then constructed from these altered diaphragm surfaces as described previously. The second method of downsampling involved fitting the original 10-frame model to the 6-frame data, with the linear interpolation being performed on the fitted surfaces during the optimisation. Therefore the SSD calculation as part of the optimisation was performed on the downsampled fitted surfaces, but the parameters were obtained using the 10-frame data.

Both of these methods were tested on the two sets of 6-frame data, which will be referred to as patient datasets B1 and B2, to ascertain which was optimal. The assessment was performed by comparing the fitted results against the segmented surfaces obtained from CT, the results of which are shown in Table 5.2.

In these two cases, the 6-frame model was found to produce smaller errors than the 10-frame model with subsequent downsampling. This 6-frame model was therefore used in all further model testing. In addition to the improved accuracy, the 6-frame model had advantages in terms of being able to use both the 10-frame and 6-frame data in a combined model and was also less computationally expensive, due to the downsampling being performed prior to model construction. Each patient dataset had approximately 3000 landmarks over all diaphragm surfaces following downsampling, compared with 5000 in the original 10-frame model.

5.4.4 Model Testing Using PET-CT Datasets

Following the addition of the two PET-CT datasets, the full set of data available for inclusion in the diaphragm SSM was 10 sets of 10-frame CT data and 2 sets of 6-frame CT data, for which corresponding PET frames had also been acquired. As with the previous model constructions, an "all-patient" model was built, that consisted of all 12 patient datasets and "leave-one-out" models were built with a single patient dataset omitted in each case (and hence consisted of 11 patients). These were constructed only using the CT portions of the studies that also included a PET acquisition. The datasets included in the construction of each are summarised in the first two columns of Table 5.3.

5.4.4.1 Obtaining Landmark Estimates from PET

The method chosen for extracting information from the PET images for input into the model fitting was to identify points on the diaphragm and align them with the nearest landmark point in the model. Although an automatic implementation of this process would be important if it were to be in routine clinical use, for the purposes of testing the overall technique, a manual identification was performed, using coronal slices through all respiratory frames of the gated PET studies. The user scrolled through the coronal slices and clicked on the diaphragm position where visible, in an interactive display, such that the x, y, z and ϕ (respiratory phase) of each click position was recorded.

The patient was then aligned to the model and a nearest-neighbour interpolation was performed to move each estimated point in x and y such that it was aligned with the nearest landmark position. The accuracy of these manually placed landmarks was then evaluated by comparison with those obtained from CT, allowing the mean and standard deviation of the differences to be calculated. Landmark placement was then repeated a further two times by the first user and performed three times by a second user, enabling variations in mean landmark error to be assessed. Model fitting was performed for each of the 6 landmark sets, to assess the effect of landmark placement variations.

5.4.4.2 Model Fitting

The model was fitted to the two PET-CT datasets (patients B1 and B2 in Table 5.3) and the accuracy with which the fitted surfaces described the true surfaces was determined. The accuracy was measured using the same method as in Section 5.3.2.2: the SSD between the landmarks of the fitted surfaces and the CT-based landmarks was calculated, from which a mean error per landmark was calculated according to Equation 5.9.

Model fitting was repeated for both patients and both model types (the all-patient model and the leave-one-out models), for different sets of landmarks. Initially, the model was fitted to the CT-based landmarks obtained from the fully segmented diaphragm surfaces, in order to provide a baseline level against which other fitting results could be compared. Two scenarios involving the PET landmarks were also tested: fitting to the PET landmarks alone, and fitting to the PET landmarks with a single frame replaced by CT (which will be referred to as the PETCT landmarks). This latter case represents the scenario where a static CT is acquired in addition to the gated PET and incorporated into the model fitting process to provide additional anatomical information. In this study, a frame from the gated CT study was used to represent a single CT acquisition and respiratory correspondence with the equivalent PET frame was assumed. The CT-derived landmarks were therefore used to directly substitute those obtained from PET for that frame. The impact of this assumption is addressed in Section 5.4.4.3.

Model Name	CT datasets used within model construction	Patient datasets fitted to	Landmark sets fitted to
All-patient model	A1-A10, B1, B2	B1, B2	CT, PET, PETCT
Leave-one-out model 1	A1-A10, B2	B1	CT, PET, PETCT, CT_{PET}, CT_{PETCT}
Leave-one-out model 2	A1-A10, B1	B2	CT, PET, PETCT, CT_{PET}, CT_{PETCT}

Table 5.3: Names assigned to each of the models, the data used within their construction and a summary of the model fittings performed. Datasets A1 – A10 refer to the ten sets of 10-frame CT data. Datasets B1 and B2 refer to the two 6-frame CT datasets for which PET data was also acquired. Each fitting combination listed was repeated for 1 to 10 modes of variation. A description of each landmark set is given in Table 5.4.

The PET and PETCT landmark sets contained only a fraction of the total number of landmarks in the model (see Section 5.3.3.2). Therefore, when fitting to these landmark sets, the optimisation was performed on only the subset of landmarks existing in these sets, but a complete set of diaphragm surfaces were produced. In this way, gaps in the input landmarks were filled.

Finally, for the leave-one-out models, fitting was also performed on the subsets of CT landmarks that corresponded with the points used in the PET and PETCT sets (referred to as CT_{PET} and CT_{PETCT}). This meant that any deterioration in the model fitting accuracy observed with the PET or PETCT landmarks could be separated into the effects of having only a limited number of points and those of landmark-placing inaccuracies in PET. This was not repeated using the all-patient model, since the presence of the CT in the model allows a good fit to be achieved when the CT-based landmarks were used, even when only a subset of points was employed. Therefore, the models that did not include the patient data to which the model was being fitted were used to assess the contributions towards the loss in model fitting accuracy. The landmark sets are summarised in Table 5.4 and the model fittings that were performed using these landmark sets are listed in Table 5.3.

5.4.4.3 Respiratory Phase Correspondence Testing

Throughout this study it was assumed that the PET and CT frames were at corresponding respiratory positions. There are two areas in which this assumption affects this study: firstly, the measures of fitting accuracy are obtained by comparison of the fitted surfaces with those obtained from CT segmentation, where mismatches in respiratory phase and the resulting anatomical mismatches would produce an artificial increase in the mean landmark error. The performance of the model in the presence of mismatches would therefore be underestimated. Secondly, the PETCT landmark set involves direct substitution of CT-based landmarks into

Name of Landmark Set	Description of Landmark Set	Number of Landmarks
CT	Obtained from CT-based diaphragm segmentations (all phases)	$\sim$ 500 per surface ($\sim$ 3000 in total)
PET	Obtained manually from PET images (all phases)	$\sim$ 50 per surface ($\sim$ 300 in total)
PETCT	Frame 1: Identical to frame 1 of the "CT" landmark set. Frames 2 to 6: Identical to frames 2 to 6 of the "PET" landmark set	Frame 1: $\sim$ 500, Frames 2 to 6: $\sim$ 50 per surface ($\sim$ 750 in total)
CT_{PET}	A subset of the CT landmarks: in the same positions as the "PET" landmarks, but containing values obtained from CT	As for "PET"
CT_{PETCT}	A subset of the CT landmarks: in the same positions as the "PETCT" landmarks, but containing values obtained from CT	As for "PETCT"

Table 5.4: Descriptions of the landmark sets used in model fitting. Frame 1 in this case corresponded with the end-inhale frame - the reasons for the selection of this frame are outlined in Section 6.4.3.

the PET frame at a corresponding phase: mismatches in this frame could therefore affect the model fitting accuracy and limit the efficacy of the technique. Both of these effects were investigated, firstly to exclude the possibility of significant anatomical mismatches in the datasets used in this study and to determine the effect of a mismatch on the PETCT fitting accuracy.

Significant phase mismatches were not expected, since inclusion in this study was dependent on the good alignment of PET and CT from a visual inspection of the cardiac activity, in addition to the CT frames being free of residual motion artefacts. Good PET–CT matching at the position of the heart and the absence of motion artefacts suggest that breathing was fairly reproducible over the course of imaging for these patients and gating was therefore successful.

Having verified the absence of major PET-CT discrepancies, the effect of a mismatch in the PETCT landmark set was then investigated by incorporating a mismatched CT frame into the PETCT landmark set. Throughout the study, the landmark substitution was performed in the end-inhale frame, initially using the end-inhale (and therefore matched) CT frame. For this investigation however, landmarks from other CT frames were used to substitute the end-inhale PET landmarks, while all other frames remained unchanged. This was repeated with each CT frame used as the substitution, for patients B1 and B2. Model fitting using the all-patient model was performed and results were assessed by calculating the SSD between the fitted surfaces and the CT-based segmentations. The results were used to determine how

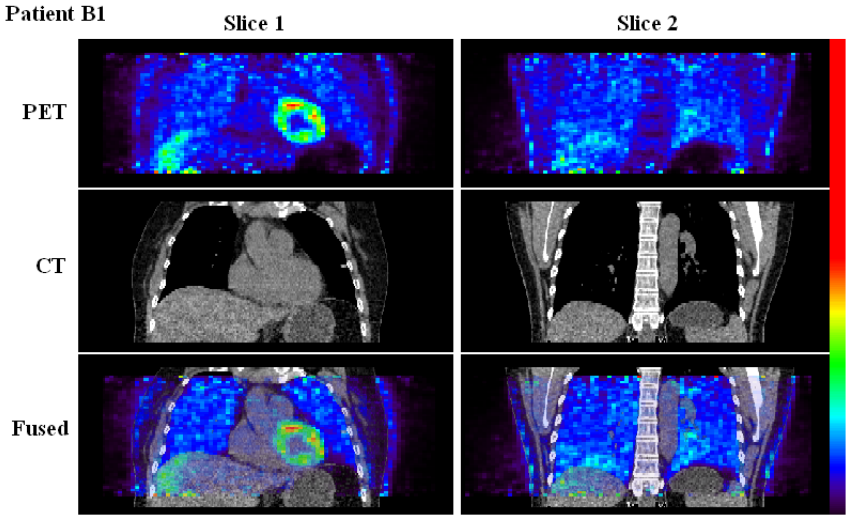

Figure 5.12: Coronal slices through a single frame of patient B1's PET-CT dataset, showing the PET, CT and fused PET-CT images for a slice traversing the heart (Slice 1) and a more posterior slice (Slice 2).

sensitive the technique is to respiratory mismatches and to assess the impact a mismatch may have on the overall success of model fitting.

5.4.5 Results

5.4.5.1 Obtaining Landmark Estimates from PET

Estimates of diaphragm position were made from the two attenuated ^{18}F-FDG PET datasets (for patients B1 and B2) as previously described. Coronal slices through the PET-CT of both patients are shown in Figures 5.12 and 5.13, which exhibit similar traits. The features indicating the position of the diaphragm were not consistent over the surfaces, with the presence of both positive and negative gradients between the thorax and abdomen occurring in different regions. This confounds the problem of diaphragm detection in already noisy images, confirming that a shape model could prove valuable in this task. The total number of counts acquired in the PET studies were 215×10^6 and 176×10^6 for patients B1 and B2 respectively, corresponding with injected activities of 9 mCi and 12 mCi. Since phase-based gating was employed, approximately equal counts were assigned to each gated frame.

In both datasets, approximately 50 estimates of diaphragm position were obtained per diaphragm surface, in positions where it was delineated most clearly. These points comprised approximately 10 % of the total number of landmarks in the model. Errors resulting from this process were calculated by comparing the estimated diaphragm positions with those

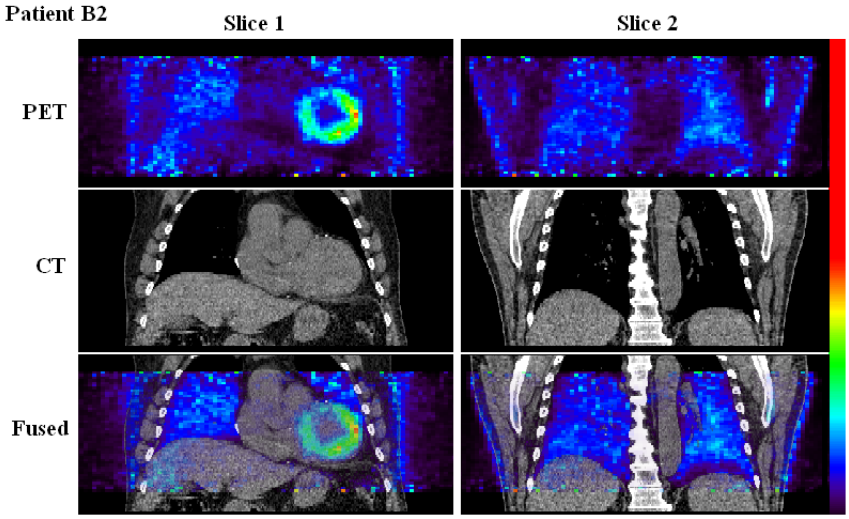

Figure 5.13: Coronal slices through a single frame of patient B2's PET-CT dataset, showing the PET, CT and fused PET-CT images for a slice traversing the heart (Slice 1) and a more posterior slice (Slice 2).

obtained from CT, from which the distribution in landmark errors could be assessed. The landmark errors for patient B1 were found to have a mean of 4.9±3.4 mm, with the equivalent values for patient B2 being 8.9 ± 7.4 mm. These are equivalent to 1.6 ± 0.9 and 2.7 ± 2.0 slices in PET.

In order to assess the intra- and inter-user variabilities, landmark placement was repeated such that 6 sets of landmarks existed for each patient (3 sets from each user). For patient B1, users 1 and 2 produced mean landmark errors of 4.8 ± 0.3 mm and 5.7 ± 0.4 mm respectively, whereas for patient B2, these values were 8.9 ± 0.6 mm and 8.7 ± 0.7 mm. The variations quoted here are the standard deviations of the 3 attempts by each user. The effect of model fitting with each of these landmark sets is summarised in Section 5.4.5.2.

From inspection of these landmarks in conjunction with the segmented surface, it was found that while the majority of points were correctly located close to or on the diaphragm, a few were misplaced, due to the difficulty in determining the correct position in the presence of low contrast and these contributed significantly to the overall errors obtained. Sample coronal slices from both patients demonstrating the landmarks identified in these slices are shown in Fig. 5.14.

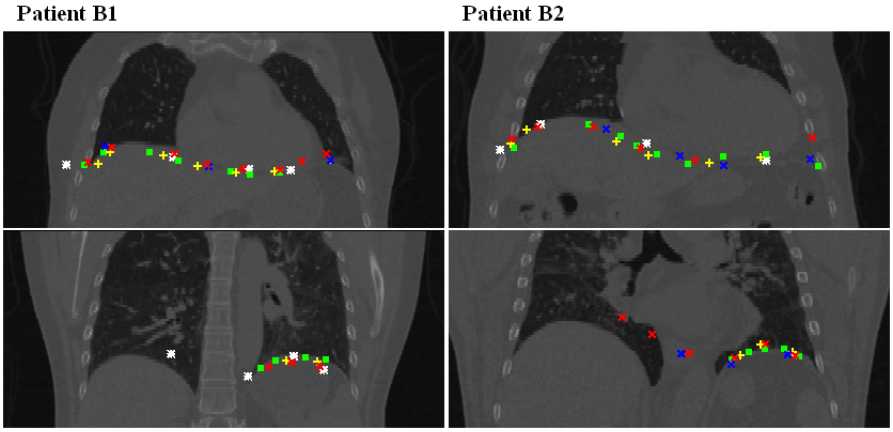

Figure 5.14: Coronal slices showing the PET landmarks identified by the two users, overlaid on the corresponding CT slices. While many of the landmarks were placed on or close to the diaphragm, some exhibit larger errors and regions exist in which there are few or no landmarks. These correspond with the poor contrast regions in PET.

	Patient B1: SSD	Patient B1: Mean error per landmark (mm)	Patient B2: SSD	Patient B2: Mean error per landmark (mm)
No fitting	12836	5.0	25330	7.0
CT	2249	2.1	683	1.2
PETCT	2777	2.3	1749	1.9
PET	6256	3.5	12783	5.0

Table 5.5: Residual errors remaining after fitting 5 modes of variation of the all-patient model (consisting of 12 datasets) to each of the landmark sets. The mean error per landmark was calculated from the SSD using Equation 5.9.

5.4.5.2 Model Fitting

All-patient Model Results

The SSD results for fitting the all-patient model to the two ^{18}F-FDG PET-CT datasets are shown in Figure 5.15. These graphs show the SSD between the fitted surfaces and true diaphragm surfaces (as determined by the CT-based landmarks), calculated over all 6 surfaces. The curves shown are the results of fitting to the 3 landmark sets: CT, PETCT and PET, as listed in Table 5.4. The SSD after fitting 5 modes of variation for each of these curves is also given in Table 5.5, along with the mean error per landmark.

These results show a similar trend between the two patients, with the following being the case in both examples:

$\mathrm{SSD_{CT}} < \mathrm{SSD_{PETCT}} < \mathrm{SSD_{PET}}$

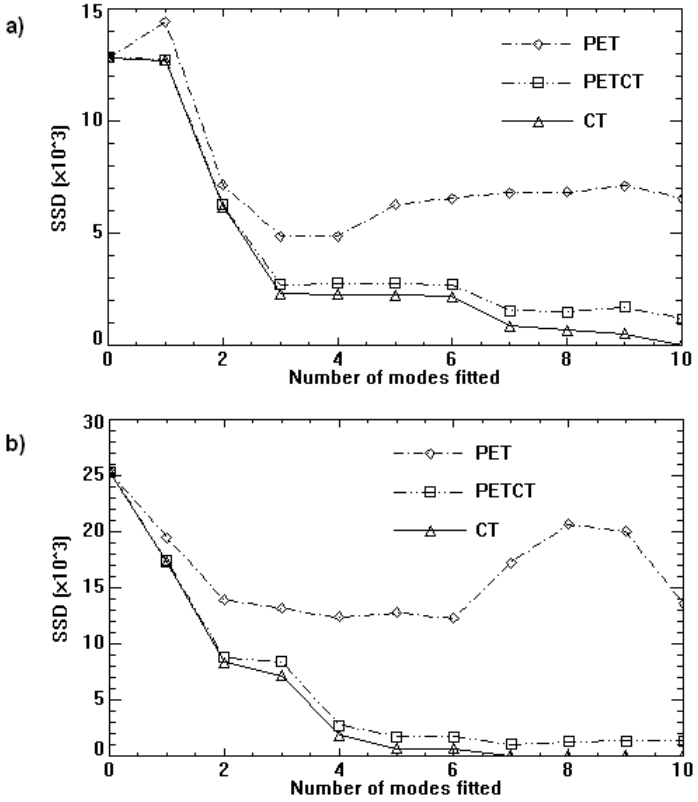

Figure 5.15: SSD as a function of the number of modes included when the all-patient model was fitted to a) patient B1 and b) patient B2, both of which were included in the model construction. The model was fitted to: the CT-derived landmarks (labelled CT), the PET-derived landmarks with a single frame of CT-derived landmarks (PETCT) and the PET landmarks alone (PET).

It was expected that CT-landmark fitting would produce the lowest errors, since these data are used in the model construction and can be defined with a greater accuracy than the PET-based landmarks. Assessing the suitability of this model in application to PET images therefore involved comparing fits obtained with the PET-based landmarks against the baseline of the CT landmarks. Slices through the surfaces obtained by fitting the all-patient model using the PETCT landmark set are shown in Figures 5.18 and 5.19.

It was found that increases in SSD resulted when PET landmarks replaced those obtained from CT in 5 of the 6 respiratory frames (the PETCT landmark set), corresponding with increases in mean landmark errors of 0.2 mm and 0.7 mm for patients B1 and B2 respectively. Using PET-derived landmarks for all 6 frames had a much more pronounced effect, with increases from the baseline of 1.4 mm and 3.8 mm per landmark. Furthermore, inspection of Figure 5.15 shows that the fits were not only significantly poorer, but also highly unstable, with increases as well as decreases in SSD occurring with the addition of modes: for patient B2, fitting 8 or 9 modes to the PET landmarks yielded little benefit from model fitting, since the SSD had reached a level comparable with the starting SSD (i.e. the difference between the patient dataset and the model mean).

The cause of these unexpected increases in SSD was found to be the fluctuation of weightings of the lower modes that occurred as higher modes were added. This is illustrated in Figure 5.16, which shows the weighting of the first mode (b_1) as a function of the number of modes fitted for patient B2 for both the CT and PET fittings. For the CT weightings, b_1 appears to be stable with changing number of modes, whereas for PET, not only is the magnitude of b_1 very different to that obtained using CT, but changes are more pronounced and continue even when the new modes being added account for insignificant proportions of variation. Since the first mode accounts for the largest proportion of variation, its weighting clearly influences the pattern of the SSD curve (as seen by comparison with Figure 5.15b), with a clear correlation between the two, particularly at the higher modes. These features point to this fit being poorly constrained and hence unstable, with the model unable to determine a suitable solution. This is in contrast to both the CT and the PETCT landmark sets, where the solution appears to be more stable.

Finally, model fitting was repeated using each of the 6 PET landmarks sets obtained by the two users to assess the effect of the different landmark selections on fitting accuracy. The mean error obtained with fitting 5 modes of variation to each PET landmark set was 3.3 ± 0.3 mm for patient B1 and 5.3 ± 0.5 mm for patient B2. The equivalent values for fitting to the PETCT landmark sets were 2.4 ± 0.1 mm for B1 and 2.4 ± 0.8 mm for B2. The larger variations observed for patient B2 are likely to be a result of the increased variation in the landmark selection accuracy and suggest that the technique could benefit from the automation of this process. However, even the poorest result obtained from the PETCT landmarks was still found to be substantially better than any instance of PET-only

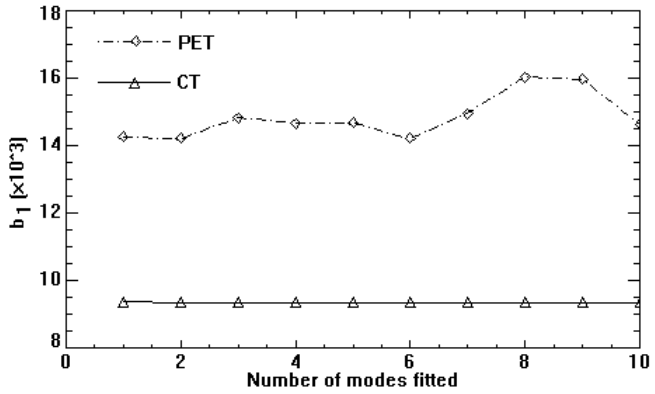

Figure 5.16: The weighting of the first mode of variation (b_1) as a function of the number of modes fitted for the CT-based landmarks and the PET-based landmarks of patient B2.

	Patient B1: SSD	Patient B1: Mean error per landmark (mm)	Patient B2: SSD	Patient B2: Mean error per landmark (mm)
No fitting	15277	5.5	30368	7.7
CT	5293	3.2	13006	5.1
PETCT	5763	3.4	14395	5.3
PET	8646	4.1	19962	6.3

Table 5.6: Residual errors remaining after fitting 5 modes of variation of the leave-one-out models (consisting of 11 datasets) to each of the landmark sets. The mean error per landmark was calculated from the SSD using Equation 5.9.

landmark fitting, further supporting the conclusion that using the PETCT landmark set is a more appropriate method of model fitting in this scenario.

Leave-one-out Model Results

The results for fitting the leave-one-out models to the two ^{18}F-FDG PET-CT datasets are shown in Figure 5.17, with the SSDs present after fitting 5 modes of variation summarised in Table 5.6. It can be seen in both cases that the SSD reduces substantially within the first few modes of variation and then reaches a stable value, with little benefit in increasing the number of modes to greater than 5 or 6. The remaining residual errors confirm the limited ability of these models to describe the datasets presented, indicating that the small number of training datasets is likely to be the main limitation of the models in their current form.

The effect of these residual errors on the fitted diaphragm surfaces is illustrated in Figures 5.18 and 5.19 for patients B1 and B2 respectively. These show slices through the fitted surfaces at end-exhale (i.e. the opposite end of the respiratory cycle to the single CT frame

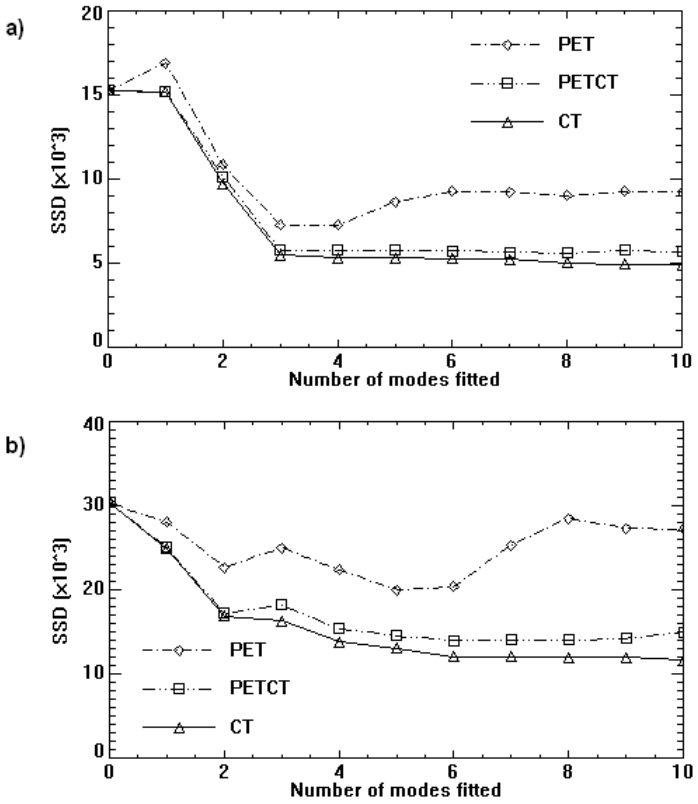

Figure 5.17: SSD as a function of the number of modes fitted for fitting the leave-one-out models to a) patient B1 and b) patient B2 (which were not included in the model construction). The models were fitted to: the CT-derived landmarks (labelled CT), the PET-derived landmarks with a single frame of CT-derived landmarks (PETCT) and the PET landmarks alone (PET).

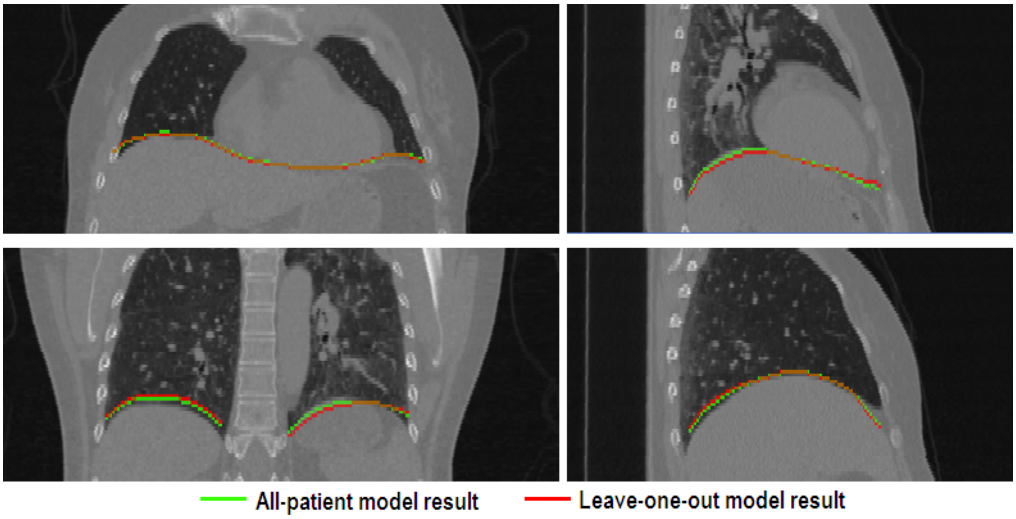

Figure 5.18: Coronal and sagittal slices through the surfaces obtained by fitting the all-patient model (green) and the leave-one-out model (red) to patient B1 using the PETCT landmark set. These slices are from the end-exhale frame, which is at the opposite extreme of the respiratory cycle from the reference frame, for which the single CT frame was used.

incorporated into model fitting) for the all-patient and leave-one-out models, superimposed onto the corresponding CT slices. These indicate that the shape model has been able to reproduce the diaphragm shape well, but that some residual errors remain, which are larger for the leave-one-out models. The increase in error in changing from the all-patient model to the leave-one-out model was 1.1 mm per landmark for patient B1, and these curves can be seen to be overlapping in large regions in Figure 5.18. The difference between the model types for patient B2 however was 3.4 mm per landmark, which is much more noticeable. A larger gap between the two curves can be seen in Figure 5.19, with the all-patient model (the green curve) exhibiting a closer fit to the true diaphragm surface. Assessing the impact of these residual errors on the overall attenuation- and motion-correction technique requires the CT transformation and subsequent attenuation-correction to be performed, with the incorporation of these fitted surfaces. These stages and the resulting accuracy achieved are investigated in subsequent chapters.

Despite the residual errors exhibited by the leave-one-out models, comparing the PET-based fitting with the CT baseline shows similar trends to those produced by the 'all-patient' model. Fitting to the combined PETCT landmark set resulted in small increases in mean landmark errors (0.2 mm increase in both patients), which increased when using the PET landmarks alone (by 0.9 mm and 1.2 mm for patients B1 and B2). The same unstable trends were observed for the PET only fitting, with obvious benefits in incorporating the single CT frame to the fitting process.

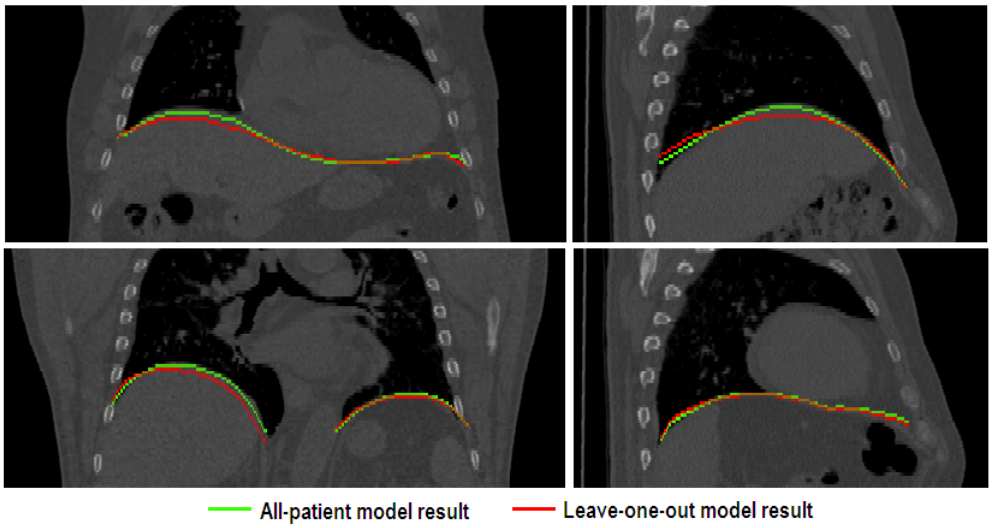

Figure 5.19: Coronal and sagittal slices through the surfaces obtained by fitting the all-patient model (green) and the leave-one-out model (red) to patient B2 using the PETCT landmark set. These slices are from the end-exhale frame, which is at the opposite extreme of the respiratory cycle from the reference frame, for which the single CT frame was used.

Fitting to Subsets of CT Landmarks

Figure 5.20 shows the changes in SSD resulting from changing the CT landmark set to those involving the PET landmarks (PETCT and PET) as well as the subsets of CT landmarks (CT_{PETCT} and CT_{PET}), when using the leave-one-out models. As with previous results, these are given for fits involving 5 modes of variation.

These results allow the overall SSD increase to be separated into its constituent parts: that resulting from the use of a subset of landmarks and that resulting from inaccuracies in the PET landmarks. Figure 5.20 shows that both of these factors adversely affected the model fitting accuracy, although the effects were relatively small in the case that a CT frame was included. An increase in error was observed in both patients in reducing the number of landmarks from the full set (CT) to the CT_{PETCT} subset (using approximately 25% of the original landmarks) and a further increase resulted from using the PET-derived landmarks in 5 of the 6 frames (although this increase was negligible for patient B1). However, both of these increases were small, with the PETCT set exhibiting errors only 0.2 mm larger than the CT baseline in both cases. The larger error introduced when using PET-derived landmarks for patient B2 are likely to be a result of the poorer accuracy with which these landmarks were initially defined.

Reducing the number of landmarks further to only those obtained from PET (CT_{PET}, comprising approximately 10 % of the total landmarks) caused a further small increase in

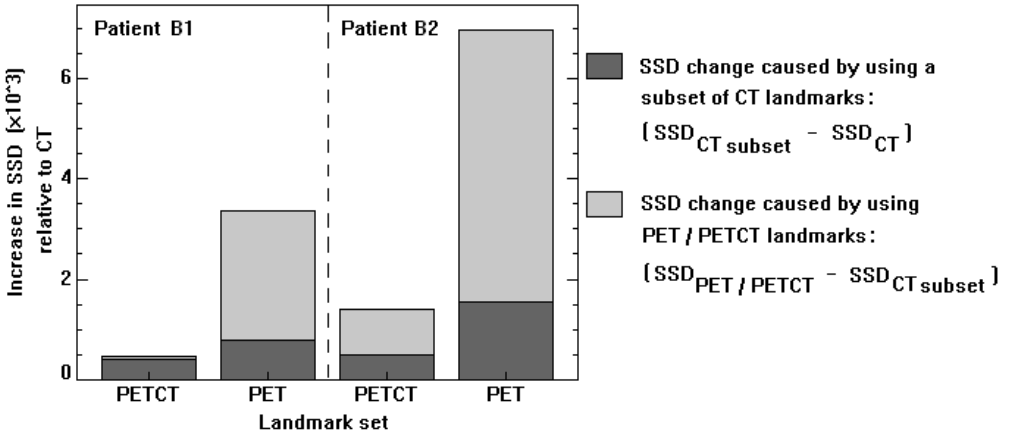

Figure 5.20: Increases in SSD introduced from the use of a subset of CT landmarks and from the introduction of PET-based landmarks. Changes are relative to the SSD achieved when 5 modes of variation are fitted to the full CT landmark set, using the leave-one-out models.

error, adding an additional 0.1 mm per landmark in both cases. However, replacing these with the equivalent PET-landmarks (CT_{PET} to PET) produced large increases in SSD; in both patients this accounted for approximately 75 % of the overall SSD increase from the CT baseline, indicating that the effect of inaccuracies in PET landmarks was the main contributor to errors in this small landmark set. It can be seen therefore that when fitting is performed to a small subset of landmark values, the results are highly susceptible to the accuracy with which the landmarks were defined. The superior results of fitting to the PETCT landmark set are therefore a result of both the improved sampling and the addition of accurately defined landmark values, where the effect of the latter is dominant. Consequently, by including a full description of the diaphragm at a single respiratory position, the requirements of the PET contribution are reduced to assisting in the detection of shape change and in obtaining the amplitude of motion. The model is then less susceptible to noise in the placement of landmarks in PET and produces an overall more robust result.

5.4.5.3 Respiratory Phase Correspondence Testing

Visual inspection of fused PET-CT images indicated that good PET-CT alignment at the position of the heart was present in all frames for both patients, except for one frame which exhibited some motion artefact in the CT. This is discussed in more detail in Section 6.6, however it does not affect the results of this study, since the mismatch was caused by an apparent distortion of the heart caused by motion, rather than a respiratory mismatch.

The model fitting results obtained when a mismatched CT frame was incorporated into the PETCT landmark set are shown in Figure 5.21. This illustrates the case where a single

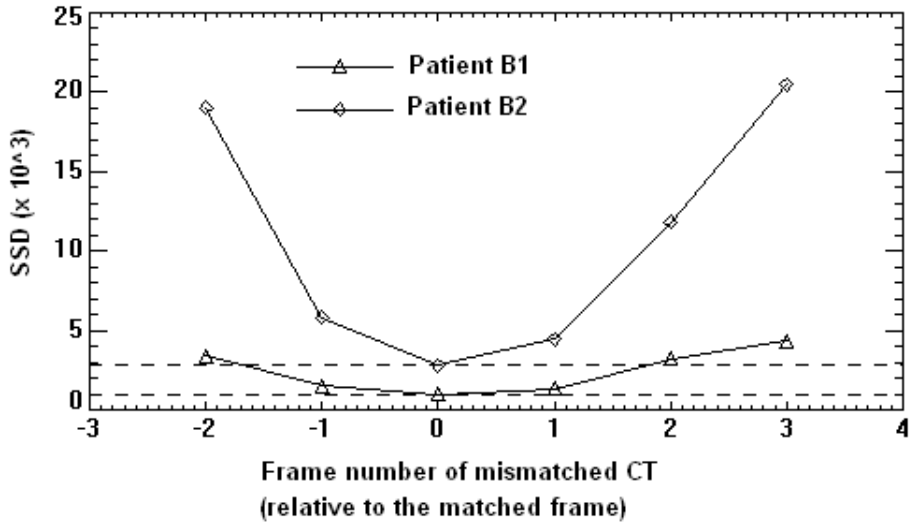

Figure 5.21: The SSD resulting from landmarks obtained in the end-inhale PET image being replaced with landmarks from matched and mismatched frames of a gated CT. Model fitting using the all-patient model was performed in each case. The dotted lines represent the minimum SSD for each patient, which occurred when the matched CT was used in both cases.

CT is wrongly assumed to be at a matched respiratory position to a frame of a gated PET study, and is used to substitute the PET landmarks in that frame. In this case, the end-inhale frame was used as the substitution frame assumed to be matched. Patients B1 and B2 exhibited similar patterns in this scenario, namely that a minimum in SSD was observed when the correct CT frame was incorporated and increases in SSD occurred as the mismatch in respiratory phase became larger. The substitution of a neighbouring frame in place of the matched frame was found to result in an average increase in error of 0.2 mm per landmark for patient B1 and 1.8 mm per landmark for patient B2. The larger deterioration experienced by patient B2 is likely to be a result of the larger amplitude of motion observed for this patient and the subsequent increased difference in diaphragm position between the mismatched frames.

It can be seen therefore that respiratory matching between the single CT frame and the PET frame it replaces is important in obtaining optimal results. However, small mismatches in respiratory phase may be tolerable, particularly if the frame in question is at the end of the respiratory cycle (either end-inhale or end-exhale), due to the reduced motion at these points. The overall amplitude of motion also appears to have an effect on the importance of respiratory mismatches, however steps should be taken to minimise these effects as far as possible in all cases.

5.4.6 Discussion

5.4.6.1 Obtaining Landmark Estimates from PET

The presence of inaccuracies as well as gaps in landmark placement confirmed that additional information would be beneficial for obtaining a full description of the diaphragm position and motion in respiratory-gated PET images. For this study, a manual landmark placement was performed, however benefits may be realised by automating the process, which would allow the inclusion of a greater number of points, without adding to the work burden of the user. This would be challenging due to the poor contrast and inconsistent appearance of the diaphragm over its surface, however as it is only the input data to the model, some missing data or inaccuracies in landmarks would be tolerable, and this could ease some of the difficulties of automation. The introduction of an automated technique would be necessary for implementation in the clinical setting as a routine application.

An alternative method of driving the model fitting would be to use image intensity information, such that the intensity change associated with the object boundary is used to guide the model fitting. Using this approach, the difference between the position of the intensity change and the model surface would be minimised with correct fitting of the model. This method was used by Tobon-Gomez et al. (2008) for segmenting the left ventricle of the heart in SPECT images, using a model constructed from CT. The high gradients in intensity at the edge of the myocardium in SPECT images make this an appropriate technique, which overcomes the need to place landmarks in the dataset to which the model is to be fitted. This approach may not be suitable for the diaphragm however, due its much poorer contrast. In some regions, the most prominent feature is not the diaphragm and this would be likely to produce difficulties in using this type of technique. Some additional information regarding image intensities could be incorporated however, by utilising the single CT, provided it has been acquired at a matched respiratory position to a PET frame. In this case, the CT could be used to ascertain which features in PET correspond with the diaphragm and search for similar features within other frames. This could be beneficial in regions where sufficient contrast is present to reliably locate the required features but would not improve the situation in areas of poor contrast. This represents an area of potential future investigation to reduce the burden of manual landmark placement and to incorporate further information to guide the process.

5.4.6.2 Model Fitting

It is clear from the results obtained that fitting only to landmarks obtained from PET is not suitable for diaphragm tracking and that additional information is required to guide the fit. This is seen in the instability of the SSD curves in Figures 5.15 and 5.17, where

increases in the SSD are sometimes seen with the addition of more modes of variation, which should result in a better description of the diaphragm surface. This feature suggests that insufficient information is available to obtain a reliable fit.

The increased stability of the combined PETCT landmarks however, suggests that reasonable model fitting accuracy could be achieved using this method, since most of the accuracy lost in using the PET only landmarks was recovered with the re-introduction of a single frame of CT-based landmarks. The improvements observed can be attributed to both the increased number of landmarks included in the model fitting optimisation and the improved accuracy of the landmarks obtained from CT, compared with PET. The main contribution to the improvement was found to be the higher accuracy with which the CT landmarks could be identified, since the deterioration to the model fitting was small when the number of CT landmarks was reduced to the level of the PET landmark set, but much larger when these landmarks were replaced with the values derived from PET images. The detailed and accurate shape information provided by the single CT is therefore an important input to the model fitting process. The reliance on the PET landmarks in this case is reduced and their primary contribution is in detecting shape change and determining the overall amplitude of motion, i.e. factors that cannot be established from a single CT. The results indicate that this combination of the CT-derived shape information and the PET-derived motion information gives sufficient information for input to the model.

Increases in error occurred when the leave-one-out models were used in place of the all-patient model, which was expected as a result of the small training set size as well as the effect of correspondence errors in landmark placement. The correspondence errors only affect the leave-one-out models as a result of the exact set of landmark points being present in the all-patient model, and hence the issue of correspondence does not arise. The training set size was expected to be the dominant factor, as already discussed in relation to the model testing using CT data in Section 5.3.4. This is due to the fact that correspondence errors were expected to be small, as a result of the nature of the diaphragm surface shape, whereas the limitations of a small training set are well documented (Davatzikos et al., 2003; Rueckert et al., 2003; Ordas et al., 2004; Koikkalainen et al., 2008).

As outlined in Section 5.2, determining the required training set size is not straightforward, since it depends on the complexity of the object being modelled and the accuracy of fitting required. Obtaining an extensive training set (e.g. of 50 to 100 patients) is beyond the scope of this study, but the small training set used here is still valuable in assessing the feasibility of utilising a shape model for this particular application. Ideally, the fitted diaphragm surfaces would exhibit sub-voxel accuracy with respect to their positions in the PET frames. This was achieved with use of the PETCT landmarks in the all-patient model in both cases, with residual errors of 0.7 and 0.6 slice-widths for patients B1 and B2. Fitting the leave-one-out models using the PETCT landmarks resulted in errors of approximately 1 slice-width for

patient B1, but 1.6 slice-widths for patient B2. An expanded training set would be expected to bring these errors closer to the all-patient model case, in which case sub-voxel accuracy should be achieved in both cases.

With regards to the practical implementation of this model in the clinical setting, it is important to note that even with an expanded training set, this model would not be suitable for all patients. For example, where abnormalities affecting either the respiratory pattern or the shape of the diaphragm are present, the shape model may not be able to provide a good fit. In the absence of a gated CT (as would normally be the case), it would not be possible to validate the fitted surfaces in all respiratory frames, however the single CT frame could be used to estimate the overall success of fitting. Since the diaphragm is fully segmented in this single CT for input to the model, the model output in this same frame could be assessed to determine how well the original shape has been described. Although this does not indicate its success in determining shape change or the amplitude of respiratory motion, a successful fit at one respiratory frame is likely to be indicative of the overall success, due to the high level of shape correspondence between frames. This could therefore provide an important assessment of the model fitting success, that could be used as a quality control measure in the clinical setting.

Prior to clinical implementation, it would also be necessary to determine the success of model fitting to the specific datasets being considered, firstly to determine the influence of differences between ^{18}F-FDG and ^{82}Rb uptakes on the model output and secondly to determine the noise limits with which the model could operate. Typical cardiac studies are likely to be noisier than the datasets used in this investigation, as explained in Section 5.4.2.2 and the effect of this on the success of model fitting would need to be fully assessed using the cardiac datasets, prior to the application of these methods.

5.4.6.3 Respiratory Phase Correspondence Testing

The results obtained from including a mismatched CT frame highlight the importance of matching the single CT to a PET frame where the CT landmarks are to directly substitute those from PET. As already discussed, mismatches between frames of gated PET and gated CT studies do occur in clinical practice: in fact this is one of the primary motivations behind developing a method that does not require a gated CT. Despite the issue of phase-matching being reduced compared with gated CT acquisitions (only a single frame needs to be matched compared with all frames using a gated CT), steps are clearly still needed to ensure the effects of mismatches are minimised.

Such steps should involve ensuring that the static CT is acquired at a respiratory position typical of the PET study, since a CT acquired outside of the normal breathing range, e.g. at deep-inhalation, would produce large mismatches and prevent the incorporation of the

CT-landmarks into model fitting. A breath-hold CT would not therefore be recommended as it often results in imaging at an atypical respiratory state (Pan et al., 2005). Small mismatches in phase are likely to be best tolerated at the ends of the normal breathing range, where organ motion is minimal. The optimal CT acquisition protocol may therefore involve normal breathing (as per the PET study) in conjunction with a respiratory signal, such that prospective gating can be used to acquire a single CT at a specified respiratory position and hence limit the presence of PET-CT mismatches. A visual quality assessment of matching using the cardiac activity is also recommended to ensure good PET-CT alignment.

Although this method means that the reliance on respiratory gating remains (albeit to a reduced level compared with a normal gated CT, involving acquisitions at several phases), it ensures that the chances of a good PET–CT match are maximised, which has been found to be important. If a change in respiratory pattern occurred between the PET and CT studies, resulting in a mismatch between the single CT and the PET frame to be replaced, it is possible that interpolation methods could be used to account for these differences, provided that the relative respiratory positions were known.

5.4.7 Conclusions

This study has shown that a statistical shape model of the diaphragm, constructed from respiratory-gated CT datasets, is beneficial in determining the diaphragm position in noisy and low contrast gated PET images. A model was constructed using 12 sets of diaphragm surfaces, which, although less than ideal, was sufficient to enable an assessment of the technique for its proposed purpose. Of particular interest was the accuracy with which the model could be fitted to data obtained from PET images, since this provided an indication of its suitability for diaphragm tracking in such images. It was found that insufficient information was available in the PET images alone, producing an unstable and poorly constrained fit, which exhibited large errors. However, when landmarks obtained from PET images were combined with a single frame of CT-based landmarks, most of the benefits of the model were recovered, indicating that this would be an appropriate method of model fitting. These improvements were found to be attributable to both the number of landmarks involved in model fitting and the accuracy with which the landmark values were defined in the anatomically detailed CT frame, with the latter being the dominant effect. Obtaining a fully-sampled and accurate description of the diaphragm shape at one respiratory position therefore provided valuable constraints to the model fitting process and resulted in a more accurate and robust fit. These benefits can be realised, provided that the CT frame is acquired at the correct respiratory position and steps should therefore be taken to ensure this is the case.

Similar trends were observed when fitting to a dataset not involved in the model construction, although higher residual errors remained due to the presence of features in the patient dataset

not previously encountered. This suggests that a larger training set would be beneficial to the model, allowing a greater degree of accuracy to be achieved in fitting to previously unseen datasets. However, fitting to the combined PET-CT landmark set still resulted in only small increases in error compared with fitting to the full set of CT landmarks, giving further support to the hypothesis that this type of model is appropriate in assisting diaphragm tracking in gated PET images, provided that information from a single frame of CT is incorporated.

5.5 Summary

This chapter has outlined both the construction of a SSM of the diaphragm and the application of the model to diaphragm tracking in gated PET studies. The end result of these methods are the fitted diaphragm surfaces, which are shown in Figures 5.18 and 5.19. In both cases, it can be seen that the general form of the diaphragm has been well reproduced, with a good level of accuracy, particularly in the first case (patient B1), indicating the validity of the approach to diaphragm tracking. The residual errors may be tolerable for the intended application, which is addressed in subsequent chapters.

The cause of the residual errors, which have been discussed throughout this chapter, can be divided into those originating from the construction of the model and those from the model fitting process and are summarised in Table 5.7. The major contributions have been identified as being that resulting from the limited training set size and that from the inaccuracies in the identification of the PET landmarks ("A" and "C" in Table 5.7). It was found that the second of these could be overcome to a large extent with the incorporation of a single CT (to produce the combined PETCT landmark set), which also had the effect of increasing the number of landmarks involved in the fitting process and hence also reducing the contribution of "D".

Data to which the model is fitted (the input data)	Model type	Contributions to the residual error
CT	All-patient	None
CT	Leave-one-out	A, B
PET / PETCT	All-patient	C, D
PET / PETCT	Leave-one-out	A, B, C, D
CT_{PET} / CT_{PETCT}	All-patient	D
CT_{PET} / CT_{PETCT}	Leave-one-out	A, B, D

Table 5.7: The contributions to the residual error exhibited by the fitted surfaces. The contributions to the overall residual error are from the following sources: A: the limited training set size, B: correspondence errors, C: inaccuracies in the input data, used to drive the model fitting and D: the limited number of input points used to drive the model fitting.

The residual error resulting from the size of the training set would need to be addressed with the inclusion of more training sets, however the use of the all-patient model gave an indication of the level of error that could be achievable if this factor was removed. The all-patient model results were found to be acceptable, both for fitting to CT-based landmarks (as in Section 5.3) and when fitting to the combined PETCT landmark set (as in Section 5.4), indicating that the overall approach is suitable and that benefits could be gained by expanding the training set. The effect of these errors on the ability to accurately transform a single CT and the subsequent effect on the attenuation-correction accuracy of PET studies are addressed in Chapters 6 and 7.

Chapter 6

Transforming a CT to Different Respiratory States

6.1 Introduction

The aim of the work outlined in this chapter is to determine suitable methods for transforming a single CT to other respiratory positions and to apply these methods to generate a synthetic gated CT series. The purpose of obtaining these transformations is to facilitate the respiratory-matched attenuation-correction of a gated PET study, without the need for a gated CT acquisition. This type of approach is also currently being investigated by other groups (Dawood et al., 2008b; Fayad et al., 2008), where the transformation of the single CT is derived from non-rigid registrations between the PET frames. This is directed more towards the motion-correction of whole-body PET images and hence the whole acquisition volume needs to be included in the transformation. The use of a non-rigid registration (optical flow in the case of Dawood et al. (2008b) and elastic registration in the case of Fayad et al. (2008)), could potentially be problematic in the presence of noisy data, particularly in regions of poor contrast, where little information is available with which to determine the transformation. However, the success of these methods, particularly in their application to clinical data has yet to be fully evaluated.

The aim here is to obtain a CT transformation specifically for cardiac studies, and hence the accurate transformation of the whole thorax is not necessary. This is due to the fact that in cardiac studies, artefacts that do not influence the appearance of the myocardium do not adversely affect the efficacy of the study and can therefore be disregarded. Therefore only the structures that were previously identified as being responsible for producing artefacts in the heart need to be transformed, which, as ascertained in the attenuation mismatch work

in Chapter 3, applies to both the heart and the diaphragm. Additionally, by incorporating the use of a diaphragm shape model (as described in Chapter 5), it was anticipated that the derived transformations would be robust to high levels of image noise and hence would produce more reliable results than techniques using information obtained solely from the PET images.

The impact of these CT transformations on the appearance of the attenuation-corrected PET images is addressed in Chapter 7; the focus of this chapter is on the methods of transforming the CT volume and the accuracy with which the synthetic CT frames could describe the original CT frames. Like the assessment methods used in relation to the model testing in Chapter 5, the original gated CT acquisition was used as a means of validation, but only a single CT would be required for normal use of this method. The datasets used for this part of the project were therefore the same as in previous investigations; the two respiratory-gated PET-CT datasets with 6 respiratory frames, as described in Section 5.4.2, from which a single frame was selected to represent a static CT acquisition and the other frames were used as a means of validation.

Due to the nature of the diaphragm shape model already constructed, it was necessary to treat the heart and diaphragm transformations separately. The diaphragm motion was already investigated through the shape model fitting described in Chapter 5 and the results obtained are briefly recapped in Section 6.2.1, together with a description of the methods used to ensure coverage of the whole diaphragm dome. The heart motion was obtained through use of a rigid registration, which is described in Section 6.2.2. Since the results of the heart registration were required prior to transforming the CT, the results of these registrations are also outlined in the Section 6.2.2.

To apply these motions to the CT volume, it was firstly necessary to define the regions that were to be transformed, which is outlined in Section 6.3. The methods of defining the abdomen region for transformation according to the diaphragm motions are described in Section 6.3.1 and those for defining the thorax, to which the heart motion estimates were to be applied are described in Section 6.3.2. Again, as the region definitions were required prior to CT transformation, the results of these are also outlined within Sections 6.3.1 and 6.3.2. The methods of applying the estimated motions to the different regions are then described in Section 6.4 and methods of measuring success are outlined in Section 6.5. The results of the transformations are given in Section 6.6 and the discussion and conclusions are presented in Sections 6.7 and 6.8.

6.2 Obtaining Motion Estimates

The first stage of CT transformation was to obtain estimates of the motions of both the diaphragm and the heart, to enable subsequent transformation. The methods of obtaining these estimates are described in the following sections.

6.2.1 Obtaining Diaphragm Motion Estimates

The 6 diaphragm surfaces over the respiratory cycle were obtained for the two PET-CT datasets by the methods described in Section 5.4, where a statistical shape model of the diaphragm was used to generate complete descriptions of the diaphragm shape and motion from limited input data. The data that were found to be suitable for input to the shape model were a combination of manually placed landmarks obtained from the gated PET frames and the landmarks from the segmented diaphragm surface in a single CT frame. Using this combined PETCT landmark set as input to the model with 5 modes of variation fitted was found to produce surfaces that described the overall shape and motion well, although some differences to the true diaphragm surfaces remained. Surfaces were generated for models in which the CT component of the patient data was included in the model construction (the all-patient model) and where the patient data was excluded from model construction (the leave-one-out models), which represented the best performance that could be expected with this method and the current level of performance. Since both of these scenarios provide useful information in determining the success of the overall approach, CT transformations based on both sets of surfaces were obtained.

The motion between each respiratory phase was calculated for every pixel in the 2D diaphragm array by taking into account the difference between the diaphragm height in the fitted model surface and the segmented surface in the reference frame (the single CT frame). Prior to transforming the diaphragm, methods were needed to ensure that the entire diaphragm dome was included in the transformation process. The fitted model surfaces did not always extend to the chest-wall, since the landmarks were placed on the intersecting area of all of the training data. Therefore, due to small differences in the shape of the diaphragm outline, some edge regions were not covered by the model. This problem was overcome by considering the segmented diaphragm surface in the reference frame of the CT. To extend the surfaces to the chest-wall, the regions of diaphragm outside of the model coverage were assumed to maintain a constant shape over the respiratory cycle and were assigned the motions of the nearest pixel within the coverage of the model. This assumption was made based on the region of diaphragm outside the model being small and consequently large shape distortions in these regions were not expected. This approach therefore allowed the model surfaces to be extended to fit any diaphragm outline, while maintaining a realistic shape and motion.

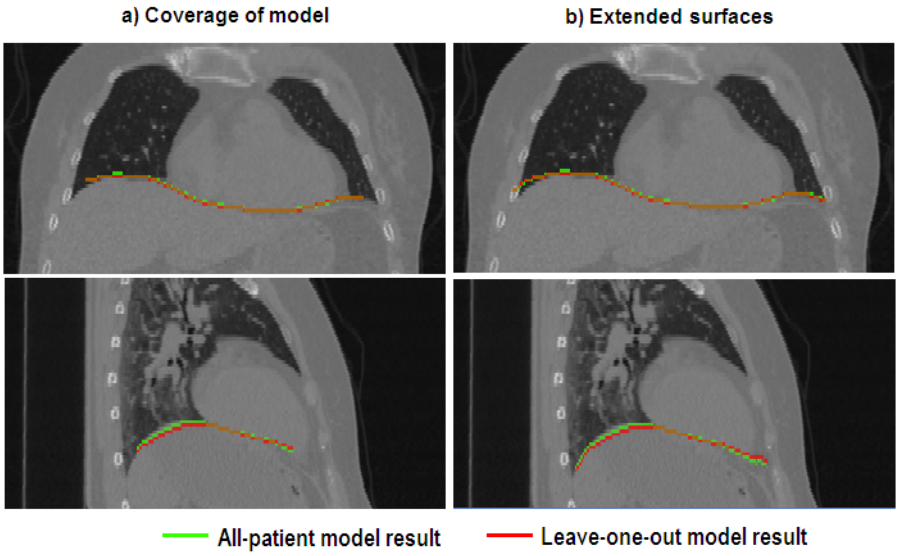

Figure 6.1: A coronal and sagittal slice through the fitted surfaces for patient 1, showing: a) the coverage of the model and b) the extended surfaces that covered the entire diaphragm. (The extended surfaces are also shown in Figure 5.18 on page 167)

The result of this process is shown in Figures 6.1 and 6.2, which shows the original and extended surfaces for sample coronal and sagittal slices for patients 1 and 2. It can be seen that the extended surfaces provide a better coverage of the diaphragm dome, which is important for enabling a realistic transformation.

6.2.2 Obtaining Heart Motion Estimates

Due to the heart being more easily identifiable in cardiac PET images compared with the diaphragm, its motion was determined by a simple rigid registration on the heart activity between the gated frames. This approach was taken since the motion of the heart with respiration is known to be approximately rigid body in nature (Korin et al., 1992; Livieratos et al., 2005) and this allowed a simple and reliable technique to be applied to the count-limited gated frames. While a non-rigid technique such as optical-flow registration as implemented by Dawood et al. (2008a) may have the ability to account for small deformations in the heart as it moves with respiration, it is possible that such a technique may become unreliable at low count levels, due to the large degree of flexibility permitted with these methods. Investigations with non-rigid registrations are continuing, however for this study, the rigid-body approximation was used and hence the number of parameters needed to describe the motion was reduced to 6; 3 translations and 3 rotations.

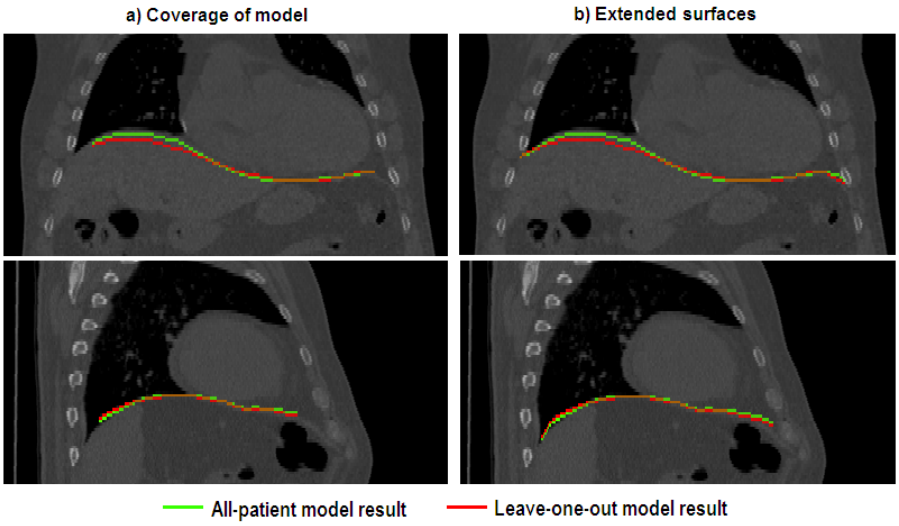

Figure 6.2: A coronal and sagittal slice through the fitted surfaces for patient 2, showing: a) the coverage of the model and b) the extended surfaces that covered the entire diaphragm. (The extended surfaces are also shown in Figure 5.19 on page 168)

The "MIR" software package (developed by Dennys Y. H. Lau, Westmead Hospital, Sydney, Australia), developed in IDL was used for these registrations, using the correlation coefficient as a cost function, as described in Section 2.7.1.1 and given by Equation 2.5. The PET images had to be processed prior to registration, to ensure that the registration results were not biased by features other than the heart in the images. This involved applying a threshold, so that only high activity regions remained and lower activity regions were masked. The value for the threshold was chosen such that as much extra-cardiac activity could be removed as possible, while retaining the appearance of the activity in the left ventricular myocardium. Due to different levels of myocardial uptake, these values were different for the two patients. Additional processing was performed to exclude the presence of high-uptake tumours, which may have exhibited different motions to the heart and therefore distort the registration results. This would not normally be required in cardiac images, however as these were acquired for oncology purposes, the PET images of both patients exhibited one or more high-uptake tumours, which required masking.

The results of the heart registration for both patients are given in Figure 6.3. It can be seen from these curves that noise does not appear to have been a significant problem for these registrations, since the curves produced appear smooth and exhibit a form that would be expected of these parameters over the respiratory cycle. In obtaining these results, the centre-of-rotation was the image centre and not the centre of the heart. This will have had an influence on the values obtained for each of the parameters and hence cannot be directly compared with the previous heart motion results obtained (see Section 4.4.3).

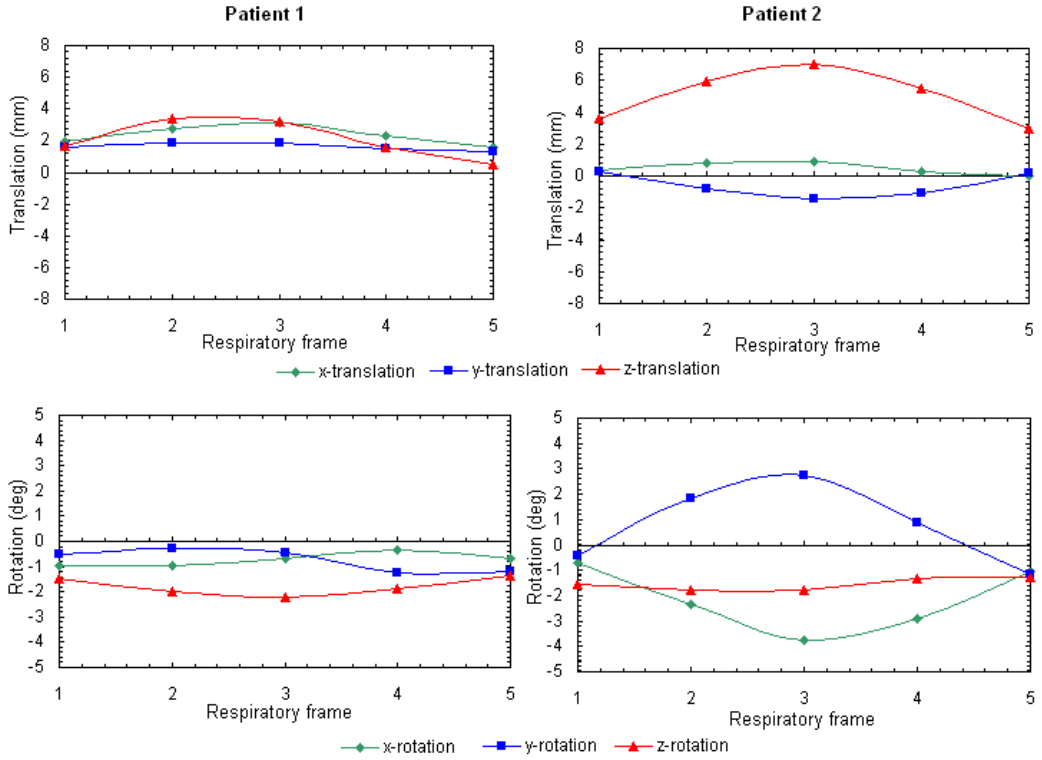

Figure 6.3: The rigid-registration results from registering the heart activity in frames 1 to 5 to frame 0 (the end-inhale frame), for both patient datasets.

Figure 6.4: The extent of the abdominal region, shown in red, superimposed onto the CT image. The diaphragm surface obtained from segmentation is the upper layer of abdomen voxels.

6.3 Defining Regions in CT

Having obtained estimates of the motions, it was then necessary to determine which regions of the CT volume would be transformed according to the obtained motions. The methods of defining the regions to be transformed, according to either the diaphragm or heart motions are described in the following sections.

6.3.1 Defining the Abdomen in CT

The assumption was made that the whole abdomen would move with the diaphragm and hence this region needed to be defined to enable its subsequent transformation. The diaphragm surface in the single CT frame had already been obtained through segmentation and since the diaphragm represents the boundary between the thorax and the abdomen, this was used to obtain the abdomen region to be transformed. The abdomen was simply defined as all voxels that lay directly inferior to the segmented diaphragm surface, as shown for an example coronal slice in Figure 6.4.

6.3.2 Defining the Thorax in CT

It was previously determined that the heart position needed to be matched between PET and CT during attenuation-correction, however rather than transforming only the heart position, it was decided that a better description of the true situation would be to also transform the rest of the thorax, where the surrounding vessels and airways move with the heart rather than remaining static. Two methods of defining the region to which the heart transformation would be applied were tested; one in which all voxels that were not already assigned to the abdomen region were transformed and another in which the thoracic cavity was separated from the chest-wall and the transformation was applied only to this segmented

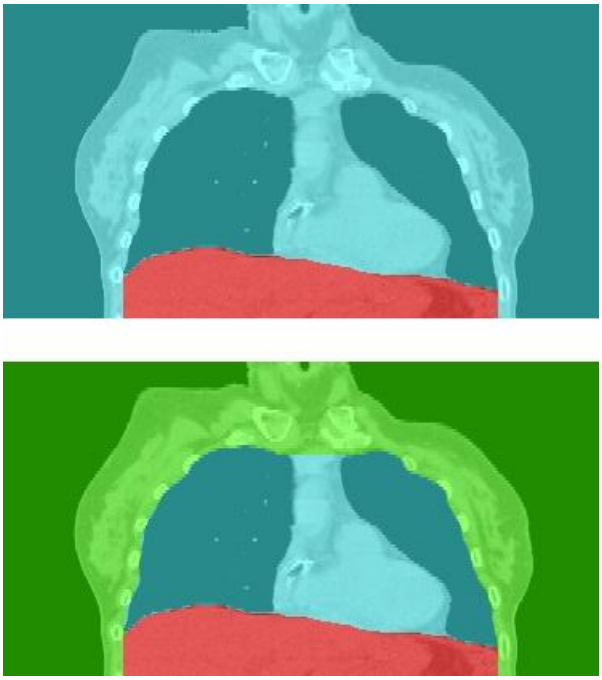

Figure 6.5: The division of a CT into 2 regions (top) and 3 regions (bottom) for subsequent transformation. The area in red represents the abdomen region to be transformed according to the shape model results, the turquoise area represents the region to be transformed according to the heart motion parameters and the green area remains static with no transformation applied.

region. These two approaches will be referred to as the two region method and the three region method, respectively, according to the number of regions the CT was divided into, including the abdomen region. These regions are illustrated in Figure 6.5.

The two region method was straightforward to implement, since all voxels that were not already assigned to the abdomen were treated as thorax, to be transformed according to the heart motion estimates. Although the chest-wall would not be expected to move with the same motion parameters as the heart, the results of earlier studies where mismatches due to chest-wall motion were found not to influence the attenuation-correction of the heart (see Chapter 3), indicated that an incorrect chest-wall transformation may not be problematic. This two region method tested this assumption by transforming all non-abdomen regions according to the heart motion.

The three region method involved defining the thoracic cavity separately from the chest-wall, such that different transformations could be applied to these different regions. This scenario was closer to the actual situation, where the motions of the chest-wall and spine, for example, are minimal and are not therefore described well by the motion of the heart. However, dividing the CT volume into three regions was more involved than the two region

method, since it required the segmentation of the thoracic cavity. The methods developed for obtaining the thoracic cavity in an automated manner are outlined in the following section.

6.3.2.1 Segmenting the Thoracic Cavity from the Chest Wall

The thoracic cavity is defined as the anatomical region within the chest wall and above the diaphragm. It includes the lungs and the heart as well as the airways and vessels associated with these organs. Separating the thoracic cavity from the chest wall and the abdomen is not straight-forward, due to the similar intensities and close proximity of the heart to both of these regions. Additionally, the thoracic cavity contains different structures with very different properties, for example the lungs have a low intensity appearance in CT, unlike the heart, blood vessels and the walls of the major airways, which have much higher CT intensities. The aim was to develop a method of segmentation that would include all of these structures, but separate them from the chest-wall and abdomen. The top priority of the segmentation was to ensure that the heart was fully included in the segmented region and separated from the chest-wall, since a poorly defined heart region would lead to part of the heart not being transformed and would likely introduce PET–CT mismatches in the heart. Due to the importance of heart matching in PET and CT during attenuation-correction, it was important to avoid this scenario.

As with the diaphragm segmentation, it was possible to evaluate existing techniques used for segmentation to determine whether they could be incorporated here. An outline of these methods is given in Section 4.2.1 on page 87. Due to the nature of the problem, it can be seen that the existing techniques would not solve the problem completely, but could be used as a basis on which to base an extended method. For a large proportion of the area, the thoracic cavity–chest-wall boundary is identified by the high contrast change between the lungs and the chest-wall. Region-growing was selected as a potentially valuable technique on which to base the segmentation, since by placing a seed within the lung tissue, it was possible to segment the lungs and thereby identify much of the thoracic cavity. A similar technique was used in the automatic determination of the diaphragm limits described in Section 4.3.4, except that for this application, masking was not applied to the superior portion so that a single region covering both lungs was obtained. From this starting point, a number of methods of obtaining the heart region were investigated before a successful method was found. These are outlined as follows:

Method 1: Region growing in the heart

Since the thoracic cavity contains structures clustered around two intensities, one approach that was investigated was to perform a second region growing, with the seed placed in the heart. This additional region could then be added to the already identified lung region to

form the complete thoracic cavity. Although the heart is not the only structure that would need to be identified by this region growing, the similarities of the CT values of the heart and the other structures, such as the blood vessels, and their close proximity to the heart would mean that a region defined in this way would be likely to extend into the vessels such that they were also included. Some airways may be missed from a single seed, but this could be overcome with either the placing of a third seed or by using methods to fill small gaps in the combined lung–heart volume.

However, this method was found to be unsuccessful due to the close proximity of the heart to the chest-wall and their similar appearances in CT. This resulted in the region growing for the heart "leaking" into the neighbouring chest-wall and therefore not separating these structures. This is illustrated in Figure 6.6, which shows a binary map of the region obtained from growing a seed placed in the heart. It can be seen that the separation of the heart from the chest-wall does not produce a sufficiently strong boundary to separate these structures with this method. Despite different threshold settings being applied for defining the heart region, it was found that in obtaining sufficient coverage of the heart, spillage of the region into the chest-wall was unavoidable. This approach was not therefore investigated any further and alternative methods were sought.

Method 2: Filling all regions between the lungs in the left–right direction

From the results of method 1, it could be seen that although problems arose with using region growing in the heart, defining the lung region in the same manner was successful, due to the high contrast boundary separating the lungs from other structures. A potential method was therefore proposed that involved including all pixels that lay between the left and right lungs in the segmented region. Although this is a simplistic approach, it would be a straight-forward method of defining the region and could be an adequate method for including the necessary structures. With this approach, the segmented lung region was obtained first and the left–right filling was performed on the binary map of the lung region. This involved determining the left and right limits of lung tissue in every row and simply assigning all voxels between these limits to the thoracic cavity region.

The result of this process is illustrated in Figure 6.7. It can be seen that the spine has been included in the region as a result of the shape of the lungs and the coverage of the heart is incomplete, particularly for patient 2. The incomplete coverage of the heart was due to the lack of lung tissue in this region, meaning that part of the heart was still excluded after the filling process has been applied.

The inclusion of the spine is not ideal, since it does not move with respiration and should not be transformed according to the motion of the heart, but the main problem is with the coverage of the heart, since this is the main priority of the segmentation process.

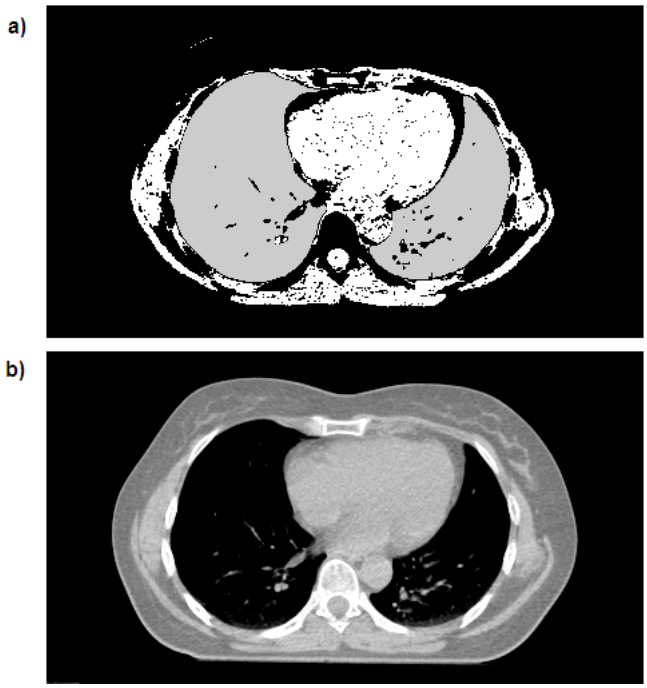

Figure 6.6: a) The result of region growing from a seed placed in the lungs (shown in grey) and in the heart (shown in white). Due to the similarity of the appearance of the heart and the adjacent chest-wall, the region has spread beyond the heart, into the chest-wall and other surrounding structures. b) The original CT slice.

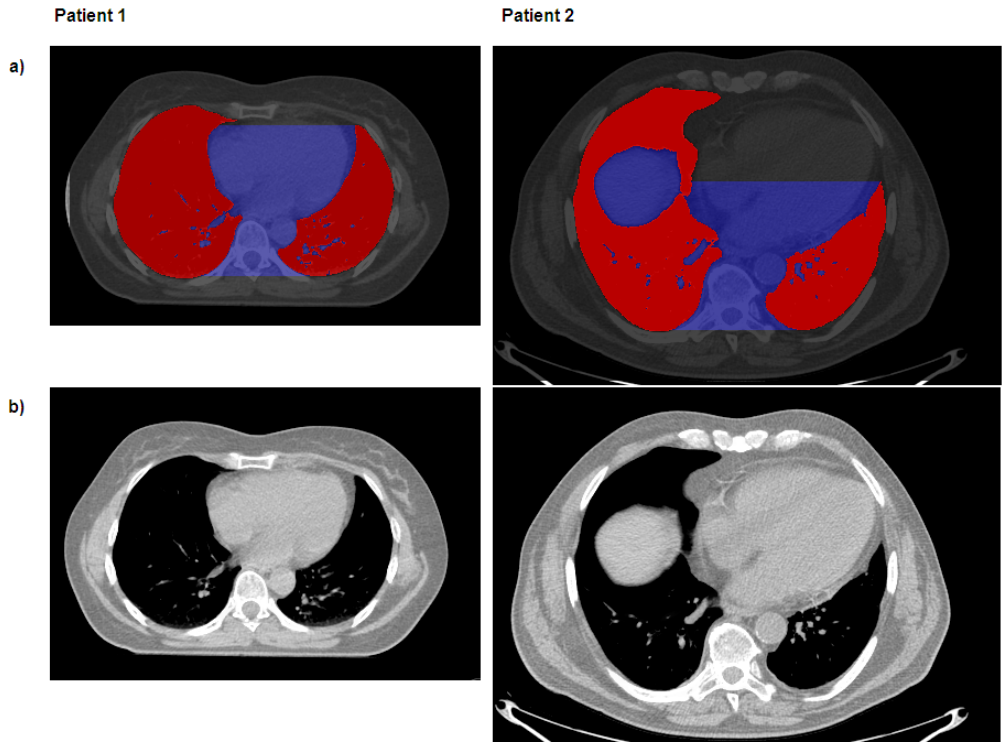

Figure 6.7: For patients 1 and 2: a) the regions obtained from the lung binary map (red) and the additional areas included by filling between the left and right lungs (blue) and b) the original CT slice. (Patients 1 and 2 correspond with patients B1 and B2 as used in Chapter 5 on page 129.)

Alternative methods would therefore be needed to ensure complete coverage of the heart, while excluding the chest-wall. It would also be preferable to exclude the spine from the region and only transform the thoracic cavity. For these reasons a third segmentation method was investigated and the left–right filling method was not developed any further.

Method 3: Using the rib-cage to provide additional information

It was clear from the previous two segmentation attempts that additional information to define the region would be advantageous in defining the thoracic cavity, in particular to ensure complete coverage of the heart. The rib-cage position was identified as a potential means of aiding this process, since the ribs are easily separable from the thoracic structures, due to their higher intensity in the CT image. Although they are not adjacent to all areas of the thoracic cavity, they do permit a partial identification of the boundary, which was expected to be valuable additional information.

The assumption was made that the volume encased by the rib-cage defines the thoracic cavity. By identifying the rib-cage and determining locations inside it, it was then possible to combine this information with the already segmented lung volumes, to obtain an improved estimate of the thoracic cavity. The steps involved in obtaining the additional information and combining it with the lung volumes are outlined as follows, and illustrated in Figures 6.8 on page 192 and 6.9 on page 193:

Identify the ribs, spine and sternum through region growing Since these structures are connected, only a single region was required to identify all of the bones surrounding the thoracic cavity. The placement of the seed was performed automatically by searching for high-intensity regions in the CT image; in both patient datasets, this was found to reliably identify the entire rib-cage. The result of this for a sample transaxial slice is shown in Figure 6.8b for patient 1 and Figure 6.9b for patient 2.

Assess radial paths for intersection with the segmented bone region To identify which voxels lay within the rib-cage, a point in the centre of the thorax was manually identified so that radial paths could be traced out from this point. Every path that intersected with bone was then stopped at the position of the intersection, such that all points along the path could be assumed to be within the thoracic cavity and paths that did not intersect with bone could be discarded. The implementation of this process actually involved tracing a path from each bone voxel to the centre point and was retained only if it did not intersect with other bone voxels along its length. This "backwards" ray-tracing allowed a more efficient execution of the process than forwards ray-tracing, i.e. from the centre outwards, since paths that did not intersect with bone at all did not need to be

considered. The result of this process is illustrated in Figures 6.8c and 6.9c for patients 1 and 2, where the radial paths are shown with the segmented rib-cage and spine.

Extensions to this technique would be possible by including more than one centre-point from which to generate radial paths, or by considering the problem in 3D, rather than on a slice-by-slice basis, as was the case here.

Combining the segmented lungs and radial paths Figures 6.8d and 6.9d show the combination of the segmented lung binary map and the binary map of the radial paths, for patients 1 and 2. In some regions it was found that the radial paths extended beyond the extent of the lung tissue, due to the presence of a small amount of chest-wall tissue between the lungs and the ribs. To overcome this, the radial paths were cropped to match the extent of the lung tissue when the limits of both were in close proximity (defined as being within 5 pixels of each other). This approach was taken as the limits of the lung tissue were taken as being a more reliable indicator of the true edge of the thoracic cavity compared with the radial paths and therefore when two estimates of the boundary position were available, the lung segmentation was used. The main contribution of the radial paths were therefore in the regions where there was limited lung tissue. Following this, all nonzero voxels in the combined map were given a value of 1, such that the two sources of obtaining voxels in the thoracic cavity were no longer separated.

Removing gaps in coverage and cropping over-extended radial paths It was found that although the combined lungs and radial paths binary maps contained many gaps and did not therefore provide a full description of the thoracic cavity, this could be overcome by using a combination of dilation and erosion operations on the combined binary map. Additionally, some of the radial paths extended beyond the thoracic cavity, which can be seen in some areas in Figure 6.9d. This could also be overcome with the same operations.

Dilating the map causes the nonzero regions to be expanded by an amount equal to the size of a structuring element, which can be described mathematically as follows:

$$C = A \oplus B = \cup_{b \in B} (A)_b \tag{6.1}$$

where C is the result of dilating image A with structuring element B. $(A)_b$ represents the translation of A by b. Therefore, for all nonzero elements of B $(b_{i,j})$, A is translated by i, j and summed into C using the "OR" operator.

Image erosion causes the reverse to occur, i.e. the nonzero region shrinks. This is performed as follows:

$$C = A \otimes B = \cap_{b \in B} (A)_{-b} \tag{6.2}$$

where C is the result of eroding image A with structuring element B. $(A)_{-b}$ represents the translation of A by b. This results in the removal of "islands" smaller than the size of the structuring element.

Performing erosion after dilation does not necessarily produce the original image, since if holes are filled during the dilation process, these will not be eroded again, since the associated boundary disappears. The same is true when performing the operations in the reverse order, since the islands that are removed by the erosion will not reappear through dilation. The position of other edges not associated with islands or holes are not affected by this process and they return to their original appearance if the opposite operation is performed.

These functions were therefore used to fill in gaps in the binary map (by performing a dilation followed by an erosion), which is known as "closing" as well as to remove small clusters of radial paths that had extended into the chest-wall (by performing an erosion followed by a dilation), known as "opening". Since the position of the ribs is different in successive transaxial slices, the process of filling gaps was applied to coronal slices, in addition to the transaxial slices, so that gaps in this direction could also be filled. This was important in obtaining a good coverage of the thoracic cavity, as can be seen in Figure 6.8, since the positions of the ribs in the slice shown would not have permitted a good coverage of the left–anterior portion of the thoracic cavity, if the slice was considered independently. By filling from slices either side however, the coverage was improved, giving rise to the final segmented region, as shown in Figure 6.8e and f. The effect of shortening the radial paths that had extended too far can be seen in Figure 6.9d and e, where the smooth outline obtained in Figure 6.9e was achieved through this process. The structuring elements in each case were circles, with radii of 20 for filling holes in the transaxial slices, 10 for filling holes in the coronal slices and 3 for removing extensions of radial paths. These radii were found to be optimal for both patient datasets.

Inspection of the volume obtained showed that good coverage of the thoracic cavity was obtained, including the heart and areas outside the thoracic cavity, such as the spine were avoided. A detailed assessment of the accuracy achieved was not performed, since the main priority of the segmentation was adequate inclusion of the heart, which was assessed visually. Small inaccuracies in the region away from the heart were not considered to be problematic, since it was the matching of the heart that was the priority. This method was therefore found to be successful for this task and these regions were used for the subsequent transformations. Although there were a number of stages in obtaining the final region, these were all automated, apart from the initial placement of the seed for region growing in the lung tissue.

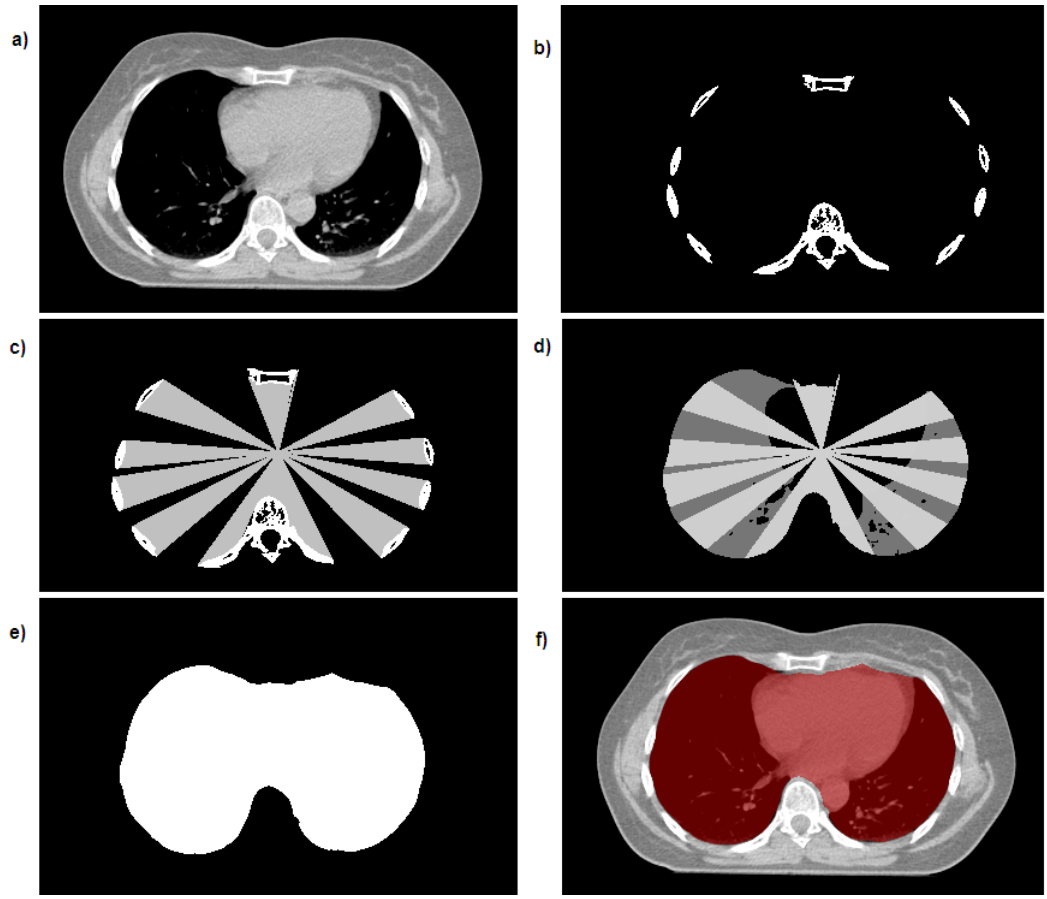

Figure 6.8: The stages of thoracic cavity segmentation using the lung region and the rib-cage as a basis for obtaining the whole volume. a) A transaxial slice through the original CT of patient 1. b) The segmented rib-cage and spine, as obtained from region growing. c) The result of tracing radial paths between the bone regions and a centre point (ribs shown in white and the radial paths in grey). d) The combined lung binary map (dark grey) and the radial paths (light grey). e) The final region obtained by dilating and eroding the volume in (d) in the transaxial and coronal slices. f) The segmented region (as in (e)) displayed in red, overlaid on the original CT slice.

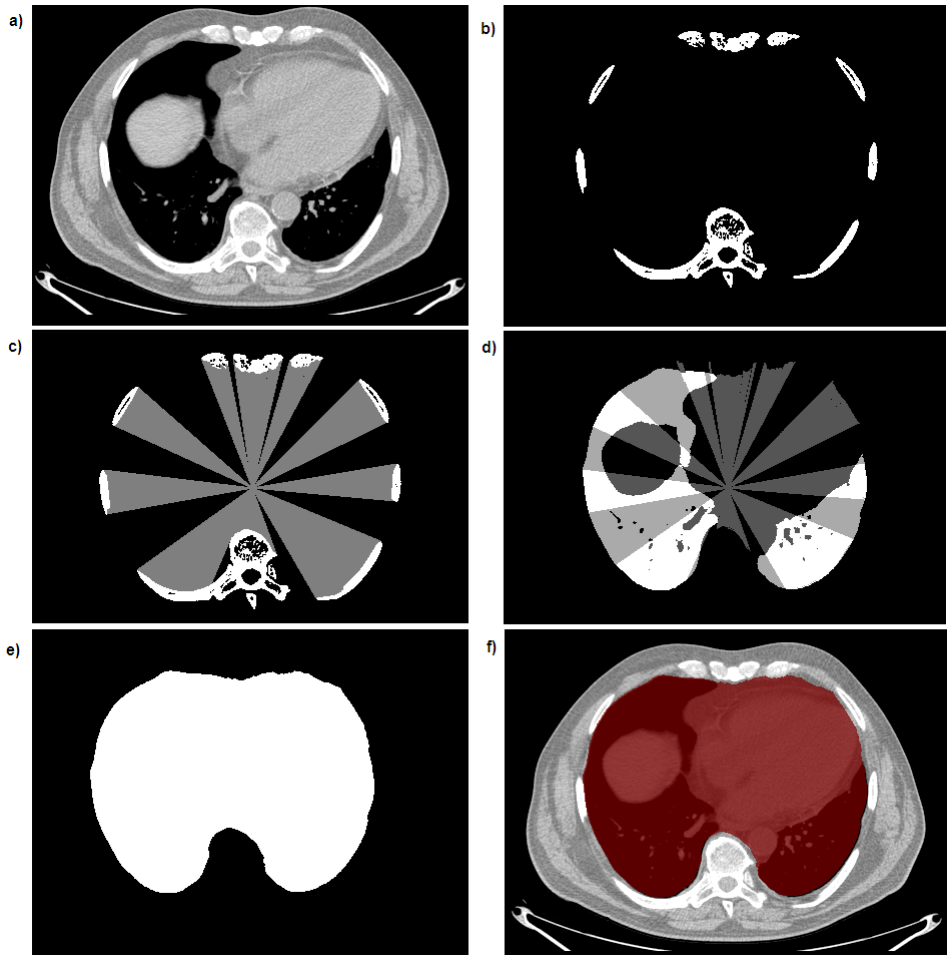

Figure 6.9: The stages of thoracic cavity segmentation using the lung region and the rib-cage as the basis for obtaining the whole volume. As for Figure 6.8, but for patient 2. Although there is some liver in the slice shown, this was included within the already defined abdomen region and was not therefore included as thorax once the regions were combined.

6.4 Applying the Transformations to the CT

Having divided the CT into the regions to be transformed, methods then had to be developed to apply the obtained transformations to the single CT volume so that a realistic transformed CT could be obtained. Separate methods were applied to transforming the abdomen and thorax regions and the transformed regions were then combined. The methods of transformation and the subsequent re-combination of the regions are described in the following sections.

6.4.1 Transforming the Abdomen Region

Methods were required to transform the abdomen region such that the transformed diaphragm matched the surfaces obtained from the fitting of the shape model. The approach taken was to transform each vertical column of voxels (lying in the superior–inferior direction) separately, where a shift was applied to the column according to the extent of motion that had occurred between the two respiratory phases at that position. This is illustrated in Figure 6.10, which shows the original abdomen region (in the end-inhale frame) and the same region following transformation to the end-exhale phase. The values of the last voxel in every column of the reference frame were used to fill in gaps created by the transformations where the shift has resulted in superior translation. As the reference frame was the end-inhale frame, this direction of shift occurred in the majority of the columns.

It can be seen that using this approach allowed realistic deformations of the diaphragm to be applied to the CT volume, such that the diaphragm surface obtained from model fitting were matched well by the transformation process. This also allowed features in the abdomen to be retained; although the priority was given to obtaining the high contrast boundary between abdomen and thorax, features such as air pockets would also ideally be transformed in a realistic manner, since the attenuation changes associated with them could potentially be important for the heart. This method, while not considering the transformations of individual abdominal structures explicitly, allowed for a transformation to be applied that was expected to be a good approximation of the actual motion. The combined effects of the accuracies of diaphragm shape and motion estimations and the transformations of the abdominal structures were assessed in relation to the overall accuracy with which the transformed CT matched the gated frames of the CT.

6.4.2 Transforming the Thorax Region

The thorax region, whether it was defined as the segmented thoracic cavity (for the 3 region method) or all non-abdominal areas (for the 2 region method), was transformed according to

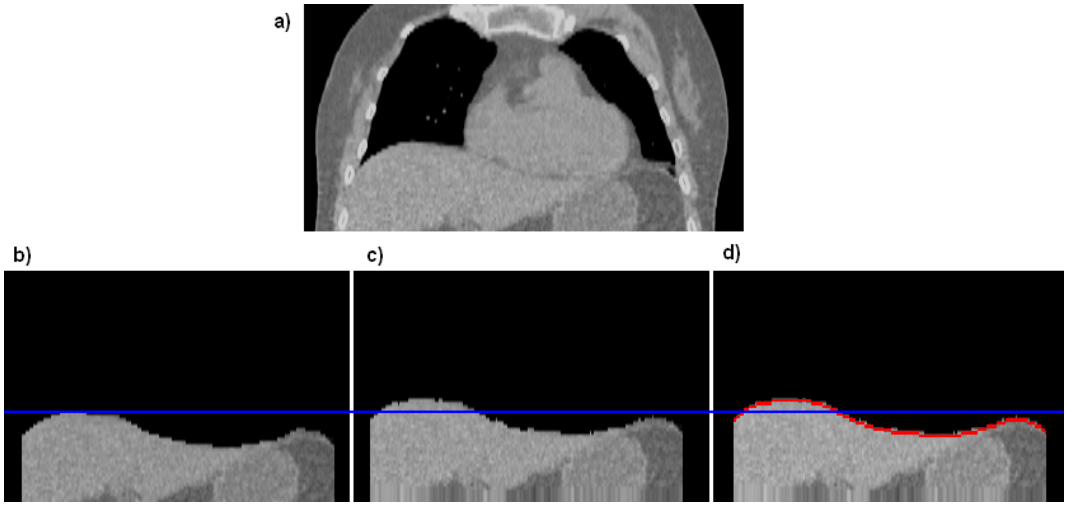

Figure 6.10: The transformation of the abdomen region from the end-inhale (reference) frame and the end-exhale frame for patient 1. a) A coronal slice of the reference CT frame, b) the abdomen region with other regions masked, c) the transformed abdomen region to match the end-exhale diaphragm position and d) the transformed region with the fitted model surface superimposed in red. The blue line is a reference point to facilitate a comparison between the diaphragm position in the original and transformed images.

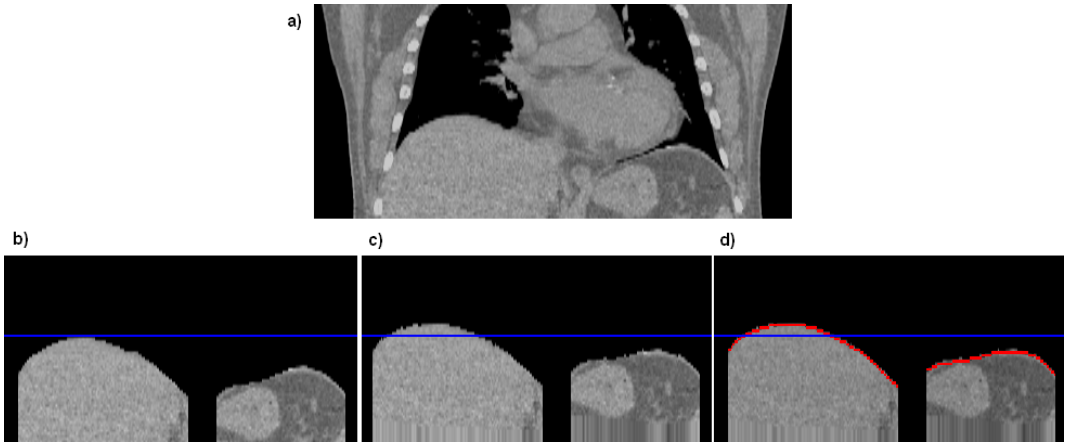

Figure 6.11: As for Figure 6.10 but for a more posterior coronal slice in the dataset of patient 2.

the registration results performed on the heart activity. This was therefore straight-forward to implement, since deformations were not included. The transformations were initially applied to the entire CT volume, with the transformed abdomen region and the static region (in the case of the 3 region method) incorporated when combining the regions, which is described in Section 6.4.3, below. At this stage therefore, the 2 and 3 region methods were identical, and involved applying a global transformation to the single CT volume.

6.4.3 Combining the Transformed Regions

In combining the regions from the different transformations, the reasons for selecting the end-inhale frame as the reference frame become clear, particularly in relation to the 3 region method. With the 3 region method, the chest-wall remained static, while the thoracic cavity was transformed inside the chest-wall boundaries. Therefore selecting the frame with the maximum volume within the thoracic cavity as the reference frame to be transformed was advantageous since it reduced the problem of overlap, which could lead to inaccuracies in the transformed volume. In particular, the heart often exhibits an anterior motion during inhalation (Shechter et al., 2004) and since it is in close proximity to the chest-wall, this could lead to overlap between the heart and the chest-wall if the transformation was applied to the end-exhale frame. Due to the importance of performing an accurate transformation of the heart and its immediate surrounds, this overlap could be problematic, with the potential of attenuation-correction artefacts in the reconstructed heart activity occurring. These problems were alleviated with the use of the end-inhale frame, due to both the tendency for the heart to move in a posterior direction during exhale and the greater volume within the thoracic cavity in which to transform the selected region. This is less of a problem for the 2 region method, in which the thoracic cavity and chest-wall are transformed together according to the same parameters, however to enable a comparison of the results from the 2 and 3 region methods, the end-inhale frame was selected as the reference frame for both approaches.

Despite the occurrence of overlaps being reduced by the selection of the end-inhale frame, it was still expected that some overlapping regions would result from the transformations, as the thorax and the abdomen had been treated separately. Additionally, gaps between regions were also expected and both had to be overcome in order to produce a complete CT volume at each of the required respiratory phases. The issue of overlap was dealt with by prioritising the higher intensity (and hence higher attenuation) voxels in CT, when two or more voxels were overlapping. Comparisons were performed on a voxel-by-voxel basis, where the value of the higher attenuating voxel was retained. The main reason for this approach being taken was to give the lung tissue a low priority and to retain the voxels associated with heart and abdomen, since these are the structures that needed to be transformed accurately.

Therefore in an overlap between lung and liver, the liver was retained over the lung tissue. The chest-wall was also retained when overlapped with lung tissue.

Overlap between the heart and the abdomen was expected to be minimal if their motions had been determined correctly. However, in the presence of an overlap, it was expected that in general, the values of the heart voxels would be retained, since the abdomen does not typically contain higher attenuating materials than the heart, but does exhibit lower attenuations in some regions. In the case that the heart attenuation is found to be similar to that of the abdomen tissues, the issue of which region is given priority is unimportant, since the effect on the resultant attenuation is minimal. Overlap between the heart and chest-wall was also expected to be small, as already discussed, but the same rules were applied in the case that this overlap did arise. The occurrence of overlap with the 3 region method can be seen for a sample coronal slice of the transformed dataset of patient 1 in Figure 6.12, where the thoracic cavity–chest-wall overlap is shown in green and the abdomen–thoracic cavity overlap is shown in blue. It can be seen that, as expected, there is overlap in all areas of the thoracic cavity–chest-wall boundary and that thoracic cavity–abdomen overlap is also present.

The effect of using the methods described for overcoming the issue of overlap can also be seen in Figure 6.12, in the transformed CT volume. Overall, the transformed volume looks to be realistic, suggesting that the method of retaining the higher voxel value in areas of overlap was successful. The only obvious errors are at the superior limits of the lungs, where the initial definition of the thoracic cavity extended into soft tissue and contains values typical of the lung tissue following the transformation of this area. This is therefore a result of errors in the thoracic cavity definition rather than in the handling of overlapped regions, but is distant to the heart, so would be unlikely to affect its appearance in attenuation-corrected images.

The selection of the end-inhale frame as the reference volume to be transformed was also expected to limit the presence of gaps between the regions, as a result of the dominant motion being in a superior direction (before returning to the position of the reference frame). The superior motion of the abdomen reduces the volume of lung tissue required to fill the thoracic cavity and hence overlaps, rather than gaps were expected. Furthermore, the superior–inferior liver motion is typically larger than that of the heart and therefore an overlap rather than a gap was expected in this part of the thorax–abdomen boundary. Where gaps between regions were present however, strategies were required to fill them in an appropriate manner. This was only an issue for the 3 region method, since all non-abdomen areas were treated as thorax in the 2 region method and hence gaps did not arise.

The method used was firstly to identify the presence of any gaps between the abdomen and thoracic regions in the superior–inferior direction and to fill these with the nearest thorax value. These voxels are identified in yellow in Figure 6.12. This approach was taken in

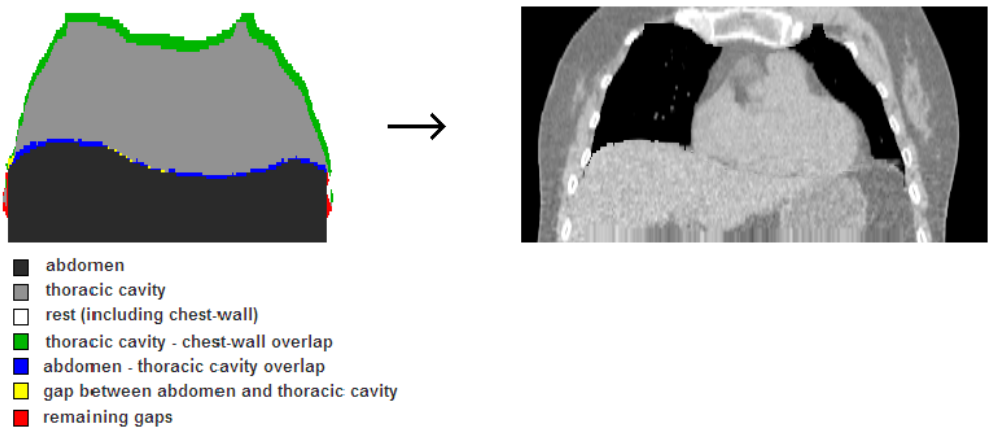

Figure 6.12: Left: the coverage of the transformed regions in a coronal slice of patient 1, including the areas of overlap and the gaps between regions. This image represents a slice through the end-exhale frame, which has been transformed from the reference (end-inhale) frame. Right: the result of retaining the higher overlapped voxel values and filling gaps on the resultant transformed CT.

order to maintain the position of the transformed diaphragm surface and to fill in the gaps with realistic lung values. The next stage was then to fill in any remaining gaps, which are identified in red in Figure 6.12. These were filled using the values from the original CT volume of the reference frame. These gaps were typically present between the abdomen and chest-wall regions in the left–right direction; since the chest-wall was not transformed in the 3 region method, filling from the original CT volume therefore simply extended the coverage of the chest-wall to remove the presence of gaps.

6.5 Assessing the Transformed CT Volumes

Transformations using both the 2 and 3 region methods were obtained for both patient datasets. Furthermore, 2 diaphragm transformations were performed, according to the all-patient shape model and the leave-one-out shape model results. Therefore 4 sets of transformations were obtained for each patient. Initially, visual assessments were performed on animations of the transformed frames to determine the overall success of the different approaches and to compare the different transformation methods.

Two sets of quantitative measures of transformation accuracy were also performed; firstly the SSD between the transformed CT and the true CT (from the gated study) was calculated for each frame and summed over all frames. This allowed a measure of the overall accuracy to be obtained, taking into account the whole volume, although as previously discussed, it was the regions that could influence the attenuation-correction accuracy of the heart that were

of particular interest. For this reason, the attenuation correction factors (ACF) were then calculated, using Equation 2.3 on page 34, since it is these values that are used to perform the attenuation-correction of the PET emission data and hence determine the accuracy of the correction. These values were stored as a set of projections, with scaling applied such that they represented the ACFs at 511 keV. These projections were then masked, so that all regions were set to zero, apart from a region-of-interest placed over the heart. The position of the non-masked region was adjusted in each projection angle so that it remained centred on the heart at all angles. The masked ACF array therefore only contained projections that traversed the heart and was hence the most important measure for determining the success of the CT transformation. The accuracies of the masked ACFs were also measured using the SSD between the transformed and original gated CT projections.

In order to put these results into context, the effect of not performing any transformation was assessed, by measuring the differences between the end-inhale frame and each of the gated CT frames. This represented the case that a single CT was used to attenuation-correct all frames of a PET study. Although the end-inhale frame represents an extreme point of the respiratory cycle, the extent of mismatch between the averaged PET data and the inhale CT frame was seen to be typical of that routinely seen in clinical images and hence this represented a clinically relevant investigation. Finally, to demonstrate the impact of the diaphragm shape model, the accuracies of the fully transformed CT volumes were compared with those obtained from transforming only the thorax region (as is currently performed in the clinical setting, as described in Section 3.4). These results are outlined in the following section.

6.6 Results

The different methods of transforming the CT were compared visually and by calculating the differences between the transformed frames and original gated CT frames. The transformed series are best viewed through the animations in Appendix B; the images shown in this section represent a single frame from each animation that corresponds with the end-exhale position (the opposite end of the respiratory cycle to the reference CT frame).

A comparison was performed between the 2 and 3 region methods, which determined whether it was optimal to transform all non-abdominal regions or only the thoracic cavity according to the heart registration results. The end-exhale frames of the transformed CT volumes using both of these methods is shown in Figure 6.13 and all transformed frames are shown in the animations in Appendix B.3. The abdomen transformations were performed according to the all-patient shape model results in every case. Additionally, the SSD calculations for the transformed CT frames are shown in Table 6.1 for both model types.

Transformation type	SSD (Patient 1)	SSD (Patient 2)
2 regions, all-patient shape model	2.34×10^{11}	3.51×10^{11}
2 regions, leave-one-out shape model	2.34×10^{11}	3.50×10^{11}
3 regions, all-patient shape model	1.16×10^{11}	2.24×10^{11}
3 regions, leave-one-out shape model	1.11×10^{11}	2.23×10^{11}

Table 6.1: The total SSDs between the original gated CT frames and the transformed frames for each transformation type.

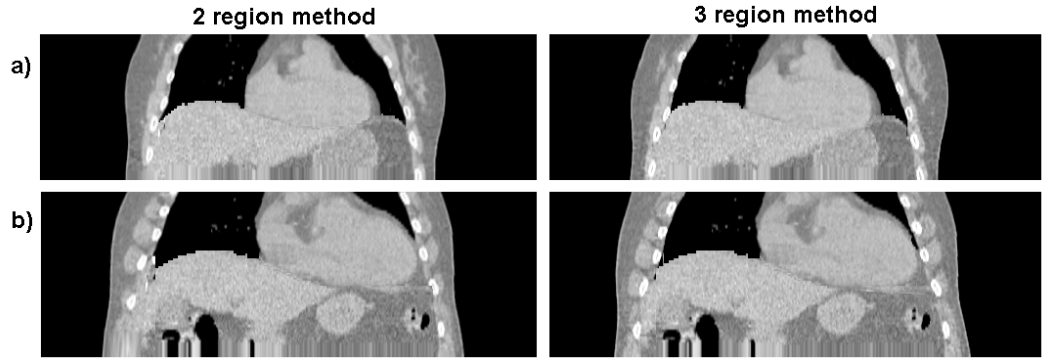

Figure 6.13: A coronal slice through the end-exhale frame of the transformed CT sets of a) patient 1 and b) patient 2, using the 2 and 3 region methods to divide the CT volume. Both transformed images were obtained using the all-patient model to transform the abdomen region. Please see the animations in Appendix B.3 to view the complete series with all respiratory frames.

By viewing the animated series of transformed frames, it can be seen that the motion of the chest-wall in the 2 region method does not appear to be realistic, due to the same motion parameters being applied to it as to the heart, which is clearly not the case. By viewing the original gated CT frames (as in Appendix B, parts B.4.1 to B.4.4), it can be seen that the motion of the chest-wall throughout the respiratory cycle is very limited. As a result, the 3 region method, where the chest-wall remains static, appears to be a better description of the overall CT motion than the 2 region method. This was confirmed with the calculation of the SSDs between the transformed and original CT frames, as given in Table 6.1. This showed that in changing from the 2 to the 3 region method, the SSD decreased by 50 % for patient 1 and 36 % for patient 2, indicating substantial improvements.

The optimal transformation method was therefore that which involved dividing the CT volume into 3 regions, such that only the thoracic cavity was transformed with the heart. Coronal and sagittal slices through the optimum transformed CT are shown for both patients and for both shape model types (the all-patient and leave-one-out models) in comparison to the original gated CT frames in Figures 6.14 to 6.17 and the animations of these same transformations are shown in Appendix B, parts B.4.1 to B.4.4.

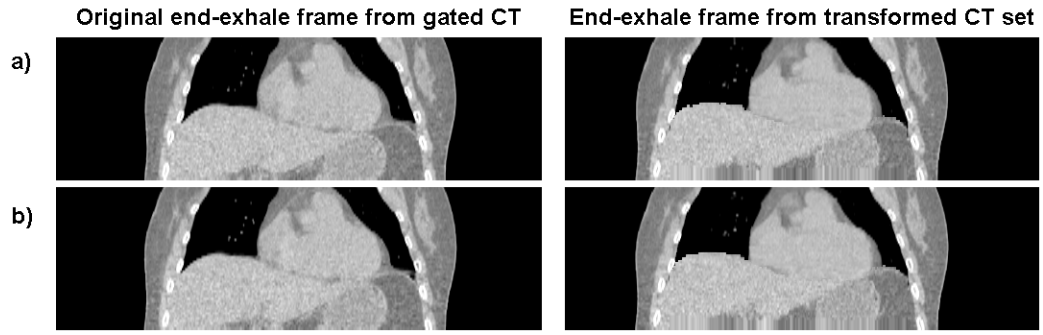

Figure 6.14: Coronal views of the end-exhale frames from the original and transformed CT datasets for patient 1, where the abdomen transformation has been obtained using a) the all-patient model shape and b) the leave-one-out shape model. Please see Appendix B.4.1 for the animations of these sets.

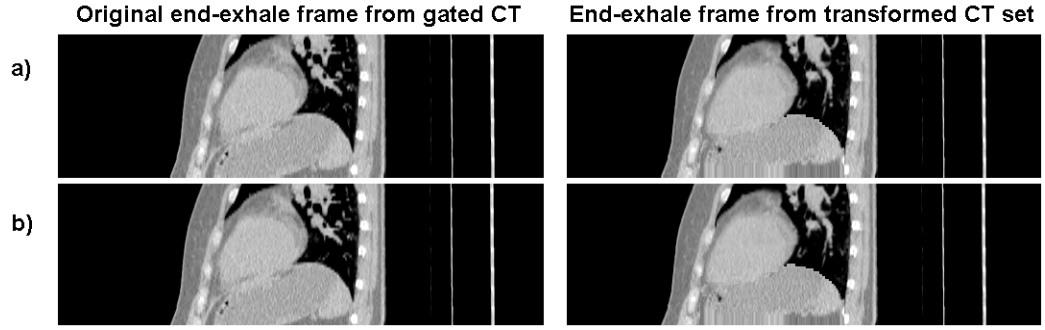

Figure 6.15: As for Figure 6.14 but for a sagittal view. Please see Appendix B.4.2 for the animations of these sets.

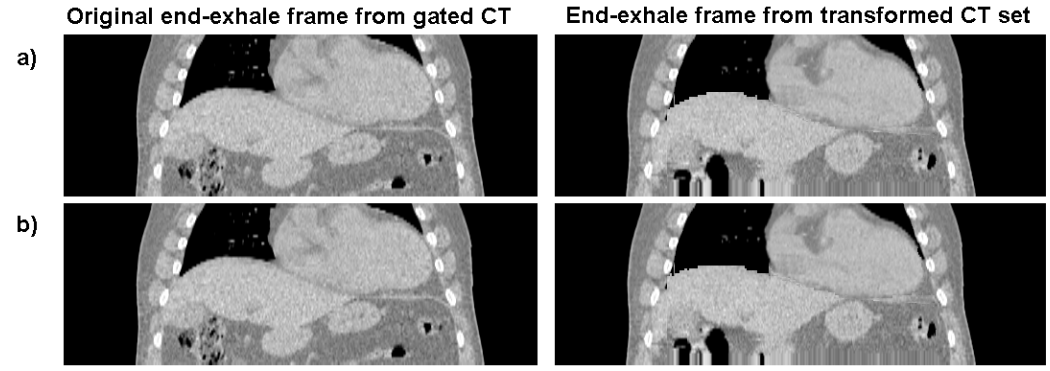

Figure 6.16: Coronal views of the end-exhale frames from the original and transformed CT datasets for patient 2, where the abdomen transformation has been obtained using a) the all-patient model shape and b) the leave-one-out shape model. Please see Appendix B.4.3 for the animations of these sets.

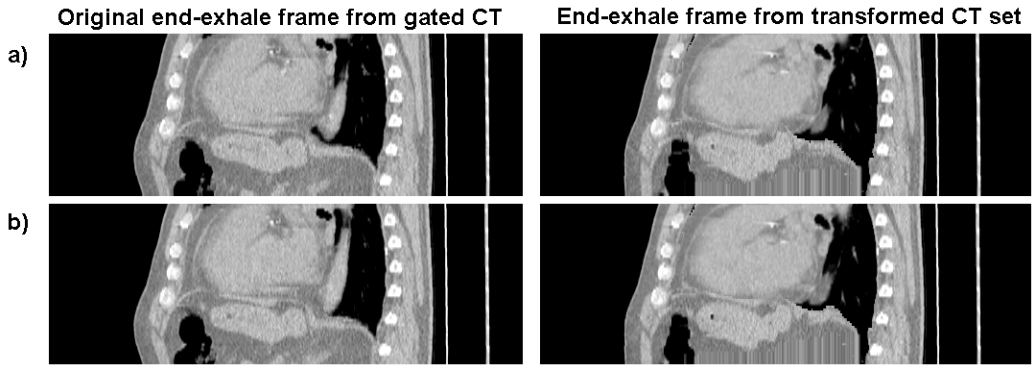

Figure 6.17: As for Figure 6.16 but for a sagittal view. Please see Appendix B.4.4 for the animations of these sets.

The results of the ACF comparisons for all transformations are shown in Figures 6.18 and 6.19 for patients 1 and 2. Inclusion in the comparison are the 2 and 3 region methods, both in combination with the all-patient model and leave-one-out model shape results, as well as the "thorax only" and "inhale CT" datasets. The "thorax only" set involved the transformation of the entire dataset according to the heart registration results, with no separate consideration of the diaphragm and was performed therefore to ascertain the impact of the diaphragm shape model. The "inhale CT" on the other hand did not involve any transformations and was used to represent a measure of the differences in the ACFs produced by using only a single frame rather than a gated series.

Initially, an unexpected trend was observed in the results of patient 2, which are shown in Figure 6.19a. The inhale CT set achieved the lowest level of error in comparison to the gated CT datasets, implying that applying no transformation gave a better description of the gated dataset compared with the transformed versions. However, inspection of each frame of the gated CT dataset indicated that a motion artefact was present in a single frame (frame 4, which is a mid-inhale frame), which affected the appearance of the heart. This is shown in Figure 6.20, where the superior portion of the heart appears distorted in the original CT frame, which can result from irregular breathing patterns as well as the motions caused by cardiac contractions in non-ECG gated studies. The equivalent frame of the transformed CT was not affected in the same manner, since it was based on the appearance of the heart in the reference frame, which did not exhibit such artefacts.

For the transformation involving 3 regions and the all-patient shape model result, it was found that this frame contributed 97 % of the total SSD for this patient, with other frames contributing < 1 % each. This was attributed to the presence of the artefact and this frame was therefore considered unsuitable as a ground-truth measure of the CT at this respiratory position. For this reason, frame 4 was removed and the analysis repeated. The results of this are shown in Figure 6.19b, which appear to be more realistic measures, with the inhale

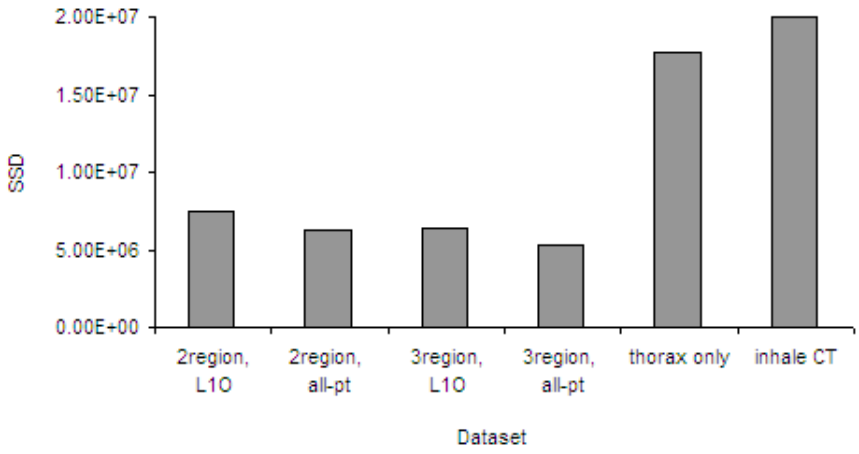

Figure 6.18: The SSD between the masked ACFs of the transformed and original CT datasets for patient 1. L1O = use of the leave-one-out shape model to transform the abdomen region, all-pt = use of the all-patient shape model for abdomen transformation. The "thorax only" dataset involved a thorax transformation, but no separate abdomen transformation and the "inhale CT" results were obtained from replicating the end-inhale frame of the gated CT dataset and treating as a transformed series.

frame now exhibiting the largest errors. The remaining frames contributed approximately equally to the total SSD, suggesting that no further distortions were present.

Following this correction, similar trends were obtained for both patient datasets. The masked ACF SSDs were found to be lower for the 3 region method than the 2 region equivalents for both patients, supporting the visual assessment obtained earlier. In both cases, the inhale CT produced the largest differences when compared against the frames of the gated studies, which was as expected, since no transformation was performed and mismatches would have been present in both the heart and the surrounding structures.

The datasets in which only the thorax region was transformed also exhibited high levels of error, which indicated that an accurate transformation of the abdomen is important in obtaining a good representation of a gated CT dataset. The thorax transformation may have actually worsened the extent of mismatch at the position of the diaphragm, as a result of the heart transformation being a poor description of the diaphragm motion. Therefore, high levels of error remained, despite the improved matching of the heart position. This shows that the impact of a mismatched diaphragm position on the ACFs for the heart can be significant. Since the ACFs are multiplied by the measured PET projections, these errors will be propagated directly into the attenuation-corrected PET data, which could then have an impact on the reconstructed activity distribution.

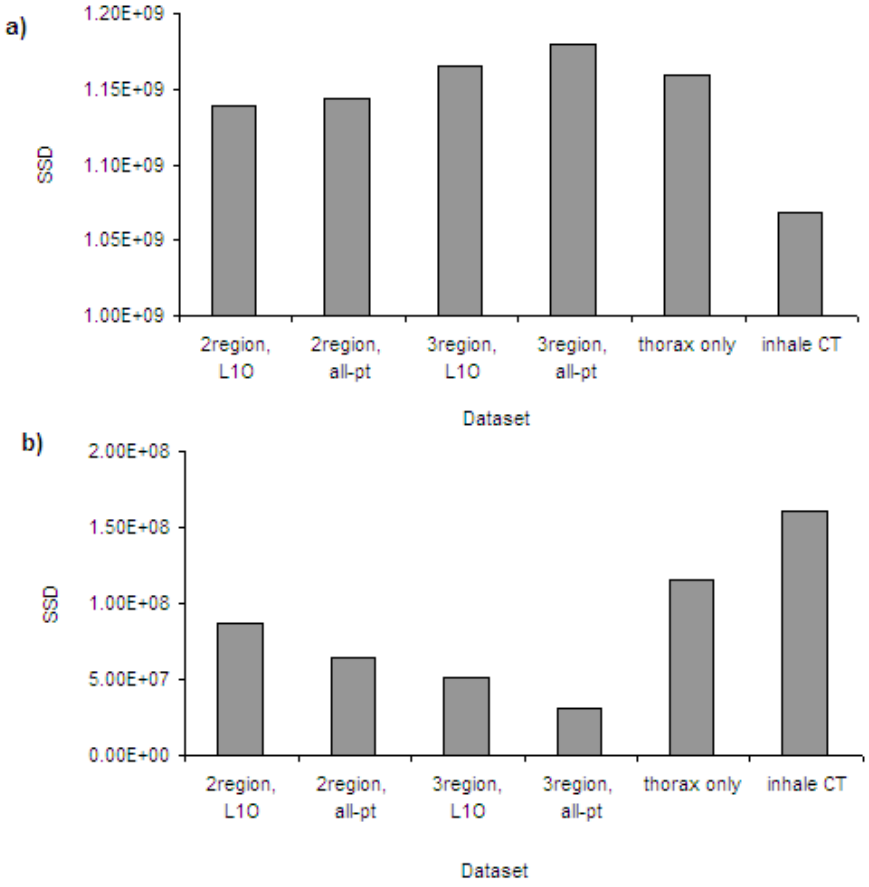

Figure 6.19: The SSD between the masked ACFs of the transformed and original CT datasets for patient 2. a) The results obtained when all frames were included in the analysis, b) the results obtained when frame 4 was excluded from the comparisons. Frame 4 was excluded as a result of a motion artefact in the heart of the gated CT frame and hence it provided an unsuitable ground-truth measure. (See Figure 6.18 for an explanation of the dataset types.)

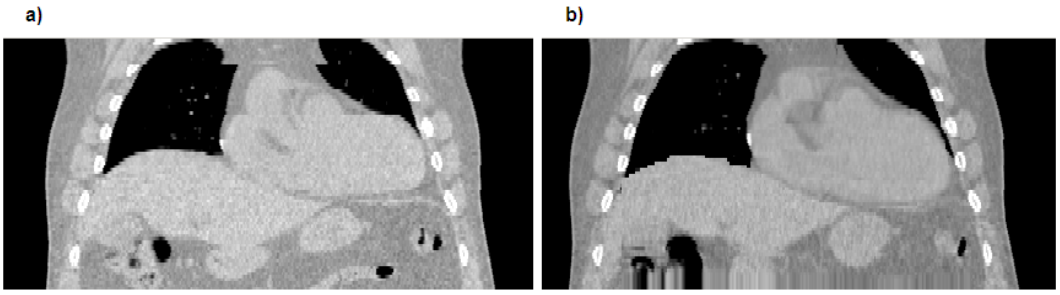

Figure 6.20: A coronal slice through frame 4 (mid-inhale) of the dataset of patient 2. a) The original CT frame and b) the transformed CT frame. An artefact affecting the superior portion of the heart can be seen in the original CT, which is not present in the transformed CT.

The importance of diaphragm matching is further highlighted in the difference between the datasets involving diaphragm matching and those that do not. The methods that incorporated the diaphragm shape model exhibited lower levels of error compared with the thorax transformation alone, and the more accurate diaphragm description obtained from the all-patient shape model produced the lowest errors in both cases. It was found that the reduction in SSD of the masked ACFs were 64 % and 56 % when the diaphragm shape model was used in addition to the thorax transformation for patients 1 and 2. These values were obtained using the leave-one-out model results and hence represent the performance of the model in its current form. Use of the all-patient model results produced reductions in SSD of 70 % and 73 % for the two patient datasets.

The differences in SSD between the inhale CT and the transformed frames with respect to the original CT were found to be 68 % for both patients when the leave-one-out model was used and 74 % and 81 % for patients 1 and 2 with use of the all-patient model. These represent the overall improvements in the ACFs of the transformed CT compared to no transformation and hence relate to improvements in both the estimated heart and the diaphragm positions. It appears from the comparison of these figures with those given in relation to introducing the abdomen transformation, that the majority of the benefit was obtained from the diaphragm transformation rather than the heart transformation, due to the similarity of the figures produced. However, as already mentioned, the thorax transformation would likely have worsened the diaphragm mismatch due to the application of the heart transformation parameters, which would have heightened the impact of the abdomen transformation. In the inhale CT case, although the diaphragm position would have been incorrect in most of the frames, the absence of any transformation meant that diaphragm mismatches were not worsened by an inappropriate transformation. While this does not allow an assessment of the relative importance of the heart and diaphragm transformations on the accuracy of the ACFs, it does indicate that both are important.

6.7 Discussion

By viewing the animations of the transformed datasets using the 3 region method (as shown in Appendix B, parts B.4.1 to B.4.4), it can be seen that a good representation of the original gated CT dataset has been obtained. For both patients, the transformations between frames appear to be a realistic representation of the effect of respiratory motion on a CT dataset, with fairly smooth motions occurring between each frame. Differences can be seen in some frames, particularly where the leave-one-out shape model, which was already known to provide a less accurate description of the diaphragm than the all-patient model, was used to transform the abdomen.

The methods of defining, transforming and recombining the regions also appear to have been successful, with no obvious discontinuities between regions and very few regions affected by region mis-assignments. The methods of segmenting the thoracic cavity were optimised at the level of the heart to ensure a good coverage in this region, however some errors in the definition of the segmented volume were present in the superior portion of the lungs, as seen in Figure 6.12. This occurred when the region defining the thoracic cavity extended too far in the superior direction, however since this is distant to the heart, these errors would not affect its appearance in the attenuation-corrected images and hence were not considered to be problematic.

By assessing the differences between the transformed volumes and the original gated CT frames, it was confirmed that the transformations improved matching with the original gated CT frames beyond that possible for a single CT. This was assessed through calculation of the SSDs of the CT volumes as well as the ACFs, which enabled comparisons between the different transformation methods to be performed. From these comparisons it was seen that accurate transformations of all structures that share projections with the heart are required to achieve the best results.

The impact of an CT-based error on the ACFs of the heart is dependent on the difference in the attenuation path caused by the error and the number of projections that traverse both the affected region and the heart. Therefore an error in the estimated heart position will produce the largest effect, since this will affect the largest number of projections. The impact of errors in other regions will be less, due to the increased distance from the heart, however the high level of attenuation associated with the liver and its close proximity to the heart means that significant errors could result from inaccuracies in its estimated position. While the contributions from individual sources were not quantified, it was seen that substantial increases in ACF error resulted from these structures being positioned incorrectly. This is consistent with the findings relating to attenuation mismatches described in Chapter 3, where heart and diaphragm mismatches between emission and transmission images during attenuation-correction were found to produce the largest errors in the reconstructed emission images.

It was also found in the attenuation mismatches work that the mismatches caused by chest-wall motion were less important and could therefore be ignored. The results obtained here indicate that this assumption is valid, provided that the chest-wall motion does not introduce large changes in the attenuation path-lengths of projections traversing the heart. The errors in the heart ACFs of the transformations involving 2 regions were found to be substantially larger than those involving 3 regions, which were attributable to the different transformations of the chest-wall (according to the heart transformation parameters in the 2 region approach and with no transformation in the 3 region approach). Therefore, although motions of the chest-wall during normal breathing may not be problematic for the heart ACFs, the unrealistic transformations of the 2 region approach were found to degrade the ACF accuracies indicating that consideration of the chest-wall is important. The approximation of the chest-wall being static appeared to be valid from inspection of the original gated CT frames, as well as from the reductions in SSDs obtained from changing from the 2 region to the 3 region methods.

The presence of a motion artefact in one of the frames of the gated CT study of patient 2 highlighted the difficulties associated with obtaining artefact-free gated images, which is one of the primary reasons for developing an approach requiring only a single CT frame. In the frame containing the artefact, it is possible that the transformed CT was a better representation of the true attenuation map at that respiratory phase than the frame of the gated study. This is difficult to verify however, due to the lack of an alternative measure of ground-truth. Additionally, the datasets involving motion artefacts that were excluded from this study (as described in Section 5.4.2.2 on page 154 and illustrated in Figure 5.11) would also likely be improved by the techniques developed here, but this was not assessed, again, due to the difficulties in validating the results obtained.

Having obtained the transformed CTs and performed a comparative assessment of the success achieved with different methods, it was then necessary to use these transformed datasets in the attenuation-correction of gated PET images, to ascertain the impact of the accuracies achieved. This is addressed in the following chapter, where the transformed maps obtained here are used in the attenuation-correction of the PET images, with subsequent reconstruction and motion-correction.

6.8 Conclusions

Methods have been developed for transforming a single CT such that it could represent other respiratory positions and hence enable a respiratory-matched attenuation-correction to be performed on gated PET images. The information used to derive the transformations was based on the results of diaphragm shape model fitting described in Chapter 5, and the results of a rigid-registration performed on the heart activity in the PET frames. These

motion estimates, in combination with the methods developed to transform the CT were found to be successful at obtaining a synthetic gated CT series, and images with realistic appearances were produced.

The accurate transformation of all structures that shared projections with the heart were found to be important, including the heart itself, the diaphragm and the chest-wall. Consequently, errors in the appearance of these structures in the derived attenuation maps will affect the correction factors that are applied to the emission projections during attenuation-correction. The incorrectly scaled emission projections could then result in artefacts in the reconstructed activity, which was observed in the attenuation-mismatches investigation described in Chapter 3. The impact of the transformations obtained here is assessed in the following chapter.

Chapter 7

Motion Correction

7.1 Introduction

The overall aim of this project was to correct for respiratory motion in cardiac PET images in order to obtain quantitatively accurate images of myocardial uptake that were free from motion effects. The previous chapters investigate potential approaches of achieving this and predominantly concentrate on overcoming the issues associated with attenuation-correction. Having developed methods for generating synthetic attenuation maps for correcting gated PET images, which is described in Chapter 6, it was then possible to perform the attenuation-correction and reconstruct the PET frames, both of which needed to be performed prior to motion-correction.

This chapter outlines these final stages in producing the attenuation-corrected PET images and the methods of aligning them to correct for motion. As described in the previous chapter, the motion of the heart was considered to be rigid-body in nature, enabling it to be described with only translations and rotations. These parameters were already obtained in the generation of respiratory-matched attenuation maps (see Section 6.2.2) and hence performing motion-correction simply involved applying these parameters to the frames of the PET study so that they were aligned to a chosen reference frame. This was performed on the two gated PET studies that were used in previous investigations.

Following motion-correction, assessments of the influence of both the attenuation-correction strategy and the motion-correction methods were required to validate the overall approach. These were performed by measuring the apparent width of the myocardial wall with the use of profiles to determine the effect of the motion-correction, and by assessing the distributions of myocardial activity to ascertain the effects of attenuation-correction. These were compared against the "gold-standard" method of attenuation-correction, which was with the gated

CT frames. Additionally, comparisons were performed with the results obtained from not performing a respiratory-matched attenuation-correction (by using only the inhale frame of the gated CT set) and those obtained by only considering the matching of the heart and not of the diaphragm. The differences between these maps and the original gated CT frames were already assessed (see Section 6.6) and although these directly relate to the scaling of the emission projections, predicting the consequent effect of emission projections errors on the reconstructed image is not straight-forward. The attenuation-correction and reconstruction of the PET data were therefore needed in order to determine the impact of the varying attenuation map accuracies. By comparing the results obtained using each of the attenuation maps, the benefit of using the synthetic CT frames against these other scenarios was evaluated.

7.2 Obtaining Reconstructed PET Images

Prior to reconstruction, attenuation-correction was performed on every frame of the two gated PET studies. This was repeated with different attenuation maps to enable the synthetic CT map results to be compared against the results from using conventional techniques. As with previous assessments, synthetic CT maps were generated using two different diaphragm models, so as to obtain two measures of success; the leave-one-out models, to provide a measure of the success of the technique as currently implemented, and the all-patient model, to indicate the upper limit of performance that could be achieved with this overall approach. These relate to the 3 region, leave-one-out and all-patient CT transformations described in Chapter 6, in which the diaphragm shape model results were both obtained through use of a combined PETCT landmark set and through the fitting of 5 modes of variation.

The gold-standard method against which other results were compared involved performing attenuation-correction using the gated CT frames, on the assumption that the PET and CT frames were acquired at corresponding respiratory positions. Obtaining similar results with the synthetic CT maps to those achieved through use of the gated CT frames would therefore indicate the success of the developed technique. The effect of not performing a respiratory-matched attenuation-correction was also investigated, by attenuation-correcting all PET frames with the end-inhale CT frame, which will be referred to as the "inhale" attenuation map. Finally, a "heart-matched" attenuation-correction was also performed, by transforming the entire CT according to the heart registration results (the "thorax only" CT dataset in Chapter 6). In this case, the matching of the heart was considered, but that of surrounding structures was not. This has similarities to a technique currently used in the clinical setting (described in Section 3.4), where a translation of the entire volume is applied

to achieve matching of the heart between the PET and CT images. Unlike the approach used here however, rotations are not included in the clinical application.

Following attenuation-correction, each set of corrected PET frames were reconstructed on the GE Advantage Workstation using OSEM with 2 iterations and 28 subsets, as described in Section 5.4.2.2. Slices of 128×128 pixels of $5.47\,\text{mm} \times 5.47\,\text{mm}$ were produced, with a slice thickness of 3.27 mm, as per the non-attenuation-corrected frames. Therefore for each patient, 5 sets of reconstructed frames were produced, which differed only in their attenuation-correction.

7.3 Performing Motion-Correction

The correction for respiratory motion was performed on the reconstructed PET frames by transforming the PET volumes according to the registration parameters described in Section 6.2.2 and illustrated in Figure 6.3. This transformation would not be appropriate for correcting the motion of other structures that exhibit a different motion to that of the heart, however it is only the appearance of the heart that is of diagnostic interest in the final motion-corrected image and hence this global transformation is appropriate.

The parameters obtained previously included 3 translations and 3 rotations that related each respiratory frame to the end-inhale frame. This frame was selected as the reference frame to which the other frames were matched for the purposes of transforming the CT frame to other respiratory phases, since the transformation was easier to perform within the larger thoracic cavity at end-inhale. The choice of reference frame for PET alignment is arbitrary, but as the parameters had already been obtained for the end-inhale frame, these same parameters were used here.

Following alignment, all frames were summed so as to recover the count statistics that would be present in a non-gated study and hence obtain an image with higher signal-to-noise ratio than in the individual gated frames. This motion-correction and summing represent the final stages in the overall process and hence, if successful, the images produced from these processes should be quantitatively accurate and free from the blurring effects present in respiratory-averaged images.

7.4 Assessment of the Motion-Free PET Images

Measures were obtained from the motion-corrected PET images in order to assess the success of both the attenuation- and motion-corrections. These two correction types have different effects on the appearance of the left-ventricular myocardium, with the motion-correction resulting in a change in the apparent width of the myocardium in the direction of motion

and the attenuation-correction potentially altering the reconstructed distribution of activity within the myocardium. Therefore different methods were used to evaluate both of these aspects, which are described in the following sections.

7.4.1 Assessing the Results of Motion-Correction

The effect of the motion-correction on the PET images was evaluated by assessing the form of profiles plotted through the myocardial activity. The profiles were plotted in three orthogonal directions (superior–inferior, anterior–posterior and left–right) through the centre of the left ventricle of the summed, motion-corrected image. Although five sets of motion-corrected images were generated for each patient, this analysis was only performed on the image generated with the all-patient shape model, since the same parameters were applied to all sets and would not therefore be expected to differ in terms of the motion-correction success. The profiles were also plotted in the summed image that had not been corrected for motion, to provide a baseline measure against which to compare the motion-corrected results. The width of the myocardium in each profile was calculated by measuring the FWHM of the peaks in intensity seen in the profiles. Since all profiles intersected the myocardium twice, two measurements were obtained in each case. It was expected that the motion-corrected images would exhibit a narrower apparent myocardial width than in the motion-averaged images and hence the decrease in the FWHM was used to evaluate the effect of the correction.

The superior–inferior profile was expected to produce the clearest measure of the benefits of motion-correction, since this is the direction in which respiratory motion is most prominent. The other profiles were plotted to ascertain whether improvements had also been achieved in these directions and to ensure that no deterioration in the myocardial appearance had arisen. Since the motion-correction was performed on clinical studies, it was not possible to obtain a ground-truth measure of the myocardial width. Consequently, the observation of a decrease in apparent width as a result of the motion-correction was used to infer a successful correction, but it was not possible to assess whether the effects of motion had been fully overcome.

7.4.2 Assessing the Success of Attenuation-Correction

As outlined in Section 7.2, five sets of motion-corrected images were obtained for both patients, corresponding with the five sets of attenuation maps generated. Therefore a comparison between these sets was necessary to determine the impact of the attenuation-corrections on the reconstructed PET images. One commonly used method of comparing the appearance of the left ventricle in different datasets is to produce polar plots of the activity, as performed for the NCAT datasets described in Chapter 3 (see Figures 3.4 and 3.5). This

enables a visual assessment of the entire left-ventricular activity to be performed as well as a semi-quantitative comparison of different datasets via the use of segmental scores. The PET datasets to be assessed were therefore reoriented to produce short-axis slices, from which polar plots were produced using the "Myovation" software (GE Healthcare, Haifa, Israel). The polar plot is generated by the software by automatically segmenting the left-ventricular activity in the short axis slices and reformatting the segmented volume to display it in polar form. Segmental values (in the formation shown in Figure 2.4 on page 33) are calculated to represent the average value in the segment in relation to the maximum value observed over the left-ventricular myocardium. These values are therefore not related to the absolute values obtained in the myocardium, but provide a means of assessing relative uptakes in different regions of the myocardium.

It should be noted that the datasets assessed here were not acquired according to a cardiac protocol and hence the appearance of the heart is likely to be different to that in a true cardiac study. It was found that both patient datasets exhibited highly non-uniform uptakes of ^{18}F-FDG, which is not necessarily related to poor cardiac function, but was likely instead to have arisen from the protocol adopted, which was optimised for oncology imaging. The datasets used in this investigation were chosen because they exhibited some cardiac uptake, although the steps taken to limit the uptake may have led to the high levels of variation across the left-ventricular myocardium. This high degree of non-uniformity was found to be problematic in the automatic segmentation required in the polar plot generation and therefore discrepancies between the datasets in terms of the extent of the region included by the segmentation arose.

This is described in more detail in Section 7.5.2, but these difficulties meant that comparing the scores of the 17 segments for these datasets would not have produced meaningful results with this approach. Therefore, the polar plots were generated, but were assessed visually, without analysis of the segmental scores. Instead, the SSD between each of the datasets and the gold-standard dataset (that corrected for attenuation with the original gated CT frames) was calculated, to enable a quantitative comparison of the datasets. In obtaining a polar plot, the absolute values of uptake are not considered and hence this only permits semi-quantitative comparisons between the activity distributions in the different datasets. Measures of the SSD however allow direct comparisons of the actual voxel values, which therefore include the regional differences in activity as well as differences in absolute value, the latter of which would not be measured with the polar plot segmental scores. The disadvantage of SSD calculations is that they do not permit an evaluation of the qualitative changes in the left-ventricular appearance, which is currently used in the clinic when forming a diagnosis. The aim here however was also to evaluate the quantitative accuracy of the datasets obtained and therefore the SSD calculations represented a more appropriate method of achieving this. To assess only the accuracy within the left ventricle, areas outside the left ventricle were masked so that they did not contribute to the SSD values.

7.5 Results

7.5.1 Assessing the Results of Motion-Correction

The results of plotting profiles through the motion-averaged and motion-corrected images are summarised in Tables 7.1 and 7.2 and the superior–inferior profiles for both patients are shown in Figures 7.1 and 7.2.

	Measurement 1			Measurement 2		
Profile Direction	Motion-averaged FWHM	Motion-corrected FWHM	Difference	Motion-averaged FWHM	Motion-corrected FWHM	Difference
Left–right	2.4 pixels	2.6 pixels	0.2 pixels (1.1 mm)	2.0 pixels	2.2 pixels	0.2 pixels (1.1 mm)
Anterior–posterior	4.6 pixels	4.5 pixels	-0.1 pixels (-0.5 mm)	4.4 pixels	4.3 pixels	-0.1 pixels (-0.5 mm)
Superior–inferior	6.0 pixels	5.7 pixels	-0.3 pixels (-1.6 mm)	5.0 pixels	4.6 pixels	-0.4 pixels (-2.2 mm)

Table 7.1: The FWHM of the left-ventricular myocardial activity, as measured from profiles plotted in 3 orthogonal directions in the motion-averaged and motion-corrected images of patient 1. The two measurements correspond with the two intersections of the myocardium with each profile. A negative difference in FWHM corresponds with a lower motion-corrected FWHM compared with the motion-averaged value.

	Measurement 1			Measurement 2		
Profile Direction	Motion-averaged FWHM	Motion-corrected FWHM	Difference	Motion-averaged FWHM	Motion-corrected FWHM	Difference
Left–right	4.1 pixels	3.9 pixels	-0.2 pixels (-1.1 mm)	2.7 pixels	2.7 pixels	0.0 pixels (0.0 mm)
Anterior–posterior	5.3 pixels	5.0 pixels	-0.3 pixels (-1.6 mm)	4.5 pixels	4.4 pixels	-0.1 pixels (-0.5 mm)
Superior–inferior	8.0 pixels	6.3 pixels	-1.7 pixels (-9.3 mm)	5.1 pixels	4.4 pixels	-0.7 pixels (-3.8 mm)

Table 7.2: As for Table 7.1, but for patient 2.

It can be seen in Tables 7.1 and 7.2 that in general, the effect of the motion-correction was to reduce the apparent width of the left-ventricular myocardium, particularly in the superior–inferior direction, as expected. One measurement showed an increase in FWHM: the mean width of the myocardium measured in the left–right direction for patient 1 showed a small increase, but the same patient experienced improvements of a similar magnitude in the other directions. All changes for this patient were modest, which is likely to be a result of a small extent of the respiratory motion experienced by the heart in this case.

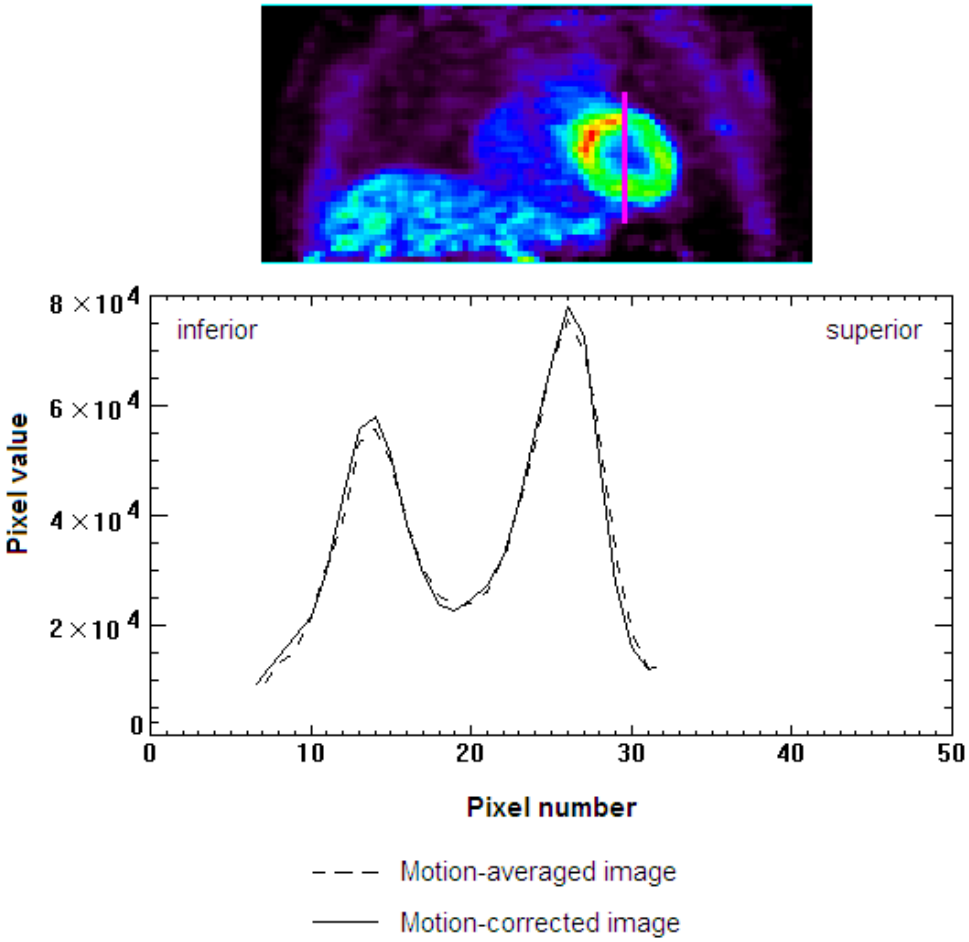

Figure 7.1: The superior–inferior profile through the left-ventricular myocardial activity of patient 1. The position of the profile is indicated by the purple line in the coronal slice and the resulting curves obtained from the motion-averaged and motion-corrected images are shown in the graph.

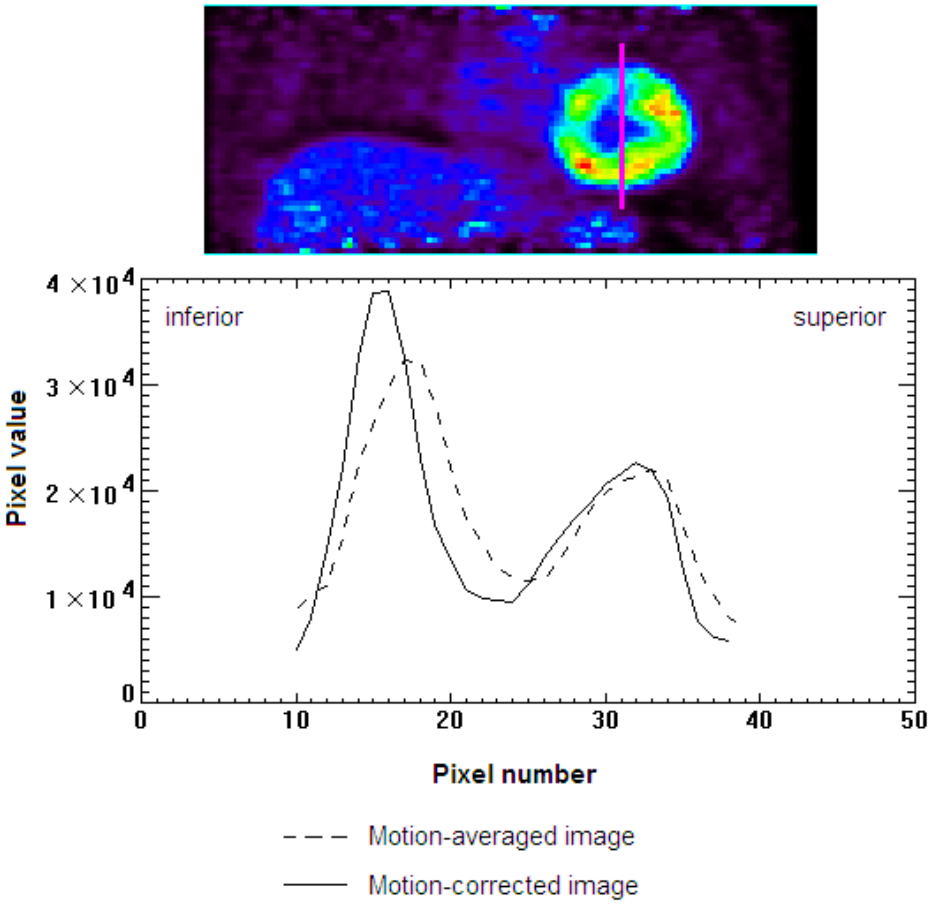

Figure 7.2: The superior–inferior profile through the left-ventricular myocardial activity of patient 2. The position of the profile is indicated by the purple line in the coronal slice and the resulting curves obtained from the motion-averaged and motion-corrected images are shown in the graph.

Patient 2 exhibited greater changes in FWHM, with the largest improvement in the superior–inferior direction. As seen in Figure 6.3, the motion in this direction is greater for this patient, so the corresponding reduction in FWHM again indicates that the motion-correction produced improvements in the appearance of the myocardium.

Both patients also exhibited an increase in the maximum counts observed in the myocardium following motion-correction, as a result of the reduced blurring. The size of the increase in counts followed the same trend as the decrease in FWHM, resulting in small changes for patient 1 (4 % mean increase in the superior–inferior direction) and a larger mean change for patient 2 (21 % and 3 % for the two walls intersected by the profile in the superior–inferior direction). These increases also indicate that some improvement in image quality was obtained through motion-correction. In the absence of a ground-truth measure of the myocardial uptake, it is not possible to confirm that the corrected results are quantitatively accurate, but it can be seen that some improvements have been gained compared with the non-corrected case.

7.5.2 Assessing the Success of Attenuation-Correction

As noted earlier, the generation of the polar plots for both patients was problematic, due to the high degree of non-uniformity exhibited by both patient datasets and the resultant segmentation problems in the short-axis slices. Figure 7.3 illustrates this problem, which shows the automatic segmentation of the short-axis slices and the resultant polar maps for the same dataset (patient 1, attenuation-corrected using the leave-one-out model dataset) when reorientation was repeated. The only difference between these two datasets was therefore in the rotations applied in generating the short-axis slices. Inspection of the activity within the slices indicates that these variations in orientation had a very small effect. Despite this, the resulting segmentation was markedly different, particularly in its determination of the extent of the left ventricle. This can be seen in the appearance of the resulting polar plots from these two sets, where a difference in scaling between the two is apparent as a result of the different coverages. Other small differences can be seen, which can be seen in the appearance of the apex (at the centre of the polar plots) and these factors make a direct comparison between datasets difficult. The segmentation as implemented in the Myovation software is fully automatic and no manual intervention to correct for these segmentation inconsistencies is permitted. As already discussed however, these were used only for visual purposes, and these differences in coverage were taken into account when viewing these polar maps.

The polar maps from each of the 5 datasets generated from the different attenuation-correction maps, as well as the non-attenuation-corrected dataset are shown for both patients in Figure 7.4. The effect of performing an attenuation-correction was very striking in both cases, as seen by the differences between polar maps of the non-attenuation-corrected dataset

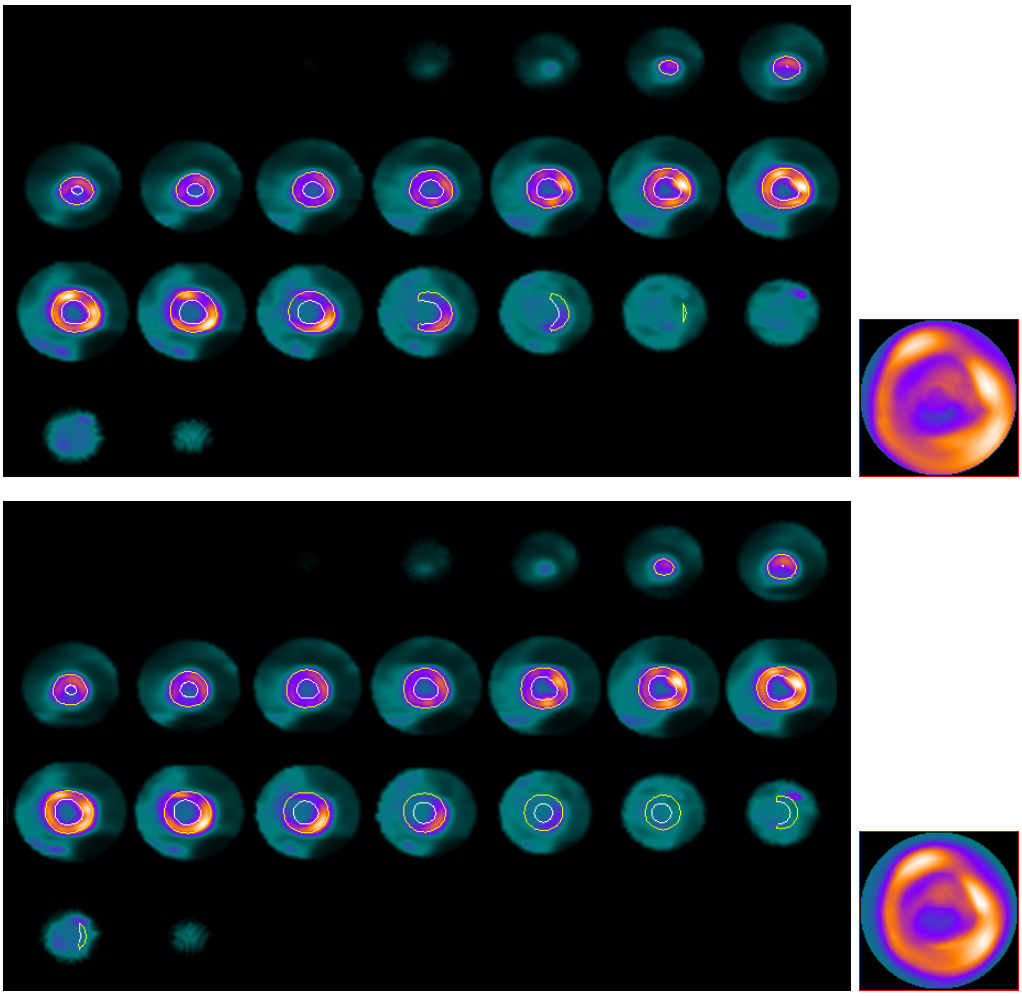

Figure 7.3: The segmented contours overlaid on the short-axis slices and the resulting polar plots. Both sets were produced from the same dataset (patient 1, attenuation-correction using the leave-one-out model dataset), with the reorientation repeated twice. The differences in the segmentations are evident in the polar plots, particularly in the position of the base and in the appearance of the apex.

and the other datasets (all of which included attenuation-correction). The counts in the septal wall in particular (the left hand side of the polar plots) are noticeably enhanced through the attenuation-correction.

The differences between the polar plots generated with the different attenuation-correction maps are less noticeable and difficult to assess in the presence of the segmentation variations already described. The differences observed appear to be of a similar magnitude to those obtained with repeated segmentation attempts (as seen in Figure 7.3) and hence it is difficult to determine whether additional changes also occurred. No obvious differences can be seen, although the segmentation variations could be obscuring more subtle changes. This is true of both patients, where the same general pattern of uptake was observed in all attenuation-corrected images, but some differences were also apparent. Given the similarity of the polar map appearances between the worst-case scenario (attenuation-correcting with the inhale CT) and the gold-standard (use of the gated CT), it is not surprising that the other attenuation-correction strategies could not be visually separated in these displays.

The assessments of the CT transformations of patient 2 (described in Chapter 6) were found to be affected by a motion artefact in the heart in a single frame (frame 4) and hence for this patient, the polar maps of each frame were assessed in addition to the summed images shown in Figure 7.4. It was found that although the polar maps from the individual frames exhibited higher levels of noise, the patterns of uptake were similar in all frames, including that of frame 4. The levels of variation between each frame were similar to those observed between the repeated segmentation attempts, shown in Figure 7.3 and hence any inaccuracies in frame 4 were not expected to contribute noticeably to the appearance of the summed polar maps.

Determining the success of the different attenuation-corrections using the polar plots is difficult, due to the influence of other factors on their appearance. Therefore alternative methods were used to enable a quantitative comparison. For this purpose, the SSD was calculated for each image compared against the dataset corrected for attenuation with the original gated CT. These results are shown for both patients in Figure 7.5, with results for patient 2 shown with and without the inclusion of frame 4.

Unlike the polar map comparisons, clear differences in the SSD results of each dataset can be seen and the same trend is present for both patients. The same pattern was also observed for the SSD results for the transformed CT datasets, indicating that the errors in the CT maps propagated into the PET data through the attenuation-correction. The datasets that incorporated the use of the diaphragm shape models in addition to heart-matching were found to produce the best results and those which ignored the diaphragm and only performed heart-matching or which involved no CT transformation over the respiratory cycle (with the inhale CT attenuation-correction) exhibited larger errors. The same trends were seen with and without frame 4 of patient 2, indicating that the artefact seen in the heart in the original

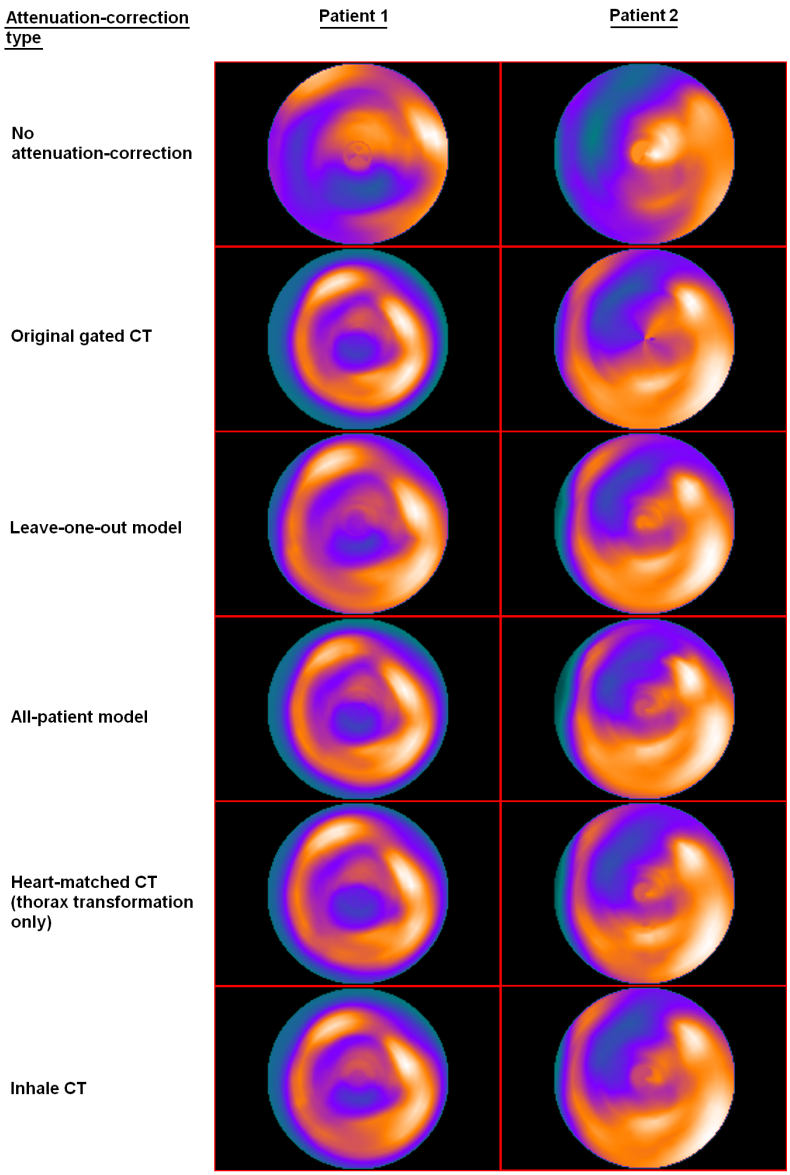

Figure 7.4: Polar plots for patients 1 and 2 for the non-attenuation-corrected dataset and the 5 attenuation-corrected datasets using different attenuation maps.

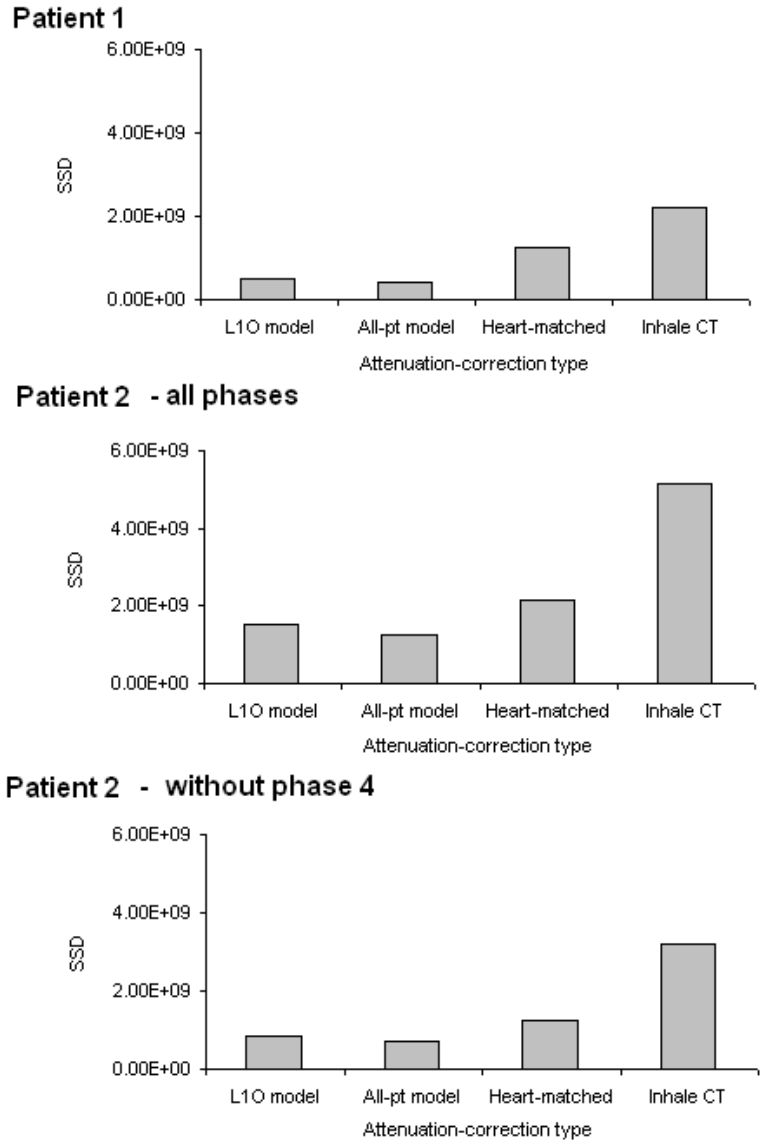

Figure 7.5: The SSDs of the reconstructed heart activities obtained with different attenuation maps compared with the gold-standard (correcting for attenuation using the original gated CT frames). These are shown for patient 1 (top), patient 2 where all phases are considered (middle) and patient 2 where phase 4 is excluded (bottom), due to a motion artefact in the heart. L1O model = use of the leave-one-out shape model to transform the CT dataset, all-pt model = use of the all-patient shape model for CT transformation. The "heart-matched" dataset involved a transformation of the thorax region, but not of the abdomen (i.e. the attenuation-correction was performed using the "thorax only" dataset described in Chapter 6) and the "inhale CT" attenuation-correction involved correcting every PET frame with the end-inhale CT frame.

Attenuation-correction type	Patient 1: error per voxel as % of the mean voxel value	Patient 2: error per voxel as % of the mean voxel value
Leave-one-out model	3.4 %	6.5 %
All-patient model	3.1 %	5.9 %
Heart-matched	5.5 %	7.8 %
Inhale CT	7.4 %	12.0 %

Table 7.3: The error per voxel in the reconstructed PET for each attenuation-correction type and for both patients. The errors are obtained by comparing the voxel values in the datasets listed in the table with those in the dataset corrected for attenuation with the gated CT frames. Only voxels in the left ventricle were considered in these calculations.

CT of this frame did not produce a large effect on the reconstructed activity. As the results did not appear to be adversely affected by its inclusion, subsequent discussion will refer to the results including all phases.

For both patients, the inhale CT produced the largest errors, with decreases in the SSD of 44 % and 58 % observed for patients 1 and 2 when heart-matching was performed. Further decreases were observed when diaphragm matching according to the leave-one-out models was performed in addition to the heart matching, reducing the SSD values to 78 % and 71 % of the inhale CT attenuation-correction error. As observed with previous results, the accuracies obtained through use of the all-patient shape model were higher than with the leave-one-out models, with the SSD for patients 1 and 2 decreasing to 82 % and 76 % of the inhale CT values.

By performing a similar calculation as that described in relation to the landmark accuracies (see Equation 5.9 on page 141) and taking into account the mean activity value, it was possible to convert these SSD values into mean errors as a percentage of the mean activity. These are shown in Table 7.3.

The reductions in error observed from the use of the transformed CT datasets indicate the importance of matching both the heart and the diaphragm positions on the quantitative accuracy of the resulting PET images. As with the attenuation mismatch artefacts described in Chapter 3, the mismatched heart position was found to produce the largest errors and the matching of the diaphragm was also found to be important. The differences between the two model types for diaphragm transformation were measurable in the SSD calculations, but small compared to the effects of not matching the diaphragm or the heart, suggesting that the shape model in its current form was valuable in improving the attenuation-correction accuracy, but small further improvements could be realised with the extension of the training set size, for example.

7.6 Discussion

The results obtained here show the effects of both the motion-correction and attenuation-correction strategies on the accuracy of the results obtained. The motion-correction, in the form of a rigid-body alignment of the respiratory frames, was found to produce only small changes in the dataset of patient 1, but more noticeable effects in the dataset of patient 2. These differences were expected as a result of the larger respiratory motion experienced by patient 2; in Figure 6.3 it can be seen that the z-translation of the heart of patient 2 was approximately double that of patient 1 and hence the blurring effects patient 2 experienced would have been greater. The improvements were seen in terms of both a reduction in the apparent width of the myocardium as well as an increase in the maximum pixel counts observed. Both of these effects are indications of reduced motion effects and hence suggest that the motion-correction was successful. As already discussed however, it is not possible from these measurements to ascertain whether the motion was fully corrected in both cases or whether further improvements could be gained from a different registration strategy, e.g. by increasing the number of parameters used to describe the heart motion. Previous authors have found rigid-body registrations to be appropriate for the heart (Korin et al., 1992; Livieratos et al., 2005). Therefore, by implementing a well-established and well-tested technique for reducing the blurring effects of motion in the heart, it was expected that successful results would be obtained.

The attenuation-correction results obtained showed the trends expected, in terms of the comparative accuracies of the different attenuation maps. Similar trends were observed in the evaluation of each CT set against the original gated CT, indicating that the errors present in the CT maps propagated into the PET datasets through the attenuation-correction process. While this association is not surprising, it had not previously been established how the errors of the CT maps generated would affect the heart activities, particularly where the errors occurred in structures other than the heart. These observations agree with the phantom-based results obtained in Chapter 6, where it was seen that structures that shared projections with the heart could influence the apparent activity within the left-ventricular myocardium through the attenuation-correction process. These same observations have now been demonstrated in clinical data. It is common in clinical practice for only the heart to be considered in the attenuation-correction process, since it is generally assumed that the effects of attenuation mismatch are local. While this local effect has been found to represent the largest contribution towards the overall error in the attenuation-corrected PET data, these results have also demonstrated that matching of the diaphragm position in addition to the heart also provides improvements in quantitative accuracy.

Despite the measured changes in the reconstructed values in the heart in the PET studies, little impact on the polar map appearances was observed, except in the scenario that no attenuation-correction was performed. An explanation for this is in the extent of mismatch

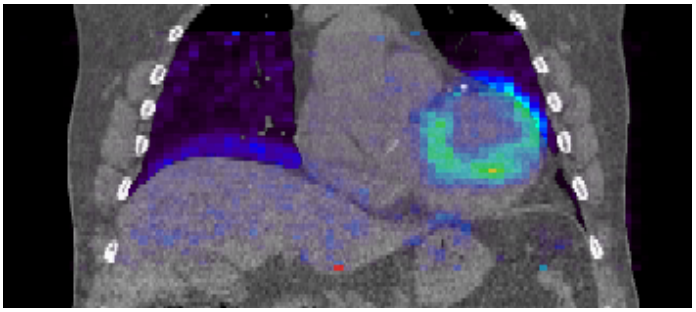

Figure 7.6: A coronal slice through the end-inhale frame of the CT dataset for patient 2, fused with the end-exhale PET frame for the same patient, demonstrating the maximum level of mismatch through use of the end-inhale CT for attenuation-correction. In this case the PET has been corrected for attenuation with the matched CT frame.

that occurred in the patient datasets through the respiratory cycle; Figure 7.6 shows a coronal slice through the dataset of patient 2, with the end-exhale PET frame fused with the end-inhale CT. While there is a noticeable mismatch between the two datasets, this has only resulted in a modest overlap of heart with lung tissue. Gould et al. (2007) found that a transaxial mismatch of > 6 mm as measured from the difference in the heart border between PET and CT, was found to be predictive of heart-mismatch artefact. The respiratory motion in the transaxial direction of patient 2 was found to be of approximately this magnitude (as seen in Figure 6.3), and hence possibly below the level at which artefacts arise. Furthermore, the frames shown in Figure 7.6 represent the maximum mismatch observed over the respiratory cycle and other frames would therefore be affected to a lesser extent. Since the polar map includes contributions from all respiratory frames, the reasons for the limited impact of mismatch on the polar maps for this patient become apparent. The respiratory motions of patient 1 were even smaller than that of patient 2 and hence the extent of mismatch was also smaller and it is not surprising therefore that visible defects were not noted in this patient either.

The 6 mm threshold for the production of visible artefacts found by Gould et al. (2007) was observed in respiratory-averaged data, which could correspond with a greater maximum mismatch if individual respiratory frames were assessed. Gould et al. (2007) also found that approximately 40 % of clinical cases were found to suffer from artefacts caused by such mismatches and hence the absence of a visible artefact in the two datasets assessed here is not contradictory to these observations. A much larger number of patients would need to be assessed to obtain an estimate of the prevalence of visibly noticeable artefacts to compare with the published figures.

The absence of a visible impact of mismatch however does not mean that all datasets had equal quantitative accuracy, as determined by the SSD results performed on the left ventricle voxels of the reconstructed PET images. These measures were free from the processing

variations to which the polar plots were subject and enabled direct quantitative comparisons of the absolute values within the left-ventricular myocardium. They were therefore able to detect differences between the datasets that could not be determined from the polar plots and hence uncovered trends regarding the comparative successes of the different attenuation-correction techniques that were not otherwise obtainable. While these differences would not have been clinically important where the diagnosis is formed on the basis of visual assessment alone, the improved accuracy of the datasets involving both heart and diaphragm matching would be important in the scenario that a quantitative measurement is required. This could be the case in the research setting, e.g. where the uptakes of different tracers in the myocardium need to be compared, or where quantitative measures of change are required in serial studies. Furthermore, the ability to produce images with an improved quantitative accuracy could lead to increased interest in such measurements in routine clinical studies to further aid the diagnostic process. It would also be expected that if the same trends obtained here were also achieved in a patient with large respiratory motions, the presence of visible artefacts in the polar plots should be overcome with the use of the transformed CTs considering both heart and diaphragm matching. While a larger number of patient datasets would need to be evaluated to estimate the general applicability of the techniques developed here, the quantitative improvements observed in both patients are promising and suggest that benefits could be obtained from their use in a large number of patients.

The required accuracy of the reconstructed activity distribution would depend on the application for which the measurement is intended. It should be noted however that the accuracy measurements were obtained using the assumption that the dataset corrected for attenuation with the original gated CT provided the correct result. This is only true if the gated PET and CT frames are perfectly matched and hence any deviation from this scenario would affect the accuracy measurements of other datasets. Therefore the figures obtained here could be overestimates of the true error associated with the transformed CT techniques if any PET–CT mismatch is present. This is also discussed in relation to the measures of diaphragm error obtained from model fitting, in Sections 5.4.4.3 and 5.4.5.3.

In assessing the results obtained with the transformed datasets, consideration of the dose associated with the technique should be given. As discussed in Section 5.1, one of the primary motivations in developing methods for transforming a single CT over the respiratory cycle were the dose issues. For the datasets investigated here, the dose associated with the transformed CT method is a factor of 6 lower than the gated CT equivalent and therefore a small compromise in quantitative accuracy may be acceptable in order to achieve this large dose reduction. In comparison to methods currently used in the clinic, where a motion-averaged PET study is corrected for attenuation with a single CT, the techniques developed here facilitate a respiratory-matched attenuation-correction, with improved quantitative accuracy and with no increase in dose.

7.7 Conclusions

The benefits of performing motion-correction with the incorporation of a respiratory-matched attenuation-correction were demonstrated here, by applying the techniques developed throughout the previous chapters to two patient datasets. Large respiratory motions were not measured for either patient and hence reductions in blurring were modest, however measurable reductions in apparent myocardial wall width were obtained in the superior–inferior direction for both patients. This reduction corresponded to an increase in the count density in the same region, also associated with reduced levels of blurring. This indicated that some improvements to image quality were realised through the use of a rigid-registration on the left-ventricular myocardial activity, however it was not established whether further improvements in these respects could be achieved through the use of alternative registration techniques.

The motion-correction benefits were considered separately from the effects of attenuation-correction, which is also an important consideration in maintaining quantitative accuracy during motion-correction. Attenuation mismatches have previously been found to produce apparent changes in the regional uptakes of the myocardium, which are measurable through the use of the segmental score comparisons obtained from left ventricle polar plots. Published results obtained from Gould et al. (2007) however, indicated that small respiratory motions did not affect the appearance of the polar plots, which was the case for both of the patient datasets investigated here.

Variations in quantitative accuracy between datasets that were not depicted in the polar plots could however be measured, through the use of SSD measurements. Therefore, although obvious artefacts were not produced, variations in error between the different attenuation-correction approaches were measured, enabling a comparison between the datasets. A consistent trend was observed in the two patient datasets, where the attenuation-correction with the inhale CT frame produced the largest errors and improvements were observed with the inclusion of both heart and diaphragm matching, with heart matching providing the largest improvement. Some residual errors remained, even when heart and diaphragm positions were both matched and whether these are tolerable depends upon the application for which measurements are required. In some scenarios, small levels of error may be considered acceptable when considering the large benefits in terms of the dose reduction these methods are able to provide. Other methods requiring only a single CT acquisition (and therefore involve equivalent doses to the methods developed here), were found to produce inferior results to the transformed CT methods, even where matching of the heart was considered and hence a clear benefit of the overall approach of CT transformation was demonstrated.

Chapter 8

Conclusions

8.1 Summary and Conclusions

The work in this thesis has concentrated on developing methods for enabling quantitatively accurate motion-corrected cardiac PET images to be obtained. While methods of splitting the acquired cardiac PET data into motion-limited frames and subsequently aligning them have already been implemented by a number of authors (Klein et al., 2001b; Bruyant et al., 2002; Livieratos et al., 2005; Kovalski et al., 2007; Dawood et al., 2008b), the effects of attenuation have not previously received as much attention, despite it being an important correction in obtaining quantitative images. Many of the motion-related issues regarding attenuation-correction are ongoing and hence the focus of this work was predominantly in the development of methods to overcome these problems, with their subsequent incorporation into an overall strategy for motion-correction.

A summary of the chapters of this thesis and the main conclusions drawn from each are given in the following sections.

Chapter 3: Characterisation of Attenuation Artefacts in Cardiac PET-CT and SPECT-CT

The first stage of the project work was to ascertain how mismatches between PET and CT due to respiratory motion affect the appearance of cardiac PET images, when the CT is used for attenuation-correction. This information was required so that subsequent investigations regarding the development of an attenuation-correction approach could be directed towards correcting the mismatches that are important for cardiac images. Using NCAT generated activity and attenuation maps, a PET acquisition was simulated, with the incorporation

of an attenuation-correction at a mismatched respiratory position. This was repeated for SPECT, since this is also used routinely for myocardial perfusion imaging and a direct comparison between the generation of attenuation-correction artefacts between PET and SPECT had not previously been undertaken.

It was seen that severe artefacts arose when mismatches in either the heart or the diaphragm positions occurred. An effect was also seen with a mismatch in the lung tissue as a result of diaphragm contraction, although this was small in comparison to the heart and diaphragm effects. Similar trends were seen in both PET and SPECT, in terms of the causes and the locations of artefacts, although, as expected, SPECT images were affected to a lesser, but still significant, extent.

Although it had been expected that a mismatch in the heart position would be responsible for producing artefacts, it was found that the effect of a diaphragm mismatch on the reconstructed activity distribution could also be severe. Current methods of addressing PET–CT mismatches used in the clinical setting are based on applying a global translation to match the heart position and do not give any consideration to the diaphragm, which could result in attenuation mismatch artefacts not being fully resolved. The focus of the investigations performed throughout the remainder of this project was therefore in developing methods of achieving heart and diaphragm matching between PET and CT, such that quantitative accuracy could be achieved once the subsequent motion-correction had been performed. Previous findings on the extent of artefact had been published, however these did not report on the individual contributions from each mismatch type and hence the relative importance of the mismatches had not been measured. These findings are also described in the journal paper listed in Appendix A.2.

Chapter 4: Diaphragm Segmentation and Tracking

Taking into account the results from Chapter 3, an approach was proposed that involved transforming a single CT over the respiratory cycle, where consideration would be given to the matching of both the heart and the diaphragm positions. Therefore only a single CT was needed and CT frames at other respiratory positions were generated in a data-driven manner for the subsequent respiratory-matched attenuation-correction. This has advantages in terms of the dose associated with this type of CT acquisition, as well as in reducing the presence of PET–CT mismatches and their associated artefacts.

For this reason, a method of segmenting the diaphragm in CT images was needed, so that its shape and motion over the respiratory cycle could be investigated in more detail. Edge-detection was used as a basis for a diaphragm segmentation algorithm and features in the edge-enhanced image were tracked, with the incorporation of suitable constraints, to generate a diaphragm surface. Although manual input was required in some instances, a good level

of accuracy was achieved and the time required to perform the segmentation was acceptable for this scenario. Very few other algorithms for diaphragm segmentation in CT images have been developed and the accuracy achieved here compared favourably with that of a recently published algorithm, based on thin-plate splines (Zhou et al., 2008). The algorithm developed therefore provides a valuable tool for accurate diaphragm segmentation, which could be extended to increase the level of automation.

An initial investigation performed using the segmented diaphragm surfaces involved tracking its motion over the respiratory cycle and comparing the measured motions with those previously obtained for the heart in the same set of patients. This is also described in the paper detailed in Appendix A.1. Although this study showed the presence of some interaction between the heart and diaphragm motions (leading to correlations in some motion parameters), it also highlighted the large level of variation present between patients, as seen by the absence of correlation in many of the parameters. Consequently, it was determined that the methods of determining the diaphragm motion for subsequent CT transformation needed to take into account these large patient variabilities observed.

Chapter 5: The Construction and Testing of a Statistical Shape Model of the Diaphragm

A Statistical Shape Model (SSM) of the diaphragm was constructed to complement the information obtainable from gated PET images and thereby enable diaphragm shape and motion to be determined. It was constructed by placing landmarks in a regular grid pattern over the segmented diaphragm surfaces in all respiratory frames and performing Principal Component Analysis on the relative landmark positions. Determining how well it could describe diaphragm shapes and motions involved fitting the model to previously unseen diaphragm surfaces and measuring the residual errors of the fitted surfaces. These errors were found to vary between patients, which can be explained by the presence of diaphragm shapes or motions that are different to those encountered in the training set. This is a particular problem associated with SSMs with small training sets, particularly where the level of variation across the population is large, which is true of the diaphragm. Rather than being a fundamental limit of this approach, reductions in the residual errors would be expected if the training set were to be expanded. However, a good level of accuracy was achieved in a number of patient datasets, despite the small training set.

Further tests were then performed to ascertain how well the model would perform in the presence of missing data and with inaccuracies in landmark position estimates to which the model is to be fitted, both of which occur with gated PET data. Initial estimates of the diaphragm position from PET were used as input into the model, with the aim of obtaining improved estimates and filling gaps with model fitting. It was found that when the landmarks obtained from PET were used to drive the model fitting, the resulting surfaces

provided a poor description of the true diaphragm surfaces and results were found to be highly unstable. To overcome this, a single CT frame was incorporated into model fitting, which not only increased the total number of landmarks used for input to the model but also allowed the inclusion of accurately defined landmarks, unlike those obtained from PET. These factors improved the accuracy of the model output, with errors returning to levels comparable with the baseline of CT landmark fitting. This combined PETCT landmark set therefore represented a suitable method of fitting the diaphragm SSM, where the results were not greatly affected by gaps or misplaced landmarks in the PET frames.

Although shape models are in widespread use, at the time of undertaking this investigation, no examples of shape models being applied to emission studies were found in the published literature. Tobon-Gomez et al. (2008) have recently described their work relating to the application of a CT-based shape model to left-ventricular segmentation in SPECT images, but different considerations are required for this application compared with a shape model for diaphragm tracking. The construction of the model and testing on CT-derived data is described in Appendix A.3 and its application to PET in Appendix A.4.

Chapter 6: Transforming a CT to Different Respiratory States

It was then necessary to use the diaphragm shape and motion information, in combination with knowledge of the heart motion, to transform the single CT to other respiratory positions. The diaphragm shape model results were used to transform the abdomen volume, where columns of voxels were shifted to match each model surface. The motion of the heart was treated separately, where the results of a rigid-registration on the myocardial activity were applied to the thoracic cavity. Methods of separating the thoracic cavity from the chest-wall were developed in order to apply this transformation to the desired region, which involved a combination of region growing in the lungs, ray-tracing using the segmented rib-cage and a series of erosion and dilation operations to obtain the required coverage of the segmented region.

The success of the transformation method was measured by comparing the transformed CT frames with the original frames of the gated CT. Firstly, the effect of not transforming the CT was measured with the use of only the end-inhale frame, which unsurprisingly was found to result in high levels of error. These were reduced when heart-matching was performed, by applying the heart registration parameters to the whole volume, and further reductions were obtained with the incorporation of diaphragm matching. This indicated that some of the emission projections that traverse the heart are incorrectly scaled when mismatches in the diaphragm position occur, which could therefore affect the quantitative accuracy of the reconstructed PET images. It is important therefore to take diaphragm motion into account during the attenuation-correction process.

While other authors are also currently investigating CT transformations to enable respiratory-matched attenuation-correction (Dawood et al., 2008b), unlike other investigations, the approach described here was developed specifically for cardiac studies and therefore ensured correct transformation of the relevant structures for this type of study, rather than the more general approach of whole thorax corrections.

Chapter 7: Motion Correction

The final stages of the overall process were the application of the respiratory-matched attenuation-correction, the reconstruction of each PET frame and their subsequent alignment according to the rigid-registration parameters already obtained.

Inspection of profiles traversing the myocardium in orthogonal directions indicated that reductions in the apparent width of the myocardium in the superior–inferior direction were achieved through the use of the rigid-registration on the gated PET frames, although the improvements were marginal in the case that respiratory motion was small. A corresponding increase in the count densities was also observed, which, like the apparent widths, was more noticeable for the patient exhibiting a larger degree of motion. Both of these measures indicated the presence of some improvement in image quality associated with reduced motion-blurring.

Large respiratory motions were not observed in either patient, which was found to prevent the occurrence of a visibly detectable artefact in the polar maps of left-ventricular myocardium in both cases, even when the end-inhale CT frame was used for attenuation-correction. Quantitative differences were observed however, by assessing the differences in the left ventricle between the dataset involving the transformed attenuation map and that involving the original gated CT frames for attenuation-correction. The same trends were observed as for the transformed CT assessments; the dataset corrected with the inhale CT exhibited the largest errors, heart-matching during attenuation-correction reduced these errors and further improvements were seen when diaphragm-matching was also performed. These observations agree with the findings of Chapter 3, where it was seen that errors in the reconstructed activity were not entirely local, i.e. mismatches in other structures could also induce errors into the measured heart activity, due to the incorrect scaling of emission projections.

Overall it can be seen that the methods developed here were able to provide improvements in quantitative accuracy, compared to the case that no matching was performed during attenuation-correction, although a larger number of datasets would be required to determine the general applicability of the methods. Furthermore, these techniques require the acquisition of only a single CT and therefore have a clear advantage over the acquisition of a gated CT, where the dose is substantially higher. Problems with artefacts in gated CT acquisition are also largely overcome with the single CT approach, since only a single artefact-free image is needed, from which the other images are derived.

This technique of combining information obtainable from the images with knowledge of typical shapes and motions (through use of the statistical shape model) was found to be an appropriate replacement of a gated CT for the two datasets tested, thereby allowing motion-correction to be performed in a quantitatively accurate manner without additional dose and with a reduced dependence on potentially problematic gating.

8.2 Summary of Developed Motion-Correction Technique

Taking into account the findings from each investigation performed, the methods within each stage of the overall motion- and attenuation-correction technique were determined, leading to the following overall implementation:

1. Acquire a gated PET and single CT study, ensuring respiratory-matching between the CT frame and one of the PET frames, e.g. with the use of prospective CT gating, where a single frame is acquired at a specified respiratory position.
2. Segment the diaphragm in the single CT frame.
3. Estimate the diaphragm position, where visible, in the gated PET frames.
4. Perform model fitting to the set of combined PET and CT landmarks obtained from stages 2 and 3, to obtain a complete description of the diaphragm surface at all respiratory positions.
5. Perform a rigid-registration on the heart activity in the PET frames.
6. Transform the single CT according to the shape model and the rigid-registration results.
7. Perform a respiratory-matched attenuation-correction using the synthetic CT frames and reconstruct each PET frame.
8. Align the PET frames according to the rigid-registration parameters and sum the aligned frames.

Some discussion on the practical implementation of each of these stages has been given in the previous chapter; for example the need for the single CT frame to be matched in respiratory position to one of the PET frames and the level of automation required for routine use. The stages that currently require manual input are (2) and (3) above, for segmenting the diaphragm in CT and placing landmarks in PET, respectively, however as discussed further in Section 8.3 below, further investigations could be performed to reduce the manual input required and therefore make the technique more suitable for routine clinical

use. Finally, a potential quality control check was proposed in Section 5.4.6.2, which would allow an estimate of the model fitting success to be obtained in the absence of a gated CT for verification. This could be valuable in the clinical setting, where it would be important to identify cases where the diaphragm shape model is not appropriate (e.g. in the presence of respiratory motion abnormalities) and hence alternative methods should be considered.

8.2.1 Summary of Significant Findings

The main findings of the thesis work can be summarised as follows:

- Identification of the sources of attenuation-correction artefacts in PET-CT and SPECT-CT, indicating that mismatches originating in both the heart and the diaphragm positions can lead to artefacts in cardiac studies.
- A direct comparison of the location, extent and severity of attenuation-correction artefacts in PET and SPECT.
- The development of a semi-automatic algorithm for segmenting the diaphragm in CT images, achieving an average accuracy of within 2 mm.
- The demonstration of the construction and application of a diaphragm statistical shape model, constructed using segmented diaphragm surfaces from anatomically detailed images and applied to poor contrast, noisy PET images.
- The development of methods to transform a CT frame to other respiratory positions, ensuring the transformation of structures of importance in the attenuation-correction of cardiac images and thereby overcoming the need to acquire a gated CT.
- The demonstration of the developed motion- and attenuation-correction technique, involving a respiratory-matched attenuation-correction and a rigid-registration alignment of the cardiac activity.

8.3 Future Direction

Extensions to the work undertaken here could be performed if a larger number of suitable datasets were made available, for both the construction of the diaphragm shape model and for applying the developed techniques. The inclusion of additional datasets in the shape model training set would reduce the probability of a given dataset exhibiting a diaphragm shape or motion that had not previously been encountered in the training set, which is associated with high residual errors following model fitting. By increasing the training set size therefore, it would be expected that residual errors would reduce, making the technique

applicable to a greater number of patients. With regards to applying the model, while it was established that the method provided quantitative improvements in both datasets tested, repeating the testing on a larger number of patients would allow the general applicability of the approach to be determined by measuring the range and mean accuracies achieved.

Since model testing was performed with ^{18}F-FDG datasets, before implementing the technique for ^{82}Rb data, further tests would need to be carried out to ascertain the effects on model fitting of the use of the different tracer. A visual comparison between ^{18}F-FDG and ^{82}Rb images was performed to verify that the same general features were visible in both, but a more detailed assessment would be required, particularly in terms of the appearance of the diaphragm.

The effect of varying noise levels is also important in the use of the shape model and hence further investigations could be performed to ascertain what noise level could be tolerated. As noise increases, the requirements of the shape model to assist in diaphragm tracking also increase, however with extremely poor count statistics, there would be insufficient information with which to drive the model and hence determining the maximum level of noise tolerable would be necessary to ascertain whether the model could be used with extremely noisy images.

Further studies could also investigate different methods of model construction and application, to determine whether improved accuracies could be achieved. Examples of such studies include the investigation of different landmark placing techniques and the methods of fitting the model to the gated PET data. The regular grid used here allowed for a simple implementation of landmark placing and was also applicable to the PET studies, since a nearest-neighbour interpolation could be performed to align the PET landmark estimates to the model landmarks. More complex techniques, where landmarks are placed according to particular anatomical features rather than in a regular array, may produce improved landmark correspondences, however applying a model constructed in such a way to PET data would produce further challenges, due to the need to identify landmarks in corresponding positions in the gated PET frames.

One potential method of overcoming this would be to perform model fitting based directly on image intensity features, rather than identifying PET landmarks. In this scenario, the model is fitted according to gradients in image intensity, such that the fitted model surface is encouraged to align with intensity features. This has been implemented for the myocardial activity of the left ventricle (Tobon-Gomez et al., 2008), however using such a technique for fitting to the poorer contrast diaphragm may not be practical, particularly as the diaphragm does not represent the most prominent feature in many regions. Investigations could therefore be performed to ascertain whether this is the case or whether modifications to this general technique could make it more applicable to diaphragm shape fitting.

This is one potential approach to reducing the manual input required in the overall technique, which would be important in enabling its implementation into routine clinical use. Alternatively, landmark placing could be automated by making use of intensity features in the PET images, from which an initial estimate of diaphragm position would be obtained. Although implementing a technique for finding the entire diaphragm surface with a good level of accuracy would be very difficult (hence the need for a shape model), this would only be required for input into the model and hence gaps and some inaccuracies would be tolerable. This would therefore ease the challenges of automatic diaphragm position estimation, particularly as regions of very poor contrast could be omitted from this estimate. Another potential aid to the process could be the use of the single respiratory position at which the single CT is acquired. Assuming anatomy is matched in position to the corresponding PET frame, the CT image could be used to ascertain which features in PET correspond to the diaphragm. Landmark placing in other respiratory frames would then involve searching for similar features to those identified in the matched frame. This would help to limit the erroneous identification of non-diaphragm features.

The diaphragm segmentation described in Chapter 4 is the other main area that currently requires manual input. The algorithm was found to be successful both in terms of the accuracy with which it was able to describe the diaphragm surface and the time benefits it provided compared with a manual segmentation. However, additional improvements could still be implemented, which could reduce further the time required. Some potential improvements are outlined in Section 4.3.10, including the implementation of a 3D approach, rather than the 2D methods currently used and the identification of the heart region, for which different constraints or scoring systems could be introduced, to take account of the poorer contrast in this area. Improvements in the level of automation achieved would improve speed and hence enable the technique to be applied to a larger number of datasets, without a prohibitive time burden. This would be useful, not only in the segmentation of the single CT frame for use in model fitting, but also in the expansion of the statistical shape model training set. While the former of these would only be required in the initial construction of the model, the latter would be required for every patient to which the technique is to be applied and therefore it is important for this to be as fully automated as possible.

With the automation of the complete process and an expansion of the training set, this technique could provide a valuable tool for motion-correcting cardiac PET images with quantitative accuracy, which is not currently available in Nuclear Medicine clinics. Furthermore, the use of a single CT frame means that this can be achieved without any increase in dose to the patient.

References

Abdelnour, A. F., Nehmeh, S. A., Pan, T., Humm, J. L., Vernon, P., Schoder, H., Rosenzweig, K. E., Mageras, G. S., Yorke, E., Larson, S. M., and Erdi, Y. E. (2007). Phase and amplitude binning for 4D-CT imaging. *Physics in Medicine and Biology*, 52(12):3515–3529.

Achenbach, S., Moselewski, F., Ropers, D., Ferencik, M., Hoffmann, U., MacNeill, B., Pohle, K., Baum, U., Anders, K., Jang, I.-k., Daniel, W. G., and Brady, T. J. (2004). Detection of calcified and noncalcified coronary atherosclerotic plaque by contrast-enhanced, submillimeter multidetector spiral computed tomography: A segment-based comparison with intravascular ultrasound. *Circulation*, 109(1):14–17.

Ackerman, M. J. (1998). The Visible Human Project. *Proceedings of the IEEE*, 86(3):504–511.

Alvarez, R. E. and Macovski, A. (1976). Energy-selective reconstructions in X-ray computerised tomography. *Physics in Medicine and Biology*, 21(5):733–744.

Bacharach, S. L. (2007). PET/CT attenuation correction: Breathing lessons. *Journal of Nuclear Medicine*, 48(5):677–679.

Badawi, R. and Marsden, P. (1999). Self-normalization of emission data in 3D PET. *IEEE Transactions on Nuclear Science*, 46(3):709–712.

Bae, K. T., Giger, M. L., Chen, C.-T., and Charles E. Kahn, J. (1993). Automatic segmentation of liver structure in CT images. *Medical Physics*, 20(1):71–78.

Bai, C., Shao, L., Silva, A. J. D., and Zhao, Z. (2003). A generalized model for the conversion from CT numbers to linear attenuation coefficients. *IEEE Transactions on Nuclear Science*, 50(5):1510–1515.

Bailey, D. L., Karp, J. S., and Surti, S. (2005). *Positron Emission Tomography - Basic Sciences*, chapter Physics and Instrumentation in PET, pages 13–40. Springer-Verlag London.

Bateman, T. M. (2004). Cardiac positron emission tomography and the role of adenosine pharmacologic stress. *The American Journal of Cardiology*, 94(2, Supplement 1):19–24.

Bax, J. J. (2005). FDG imaging should be considered the preferred technique for accurate assessment of myocardial viability. *European Journal of Nuclear Medicine and Molecular Imaging*, 32(7):829–831.

Beichel, R., Bischof, H., Leberl, F., and Sonka, M. (2005). Robust active appearance models and their application to medical image analysis. *IEEE Transactions on Medical Imaging*, 24(9):1151–1169.

Beichel, R., Mitchell, S., Sorantin, E., Leberl, F., Goshtasby, A., and Sonka, M. (2001). Shape- and appearance-based segmentation of volumetric medical images. In *International Conference on Image Processing*, volume 2, pages 589–592.

Berbeco, R. I., Nishioka, S., Shirato, H., Chen, G. T. Y., and Jiang, S. B. (2005b). Residual motion of lung tumours in gated radiotherapy with external respiratory surrogates. *Physics in Medicine and Biology*, 50(16):3655–3667.

Bettinardi, V., Danna, M., Savi, A., Lecchi, M., Castiglioni, I., Gilardi, M. C., Bammer, H., Lucignani, G., and Fazio, F. (2004). Performance evaluation of the new whole-body PET/CT scanner: Discovery ST. *European Journal of Nuclear Medicine and Molecular Imaging*, 31(6):867–881.

Beyer, T., Antoch, G., Muller, S., Egelhof, T., Freudenberg, L. S., Debatin, J., and Bockisch, A. (2004). Acquisition protocol considerations for combined PET/CT imaging. *Journal of Nuclear Medicine*, 45(1):25S–35.

Beyer, T., Townsend, D. W., Brun, T., Kinahan, P. E., Charron, M., Roddy, R., Jerin, J., Young, J., Byars, L., and Nutt, R. (2000). A combined PET/CT scanner for clinical oncology. *Journal of Nuclear Medicine*, 41(8):1369–1379.

Biancia, C. D., Yorke, E., Chui, C.-S., Giraud, P., Rosenzweig, K., Amols, H., Ling, C., and Mageras, G. S. (2005). Comparison of end normal inspiration and expiration for gated intensity modulated radiation therapy (IMRT) of lung cancer. *Radiotherapy and Oncology*, 75(2):149–156.

Blackall, J. M., Ahmad, S., Miquel, M. E., McClelland, J. R., Landau, D. B., and Hawkes, D. J. (2006). MRI-based measurements of respiratory motion variability and assessment of imaging strategies for radiotherapy planning. *Physics in Medicine and Biology*, 51(17):4147–4169.

Blodgett, T. M., McCook, B. M., and Federle, M. P. (2006). Positron emission tomography/computed tomography: Protocol issues and options. *Seminars in Nuclear Medicine*, 36(2):157–168.

Bloomfield, P. M., Spinks, T. J., Reed, J., Schnorr, L., Westrip, A. M., Livieratos, L., Fulton, R., and Jones, T. (2003). The design and implementation of a motion correction scheme for neurological PET. *Physics in Medicine and Biology*, 48(8):959–978.

Bockisch, A., Beyer, T., Antoch, G., Freudenberg, L. S., Kühl, H., Debatin, J. F., and Müller, S. P. (2004). Positron emission tomography/computed tomography-imaging protocols, artifacts, and pitfalls. *Molecular Imaging & Biology*, 6(4):188–199.

Boldea, V., Sharp, G. C., Jiang, S. B., and Sarrut, D. (2008). 4D-CT lung motion estimation with deformable registration: Quantification of motion nonlinearity and hysteresis. *Medical Physics*, 35(3):1008–1018.

Boucher, L., Rodrigue, S., Lecomte, R., and Benard, F. (2004). Respiratory gating for 3-Dimensional PET of the thorax: Feasibility and initial results. *Journal of Nuclear Medicine*, 45(2):214–219.

Brett, A. and Taylor, C. (2008). A framework for automated landmark generation for automated 3D statistical model construction. In *Information Processing in Medical Imaging*, pages 376–381. Springer-Verlag.

Bruyant, P. P., King, M. A., and Pretorius, P. H. (2002). Correction of the respiratory motion of the heart by tracking of the center of mass of thresholded projections: a simulation study using the dynamic MCAT phantom. *IEEE Transactions on Nuclear Science*, 49(5):2159–2166.

Bruyant, P. P., Rest, C. C. L., Turzo, A., Jarritt, P., Carson, K., and Visvikis, D. (2007). A method for synchronizing an external respiratory signal with a list-mode PET acquisition. *Medical Physics*, 34(11):4472–4475.

Bundschuh, R., Martínez-Möller, A., Essler, M., Nekolla, S., Ziegler, S., and Schwaiger, M. (2008). Local motion correction for lung tumours in PET/CT - first results. *European Journal of Nuclear Medicine and Molecular Imaging*, 35(11):1981–1988.

Cai, J., Read, P. W., Altes, T. A., Molloy, J. A., Brookeman, J. R., and Sheng, K. (2007). Evaluation of the reproducibility of lung motion probability distribution function (PDF) using dynamic MRI. *Physics in Medicine and Biology*, 52(2):365–373.

Camara, O., Delso, G., and Bloch, I. (2002). Evaluation of a thoracic elastic registration method using anatomical constraints in oncology. In *Proceedings of the Second Joint EMBS/BMES Conference*, volume 2, pages 1011–1012.

Cao, Z., Gilland, D. R., Mair, B. A., and Jaszczak, R. J. (2003). Three-dimensional motion estimation with image reconstruction for gated cardiac ECT. *IEEE Transactions on Nuclear Science*, 50(3):384–388.

Cerqueira, M. D., Weissman, N. J., Dilsizian, V., Jacobs, A. K., Kaul, S., Laskey, W. K., Pennell, D. J., Rumberger, J. A., Ryan, T., and Verani, M. S. (2002). Standardized myocardial segmentation and nomenclature for tomographic imaging of the heart: A statement for healthcare professionals from the Cardiac Imaging Committee of the Council on Clinical Cardiology of the American Heart Association. *Circulation*, 105(4):539–542.

Chatziioannou, A., Dahlbom, M., and Hoh, C. (1994). Study on the use of transmission scans for whole body PET attenuation correction. *IEEE Transactions on Nuclear Science*, 41(4):1545–1550.

Chen, M., Kanade, T., Pomerleau, D., and Schneider, J. (1999). 3-D deformable registration of medical images using a statistical atlas. *Lecture Notes in Computer Science*, 1679:621–630.

Chi, P.-C. M., Balter, P., Luo, D., Mohan, R., and Pan, T. (2006). Relation of external surface to internal tumor motion studied with cine CT. *Medical Physics*, 33(9):3116–3123.

Chin, B. B., Nakamoto, Y., Kraitchman, D. L., Marshall, L., and Wahl, R. (2003). PET-CT evaluation of 2-deoxy-2-[18F]fluoro-d-glucose myocardial uptake: Effect of respiratory motion. *Molecular Imaging & Biology*, 5(2):57–64.

Clifford, M. A., Banovac, F., Levy, E., and Cleary, K. (2002). Assessment of hepatic motion secondary to respiration for computer assisted interventions. *Computer Aided Surgery*, 7(5):291–299.

Cluzel, P., Similowski, T., Chartrand-Lefebvre, C., Zelter, M., Derenne, J.-P., and Grenier, P. A. (2000). Diaphragm and chest wall: Assessment of the inspiratory pump with MR imaging-preliminary observations. *Radiology*, 215(2):574–583.

Collins, D. L., Holmes, C. J., Peters, T. M., and Evans, A. C. (1995). Automatic 3-D model-based neuroanatomical segmentation. *Human Brain Mapping*, 3:190–208.

Comon, P. (1994). Independent component analysis, a new concept? *Signal Processing*, 36(3):287–314.

Cook, R., Carnes, G., Ting-Yim, L., and Wells, R. G. (2005). 4D CT for respiratory gated attenuation corrections in canine cardiac PET imaging. *IEEE Nuclear Science Symposium Conference Record*, 4:2408–2412.

Cootes, T. F., Taylor, C. J., Cooper, D. H., and Graham, J. (1995). Active shape models-their training and application. *Computer Vision and Image Understanding*, 61(1):38–59.

Dalal, P., Munsell, B. C., Wang, S., Tang, J., Oliver, K., Ninomiya, H., Zhou, X., and Fujita, H. (2007). A fast 3D correspondence method for statistical shape modeling. In Munsell, B. C., editor, *Computer Vision and Pattern Recognition*, pages 1–8.

Danias, P. G., Stuber, M., Botnar, R. M., Kissinger, K. V., Edelman, R. R., and Manning, W. J. (1999). Relationship between motion of coronary arteries and diaphragm during free breathing: lessons from real-time MR imaging. *American Journal of Roentgenology*, 172(4):1061–1065.

Daube-Witherspoon, M., Carson, R., and Green, M. (1988). Post-injection transmission attenuation measurements for PET. *IEEE Transactions on Nuclear Science*, 35(1):757–761.

Davatzikos, C., Tao, X., and Shen, D. (2003). Hierarchical active shape models, using the wavelet transform. *IEEE Transactions on Medical Imaging*, 22(3):414–423.

Davies, R. H., Twining, C. J., Cootes, T. F., Waterton, J. C., and Taylor, C. J. (2002). A minimum description length approach to statistical shape modeling. *IEEE Transactions on Medical Imaging*, 21(5):525–537.

Davies, S. C., Hill, A. L., Holmes, R. B., Halliwell, M., and Jackson, P. C. (1994). Ultrasound quantitation of respiratory organ motion in the upper abdomen. *British Journal of Radiology*, 67(803):1096–1102.

Dawood, M., Buther, F., Jiang, X., and Schafers, K. P. (2008a). Respiratory motion correction in 3-D PET data with advanced optical flow algorithms. *IEEE Transactions on Medical Imaging*, 27(8):1164–1175.

Dawood, M., Kösters, T., Fieseler, M., Büther, F., Jiang, X., Wübbeling, F., and Schäfers, K. P. (2008b). Motion correction in respiratory gated cardiac PET/CT using multi-scale optical flow. *Lecture Notes in Computer Science*, 5242:155–162.

Dawood, M., Lang, N., Xiaoyi, J., and Schafers, K. P. (2006). Lung motion correction on respiratory gated 3-D PET/CT images. *IEEE Transactions on Medical Imaging*, 25(4):476–485.

DeGrado, T. R., Bergmann, S. R., Ng, C. K., and Raffel, D. M. (2000). Tracer kinetic modeling in nuclear cardiology. *Journal of Nuclear Cardiology*, 7(6):686–700.

deKemp, R. A. and Nahmias, C. (1994). Attenuation correction in PET using single photon transmission measurement. *Medical Physics*, 21(6):771–778.

DePuey, E. G., Garcia, E. V., and Berman, D. S., editors (2000). *Cardiac SPECT Imaging*. Lippincott Williams and Wilkins, 2nd edition.

Dey, J., Pan, T., Smyczynski, M., Pretorius, H., Choi, D., and King, M. A. (2005). Investigation of respiration motion of the heart based on semi-automated segmentation and modeling of respiratory-gated CT data. *IEEE Nuclear Science Symposium Conference Record*, 5:2557–2560.

Duda, R. O. and Hart, P. E. (1973). *Pattern Classification and Scene Analysis*. Wiley, New York.

Einstein, A. J., Moser, K. W., Thompson, R. C., Cerqueira, M. D., and Henzlova, M. J. (2007b). Radiation dose to patients from cardiac diagnostic imaging. *Circulation*, 116(11):1290–1305.

Erdi, Y. E., Nehmeh, S. A., Pan, T., Pevsner, A., Rosenzweig, K. E., Mageras, G., Yorke, E. D., Schoder, H., Hsiao, W., Squire, O. D., Vernon, P., Ashman, J. B., Mostafavi, H., Larson, S. M., and Humm, J. L. (2004). The CT motion quantitation of lung lesions and its impact on PET-measured SUVs. *Journal of Nuclear Medicine*, 45(8):1287–1292.

Fayad, H., Lamare, F., Bettinardi, V., Roux, C., and Visvikis, D. (2008). Respiratory synchronized ct image generation from 4d pet acquisitions. In *IEEE Nuclear Science Symposium Conference Record, 2008*, pages 5488–5492.

Fitzpatrick, G. M. and Wells, R. G. (2006). Simulation study of respiratory-induced errors in cardiac positron emission tomography/computed tomography. *Medical Physics*, 33(8):2888–2895.

Ford, E. C., Mageras, G. S., Yorke, E., and Ling, C. C. (2003). Respiration-correlated spiral CT: A method of measuring respiratory-induced anatomic motion for radiation treatment planning. *Medical Physics*, 30(1):88–97.

Frangi, A., Rueckert, D., Schnabel, J., and Niessen, W. (2002). Automatic construction of multiple-object three-dimensional statistical shape models: application to cardiac modeling. *IEEE Transactions on Medical Imaging*, 21(9):1151–1166.

Fujita, T., Chandrasekhar, R., Singh, B., and Finucane, K. E. (2005). Semi-automatic tracking of the diaphragm contour in x-ray image sequences: Preliminary results. In *Proceedings of the Digital Imaging Computing: Techniques and Applications*, pages 330–336.

Gauthier, A. P., Verbanck, S., Estenne, M., Segebarth, C., Macklem, P. T., and Paiva, M. (1994). Three-dimensional reconstruction of the in vivo human diaphragm shape at different lung volumes. *Journal of Applied Physiology*, 76(2):495–506.

Germano, G. and Hoffman, E. (1990). A study of data loss and mispositioning due to pileup in 2-D detectors in PET. *IEEE Transactions on Nuclear Science*, 37(2):671–675.

Gilland, D. R., Mair, B. A., Bowsher, J. E., and Jaszczak, R. J. (2002). Simultaneous reconstruction and motion estimation for gated cardiac ECT. *IEEE Transactions on Nuclear Science*, 49(5):2344–2349.

Gilland, D. R., Mair, B. A., and Parker, J. G. (2008). Motion estimation for cardiac emission tomography by optical flow methods. *Physics in Medicine and Biology*, 53(11):2991–3006.

Goerres, G. W., Burger, C., Kamel, E., Seifert, B., Kaim, A. H., Buck, A., Buehler, T. C., and von Schulthess, G. K. (2003). Respiration-induced attenuation artifact at PET/CT: Technical considerations. *Radiology*, 226(3):906–910.

Goerres, G. W., Kamel, E., Heidelberg, T.-N. H., Schwitter, M. R., Burger, C., and von Schulthess, G. K. (2002a). PET-CT image co-registration in the thorax: influence of respiration. *European Journal of Nuclear Medicine and Molecular Imaging*, 29(3):351–360.

Gould, K. L., Nakagawa, Y., Nakagawa, K., Sdringola, S., Hess, M. J., Haynie, M., Parker, N., Mullani, N., and Kirkeeide, R. (2000). Frequency and clinical implications of fluid dynamically significant diffuse coronary artery disease manifest as graded, longitudinal, base-to-apex myocardial perfusion abnormalities by noninvasive positron emission tomography. *Circulation*, 101(16):1931–1939.

Gould, K. L., Pan, T., Loghin, C., Johnson, N. P., Guha, A., and Sdringola, S. (2007). Frequent diagnostic errors in cardiac PET/CT due to misregistration of CT attenuation and emission PET images: A definitive analysis of causes, consequences, and corrections. *Journal of Nuclear Medicine*, 48(7):1112–1121.

Gould, K. L., Pan, T., Loghin, C., Johnson, N. P., and Sdringola, S. (2008). Reducing radiation dose in rest-stress cardiac PET/CT by single poststress cine CT for attenuation correction: Quantitative validation. *Journal of Nuclear Medicine*, 49(5):738–745.

Gravier, E., Yang, Y., King, M. A., and Jin, M. (2006). Fully 4D motion-compensated reconstruction of cardiac SPECT images. *Physics in Medicine and Biology*, 51(18):4603–4619.

Gravier, E. J. and Yang, Y. (2005). Motion-compensated reconstruction of tomographic image sequences. *IEEE Transactions on Nuclear Science*, 52(1):51–56.

Hanley, J., Debois, M. M., Mah, D., Mageras, G. S., Raben, A., Rosenzweig, K., Mychalczak, B., Schwartz, L. H., Gloeggler, P. J., Lutz, W., Ling, C. C., Leibel, S. A., Fuks, Z., and Kutcher, G. J. (1999). Deep inspiration breath-hold technique for lung tumors: the potential value of target immobilization and reduced lung density in dose escalation. *International Journal of Radiation Oncology*Biology*Physics*, 45(3):603–611.

Hany, T. F., Steinert, H. C., Goerres, G. W., Buck, A., and von Schulthess, G. K. (2002). PET diagnostic accuracy: Improvement with in-line PET-CT system: Initial results. *Radiology*, 225(2):575–581.

Haralick, R. M. and Shapiro, L. G. (1985). Image segmentation techniques. *Computer Vision, Graphics, and Image Processing*, 29(1):100–132.

Hausleiter, J., Meyer, T., Hadamitzky, M., Huber, E., Zankl, M., Martinoff, S., Kastrati, A., and Schomig, A. (2006). Radiation dose estimates from cardiac multislice computed tomography in daily practice: Impact of different scanning protocols on effective dose estimates. *Circulation*, 113(10):1305–1310.

Hill, A., Taylor, C. J., and Brett, A. D. (2000). A framework for automatic landmark identification using a new method of nonrigid correspondence. *IEEE Transactions on Pattern Analysis and Machine Intelligence*, 22(3):241–251.

Hoffmann, U., Ferencik, M., Cury, R. C., and Pena, A. J. (2006). Coronary CT angiography. *Journal of Nuclear Medicine*, 47(5):797–806.

Hudson, H. M. and Larkin, R. S. (1994). Accelerated image reconstruction using ordered subsets of projection data. *IEEE Transactions on Medical Imaging*, 13(4):601–609.

Huesman, R., Derenzo, S., Cahoon, J., Geyer, A., Moses, W., Uber, D., Vuletich, T., and Budinger, T. (1988). Orbiting transmission source for positron tomography. *IEEE Transactions on Nuclear Science*, 35(1):735–739.

Hyvärinen, A., Karhunen, J., and Oja, E. (2001). *Independent component analysis*. John Wiley and Sons, New York.

Kamel, E., Hany, T. F., Burger, C., Treyer, V., Lonn, A. H. R., von Schulthess, G. A., and Buck, A. (2002). CT vs 68Ge attenuation correction in a combined PET/CT system: evaluation of the effect of lowering the CT tube current. *European Journal of Nuclear Medicine and Molecular Imaging*, 29(3):346–350.

Karp, J. S., Muehllehner, G., Qu, H., and Yan, X.-H. (1995). Singles transmission in volume-imaging PET with a 137Cs source. *Physics in Medicine and Biology*, 40:929–944.

Kass, M., Witkin, A., and Terzopoulos, D. (1988). Snakes: Active contour models. *International Journal of Computer Vision*, 1:321–331.

Kaus, M., Pekar, V., Lorenz, C., Truyen, R., Lobregt, S., and Weese, J. (2003). Automated 3-D PDM construction from segmented images using deformable models. *IEEE Transactions on Medical Imaging*, 22(8):1005–1013.

Keall, P. J., Kini, V. R., Vedam, S. S., and Mohan, R. (2001). Motion adaptive x-ray therapy: a feasibility study. *Physics in Medicine and Biology*, 46(1):1–10.

Keall, P. J., Mageras, G. S., Balter, J. M., Emery, R. S., Forster, K. M., Jiang, S. B., Kapatoes, J. M., Low, D. A., Murphy, M. J., Murray, B. R., Ramsey, C. R., Van Herk,

M. B., Vedam, S. S., Wong, J. W., and Yorke, E. (2006). The management of respiratory motion in radiation oncology report of AAPM Task Group 76. *Medical Physics*, 33(10):3874–3900.

Keall, P. J., Starkschall, G., Shukla, H., Forster, K. M., Ortiz, V., Stevens, C. W., Vedam, S. S., George, R., Guerrero, T., and Mohan, R. (2004). Acquiring 4D thoracic CT scans using a multislice helical method. *Physics in Medicine and Biology*, 49(10):2053–2067.

Keegan, J., Gatehouse, P., Yang, G.-Z., and Firmin, D. (2002). Coronary artery motion with the respiratory cycle during breath-holding and free-breathing: Implications for slice-followed coronary artery imaging. *Magnetic Resonance in Medicine*, 47(3):476–481.

Kelemen, A., Szekely, G., and Gerig, G. (1999). Elastic model-based segmentation of 3-D neuroradiological data sets. *IEEE Transactions on Medical Imaging*, 18(10):828–839.

Khoo, V. S., Dearnaley, D. P., Finnigan, D. J., Padhani, A., Tanner, S. F., and Leach, M. O. (1997). Magnetic resonance imaging (MRI): Considerations and applications in radiotherapy treatment planning. *Radiotherapy and Oncology*, 42:1–15.

Kinahan, P., MacDonald, L., Ng, L., Alessio, A., Segars, P., Tsui, B., and Pathak, S. (2006). Compensating for patient respiration in PET/CT imaging with the registered and summed phases (RASP) procedure. In *Biomedical Imaging: Macro to Nano*, pages 1104–1107. IEEE.

Kinahan, P. E., Townsend, D. W., Beyer, T., and Sashin, D. (1998). Attenuation correction for a combined 3D PET/CT scanner. *Medical Physics*, 25(10):2046–2053.

Klein, G. J., Reutter, B. W., Ho, M. H., Reed, J. H., and Huesman, R. H. (1998b). Real-time system for respiratory-cardiac gating in positron tomography. *IEEE Transactions on Nuclear Science*, 45(4):2139–2143.

Klein, G. J., Reutter, B. W., and Huesman, R. H. (1997). Non-rigid summing of gated PET via optical flow. *IEEE Transactions on Nuclear Science*, 44(4):1509–1512.

Klein, G. J., Reutter, R. W., and Huesman, R. H. (2001b). Four-dimensional affine registration models for respiratory-gated PET. *IEEE Transactions on Nuclear Science*, 48(3):756–760.

Kluetz, P. G., Meltzer, C. C., Villemagne, V. L., Kinahan, P. E., Chander, S., Martinelli, M. A., and Townsend, D. W. (2000). Combined PET/CT imaging in oncology: Impact on patient management. *Clinical Positron Imaging*, 3(6):223–230.

Koikkalainen, J. and Lotjonen, J. (2004). Image segmentation with the combination of the PCA- and ICA-based modes of shape variation. In *IEEE International Symposium on Biomedical Imaging: Nano to Macro*, pages 149–152 Vol. 1.

Koikkalainen, J., Tolli, T., Lauerma, K., Antila, K., Mattila, E., Lilja, M., and Lotjonen, J. (2008). Methods of artificial enlargement of the training set for statistical shape models. *IEEE Transactions on Medical Imaging*, 27(11):1643–1654.

Korin, H. W., Ehman, R. L., Riederer, S. J., Felmlee, J. P., and Grimm, R. C. (1992). Respiratory kinematics of the upper abdominal organs: A quantitative study. *Magnetic Resonance in Medicine*, 23(1):172–178.

Kotcheff, A. C. and Taylor, C. J. (1998). Automatic construction of eigenshape models by direct optimization. *Medical Image Analysis*, 2(4):303–314.

Kovalski, G., Israel, O., Keidar, Z., Frenkel, A., Sachs, J., and Azhari, H. (2007). Correction of heart motion due to respiration in clinical myocardial perfusion SPECT scans using respiratory gating. *Journal of Nuclear Medicine*, 48(4):630–636.

Kubo, H. D. and Hill, B. C. (1996). Respiration gated radiotherapy treatment: a technical study. *Physics in Medicine and Biology*, 41:83–91.

Kubo, H. D., Len, P. M., Minohara, S.-i., and Mostafavi, H. (2000). Breathing-synchronized radiotherapy program at the University of California Davis Cancer Center. *Medical Physics*, 27(2):346–353.

LaCroix, K., Tsui, B., Hasegawa, B., and Brown, J. (1994). Investigation of the use of X-ray CT images for attenuation compensation in SPECT. *IEEE Transactions on Nuclear Science*, 41(6):2793–2799.

Lamare, F., Carbayo, M. J. L., Cresson, T., Kontaxakis, G., Santos, A., Rest, C. C. L., Reader, A. J., and Visvikis, D. (2007a). List-mode-based reconstruction for respiratory motion correction in PET using non-rigid body transformations. *Physics in Medicine and Biology*, 52(17):5187–5204.

Lamare, F., Cresson, T., Savean, J., Rest, C. C. L., Reader, A. J., and Visvikis, D. (2007b). Respiratory motion correction for PET oncology applications using affine transformation of list mode data. *Physics in Medicine and Biology*, 52(1):121–140.

Larie, S. M. and Abukmeil, S. S. (1998). Brain abmormailty in schizophrenia: A systematic and quantitative review of volumetric magnetic resonance imaging studies. *Journal of Psychology*, 172:110–120.

Lautamäki, R., Brown, T., Merrill, J., and Bengel, F. (2008). CT-based attenuation correction in 82Rb-myocardial perfusion PET-CT: incidence of misalignment and effect on regional tracer distribution. *European Journal of Nuclear Medicine and Molecular Imaging*, 35(2):305–310.

Le Meunier, L., Maass-Moreno, R., Carrasquillo, J. A., Dieckmann, W., and Bacharach, S. L. (2006). PET/CT imaging: Effect of respiratory motion on apparent myocardial uptake. *Journal of Nuclear Cardiology*, 13(6):821–830.

Lekadir, K., Merrifield, R., and Yang, G.-Z. (2007). Outlier detection and handling for robust 3-D active shape models search. *IEEE Transactions on Medical Imaging*, 26(2):212–222.

Li, T., Thorndyke, B., Schreibmann, E., Yang, Y., and Xing, L. (2006b). Model-based image reconstruction for four-dimensional PET. *Medical Physics*, 33(5):1288–1298.

Livieratos, L., Stegger, L., Bloomfield, P. M., Schafers, K., Bailey, D. L., and Camici, P. G. (2005). Rigid-body transformation of list-mode projection data for respiratory motion correction in cardiac PET. *Physics in Medicine and Biology*, 50(14):3313–3322.

Lodge, M. A., Braess, H., Mahmoud, F., Suh, J., Englar, N., Geyser-Stoops, S., Jenkins, J., Bacharach, S. L., and Dilsizian, V. (2005). Developments in nuclear cardiology: Transition from single photon emission computed tomography to positron emission tomography/computed tomography. *Journal of Invasive Cardiology*, 17:491–496.

Loghin, C., Sdringola, S., and Gould, K. L. (2004). Common artifacts in PET myocardial perfusion images due to attenuation-emission misregistration: Clinical significance, causes, and solutions. *Journal of Nuclear Medicine*, 45(6):1029–1039.

Low, D. A., Nystrom, M., Kalinin, E., Parikh, P., Dempsey, J. F., Bradley, J. D., Mutic, S., Wahab, S. H., Islam, T., Christensen, G., Politte, D. G., and Whiting, B. R. (2003). A method for the reconstruction of four-dimensional synchronized CT scans acquired during free breathing. *Medical Physics*, 30(6):1254–1263.

Lu, W. and Mackie, T. R. (2002). Tomographic motion detection and correction directly in sinogram space. *Physics in Medicine and Biology*, 47(8):1267–1284.

Lu, W., Parikh, P. J., Hubenschmidt, J. P., Bradley, J. D., and Low, D. A. (2006b). A comparison between amplitude sorting and phase-angle sorting using external respiratory measurement for 4D CT. *Medical Physics*, 33(8):2964–2974.

Lu, W., Parikh, P. J., Naqa, I. M. E., Nystrom, M. M., Hubenschmidt, J. P., Wahab, S. H., Mutic, S., Singh, A. K., Christensen, G. E., Bradley, J. D., and Low, D. A. (2005b). Quantitation of the reconstruction quality of a four-dimensional computed tomography process for lung cancer patients. *Medical Physics*, 32(4):890–901.

Mageras, G. S., Pevsner, A., Yorke, E. D., Rosenzweig, K. E., Ford, E. C., Hertanto, A., Larson, S. M., Lovelock, D. M., Erdi, Y. E., Nehmeh, S. A., Humm, J. L., and Ling, C. C. (2004). Measurement of lung tumor motion using respiration-correlated CT. *International Journal of Radiation Oncology*Biology*Physics*, 60(3):933–941.

Martinez-Möller, A., Souvatzoglou, M., Navab, N., Schwaiger, M., and Nekolla, S. G. (2007a). Artifacts from misaligned CT in cardiac perfusion PET/CT studies: Frequency, effects, and potential solutions. *Journal of Nuclear Medicine*, 48(2):188–193.

Mattes, D., Haynor, D. R., Vesselle, H., Lewellen, T. K., and Eubank, W. (2003). PET-CT image registration in the chest using free-form deformations. *IEEE Transactions on Medical Imaging*, 22(1):120–128.

McCall, K. C. and Jeraj, R. (2007). Dual-component model of respiratory motion based on the periodic autoregressive moving average (periodic ARMA) method. *Physics in Medicine and Biology*, 52(12):3455–3466.

McCord, M. E., Bacharach, S. L., Bonow, R. O., Dilsizian, V., Cuocolo, A., and Freedman, N. (1992). Misalignment between PET transmission and emission scans: Its effect on myocardial imaging. *Journal of Nuclear Medicine*, 33(6):1209–1214.

McCullough, E. C. (1975). Photon attenuation in computed tomography. *Medical Physics*, 2(6):307–320.

McInerney, T. and Terzopoulos, D. (1996). Deformable models in medical image analysis: a survey. *Medical Image Analysis*, 1(2):91–108.

McLeish, K., Hill, D. L. G., Atkinson, D., Blackall, J. M., and Razavi, R. (2002). A study of the motion and deformation of the heart due to respiration. *IEEE Transactions on Medical Imaging*, 21(9):1142–1150.

Meikle, S. R., Dahlbom, M., and Cherry, S. R. (1993). Attenuation correction using count-limited transmission data in positron emission tomography. *Journal of Nuclear Medicine*, 34(1):143–150.

Menke, M., Atkins, M. S., and Buckley, K. R. (1996). Compensation methods for head motion detected during PET imaging. *IEEE Transactions on Nuclear Science*, 43(1):310–317.

Morin, R. L., Gerber, T. C., and McCollough, C. H. (2003). Radiation dose in computed tomography of the heart. *Circulation*, 107(6):917–922.

Nagel, C. C. A., Bosmans, G., Dekker, A. L. A. J., Ollers, M. C., De Ruysscher, D. K. M., Lambin, P., Minken, A. W. H., Lang, N., and Schafers, K. P. (2006). Phased attenuation correction in respiration correlated computed tomography/positron emitted tomography. *Medical Physics*, 33(6):1840–1847.

Nehmeh, S. A. and Erdi, Y. E. (2008). Respiratory motion in positron emission tomography/computed tomography: A review. *Seminars in Nuclear Medicine*, 38(3):167–176.

Nehmeh, S. A., Erdi, Y. E., Ling, C. C., Rosenzweig, K. E., Schoder, H., Larson, S. M., Macapinlac, H. A., Squire, O. D., and Humm, J. L. (2002a). Effect of respiratory gating on quantifying PET images of lung cancer. *Journal of Nuclear Medicine*, 43(7):876–881.

Nehmeh, S. A., Erdi, Y. E., Meirelles, G. S. P., Squire, O., Larson, S. M., Humm, J. L., and Schoder, H. (2007). Deep-inspiration breath-hold PET/CT of the thorax. *Journal of Nuclear Medicine*, 48(1):22–26.

Nehmeh, S. A., Erdi, Y. E., Pan, T., Pevsner, A., Rosenzweig, K. E., Yorke, E., Mageras, G. S., Schoder, H., Phil, V., Squire, O., Mostafavi, H., Larson, S. M., and Humm, J. L. (2004a). Four-dimensional (4D) PET/CT imaging of the thorax. *Medical Physics*, 31(12):3179–3186.

Nehmeh, S. A., Erdi, Y. E., Pan, T., Yorke, E., Mageras, G. S., Rosenzweig, K. E., Schoder, H., Mostafavi, H., Squire, O., Pevsner, A., Larson, S. M., and Humm, J. L. (2004b). Quantitation of respiratory motion during 4D-PET/CT acquisition. *Medical Physics*, 31(6):1333–1338.

Nehrke, K., Bornert, P., Manke, D., and Bock, J. C. (2001). Free-breathing cardiac MR imaging: Study of implications of respiratory motion - initial results. *Radiology*, 220(3):810–815.

Nelder, J. and Mead, R. (1965). The downhill simplex method. *Computer Journal*, 7:308–313.

Nye, J. A., Esteves, F., and Votaw, J. R. (2007). Minimizing artifacts resulting from respiratory and cardiac motion by optimization of the transmission scan in cardiac PET/CT. *Medical Physics*, 34(6):1901–1906.

Ohara, K., Okumura, T., Akisada, M., Inada, T., Mori, T., Yokota, H., and Calaguas, M. J. (1989). Irradiation synchronized with respiration gate. *International Journal of Radiation Oncology*Biology*Physics*, 17(4):853–857.

Ordas, S., Boisrobert, L., Bossa, M., Huguet, M., Laucelli, M., Olmos, S., and Frangi, A. (2004). Grid-enabled automatic construction of a two-chamber cardiac PDM from a large database of dynamic 3D shapes. *IEEE International Symposium on Biomedical Imaging: Nano to Macro*, 1:416–419.

Pal, N. R. and Pal, S. K. (1993). A review on image segmentation techniques. *Pattern Recognition*, 26(9):1277–1294.

Pan, T., Lee, T.-Y., Rietzel, E., and Chen, G. T. Y. (2004). 4D-CT imaging of a volume influenced by respiratory motion on multi-slice CT. *Medical Physics*, 31(2):333–340.

Pan, T., Mawlawi, O., Nehmeh, S. A., Erdi, Y. E., Luo, D., Liu, H. H., Castillo, R., Mohan, R., Liao, Z., and Macapinlac, H. A. (2005). Attenuation correction of PET images with respiration-averaged CT images in PET/CT. *Journal of Nuclear Medicine*, 46(9):1481–1487.

Pham, D. L., Xu, C., and Prince, J. L. (2000). Current methods in medical image segmentation. *Annual Review of Biomedical Engineering*, 2(1):315–337.

Plathow, C., Zimmermann, H., Fink, C., Umathum, R., Schobinger, M., Huber, P., Zuna, I., Debus, J., Schlegel, W., and Meinzer, H.-P. (2005). Influence of different breathing maneuvers on internal and external organ motion: Use of fiducial markers in dynamic MRI. *International Journal of Radiation Oncology*Biology*Physics*, 62(1):238–245.

Polakowski, W., Cournoyer, D., Rogers, S., DeSimio, M., Ruck, D., Hoffmeister, J., and Raines, R. (1997). Computer-aided breast cancer detection and diagnosis of masses using difference of gaussians and derivative-based feature saliency. *IEEE Transactions on Medical Imaging*, 16(6):811–819.

Ponisch, F., Richter, C., Just, U., and Enghardt, W. (2008). Attenuation correction of four dimensional (4D) PET using phase-correlated 4D-computed tomography. *Physics in Medicine and Biology*, 53(13):N259–N268.

Qi, J. and Huesman, R. H. (2002). List mode reconstruction for PET with motion compensation: a simulation study. In *IEEE International Symposium on Biomedical Imaging*, pages 413–416.

Qiao, F., Pan, T., Clark Jr., J. W., and Mawlawi, O. R. (2006b). A motion-incorporated reconstruction method for gated PET studies. *Physics in Medicine and Biology*, 51(15):3769–3783.

Rahmim, A., Bloomfield, P., Houle, S., Lenox, M., Michel, C., Buckley, K. R., Ruth, T. J., and Sossi, V. (2004). Motion compensation in histogram-mode and list-mode EM reconstructions: beyond the event-driven approach. *IEEE Transactions on Nuclear Science*, 51(5):2588–2596.

Reutter, B., Klein, G. J., and Huesman, R. H. (1997). Automated 3-D segmentation of respiratory-gated PET transmission images. *IEEE Transactions on Nuclear Science*, 44(6):2473–2476.

Reza, F. M. (1994). *An Introduction to Information Theory.* Constable and Company, Dover, New York.

Rietzel, E., Pan, T., and Chen, G. T. Y. (2005). Four-dimensional computed tomography: Image formation and clinical protocol. *Medical Physics*, 32(4):874–889.

Ritchie, C. J., Hsieh, J., Gard, M. F., Godwin, J. D., Kim, Y., and Crawford, C. R. (1994). Predictive respiratory gating: a new method to reduce motion artifacts on CT scans. *Radiology*, 190(3):847–852.

Rosamond, W., Flegal, K., Friday, G., Furie, K., Go, A., Greenlund, K., Haase, N., Ho, M., Howard, V., Kissela, B., Kittner, S., Lloyd-Jones, D., McDermott, M., Meigs, J., Moy, C., Nichol, G., O'Donnell, C. J., Roger, V., Rumsfeld, J., Sorlie, P., Steinberger, J., Thom, T., Wasserthiel-Smoller, S., Hong, Y., for the American Heart Association Statistics Committee, and Subcommittee, S. S. (2007). Heart disease and stroke statistics - 2007 update: A report from the American Heart Association Statistics Committee and Stroke Statistics Subcommittee. *Circulation*, 115(5):e69–e171.

Ruan, D., Fessler, J. A., Balter, J. M., Berbeco, R. I., Nishioka, S., and Shirato, H. (2008b). Inference of hysteretic respiratory tumor motion from external surrogates: a state augmentation approach. *Physics in Medicine and Biology*, 53(11):2923–2936.

Ruan, D., Fessler, J. A., Balter, J. M., and Sonke, J.-J. (2006). Exploring breathing pattern irregularity with projection-based method. *Medical Physics*, 33(7):2491–2499.

Rueckert, D., Frangi, A., and Schnabel, J. (2003). Automatic construction of 3-D statistical deformation models of the brain using nonrigid registration. *IEEE Transactions on Medical Imaging*, 22(8):1014–1025.

Rueckert, D., Sonoda, L. I., Hayes, C., Hill, D. L. G., Leach, M. O., and Hawkes, D. J. (1999). Nonrigid registration using free-form deformations: application to breast MR images. *IEEE Transactions on Medical Imaging*, 18(8):712–721.

Sanchez-Crespo, A., Andreo, P., and Larsson, S. A. (2004). Positron flight in human tissues and its influence on PET image spatial resolution. *European Journal of Nuclear Medicine and Molecular Imaging*, 31(1):44–51.

Schleyer, P. J., O'Doherty, M. J., Barrington, S. F., and Marsden, P. K. (2009). Retrospective data-driven respiratory gating for PET/CT. *Physics in Medicine and Biology*, 54(7):1935–1950.

Schwaiger, M. (1995). *The Heart: Left Ventricular Failure.* W. B. Saunders Company, Bellingham, Washington, Philadelphia, 2nd edition.

Segars, P. (2001). *Development and application of the new dynamic NURBS-based cardiac-torso (NCAT) phantom.* PhD thesis, University of North Carolina.

Segars, W. P., Lalush, D. S., and Tsui, B. M. W. (1999). A realistic spline-based dynamic heart phantom. *IEEE Transactions on Nuclear Science*, 46(3):503–506.

Segars, W. P., Lalush, D. S., and Tsui, B. M. W. (2001). Modeling respiratory mechanics in the MCAT and spline-based MCAT phantoms. *IEEE Transactions on Nuclear Science*, 48(1):89–97.

Segars, W. P., Mahesh, M., Beck, T. J., Frey, E. C., and Tsui, B. M. W. (2008). Realistic CT simulation using the 4D XCAT phantom. *Medical Physics*, 35(8):3800–3808.

Segars, W. P., Tsui, B. M. W., Frey, E. C., and Fishman, E. K. (2003). Extension of the 4D NCAT phantom to dynamic X-ray CT simulation. *IEEE Nuclear Science Symposium Conference Record*, 5:3195–3199.

Selwyn, A. P., Allan, R. M., L'Abbate, A., Horlock, P., Camici, P., Clark, J., O'Brien, H. A., and Grant, P. M. (1982). Relation between regional myocardial uptake of rubidium-82 and perfusion: Absolute reduction of cation uptake in ischemia. *The American Journal of Cardiology*, 50(1):112–121.

Seppenwoolde, Y., Shirato, H., Kitamura, K., Shimizu, S., van Herk, M., Lebesque, J. V., and Miyasaka, K. (2002). Precise and real-time measurement of 3D tumor motion in lung due to breathing and heartbeat, measured during radiotherapy. *International Journal of Radiation Oncology*Biology*Physics*, 53(4):822–834.

Shechter, G., Ozturk, C., Resar, J. R., and McVeigh, E. R. (2004). Respiratory motion of the heart from free breathing coronary angiograms. *IEEE Transactions on Medical Imaging*, 23(8):1046–1056.

Shen, D., Herskovits, E., and Davatzikos, C. (2001). An adaptive-focus statistical shape model for segmentation and shape modeling of 3-D brain structures. *IEEE Transactions on Medical Imaging*, 20(4):257–270.

Shirato, H., Shimizu, S., Kitamura, K., Nishioka, T., Kagei, K., Hashimoto, S., Aoyama, H., Kunieda, T., Shinohara, N., Dosaka-Akita, H., and Miyasaka, K. (2000). Four-dimensional treatment planning and fluoroscopic real-time tumor tracking radiotherapy for moving tumor. *International Journal of Radiation Oncology*Biology*Physics*, 48(2):435–442.

Simon, B. A. (2005). Regional ventilation and lung mechanics using X-ray CT. *Academic Radiology*, 12(11):1414–1422.

Souvatzoglou, M., Bengel, F., Busch, R., Kruschke, C., Fernolendt, H., Lee, D., Schwaiger, M., and Nekolla, S. (2007). Attenuation correction in cardiac PET/CT with three different CT protocols: a comparison with conventional PET. *European Journal of Nuclear Medicine and Molecular Imaging*, 34(12):1991–2000.

Studholme, C., Hill, D. L. G., and Hawkes, D. J. (1999). An overlap invariant entropy measure of 3D medical image alignment. *Pattern Recognition*, 32(1):71–86.

Styner, M., Rajamani, K., Nolte, L.-P., Zsemlye, G., Székely, G., Taylor, C., and Davies, R. (2003). Evaluation of 3D correspondence methods for model building. In *Information Processing in Medical Imaging*, pages 63–75. Springer-Verlag.

Suzuki, Y., Slomka, P. J., Wolak, A., Ohba, M., Suzuki, S., De Yang, L., Germano, G., and Berman, D. S. (2008). Motion-frozen myocardial perfusion SPECT improves detection of coronary artery disease in obese patients. *Journal of Nuclear Medicine*, 49(7):1075–1079.

Taylor, P. (1995). Invited review: Computer aids for decision-making in diagnostic radiology - a literature review. *British Journal of Radiology*, 68(813):945–957.

Ter-Pogossian, M. M. (1995). *Principles of Nuclear Medicine*, chapter Positron Emission Tomography (PET): General Principles, pages 342–346. W.B. Saunders Company, Philadelphia, Philadelphia, 2nd edition.

Ter-Pogossian, M. M., Bergmann, S. R., and Sobel, B. E. (1982). Influence of cardiac and respiratory motion on tomographic reconstructions of the heart: Implications for quantitative nuclear cardiology. *Journal of Computer Assisted Tomography*, 6(6):1148–1155.

Teräs, M., Tolvanen, T., Johansson, J., Williams, J., and Knuuti, J. (2007). Performance of the new generation of whole-body PET/CT scanners: Discovery STE and Discovery VCT. *European Journal of Nuclear Medicine and Molecular Imaging*, 34(10):1683–1692.

Thielemans, K., Mustafovic, S., and Schnorr, L. (2003). Image reconstruction of motion corrected sinograms. *IEEE Nuclear Science Symposium Conference Record*, 4:2401–2406.

Thorndyke, B., Schreibmann, E., Koong, A., and Xing, L. (2006). Reducing respiratory motion artifacts in positron emission tomography through retrospective stacking. *Medical Physics*, 33(7):2632–2641.

Tobon-Gomez, C., Butakoff, C., Aguade, S., Sukno, F., Moragas, G., and Frangi, A. F. (2008). Automatic construction of 3D-ASM intensity models by simulating image acquisition: Application to myocardial gated SPECT studies. *IEEE Transactions on Medical Imaging*, 27(11):1655–1667.

Townsend, D. W. and Beyer, T. (2002). A combined PET/CT scanner: the path to true image fusion. *British Journal of Radiology*, 75:S24–30.

van Assen, H., Danilouchkine, M., Dirksen, M., Reiber, J., and Lelieveldt, B. (2008). A 3-D Active Shape Model driven by fuzzy inference: Application to cardiac CT and MR. *IEEE Transactions on Information Technology in Biomedicine*, 12(5):595–605.

Vedam, S. S., Keall, P. J., Kini, V. R., and Mohan, R. (2001). Determining parameters for respiration-gated radiotherapy. *Medical Physics*, 28(10):2139–2146.

Vedam, S. S., Keall, P. J., Kini, V. R., Mostafavi, H., Shukla, H. P., and Mohan, R. (2003a). Acquiring a four-dimensional computed tomography dataset using an external respiratory signal. *Physics in Medicine and Biology*, 48(1):45–62.

Vedam, S. S., Kini, V. R., Keall, P. J., Ramakrishnan, V., Mostafavi, H., and Mohan, R. (2003b). Quantifying the predictability of diaphragm motion during respiration with a noninvasive external marker. *Medical Physics*, 30(4):505–513.

Verschakelen, J. A., Van fraeyenhoven, L., Laureys, G., Demedts, M., and Baert, A. L. (1993). Differences in CT density between dependent and nondependent portions of the lung: influence of lung volume. *American Journal of Roentgenology*, 161(4):713–717.

Viola, P. and Wells, W. M. (1995). Alignment by maximization of mutual information. *International Journal of Computer Vision*, 24:137–154.

Visvikis, D., Barret, O., Fryer, T., Turzo, A., Lamare, F., Cheze Le Rest, C., and Bizais, Y. (2003). A posteriori respiratory motion gating of dynamic PET images. *IEEE Nuclear Science Symposium Conference Record*, 5:3276–3280.

Visvikis, D., Barret, O., Fryer, T. D., Lamare, F., Turzo, A., Bizais, Y., and Le Rest, C. C. (2004). Evaluation of respiratory motion effects in comparison with other parameters affecting PET image quality. *IEEE Nuclear Science Symposium Conference Record*, 6:3668–3672.

Wade, O. L. (1954). Movements of the thoracic cage and diaphragm in respiration. *Journal of Physiology*, 124(2):193–212.

Wagman, R., Yorke, E., Ford, E., Giraud, P., Mageras, G., Minsky, B., and Rosenzweig, K. (2003). Respiratory gating for liver tumors: use in dose escalation. *International Journal of Radiation Oncology*Biology*Physics*, 55(3):659–668.

Wang, Y., Riederer, S. J., and Ehman, R. L. (1995). Respiratory motion of the heart: Kinematics and the implications for the spatial resolution in coronary imaging. *Magnetic Resonance in Medicine*, 33(5):713–719.

Woo, S.-K., Choi, J. Y., Song, T. Y., Choi, Y., Lee, K.-H., and Kim, B.-T. (2004). Development of a motion correction system for respiratory-gated PET study. *IEEE Nuclear Science Symposium Conference Record*, 4:2366–2369.

Worth, A. J., Makris, N., Caviness, V. S., and Kennedy, D. N. (1997). Neuroanatomical segmentation in MRI: Technological objectives. *International Journal of Pattern Recognition and Artificial Intelligence*, 11:1161–1187.

Wu, T.-H., Huang, Y.-H., Lee, J. S., Wang, S.-Y., Wang, S.-C., Su, C.-T., Chen, L.-K., and Chu, T.-C. (2004). Radiation exposure during transmission measurements: comparison

between CT- and germanium-based techniques with a current PET scanner. *European Journal of Nuclear Medicine and Molecular Imaging*, 31(1):38–43.

Yakimovsky, Y. (1976). Boundary and object detection in real world images. *Journal of the Association for Computing Machinery*, 23(4):599–618.

Zhang, Y. J. (1996). A survey on evaluation methods for image segmentation. *Pattern Recognition*, 29(8):1335–1346.

Zhou, X., Ninomiya, H., Hara, T., Fujita, H., Yokoyama, R., Chen, H., Kiryu, T., and Hoshi, H. (2008). Automated estimation of the upper surface of the diaphragm in 3-D CT images. *IEEE Transactions on Biomedical Engineering*, 55(1):351–353.

Üzümcü, M., Frangi, A., Sonka, M., Reiber, J., and Lelieveldt, B. (2003). ICA vs. PCA active appearance models: Application to cardiac MR segmentation. *Lecture Notes in Computer Science*, 2878:451–458.

Appendix A

Publications Arising From Thesis Work

Please note: Publications prior to 2008 are in my maiden name, Sarah Martin. After this date, publications are in my married name, Sarah McQuaid.

A.1 Segmenting and Tracking Diaphragm and Heart Regions in Gated-CT Datasets as an Aid to Developing a Predictive Model for Respiratory Motion-Correction

Martin, S. J. Dey, J., King, M. A. and Hutton, B. F. (2007). Segmenting and Tracking Diaphragm and Heart Regions in Gated-CT Datasets as an Aid to Developing a Predictive Model for Respiratory Motion-Correction. *IEEE Nuclear Science Symposium Conference Record*, 2680-2685.

A.2 Sources of Attenuation-Correction Artefacts in Cardiac PET/CT and SPECT/CT

McQuaid, S. J. and Hutton, B. F. (2008). Sources of attenuation-correction artefacts in cardiac PET/CT and SPECT/CT. *European Journal of Nuclear Medicine and Molecular Imaging*, 35:1117-1123.

A.3 Statistical Shape Modeling of the Diaphragm for Application to Rb-82 Cardiac PET-CT Studies

McQuaid, S. J., Lambrou, T and Hutton, B. F. (2008). Statistical Shape Modeling of the Diaphragm for Application to Rb-82 Cardiac PET-CT Studies. *IEEE Nuclear Science Symposium Conference Record*, 3651 - 3655.

A.4 The Application of a Statistical Shape Model to Diaphragm Tracking in Respiratory-Gated Cardiac PET Images

McQuaid, S. J., Lambrou, T., Cunningham, V., Bettinardi, V., Gilardi, M. C. and Hutton, B. F. (2009). The Application of a Statistical Shape Model to Diaphragm Tracking in Respiratory-Gated Cardiac PET Images. *Proceedings of the IEEE (Special Issue on Computational Anthropomorphic Models)*, in press.

Appendix B

Contents of Accompanying CD

The accompanying CD contains an electronic version of this thesis (SJMcQuaid_PhDThesis.pdf) and the animation files, which are associated with figures in the body of this document.

All animations are given in the Powerpoint file on the CD: All_animations.pps. In the case that Powerpoint cannot be accessed, the individual animation files can also be viewed by opening the files on the CD in the locations shown in the following sections. Software for showing MPEG files and animated GIF files are required for viewing the animations in this way.

The following sections include a description of each animation, the reference to the figure in the body of the thesis it is associated with and the location of the animation on the CD.

B.1 The Motion of the Segmented Diaphragm Surfaces with Respiration

The segmented diaphragm surfaces of a single patient at 10 positions over the respiratory cycle, equally spaced in phase.

A single frame from this sequence (the end-inhale frame) is also displayed in Figure 4.13 on page 113.

Animation file on CD:

AnimationFiles/B-1_DiaphragmSurfaces.mpg

B.2 The Output of the Diaphragm Statistical Shape Model

B.2.1 The Variation of the End-Inhale Fitted Diaphragm Surfaces with Varying Eigenvector Weightings

The output of the diaphragm shape model for the end-inhale respiratory position. The first 9 modes of variation are shown, where the weighting of each mode is varied between $\pm 2\sqrt{\lambda_k}$ in steps of $\frac{\lambda_k}{4}$, where λ_k is the eigenvalue associated with mode k. The weighting of all other modes is set to 0.

The shapes produced by the first 5 modes of variation at $+2\sqrt{\lambda_k}$ and $-2\sqrt{\lambda_k}$ are shown in Figure 5.2 on page 142.

Animation on CD:

AnimationFiles/B-2-1_ShapeModelOutput_allModes.gif

B.2.2 The Motion of the Fitted Diaphragm Surfaces Over the Respiratory Cycle

The diaphragm shapes produced with b_1 set to $+2\sqrt{\lambda_1}$ (top), 0 (middle) and $-2\sqrt{\lambda_1}$ (bottom) at 10 positions over the respiratory cycle, equally spaced in phase. Weightings of all other modes are set to zero (i.e. $b_{k>1} = 0$).

The end-inhale and end-exhale frames from this sequence is shown in Figure 5.3 on page 143.

Animation on CD:

AnimationFiles/B-2-2_ShapeModelOutput_allPhases.gif

B.3 The Transformed CT Datasets: Comparison of the 2 Region and 3 Region Methods

A coronal slice through all respiratory frames of the transformed CT sets of a) patient 1 and b) patient 2, using the 2 and 3 region methods to divide the CT volume. Both transformed datasets were obtained using the all-patient model to transform the abdomen region.

The end-exhale frames of these sequences are shown in Figure 6.13 on page 200.

Animation on CD:

a): AnimationFiles/B-3-a_TransCT_Pt1_2regv3reg.gif

b): AnimationFiles/B-3-b_TransCT_Pt2_2regv3reg.gif

B.4 The Transformed CT Datasets: Comparison with the Original Gated CT Datasets

B.4.1 Coronal Views of the Original and Transformed CT Datasets of Patient 1

The original and transformed CT datasets for patient 1 at 6 respiratory positions over the respiratory cycle, equally spaced in phase. Abdomen transformation was according to a) the all-patient shape model results and b) the leave-one-out shape model results. In both cases the 3 region method was used for dividing the CT volume for transformation.

The end-exhale frames from these sequences are shown in Figure 6.14 on page 201.

Animation on CD:

a): AnimationFiles/B-4-1-a_TransCT_Pt1_cor_allptModel.gif

b): AnimationFiles/B-4-1-b_TransCT_Pt1_cor_L1OModel.gif

B.4.2 Sagittal Views of the Original and Transformed CT Datasets of Patient 1

The original and transformed CT datasets for patient 1 at 6 respiratory positions over the respiratory cycle, equally spaced in phase. Abdomen transformation was according to a) the all-patient shape model results and b) the leave-one-out shape model results. In both cases the 3 region method was used for dividing the CT volume for transformation.

The end-exhale frames from these sequences are shown in Figure 6.15 on page 201.

Animation on CD:

a): AnimationFiles/B-4-2-a_TransCT_Pt1_sag_allptModel.gif

b): AnimationFiles/B-4-2-b_TransCT_Pt1_sag_L1OModel.gif

B.4.3 Coronal Views of the Original and Transformed CT Datasets of Patient 2

The original and transformed CT datasets for patient 2 at 6 respiratory positions over the respiratory cycle, equally spaced in phase. Abdomen transformation was according to a) the all-patient shape model results and b) the leave-one-out shape model results. In both cases the 3 region method was used for dividing the CT volume for transformation.

The end-exhale frames from these sequences are shown in Figure 6.16 on page 201.

Animation on CD:

a): AnimationFiles/B-4-3-a_TransCT_Pt2_cor_allptModel.gif

b): AnimationFiles/B-4-3-b_TransCT_Pt2_cor_L1OModel.gif

B.4.4 Sagittal Views of the Original and Transformed CT Datasets of Patient 2

The original and transformed CT datasets for patient 2 at 6 respiratory positions over the respiratory cycle, equally spaced in phase. Abdomen transformation was according to a) the all-patient shape model results and b) the leave-one-out shape model results. In both cases the 3 region method was used for dividing the CT volume for transformation.

The end-exhale frames from these sequences are shown in Figure 6.17 on page 202.

Animation on CD:

a): AnimationFiles/B-4-4-a_TransCT_Pt2_sag_allptModel.gif

b): AnimationFiles/B-4-4-b_TransCT_Pt2_sag_L1OModel.gif